

Synthesis and Characterisation of Porous PMMA for Use in the Pressure Casting of Ceramics

Thesis submitted to The University of Manchester for the degree of Doctor of
Philosophy in the Faculty of Engineering and Physical Sciences

2013
Catherine M Gibson

The School of Materials

Table of Contents

Table of Contents	2
List of Figures	7
List of Tables	17
Abbreviations	19
Abstract	20
Declaration	21
Copyright Statements	21
Acknowledgements	22
1. Introduction	23
1.1 Aims	23
1.2 The Casting of Ceramics	24
1.2.1 Die Casting	24
1.2.2 Slip Casting	25
1.2.3 Pressure Casting	26
1.2.4 Casting of Sanitaryware	27
1.3 Free Radical Polymerisation	28
1.3.1 Mechanism for Free-Radical Polymerisation of Porous PMMA	30
1.3.2 Polymerisation Kinetics	36
1.4 Polymerisation Processes	38
1.4.1 Bulk Polymerisation	38
1.4.2 Solution Polymerisation	39
1.4.3 Suspension Polymerisation	39
1.4.4 Emulsion Polymerisation	39
1.4.5 The Polymerisation Process in the Preparation of Porous PMMA Materials	42

2. Review of Porosity and Porous Materials	43
2.1 Porous Materials	43
2.2 Measuring Porosity	45
2.1.1 Intrusion Methods	46
2.1.2 Fluid Displacement.....	46
2.1.3 Optical Methods.....	47
2.2.3 Gas Adsorption.....	47
2.3 Formation of Porous Polymers/Cellular Materials	48
2.3.1 Microporous Materials	48
2.3.2 Compacting	50
2.3.3 Subtractive Porosity	54
2.3.4 Foaming.....	55
2.4 Porous PMMA for use as Bone Cement and Surgical Dressings	56
2.5 Porous PMMA in the Making of Ceramics	58
2.6 Summary	60
3. Experimental Details for the Synthesis and Characterisation of Porous PMMA	61
3.1 Characterisation of the Starting Materials	61
3.1.1 PMMA Bead characterisation using Gel Permeation Chromatography (GPC)	62
3.1.2 Surfactant Characterisation	66
3.2 Preparation of Porous PMMA.....	73
3.3 Characterisation of Porous PMMA Materials and their Emulsions	74
3.3.1 Characterisation of the Emulsion.....	74
3.3.2 Characterisation of Porous PMMA	79
3.3.3 Thermal Properties	86
3.3.4 Porosity and Permeability	88
3.3.5 Visualisation Techniques.....	92
4. Establishing Experimental Methodologies.....	97
4.1 Introduction	97

4.2 Evolution of the Standard Blend Methodology	97
4.3 Effect of Surface Area: Volume Ratio.....	100
4.4 Effect of Oxygen.....	102
4.5 Oven Temperature.....	104
4.6 PMMA Bead Properties.....	105
4.6.1 Diameter of the PMMA Bead.....	106
4.6.2 Molar Mass of PMMA Beads.....	109
4.7 Monomer Droplet Size	111
4.8 Summary	116
5. Effect of Surfactant on the Properties of Porous PMMA.....	117
5.1 Introduction	117
5.2 Characterisation of Surfactants	118
5.2.1 NMR Structure Elucidation	119
5.2.2 Critical Micelle Concentration (CMC).....	128
5.2.3 Solubility Constant	131
5.3 Partitioning of the Emulsion	134
5.3 Varying the Tail Group of the Surfactant	144
5.4 Varying the Hydrophilic-Lipophilic Balance	146
5.5 Varying the Level of Surfactant.....	149
5.5.1 Triton X100.....	150
5.5.2 Lutensol TO Surfactant Range.....	153
5.6 Anionic Surfactants	157
5.7 Effect of Surfactant on the Glass Transition Temperature (T_g).....	164
5.8 Summary	168
6. Varying the Monomer to Water Concentration	172
6.1 Introduction	172
6.2 Varying the MMA:Water Ratio with Triton X100.....	173
6.3 Varying the MMA:Water Ratio with Lutensol TO3 and Lutensol TO109	176

6.4 Summary	182
7. Alternative Monomers	183
7.1 Introduction	183
7.2 Substitution of MMA by Styrene	183
7.3 Substitution of MMA with Isobutyl Methacrylate and Tert-butyl Methacrylate	190
7.4 Summary	194
8. Toughening of PMMA Ligaments.....	195
8.1 Introduction	195
8.2 Overview of Literature on the Toughening of Brittle Plastics.....	195
8.2.1 Toughening of Brittle Plastics by Using a Rubber	195
8.2.2 Examples of the Rubber-Toughening of Brittle Plastics.....	199
8.2.3 Toughening of Brittle Plastics by Using Rigid Particles	203
8.2.4 Toughening of Porous PMMA.....	206
8.2.5 Literature Review Summary.....	208
8.3 Toughening of Porous PMMA with Rubber Toughening Particles (XC42)	209
8.3.1 Synthesis of Porous PMMA with XC42.....	209
8.3.2 Results and Discussion	209
8.4 Toughening with Polybutadiene Diacrylate (PBDDA)	214
8.4.1 Characterisation of PBDDA	214
8.4.2 Synthesis of Porous PMMA with PBDDA	217
8.4.3 Results and Discussion	218
8.5 Copolymer of PMMA-PBDDA.....	220
8.5.1 Synthesis of PMMA-PBDDA Copolymer.....	220
8.5.2 Characterisation of PMMA-PBDDA Copolymer	221
8.5.3 Synthesis of Porous PMMA with PMMA-PBDDA Copolymer	224
8.5.4 Results and Discussion of Porous PMMA with PMMA-PBDDA Copolymer	224
8.6 Conclusions	228
9. Visualisation of the Ligaments	229

9.1 Optical Microscopy	229
9.2 Scanning Electron Microscopy (SEM)	231
9.3 Confocal Fluorescence Microscopy	235
9.3 X-Ray Computerised Tomography	236
9.3.1 Varying the Surfactant Level	238
9.3.2 Variation of MMA content	241
9.3.3 Additional Samples Analysed using X-ray Tomography	250
9.4 Conclusions	250
10. Conclusions and Suggestions for Further Work.....	252
10.1 Mechanistic Understanding	252
10.2 MMA:Water Concentration	256
10.3 Surfactant.....	256
10.4 Alternative Monomers.....	257
10.5 Toughening	257
10.6 Suggestions for Further Work.....	258
11. References	259
Appendix 1: Testing of Porous PMMA, Division of the Material	269
Appendix 2: Additional Data Tables and Graphs	271
Appendix 2.1: Triton X100	271
Appendix 2.2 Hydrophilic Lipophilic Balance (HLB) of the surfactant	272
Appendix 2.3 Lutensol TO3	272
Appendix 2.4 Lutensol TO6	273
Appendix 2.5 Lutensol TO109	274
Appendix 2.6 Stacked Graphical Figure for Compressive Properties of Different Surfactants	275
Appendix 2.7 MMA Variation with Triton X100.....	276
Appendix 2.8 Polybutadiene Dimethacrylate Addition to PMMA.....	276

Final word count: 74,298 words

List of Figures

Figure 1.1: Diagrams of slip casting process detailing the difference between drain and solid casting[11].....	25
Figure 1.2: Schematic of slip pressing taken from paper by Bauer ⁹	27
Figure 1.3: Orbital depiction for electron withdrawing substituents and electron donating substituents where the blue arrow signifies the energy change.....	29
Figure 1.4: Typical sp^2 hybridisation of a carbon radical	30
Figure 1.5: Thermal homolysis of a peroxide bond	31
Figure 1.6: Initiation of benzoyl peroxide by N,N- dimethyl- <i>p</i> -toluidene.....	31
Figure 1.7: β scission of benzoyloxy radical	31
Figure 1.8: S_N2 mechanism for donation of a pair of electrons to destabilise the peroxide bond with resulting products.....	32
Figure 1.9: Initiation of methyl methacrylate in porous PMMA by initiation by benzoyloxy radical formed in the redox reaction between DMPT and BPO	32
Figure 1.10: Side reactions in initiation using benzoyl peroxide	33
Figure 1.11: Propagation step showing head to tail addition.....	33
Figure 1.12: Generic mechanism for propagation in MMA free-radical polymerisation	34
Figure 1.13: Mechanism for disproportionation.....	34
Figure 1.14: Generic scheme depicting the mechanism of chain transfer	35
Figure 1.15: Mechanism of backbiting to form an internal radical shown for the polymerisation of ethylene.....	36
Figure 1.16: Schematic showing the mechanism for emulsion polymerisation showing the three phases (i) the aqueous phase containing surfactant above its CMC, small amounts of dissolved monomer (M) and initiator (I^\bullet); (ii) monomer-swollen micelles stabilised by surfactant and (iii) large monomer droplets shown in part.[29]	40
Figure 1.17: Illustration to show the formation of PMMA ligaments between the pre-formed PMMA beads.....	42
Figure 2.1: Classification of pores by size[35].....	43
Figure 2.2: Defining porosity by pore type	44
Figure 2.3: Schematic of a porous solid showing variations in pore shape.....	44
Figure 2.4: Part of the framework structure of naturally occurring zeolites, tschortnerite (lhs) and boggsite (rhs). Only the tetrahedrally coordination framework cations are shown for clarity[45].	49

Figure 2.5: Example of a calixarenes with para-ter-butyl substituents showing chemical structure and 3D representation of the cone formed	49
Figure 2.6: Condensation of aniline with benzaldehyde which forms N-benzylidene-aniline. This is then reacted with the product of D and E which join together to produce a tetrahedral structure, G [50].....	50
Figure 2.7: Diagrams of a cell indicating nomenclature used and of a body-centred cubic cell	50
Figure 2.8: Diagrams showing face-centred cubic packing structures	52
Figure 2.9: Sintering a powder. Stage 1; powder particles after pressing. Stage 2; particle coalescence and pore formation begins. Stage 3; as sintering proceeds, pores change size and shape.....	53
Figure 2.10: Effect of pressure on porous PMMA formed by the super-critical foaming of CO ₂ at (a) 25 MPa, (b) 20 MPa and (c) 15 MPa[67].	56
Figure 2.11: Influence of mixing time on porosity (from left to right) 30 s, 60 s, 90 s and 120 s [76] of an acrylic dough with a cellulose gel.	57
Figure 2.12: Diagram of simple cubic structure of large beads (red) encasing the smaller bead (yellow)	59
Figure 3.1: Separation in a GPC column by molecular size [89]	63
Figure 3.2: Calibration curve for GPC using PMMA standards with known molar mass.....	66
Figure 3.3: Divergence of energy levels on applying a magnetic field.....	67
Figure 3.4: Visualisation of frequency shift due to shielding[90]	68
Figure 3.5: Diagram showing the parameter in the Laplace equation for pendant drop analysis.....	70
Figure 3.6: Surface tension against log(concentration) for a surfactant in water highlighting detection of the CMC[96]	72
Figure 3.7: UV calibration for Triton X100 in MMA for absorption at 254 nm	76
Figure 3.8: Diagram showing light ray passing through two different mediums	76
Figure 3.9: Diagram showing key parameters for determination of refractive index in an Abbe Refractometer	78
Figure 3.10: Diagram of Abbe refractometer reading with illuminated and dark regions dissecting the crosshairs	78
Figure 3.11: Abbe calibration curves for refractive index of Lutensol surfactants dissolved in MMA	79
Figure 3.12: Determination of K for MMA using butan-1-ol as an internal standard	81

Figure 3.13: Diagram showing key points along the stress-strain curve	83
Figure 3.14: Variations in stress concentration around defects[108]	85
Figure 3.15: Features of a DSC trace for an amorphous sample of a crystalline polymer	87
Figure 3.16: Example of a typical DSC trace.....	88
Figure 3.17: Schematic of the permeability rig designed and built at the University of Manchester	90
Figure 3.18: Photographs of (a) the permeability rig and (b) the test cell	91
Figure 3.19: Interaction of a high velocity electron atoms[115] (a) backscattered electrons, (b) secondary imaging mode, (c) emission of a photon.	93
Figure 3.20: Effect of surface topography on the secondary electron signal showing a) dark regions and b) light regions[116]	93
Figure 3.21: SEM micrograph showing dark artefacts in the image	94
Figure 4.1: Pre- and post-compression testing of porous PMMA material after 30 minutes stirring of the emulsion. The red arrows highlight the propagation of the crack through the ligaments.....	99
Figure 4.2: Micrographs of fatigue crack paths in bone cement (on the left) and acrylic glass (on the right). Taken from D.Hoey & D. Taylor[126]. The white arrows signify the crack propagation through the sample.....	100
Figure 4.3: Formation of a peroxy radical.....	102
Figure 4.4: Effect of oxygen on the set time at different surface area to volume ratios	103
Figure 4.5: Photograph of the purpose-built temperature controlled chamber.....	104
Figure 4.6: Plot showing how the PMMA bead size affects the compressive properties of porous PMMA materials.....	107
Figure 4.7: SEM pictures showing a) samples made with 93 μm diameter beads and b) samples made with 42 μm diameter beads highlighting the difference in connectivity	108
Figure 4.8: Effect of stirring time on the compressive performance of porous PMMA.	113
Figure 4.9: Effect of stirring time on porosity and permeability	114
Figure 4.10: SEM of porous PMMA at 1 kX after a) 3 minutes stirring and b) 30 minutes stirring. Highlighted are regions showing differences in ligament volume	115
Figure 4.11: Comparing the effects of sonication and mechanical mixing on the average maximum compressive stress of porous PMMA samples	115
Figure 5.1: Structure of a Lutensol TO surfactant where x signifies the ethylene oxide chain length	118
Figure 5.2: NMR structure elucidation and peak analysis of Triton X100	120

Figure 5.3: NMR structure elucidation and peak analysis of Lutensol TO3	121
Figure 5.4: NMR spectra of Disponil FES32 and assignment of resonances.....	124
Figure 5.5: NMR spectra of Disponil A1080 and assignment of resonances	125
Figure 5.6: CMC of Triton X100, Lutensol TO109, Lutensol TO6, Lutensol TO3 in a) water and b) an MMA-saturated aqueous solution.....	128
Figure 5.7: Surface tension against concentration for a surfactant in water highlighting the CMC value[148].....	129
Figure 5.8: Cartoon of a micelle in water showing the formation and how a hydrophobic substance A can become solubilised by dissolution in the central core.	131
Figure 5.9: Structures of Lutensol TO109 and Triton X100 as derived from NMR	144
Figure 5.10: Effect of surfactant HLB on the set time of porous PMMA	147
Figure 5.11: Effect of HLB on permeability and porosity	147
Figure 5.12: SEM image of void left by trapped air bubble for a materials made with Lutensol TO20	148
Figure 5.13: Effect of changing the HLB of the surfactant on the compressive properties of the materials	149
Figure 5.14: Effect of surfactant concentration as a percentage of the total wt on the compressive performance of porous PMMA.....	150
Figure 5.15: Effect of Triton X100 levels on the fatigue performance of porous PMMA showing a) effect on the average maximum compressive stress, b) strain difference and height loss after 10,000 cycles at 14 kN and c) the correlation of fatigue against compressive stress.....	151
Figure 5.16: Effect of T_g as measured by DSC on average maximum compressive stress for materials made with Triton X100	152
Figure 5.17: Effect of surfactant level on permeability	153
Figure 5.18: Structures of a) Lutensol TO3, b) TO6 and c) TO109 as derived from NMR (see Section 5.2.1)	153
Figure 5.19: Effect of surfactant treat rate on average maximum compressive stress.....	154
Figure 5.20: Fatigue results at 14 kN \pm 2 kN varying the surfactant level for Triton X100, Lutensol TO109 and Lutensol TO3 showing a) height loss after 10,000 cycles and b) strain difference	155
Figure 5.21: Effect of surfactant level on T_g	156
Figure 5.22: Structure of FES32 (derived from NMR, see Section 5.2.1) and SDS.....	158

Figure 5.23: SEMs of a) Disponil FES32 based materials and b) materials made using the standard formation	159
Figure 5.24: Extent of polymerisation of MMA using Triton X100 and FES-32 as a surfactant as monitored by a) GC b) precipitation.....	162
Figure 5.25: UV spectra of DMPT in a) the presence of FES32 (blue) against a control where no surfactant is present (red) and b) in the presence of FES32 in water (blue) and a control of acidified water (red)	163
Figure 5.26: Mechanism for redox initiation of benzoyl peroxide with DMPT.....	163
Figure 5.27: Protonation of DMPT in more acidic media	164
Figure 5.28: Depression of T_g as the concentration of surfactant increases	165
Figure 5.29: Effect of changing the volume fraction of the polymer (V_p) to solvent on the T_g of MMA [181].....	166
Figure 5.30: Comparison of experimental T_g s and calculated T_g at different volume fractions of PMMA	166
Figure 5.31: Effect of T_g on compressive properties for porous PMMA made using Triton X100	167
Figure 5.32: Comparison of model study to actual results obtained from PMMA samples	168
Figure 6.1: Micrographs of fatigue crack paths in bone cement (on the left) and acrylic glass (on the right). Taken from Hoey and Taylor[188].....	172
Figure 6.2: Effect of increasing the monomer %wt on the compressive properties of porous PMMA	173
Figure 6.3: SEM images for materials made with a) 8.75 b) 9.41 c) 10.52 d) 11.10 e) 12.02 monomer %wt of the total mass of components.....	174
Figure 6.4: Effect of monomer level on a) porosity and b) permeability	175
Figure 6.5: Amount of MMA and its effect on set time.....	175
Figure 6.6: Effect of changing the monomer wt% compared to the total wt % of components on the average maximum compressive stress with Lutensol TO109, Lutensol TO3 and Triton X100	176
Figure 6.7: Effect of changing the wt % of monomer compared to the total wt % of components on the permeability for Triton X100, Lutensol TO109 and Lutensol TO3.....	177
Figure 6.8: SEM images for materials made with Lutensol TO3 using a)8.59 b)10.38 c)11.37 d)11.65 e)11.91 monomer wt% compared to the total wt % of components	178
Figure 6.9: SEM images for materials made with Lutensol TO109 using a)8.42 b)9.09 c)11.23 d)11.52 e)11.79 wt % of monomer compared to the total wt % of components	179

Figure 6.10: Fatigue results for porous PMMA materials made with different wt % of monomer compared to the total wt % of components using Triton X100 and Lutensol TO3 as a surfactant.....	180
Figure 6.11: SEM images highlighting crack propagation through ligaments at 250x, 500x, and 1k x magnification. The images show the beads are undamaged by compression testing, however, a lack of ligaments branching the gap indicates they have been severed	180
Figure 6.12: Schematic of expansion of fatigue crack zone due to the presence of porosity where a) no pores are present and b) pores are in the vicinity of the crack[190]	181
Figure 7.1: MMA conversion to polymerisation with time.....	184
Figure 7.2: Data from bulk polymerisation a) conversion of MMA with time b) conversion of styrene with time	187
Figure 7.3: Differential analysis of DSC data with styrene as a comonomer using a) 100% styrene and b) 20 % styrene	190
Figure 7.4: DSC data for a porous PMMA-based materials prepared from a) styrene and b) iso-BMA c) tert-BMA (see Table 7.3)	193
Figure 7.5: SEM images of materials made with iso-butyl methacrylate	194
Figure 7.6: SEM images of materials made with tert-butyl methacrylate.....	194
Figure 8.1: An elliptical crack of length $2a$, width $2b$ with a stress σ at the crack tip. The blue-shaded area represents a stress-free zone above and below the crack.	197
Figure 8.2: Structure of trifunctional macromonomer PIB(MMA)	200
Figure 8.3: Schematic of a 3-layer rubber-toughened particle as used by Lovell et al[217].	201
Figure 8.4: Schematic of crack pinning mechanism where (i) is the materials prior to fracture (ii) the pinning stage ((iii) bowing and (iv) break-away[16]	203
Figure 8.5: Effect of addition of 5 % clay on the maximum compressive stress on porous PMMA[85] where F is the applied force and U the crack propagation in mm in a notched specimen.	206
Figure 8.6: Effect of XC42 on compressive properties.....	211
Figure 8.7: Effect of XC42 on fracture toughness	211
Figure 8.8: SEM of porous PMMA with addition of 1 % XC42 particles.....	212
Figure 8.9: SEM of porous PMMA with addition of 0.5 % XC42 particles.....	212
Figure 8.10: SEM image of porous PMMA with 0.1 % XC42 with 20 minutes high shear mixing.....	213

Figure 8.11: Stress-strain curves showing the fracture nature of materials made using the standard blend and by those with XC42 particles at 0.5% with degassing of the mixture prior to use. The arrows indicate the approximate point at which a visible crack appears	213
Figure 8.12: ^1H NMR spectra of polybutadiene diacrylate and assignment of resonances.	216
Figure 8.13: ^{13}C NMR spectra of polybutadiene diacrylate and assignment of resonances	217
Figure 8.14: Effect on compressive properties of incorporation of PBDDA	218
Figure 8.15: Effect of PBDDA incorporation on fracture toughness.....	219
Figure 8.16: SEM images of porous PMMA materials with 10% PBDDA	220
Figure 8.17: ^1H -NMR spectrum of PMMA and polybutadiene diacrylate graft and assignment of resonances	223
Figure 8.18: GPC chromatograms and molar mass data for polybutadiene diacrylate and its graft copolymer with MMA	224
Figure 8.19: Effect of PMMA-PBDDA addition on compressive properties.....	225
Figure 8.20: Effect of PMMA-PBDDA concentration of porosity and permeability.....	226
Figure 8.21: Effect of PBDDA on toughness of the materials with a) PBDDA (in red) and b) PMMA-PBDDA graft copolymer (blue)	226
Figure 8.22: SEM images of materials made using 1.04 wt % of Triton X100 with a) 15 % PMMA-PBDDA incorporation at 1.5K magnification, b) 15 % PMMA-PBDDA incorporation at 500x magnification c) 55% PMMA-PBDDA at 1.5K times magnification d) 0% PMMA-PBDDA at 1.5K magnification.	227
Figure 8.23: SEM image of a standard material which contains 1.04 wt % of Triton X100 indicating smooth ligaments.....	228
Figure 9.1: Optical microscopy images using a) reflection and b) transmission settings on a standard sample of porous PMMA.....	229
Figure 9.2: Images obtained from transmission optical microscopy for materials made with a) 10.79 % MMA, b) 10.0 % MMA and c) 8.16 % MMA	230
Figure 9.3: Images showing considerable contamination from the saw blade used in the preparation of samples made using the standard blend formulation (4.99 wt% MMA)	230
Figure 9.4: Images indicating secondary porosity caused by air being trapped in the mould material during blending in samples made with 8.16 wt% MMA.	231
Figure 9.5: Improvements in optical microscopy highlighting ligaments between beads for materials made using 11.33 wt % of MMA.....	231

Figure 9.6 Example of an SEM indicating damage caused by fracture technique for samples made using the standard blend procedure.	232
Figure 9.7: SEM micrograph showing dark artefacts in the image caused by burning of the sample for a material made with Lutensol TO15 as a surfactant at 1.10 wt%.	232
Figure 9.8: SEM images of porous PMMA materials produced with monomer levels at a) 6.60 wt %, b) 10.38 wt%, c) 14.80 wt% and d) 16.05 wt % showing thickening of ligaments as the level increases with Triton X100	233
Figure 9.9: SEM images indicating the effect of differences in formulation from a) styrene with Triton X100 to b) styrene with TO3	233
Figure 9.10: SEM images of materials made where the standard emulsion mix has been stirred at different intensities for 10 minutes where a) is from a mechanical overhead stirring b) is from high intensity shearing and c) is from sonication	234
Figure 9.11: SEM images of materials with 1.76 wt % of Triton X100 a) without washing b) post-wash and c) a higher magnification image of an unwashed sample highlighting surfactant around beads.....	235
Figure 9.12: Fluorescent image of porous PMMA produced with 1% fluorescein- σ -methacrylate	236
Figure 9.13: X-ray tomography images of orthoslices of porous PMMA materials made using 8.86 wt % showing an orthoslice in the x plane and orthoslices in the x,y plane. Each orthoslice is built up around a single point allow a 3-D image to be recreated.....	237
Figure 9.14: X-ray tomography segmentation of a porous PMMA material made with 0.36 wt % of Lutensol TO109 with 146.66 g of MMA a) the PMMA material beads and ligaments b) the open porosity c) the closed porosity	239
Figure 9.15: Reconstructed images for materials made with a) 3.46 wt % of Triton X100 and b) 1.34 wt % of Triton X100 where blue signifies pores and cream the PMMA (beads and ligaments)	240
Figure 9.16 Reconstructed images for materials made with a) 4.45 wt % of Lutensol TO109 and b) 0.36 wt % of Lutensol TO109 blue signifies pores and cream, PMMA (beads and ligaments)	240
Figure 9.17: Reconstructed 3D images of materials made with a) Triton X100 and MMA at 8.59 wt%, b)) Triton X100 and MMA at 11.65 wt%, d) Lutensol TO3 and MMA at 8.59 wt%, and d) Lutensol TO3 and MMA at 11.60 wt%.....	241

Figure 9.18: X-ray tomography segmentation of a porous PMMA material made with 8.84 % MMA with Lutensol TO3 showing a) the PMMA beads and ligaments b) the open porosity c) the closed porosity.....	242
Figure 9.19: SEM image of a large pores most likely caused by the trapping of air in the mixing stage of the materials for a sample with 8.84 wt % MMA with Lutensol TO3	243
Figure 9.20: X-ray tomography images selecting the polymer, the open pores and the closed pores for materials made with a) 8.59 wt% of MMA with Triton X100 b) 11.65 wt% of MMA with Triton X100 and c) 11.60 wt% of MMA with Lutensol TO3	243
Figure 9.21: X-ray tomography segmentation of a porous PMMA material made with 11.65 % MMA with Triton X100 showing a) the open porosity b) the closed porosity and c) the interconnected porous network when the lighter areas signify higher flow through the area based on pore width.	244
Figure 9.22: X-ray tomography images highlighting pore channels in materials with a) low levels of MMA (8.95 wt%) and b) high levels of MMA (11.95 wt%) with Triton X100	244
Figure 9.23: Layer by layer porosity from X-ray tomography for sample with high levels of MMA (11.60 wt%) and low levels of MMA (8.84 wt%) made with Triton X100 as surfactant. Straight lines indicate the average value of porosity.	246
Figure 9.24: X-ray Tomography reconstructed images indicating large voids in the matrix material of materials with high levels of MMA (11.60 wt%) with Triton X100 as a surfactant	246
Figure 9.25: SEM images of materials with high levels of MMA (13.35 wt%) indicating large air void	246
Figure 9.26: Layer by layer porosity from X-ray tomography samples for high (11.65 wt %) and low (8.58 wt %) levels of MMA with Lutensol TO3 as surfactant. Straight lines indicate the average value of porosity.	247
Figure 9.27: Segregation steps: a) section of a porous PMMA specimen b) PMMA segregation with too low a threshold, c) PMMA segregation with too high a threshold value d) PMMA segregation with an ideal threshold [265].....	248
Figure 9.28: a) Representation of the voxel separation with a threshold grey value of 30, b) 3D image of the PMMA in the cube, c) 3D image of the pore network, and d) Assembly of a full 3D image for the material.....	248
Figure 9.29: Graphical representation for variation of porosity (lhs) and permeability (rhs) with wt % MMA from X-ray tomography and laboratory experiments.....	249
Figure 10.1: Schematic diagram showing partitioning of the emulsion components	253

Figure 10.2 Cartoon depicting addition of PMMA beads and formation of ligaments through coalescence of monomer droplets	254
---	-----

List of Tables

Table 2.1: Examples of porous materials and their properties[9]	45
Table 3.2: Table of materials.....	62
Table 3.1: Chemical shifts on CH ₃ X	69
Table 3.2: Literature values for CMC of Triton X100, Lutensol TO109, Lutensol TO6, and Lutensol TO3 compared to experimental data	72
Table 4.1: Comparison of methodologies for the formation of porous PMMA (standard deviation given in parenthesis).....	98
Table 4.2: Comparison of maximum temperature and compressive stress at different surface area to volume ratios for the production of porous PMMA (standard deviation given in parenthesis).....	101
Table 4.3: Results of changing oven temperature (standard deviation given in parenthesis)	105
Table 4.4: Results of varying the PMMA bead size on the properties of porous PMMA (standard deviation given in parenthesis)	106
Table 4.5: Effect of PMMA bead molecular weight on the porosity and compressive properties of porous PMMA (standard deviation given in parenthesis)	109
Table 4.6: Effects of the stirring intensity on the properties of porous PMMA (standard deviation given in parenthesis).....	112
Table 5.1: Structure derivation for Lutensol surfactants from NMR where the integrals for each region is given.....	122
Table 5.2: Structure derivation for Congis surfactants from NMR where the integral for each region is given	126
Table 5.3: Structure comparison of data obtained from NMR and supplier data sheets ...	127
Table 5.4: Details of experimentally obtained CMC and N_A/Γ_s for Triton X100, Lutensol TO109, Lutensol TO6, and Lutensol TO3.....	130
Table 5.5: Derivation of solubility parameters for Triton X100 and Lutensol TO surfactants	133
Table 5.6: Data used in the calculation of phase partitioning	135
Table 5.7: Partitioning calculations and results for Triton X100 in a standard blend formulation	139
Table 5.8 Output for partitioning calculations for Triton X100	140
Table 5.9: Constants for Lutensol surfactants	141

Table 5.10: Output from partitioning calculations for Lutensol surfactants	142
Table 5.11: Comparison of materials made using Triton X100 and Lutensol TO109 as a surfactant (numbers in parenthesis are standard deviations)	145
Table 5.12: Results for lower concentrations of Disponil FES32 (numbers in parenthesis are standard deviations)	159
Table 5.13: Results for the comparative Triton X100 study at low levels (numbers in parenthesis are standard deviations)	160
Table 7.1: Results of exchanging MMA for styrene in the standard formulation with Triton X100 (numbers in parenthesis are standard deviations).....	185
Table 7.2: Substitution of MMA by styrene at 10 %, and 20 % in an optimised blend formulation (standard deviation given in parenthesis)	188
Table 7.3: Substitution for MMA of tert-BMA and iso –BMA, styrene using Lutensol TO3 as a surfactant (standard deviations are given in parenthesis)	192
Table 8.1: Results for materials containing varying levels of rubber-toughening XC-42 particles (standard deviations are given in parenthesis).....	210
Table 8.2: Results in varying the level of polybutadiene diacrylate to porous PMMA.....	219
Table 8.3: Results for porous PMMA made with varying levels of polybutadiene diacrylate-MMA graft copolymer.....	225
Table 9.1: Blend formulations for X-ray tomography samples	238
Table 9.2: Percentage porosity obtained from segmentation analysis of reconstructed X-ray images with different levels of surfactant	240
Table 9.3: Percentage porosity obtained from segmentation analysis of reconstructed X-ray images with different levels of surfactant	242
Table 9.4: Comparison of porosity and permeability data obtained from X-ray tomography and lab experiments for materials with varying MMA levels	245
Table 9.5: Comparison of porosity and permeability data determined using X-ray tomography data and laboratory techniques.....	249
Table 9.6: Summary of porosity and permeability measurements obtained for additional samples analysed by X-ray tomography	250

Abbreviations

BPO	Benzoyl peroxide
ⁱ BMA	Iso-butyl methacrylate
^t BMA	Tertiary- butyl methacrylate
CMC	Critical micelle concentration
DMPT	Dimethyl- <i>para</i> -toluidine
DSC	Differential scanning calorimetry
GC	Gas chromatography
GPC	Gel permeation calorimetry
IR	Infrared
IUPAC	International union of applied chemistry
MMA	Methyl methacrylate
NMR	Nuclear magnetic resonance
PBDDA	Polybutadiene diacrylate
PMMA	Poly(methyl methacrylate)
RI	Refractive index
SEM	Scanning electron microscopy
SI	International system (of units)
SOMO	Singularly occupied molecular orbital
SN ₂	Nucleophilic substitution
TA	Transfer agent
T _g	Glass transition temperature
UV	Ultra violet

Abstract

The University of Manchester

Catherine Mary Gibson

Doctor of Philosophy in the Faculty of Engineering and Physical Sciences

The Synthesis and Characterisation of MMA for the Use in the Pressure Casting of Ceramics

Gypsum has been used almost exclusively as the mould material for casting sanitary-ware due to its high versatility, strength and homogenous pore distribution. However gypsum moulds have a number of disadvantages including deterioration on contact with water, deformation, long set times and short mould lives such that a large number of moulds are required for a commercial manufacturing processes. These drawbacks have led to attempts to find a new synthetic material to create moulds with similar properties to gypsum with respect to fine homogeneous pores, but with increased durability. Porous PMMA was developed in 1971 for the purpose of moulding ceramics. The basic approach to making the materials has remained unchanged since its commercial introduction with few academic studies undertaken on the formulations. This thesis describes an investigation into porous PMMA from an academic perspective studying the mechanism of formation of the materials and the role of the components in polymerisation. In particular: the surfactant type and level, monomer type, water to monomer ratio and bead size have been probed to assess their effect on the porosity and mechanical strength.

A particular importance has been placed on the commercial viability of formulations because gypsum is a relatively inexpensive material and, due to its versatility and ease of manufacture, is still used throughout the ceramics industry. To increase cost competitiveness through spreading the higher cost of the raw materials and capital investment, the mechanical strength of porous PMMA materials has to be significantly greater to increase the number of casting cycles from each mould. In addition, to achieve competitive advantage in the marketplace, a deep understanding of the formulation was undertaken. This should allow for tailoring of the mould properties allowing for specialised moulds for different applications. In addition, this focused approach facilitates cost-savings allowing for the minimum input of raw materials.

The thesis is a comprehensive body of work which looks individually at the components assessing their effect on the properties of the final material. In addition, the formation mechanism of the materials has been explored by breaking down the polymerisation into key stages. Highlighted is the excessive use of surfactant in a commercial formulation and the influence of plasticisation of the ligaments by the surfactant and excess monomer. The theory behind the polymerisation process, which generates the ligaments and traps the polymer beads in an immobile matrix, is developed; forming a comprehensive understanding of the formation of porous PMMA materials and factors influencing their development and final properties.

Declaration

No portion of the work referred to in this thesis has been submitted in support of an application for another degree or qualification of this or any other university or other institute of learning.

Catherine Gibson

Copyright Statements

- i. The author of this thesis (including any appendices and/or schedules to this thesis) owns certain copyright or related rights in it (the “Copyright”) and s/he has given The University of Manchester certain rights to use such Copyright, including for administrative purposes.
- ii. Copies of this thesis, either in full or in extracts and whether in hard or electronic copy, may be made **only** in accordance with the Copyright, Designs and Patents Act 1988 (as amended) and regulations issued under it or, where appropriate, in accordance with licensing agreements which the University has from time to time. This page must form part of any such copies made.
- iii. The ownership of certain Copyright, patents, designs, trade marks and other intellectual property (the “Intellectual Property”) and any reproductions of copyright works in the thesis, for example graphs and tables (“Reproductions”), which may be described in this thesis, may not be owned by the author and may be owned by third parties. Such Intellectual Property and Reproductions cannot and must not be made available for use without the prior written permission of the owner(s) of the relevant Intellectual Property and/or Reproductions.
- iv. Further information on the conditions under which disclosure, publication and commercialisation of this thesis, the Copyright and any Intellectual Property and/or Reproductions described in it may take place is available in the University IP Policy (see <http://documents.manchester.ac.uk/DocuInfo.aspx?DocID=487>), in any relevant Thesis restriction declarations deposited in the University Library, The University Library’s regulations (see <http://www.manchester.ac.uk/library/aboutus/regulations>) and in The University’s policy on Presentation of Theses

Acknowledgements

I would like to start by thanking all of the staff and my colleagues at the Materials Science Centre for their guidance and support throughout my PhD and beyond. I would particularly like to express my gratitude to Pete Lovell for his encouragement and dissemination of knowledge, guiding me throughout my three years and into the writing-up process. Thankyou for accepting me onto the course and providing an invaluable insight into research and the thoroughness required to complete a project. I only hope that I can continue to implement the learning's throughout my career. I would also like to thank Mike Chisholm, Sera Abed-Ali, David McDonald and Helen Harte at Lucite International for sponsoring my PhD and providing guidance and assistance throughout. Your contributions were greatly received in particular providing the business perspective, thereby adding context to the work.

From the department I would particularly like to highlight the help I received from Polly Crook both in the lab and with wedding planning; Ivan Easdon for keeping me grounded, sane and fed, and all the workshop staff for the considerable effort made to process the materials. I would like to continue this thanks to all the staff that helped train me on various pieces of equipment and who were there in a crisis. To Lizzie; thankyou for "red-penning" my work- you are a true friend. I only hope I can return the favour. To the rest of the Lovell group and beyond, both past and present, you were a great support throughout and in many cases also true friends.

Thankyou to my family for helping me reach this stage in my education. To my brother who insisted I continue on with chemistry when in my first year of undergrad I decided it wasn't for me; to my mum for always pushing me forward you have been my inspiration for many years and to my dad for being a immobile rock in the background. Lastly I would like to thank my husband, Adam. Thankyou for supporting me through thick and thin and understanding when you find me at 4am sat infront of a computer screen. Thankyou for your undying patience and always being there when I needed you, despite often being miles away. In particular, I appreciated the great lengths you went to call me from Afghanistan, often at ungodly hours to provide support when I had a bad day. Those calls kept me driving forward; and, despite everything, thankyou for asking me to marry you. It truly was the best day of my life.....so far.

1. Introduction

In the ceramics industry there are a number of well established methods for the shaping of objects, all of which centre around either casting materials in a liquid state which later solidifies or the dry pressing of a powder[1]. Gypsum has been used almost exclusively as the mould material for casting sanitary-wear due to its high versatility, strength and homogenous pore distribution. However, gypsum moulds have a number of disadvantages including deterioration on contact with water, deformation, and long set times with a large number of moulds being required to create a viable product for manufacturing processes[2-3]. These drawbacks have led to attempts to find a new synthetic material to create moulds with similar properties to gypsum with respect to fine homogeneous pores but increased durability.

Synthetic moulds struggled to meet the performance standards of gypsum until pressure casting was developed in the 1971 in which moulds produced from poly(methyl methacrylate) (PMMA) beads were employed. Pressure casting creates a positive pressure around the mould by blowing dry, compressed air through the pore network. This shortens the drying time of the mould, enabling a greater number of articles to be made in one day thereby increasing efficiency [4]. Key requirements for pressure casting are high strength and consistent permeability coupled with high elasticity to decrease shrinkage [5]. Despite their commercial importance, porous PMMA materials have received little academic research attention. The main objective of the project discussed in this thesis was to establish the fundamental understanding of the processes involved in the manufacture of the materials by systematically varying the components and looking at the effects on morphology, pore size and mechanical properties to produce a scientifically based rationale for formation of these materials. Previous research has mainly focussed on the toughening of porous PMMA materials, with little effort spent on developing understanding of how the materials form and how different components affect the final properties of the materials.

1.1 Aims

The purpose of this thesis was to expand understanding of porous PMMA materials. Starting with first principles, the various components in porous PMMA formulations have been systematically varied and their effects on the material properties investigated. This

thesis endeavours to explain the intricacies behind the results using model studies focussing on specific components. The original aims are detailed explicitly below:

- To establish a repeatable and reliable synthesis for the making of porous PMMA.
- To methodically test blend components for their effects on the properties of porous PMMA.
- To support results and findings with fundamental chemistry knowledge thereby increasing understanding and allowing for rational design of products.
- To improve the mechanical properties of the porous PMMA by increasing the fatigue life of the materials thereby increasing the efficiency of the materials by increasing the number of artefacts that can be manufactured from one mould.

1.2 The Casting of Ceramics

Today there are three principal methods for the casting ceramic materials: die casting, slip casting and pressure casting, of which only the latter two are suitable for use with polymeric moulds.

1.2.1 Die Casting

Die casting was first used in the metal industry in the mid-1800s to form metal objects by injecting molten metal under pressure into dies, or moulds. Initially, the process was limited to the printing process. However, by the mid-1890s, development of dies allowed for the mass production of parts across a wide range of industries[6]. Industrialisation and the development of the assembly line increased the use of die casting and it is still used widely today in automobile assembly production, due to the ability to cast large and small pieces alike with variable surface finishes[7]. Ceramics can similarly be die cast by pressing a dry powder into a mould, e.g in the fabrication of clay and non-clay compositions for brick, tiles and magnetic ceramics[8]. In dry pressing, the powder is milled and inserted into a hydraulic powder compacting press. The piston is lowered and the dry powder is automatically discharged into the steel die which punches the powder into the preformed shape. However, difficulties can arise when removing the ceramic from the mould.

1.2.2 Slip Casting

Slip casting was developed in the 1940s using gypsum moulds. It is a filtration process in which a powdered suspension, the slip, is poured into a porous plaster mould and the excess liquid removed via capillary forces and/or cation exchange through the mould wall. As the liquid filtrate is sucked into the mould, the powdered particles are forced towards the mould walls resulting in a consolidated layer.

The process can be divided into two classes, drain casting and solid casting, as shown in Figure 1.1 [9]. In drain casting, the mould is filled as above until the filter cake is of a desired thickness, upon which the mould is inverted and the excess slip is drained off. Resulting in a consolidated ceramic layer inside the walls of the mould. Solid casting involves the continued filling of the mould until the two ends of the slip meet, creating a solid piece. In both cases, the 'green' article is later removed from the cast piece for further drying and sintering [10].

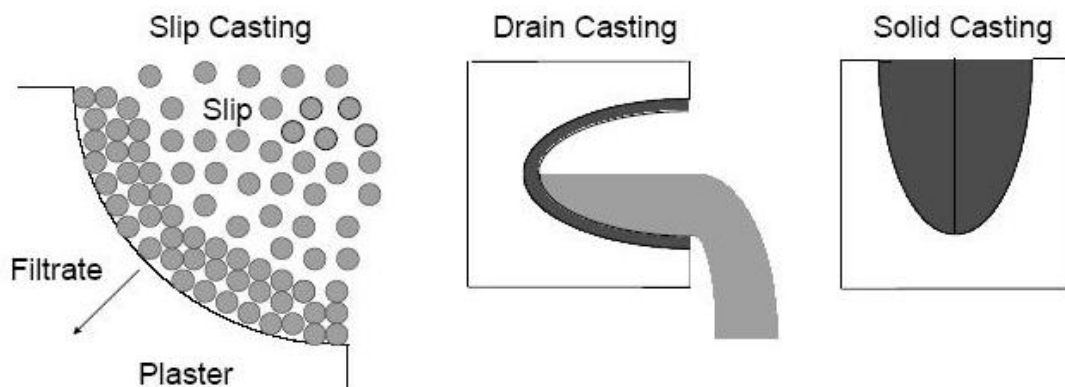


Figure 1.1: Diagrams of slip casting process detailing the difference between drain and solid casting[11]

Slip casting allows for a range of geometries to be cast with good homogeneity throughout the cast piece. In addition, the cost of the mould material is relatively low. However, gypsum moulds have a number of disadvantages including the tendency to erode on contact with water, short mould lifetimes owing to deformation of the mould and long set up times with large numbers of moulds being required to maintain an efficient commercial process. Overall, the lifetime of the mould is limited to approximately 100 cycles, with each casting taking up to half a day before the green article can be removed. A green article is a pre-fired ceramic artefact in which the composition of the clay still contains approximately 30- 40 % water. This water has to be removed by firing in a kiln prior to use to ensure the ceramic is hardened.

1.2.3 Pressure Casting

Pressure casting or pressure-slip casting was developed in the 1971 as a solution to the shortcomings of slip-casting. To reduce the drying time of the mould, an external pressure of approximately 10-15 bar is applied, forcing the water out and therefore enabling the mould to be reused immediately after casting. However, gypsum moulds were found to crack under the increased pressure, so a new, stronger material was needed. Polymers were designed for pressure casting by artificially creating pores to enable the drainage of water from the slip under pressure[10]. In 1971, the production of casting ceramic moulds from porous PMMA was developed and patented by the Swiss company, AG fur Keramische Industrie Laifen [12]. A number of other monomers could also be polymerised to give porous moulds, including those based on vinyl chloride, vinyl acetate, styrene, acrylate, acrylic or methacrylic acid. In particular, methyl methacrylate was shown to have the desired properties whilst being commercially available and cost effective. Using a pressure of 10-80 bar to remove the water from the mould, drying was no longer dependent on the capillary-sucking properties of the material and instead utilised the pressure difference across the mould based upon the equation below[12].

$$\frac{L^2}{T} = \frac{2PgE^2}{5(Sp)^2 \eta (y-1)(1-E)^2}$$

where L is the thickness of the filter cake in centimetres, T is the duration of the filtration in seconds, P is the filtration pressure in g cm^{-2} , E is the proportion of pores in the filter cake, Sp is the specific surface area of the solids in cm^2 , η is the viscosity of the slurry in Poise, g is the gravitational constant in cm s^{-1} and y is the concentration of the slurry. In addition, the pressurised air helps to remove slurry particles trapped in the mould therefore increasing mould lifetime.

However, pressure casting still has disadvantages. Compared to slip casting, the equipment is expensive and specialist with much secrecy surrounding mould formulations between companies[13].

Alternative methods to the traditional slip and pressure casting detailed above regularly arise in the open literature. However, little follow-up to these findings has been made by industry as they require new equipment, often with a large initial capital investment being needed. An example of development is a worldwide patent granted in 1997 to British

Ceramic Research Limited, which offers a reduced pressure alternative to improve slip casting by having an extended network of pipes extended through the mould[14].

Further ideas are to combine die pressing and slip casting processes; named slip-pressing and patented by Bauer in 1999 [15]. Slip-pressing enables the manufacturing of ceramic artefacts with particular relevance to microcomponents using non-porous moulds made from PMMA. By using a wet slip, agglomerates are discouraged from forming, thereby enabling a homogeneous artefact with few faults. The wet slip further exhibits beneficial flow characteristics, filling all the cavities without application of high pressures. The slip is consolidated into a powder pressed format by a permeable piston which simultaneously removes the air pockets from the powder. The process enables the powder to be pushed into the mould whilst releasing the liquid through the top of the piston (see Figure 1.2.)

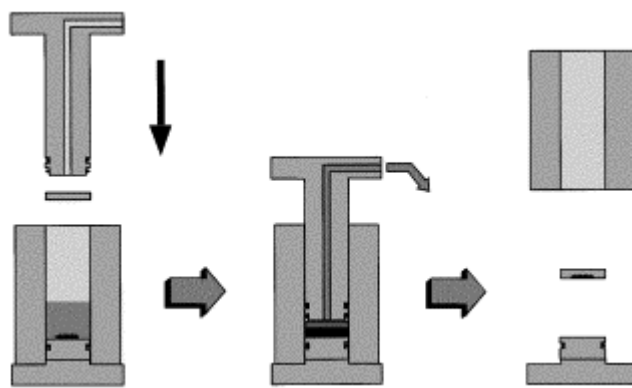


Figure 1.2: Schematic of slip pressing taken from paper by Bauer⁹

1.2.4 Casting of Sanitaryware

A number of different techniques are available for the preparation of ceramic artefacts all of which compete for market share. Slip casting and pressure casting are the most wide spread with pressure casting dominating in the formation of ceramics for the sanitaryware industry. However, porous PMMA is not widely used despite its praise in literature for the formation of ceramics. This is due to high capital investment which cannot be regained without increasing the cost of the product coupled with lack of understanding of the mould material. At present, porous PMMA moulds are used only in the standard range, forming the staple collection of bathroom pieces which are sold over multiple seasons, thereby the higher capital cost of equipment and materials is spread over a larger number of moulds. This project aimed to develop understanding of the formation of porous PMMA moulds by

establishing the effects of formulation components and properties of the final mould material. In addition, understanding the synthesis of porous PMMA would aid the development of the procedure, thereby allowing for value to be added to the industry by facilitating specialisation of the moulds for various different applications. The project sponsors, Lucite International, wanted to use the results of this project to differentiate themselves from their competitors by using the understanding gained to develop the moulds, allowing for growth both within the European market and emerging markets, which include China and India.

1.3 Free Radical Polymerisation

Porous PMMA is made by initiating a free-radical polymerisations of MMA using a redox initiator system of benzoyl peroxide (BPO) and dimethyl-*p*-toluidene (DMPT). The reaction is carried out in water with a surfactant to aid stability of the emulsion.

Free radicals are species with an unpaired electron. Free radical polymerisation are used almost exclusively for the preparation of polymers containing a $\text{CH}_2=\text{CR}_1\text{R}_2$ structure[16]. First synthesised in the early 1900's, at present, approximately 45 % of plastics and 40 % of synthetic rubbers are manufactured using this process [17]. Free radical polymerisation is a robust technique allowing for the use of a wide range of monomers and functionalities, which permits the polymerisation of almost all unsaturated monomers, i.e. those which contain a π -bond ($\text{C}=\text{C}$). However the reactions are non-selective and random, therefore the resulting sample will have macromolecules of differing chain lengths and hence the product is a non-uniform, irregular polymer as per the 1996 IUPAC definition[18]. This distribution of molar masses can be measured and is referred to as the dispersity (D_M) is defined as

$$D_M = \frac{\overline{M}_w}{\overline{M}_n}$$

where M_w is the weight-average molar mass and M_n the number-average molar mass.

Recent developments in the field of controlled radical polymerisation have led to a renewed interest in the area of increased product control, and hence producing polymeric materials with lower dispersities allowing for specialist applications, for example drug delivery. As it is inapplicable to the work described herein on porous PMMA, controlled radical polymerisation will not be discussed further in this thesis.

A radical species contains an unpaired electron which is usually highly reactive, and hence typically has a short lifetime[19]. The radical stability, and hence reactivity, depends on the surrounding atoms and their ability to stabilise the unpaired electron. Electron withdrawing groups adjacent to the radical site stabilise the electron in a SOMO (singly occupied molecular orbital) of lower energy. Conversely, electron rich groups such as alkoxy -OR, have relatively high-energy filled n-orbitals due to their lone pairs. The interaction with the radical therefore gives a SOMO higher in energy than the original orbital; this results in a more reactive species, see Figure 1.3.

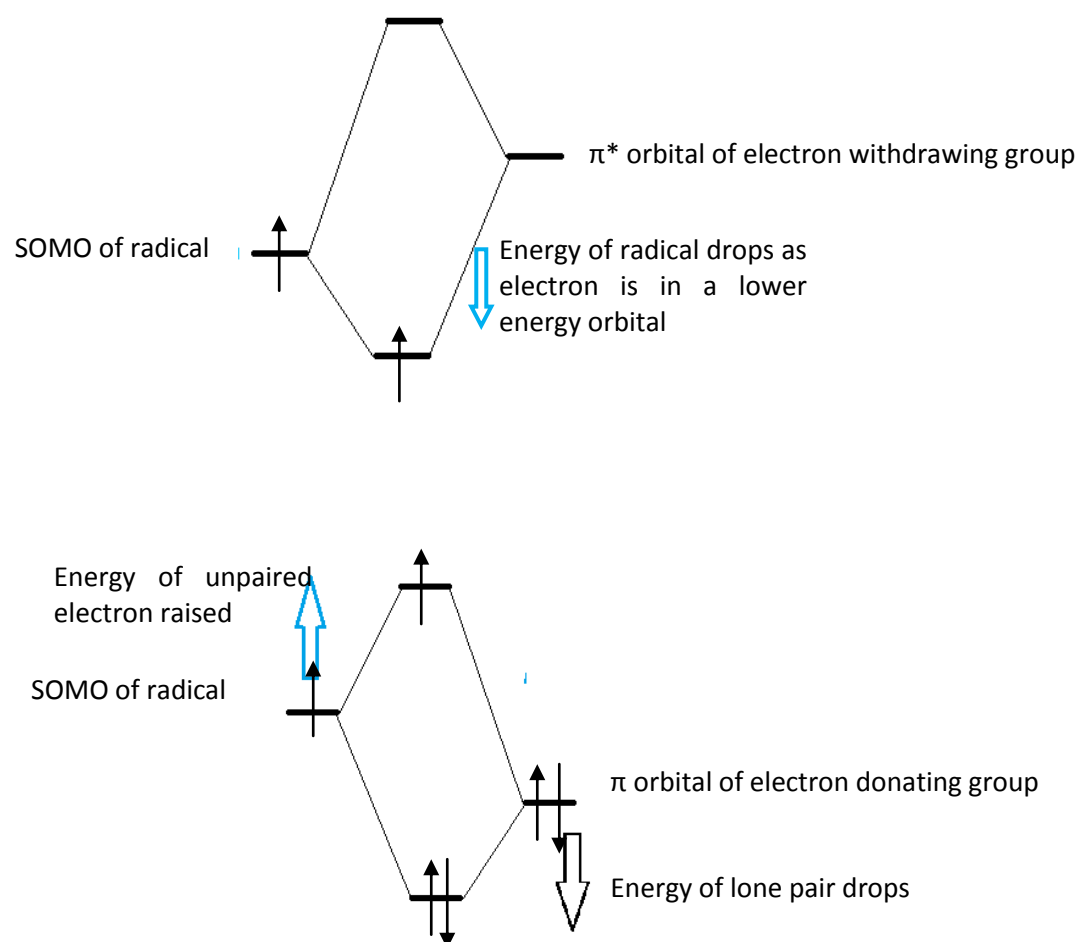


Figure 1.3: Orbital depiction for electron withdrawing substituents and electron donating substituents where the blue arrow signifies the energy change

Similar to carbocations, stability of the radical can also be derived from steric hindrance, where large bulky groups such as phenyls can shield the lone electron on the carbon atom. This concept is exploited in controlled radical polymerisation where sterically-hindered

molecular radicals such as (2,2,6,6-Tetramethylpiperidin-1-yl)oxyl (TEMPO) are added to allow for the temporary formation of a stabilised unreactive radical[20]

A carbon-based free radical typically has sp^2 hybridised orbitals, and has the generic structure given in Figure 1.4.



Figure 1.4: Typical sp^2 hybridisation of a carbon radical

1.3.1 Mechanism for Free-Radical Polymerisation of Porous PMMA

The mechanism for free-radical polymerisation can be divided into three distinct stages: initiation, propagation and termination. A further process known as ‘chain transfer’ can also occur and can make a significant contribution to the properties of the final polymer product. The following four sections detail the mechanism with respect to the polymerisation of methyl methacrylate (MMA).

1.3.1.1 Initiation

Initiation involves the creation of a radical species, and hence a reactive centre. This mechanism can be divided into two parts. Firstly, the formation of a radical from the dissociation of an initiator species in which a weak, and therefore unstable, bond is broken. Secondly, the attack of this newly-formed radical on the unsaturated bond in the monomer molecules.

A radical species can be initially formed in two ways; either by the homolysis of weak σ bond under the application of heat or UV-light (as just indicated), or electron transfer, whereby a single electron is donated to or from a molecule, in what is often termed a ‘single electron process’.

In homolysis, a weak bond is cleaved by the application of heat, termed ‘thermolysis’, or UV light, ‘photolysis’. In thermolysis, a peroxide (O-O) or azo (N=N) bond is cleaved at temperatures in excess of 50 °C, the mechanism of which is shown in Figure 1.5. Photolysis has an advantage over thermolysis in that radicals form only when exposed to UV light. For this reason, the formation of radicals ceases as soon as the light source is removed.

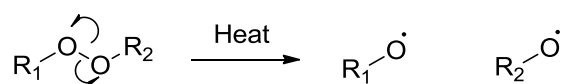


Figure 1.5: Thermal homolysis of a peroxide bond

Redox reactions are used to generate the active species when the free-radical polymerisation is required to be undertaken at low temperature (less than 50 °C). The synthesis of porous PMMA both in the industrial methodology and the methods used throughout this project utilise a redox initiator thereby allowing the reaction to be undertaken at room temperature without the need for thermal stimulation. The specific system used is the reaction of benzoyl peroxide with *N,N* dimethyl-*p*-toluidene.

Studying the literature, two slightly different methodologies are apparent as to the mechanism of activation in this redox system. Firstly, Horner hypothesised that a single electron is donated to the benzoyl peroxide (the initiator) resulting in the cleaving of the peroxide bond[21]. Two radicals are formed: a benzoyloxy radical and an aminyl radical-cation (see Figure 1.6). A benzoate anion is also formed as a by-product.

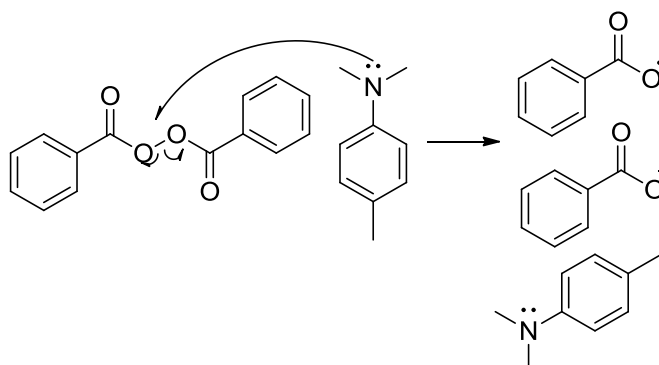


Figure 1.6: Initiation of benzoyl peroxide by *N,N*- dimethyl-*p*-toluidene

The benzoyloxy radical can undergo β -scission and decompose to form the phenyl radical and carbon dioxide, as shown in Figure 1.7. Both the benzoyloxy radical and the phenyl radical can initiate polymerisation, but it is currently unknown what effect the amine anion has on the reaction mechanism.

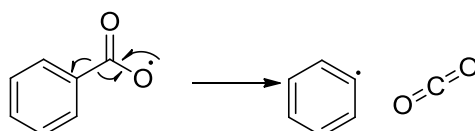


Figure 1.7: β scission of benzoyloxy radical

Pryor and Hendrickson proposed an S_N2 mechanism, detailed in Figure 1.8, after studying the reaction using the kinetic isotope effect[22]. The mechanism involves the movement of a pair of electrons from the tertiary amine to the peroxide bond which is subsequently cleaved.

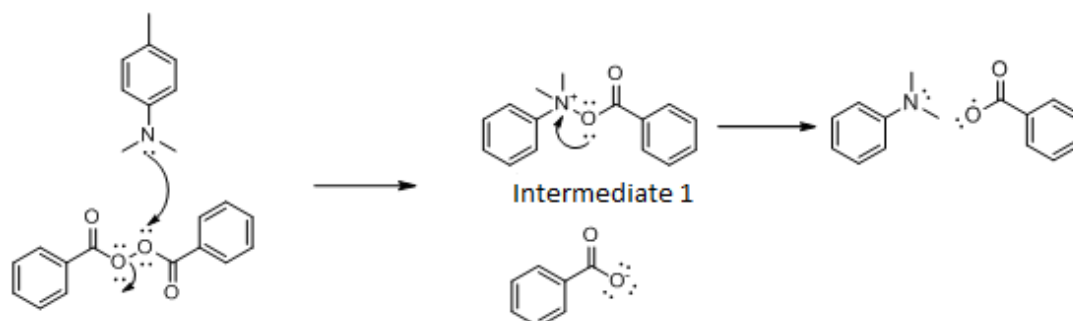


Figure 1.8: S_N2 mechanism for donation of a pair of electrons to destabilise the peroxide bond with resulting products

Intermediate 1 can then decompose to form a benzoyloxy radical, which initiates polymerisation. The amine radical cation can also initiate polymerisation through loss of a proton, as was demonstrated by spin trapping experiments performed by Sato et al[23].

Brauer and in later publications Horner himself concluded that both mechanisms operated simultaneously[24-25].

The benzoyloxy radical formed by either of the mechanisms shown in Figures 1.7 and 1.8 can then go on to initiate polymerisation via a head-to-tail addition to the unsaturated carbon-carbon double bond in the monomer species. Although two possible modes of addition are possible, head-to-tail addition predominates as the unsaturated CH_2 carbon is less sterically hindered and yields a more stable tertiary radical (see Figure 1.9).

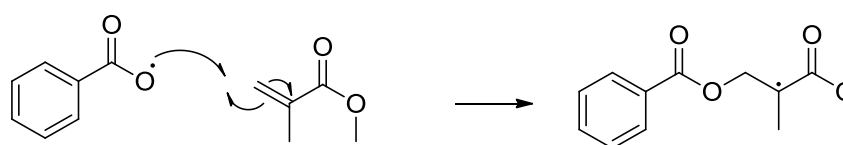


Figure 1.9: Initiation of methyl methacrylate in porous PMMA by initiation by benzoyloxy radical formed in the redox reaction between DMPT and BPO

As radical reactions are non-specific, not all of the radicals formed in initiation react with the monomer. Some are lost in side reactions, such as those shown in Figure 1.10, and are reflected in the initiator efficiency, f . For a 100 % efficient initiator, $f = 1$, however most initiators have a value of f from 0.3 to 0.8. Induced decomposition, as shown in Example 3 Figure 1.10, results in significant wastage of the peroxide initiators and very low initiator efficiencies of approximately 0.25[16, 26].

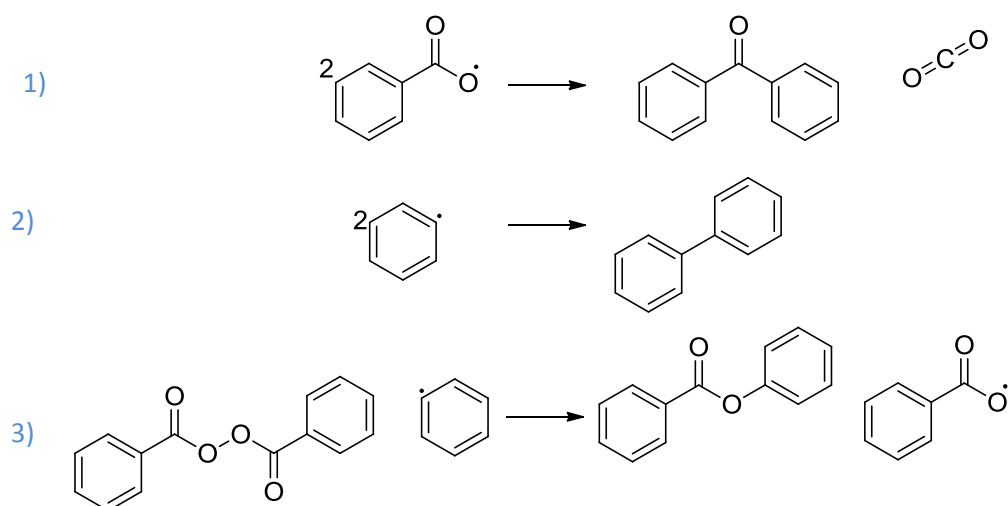


Figure 1.10: Side reactions in initiation using benzoyl peroxide

1.3.1.2 Propagation

Propagation is the growth of a polymer chain via sequential addition of monomer units. Each monomer addition occurs in a timescale of milliseconds, so therefore several thousand propagation steps can occur within one second[16]. Propagation, as in the previous initiation step, occurs predominately via head-to-tail addition, as shown Figure 1.11.

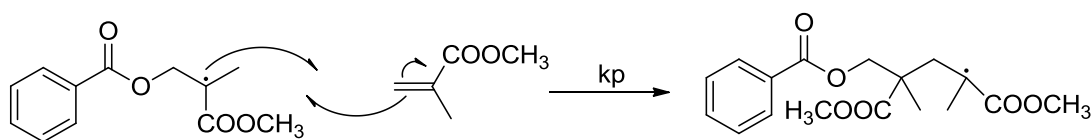


Figure 1.11: Propagation step showing head to tail addition

This can be represented in a general form for PMMA where n is the degree of polymerisation prior to addition and $X = \text{COOCH}_3$ (see Figure 1.12):

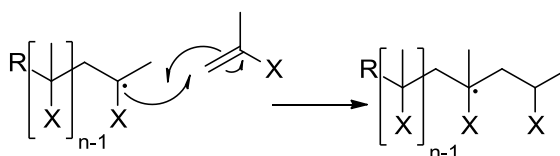


Figure 1.12: Generic mechanism for propagation in MMA free-radical polymerisation

1.3.1.3 Termination

Termination irreversibly destroys the active radical thus stopping propagation. There are two mechanisms of termination: combination, where two growing chains couple together to form a single polymer molecule, and disproportionation, as shown in Figure 1.13, in which β -hydrogen abstraction from the terminal chain unit occurs, thereby forming an unsaturated end group on one of the polymer chains produced. Both types of termination mechanism occur in the polymerisation of methyl methacrylate. However above 333 K, disproportionation dominates whereas below 298 K neither process is observed to dominate [27]. Disproportionation is likely in the polymerisation of MMA as the carbon atom adjacent to the radical has 3 methyl hydrogen atoms which are readily extracted, resulting in an unsaturated polymer chain end.

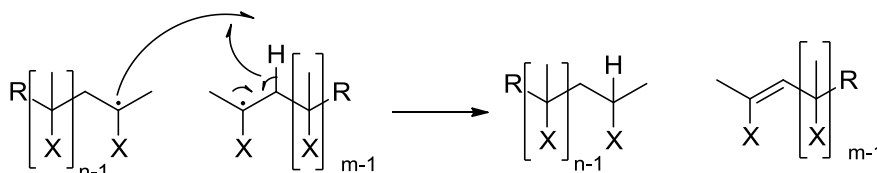


Figure 1.13: Mechanism for disproportionation

1.3.1.4 Chain Transfer

The kinetic chain length, \bar{v} is defined as the average number of repeat units that add to a single chain prior to termination of the radical. Under steady state conditions, \bar{v} , can be defined by the ratio of the rate of propagation to termination[16].

$$\bar{v} = \frac{k_p[M^\bullet][M]}{2k_t[M^\bullet]} = \frac{k_p[M]}{2k_t^{1/2}(\frac{R_i}{2})^{1/2}}$$

Termination usually occurs by reaction between two active centres as described in Section 1.2.3. However, Flory found that the chain length predicted using solely the above mechanisms would limit the number average degree of polymerisation (\bar{x}_n) to: \bar{v} if disproportionation dominates and $2\bar{v}$ if combination is the main termination process.

In the absence of chain transfer, \bar{x}_n is defined as

$$(\bar{x}_n)_0 = \frac{k_p[M][M^\bullet]}{k_{tc}[M] + 2k_{td}[M^\bullet]^2}$$

where k_{tc} is the rate constant for termination by combination and k_{td} , the rate constant for termination by disproportionation. Under steady state conditions, the total concentration of all radical species can be defined as

$$[M^\bullet] = \left(\frac{R_i}{2k_t} \right)^{1/2}$$

which when substituted in the previous equation for $(\bar{x}_n)_0$ results in

$$(\bar{x}_n)_0 = \frac{k_p[M]}{(1+q)k_{tc}^{1/2} \left(\frac{R_i}{2} \right)^{1/2}}$$

where q is the fraction of termination that proceeds by disproportionation (k_{td}/k_t). The kinetic chain length can simplify the equation so that

$$(\bar{x}_n)_0 = \left(\frac{2}{(1+q)} \right) \bar{v}$$

Usually, x_n will lie with the values of \bar{v} and $2\bar{v}$. However, Flory found that premature chain termination was possible if the radical reacts with another active species through collision for example; monomer, initiator, solvent, or deliberately added transfer agents [27]. Flory deduced that the active radical centre abstracts a small molecule from the transfer agent, TA, as shown in Figure 1.14.

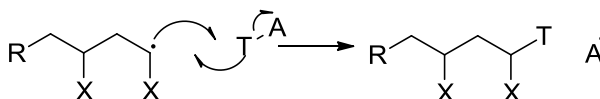
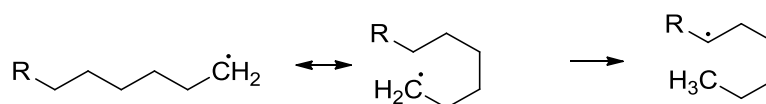


Figure 1.14: Generic scheme depicting the mechanism of chain transfer

Chain transfer to the polymer can also occur in the polymerisation of some monomers, in particular ethylene, which leads to the occurrence of branched architectures. Backbiting is an intramolecular reaction where a hydrogen atom is abstracted from further down the chain resulting in the stabilisation of the radical by forming a more substituted species. Propagation from this internal radical results in the branching of the polymer (see Figure 1.15.)



Since the formation of R^\bullet is so much slower than the attack of the radical on the monomer, it is this first step which is rate determining for the reaction. Therefore, the rate of initiation can be determined by:

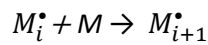
$$R_i = \frac{d[R^\bullet]}{dt} = 2k_d f [I]$$

where k_d is the rate coefficient of decomposition of the initiator and f the initiator efficiency.

For porous PMMA, a redox initiator system of benzoyl peroxide (BPO) and N,N, dimethyl-*p*-toluidene (DMPT) is used and hence only one radical is formed per molecule of initiator.

$$R_i = 2k_d f [I] = f k_r [BPO][DMPT]$$

Similarly, propagation can be denoted as:



Simplifying and assuming that $[M^\bullet]$ is the total concentration of all radical species:

$$R_p = -\frac{d[M]}{dt} = k_p [M][M^\bullet]$$

assuming steady state kinetics,

$$[M^\bullet] = \left(\frac{R_i}{2k_t} \right)^{1/2}$$

hence

$$R_p = -\frac{d[M]}{dt} = k_p [M] \left(\frac{R_i}{2k_t} \right)^{1/2}$$

For porous PMMA, R_p can be rewritten as

$$R_p = k_p \left(\frac{f k_r}{2k_t} \right)^{1/2} [M][DMPT]^{1/2}[BPO]^{1/2}$$

Termination is a bimolecular process, depending only on $[M^\bullet]$ which encompasses both termination mechanisms: combination and termination. Hence the total rate of termination, R_t can be defined as:

$$R_t = -\frac{d[M^\bullet]}{dt} = 2k_t[M^\bullet][M^\bullet]$$

where k_t is the rate constant for termination and is equal to the sum of the rate constant for termination by combination (k_{tc}) and the rate constant for termination by disproportionation (k_{td}).

1.4 Polymerisation Processes

There are four main processes by which polymerisation can be carried out: bulk, solution, suspension and emulsion. Each process has advantages and disadvantages.

1.4.1 Bulk Polymerisation

Bulk polymerisation is the simplest process, involving only monomer and a monomer-soluble initiator, in which the concentration of the monomer controls the molecular weight of the final polymer, $R_p \propto [M]/[I]^{0.5}$. However, there is a marked increase in the rate of polymerisation towards the end of a reaction. Autoacceleration was first noted by Norrish, Smith and Trommsdorff, after which the process is named, where a rise in the viscosity is apparent as monomer is converted to polymer[28]. As the viscosity of the medium increases, one or more of the species can have a lower rate of diffusion, which therefore becomes the rate-determining step of the polymerisation. As the chain grows in size, the translation diffusion of the propagating chain becomes very low, effectively freezing the polymer into position. With only small, short chain radicals able to move freely, termination becomes purely between these short chains and the immobile long chain radicals. Therefore, termination is controlled by translational diffusion resulting in a larger reduction in k_t , which results in a large increase in R_p . In addition, as free-radical polymerisations are exothermic, energy is released which if not dissipated effectively, explosions can occur. To avoid this, reactions are halted at low conversion and the remaining monomer separated from the polymer and recycled. Bulk polymerisation is used industrially in the production of sheet PMMA, poly(styrene) and poly(vinyl-acetate), producing high optical clarity materials that are free from contaminants.

1.4.2 Solution Polymerisation

The presence of solvent facilitates heat transfer and reduces the viscosity of the medium, reducing the likelihood of autoacceleration occurring. However, the solvent must be carefully selected to enable dissolution of the monomer, initiator and polymer as well as to minimise chain transfer effects. Once reacted, the polymer must be isolated from the solvent by either solvent evaporation or precipitation, which limits its practicality for industrial use.

1.4.3 Suspension Polymerisation

Suspension polymerisation consists of droplets of water-insoluble monomer suspended in an aqueous phase. It can essentially be viewed as a multitude of miniature bulk polymerisations suspended in an inert medium by vigorous agitation to facilitate heat transfer. The monomer, initiator and polymer must all be insoluble in the suspension medium. Stabilisers are added to the aqueous dispersion in order to stop coagulation, resulting in the formation of polymer beads from the droplets. The polymer beads are later isolated by filtration or centrifugation. To prevent plasticisation by unreacted monomer, the polymerisation must be taken to 100 % conversion. Suspension polymerisation is widely used industrially for the polymerisation of styrene, PMMA and vinyl acetate, although care has to be taken to remove the dispersion stabilisers before processing.

1.4.4 Emulsion Polymerisation

Emulsion polymerisation is widely used industrially in the preparation of acrylic polymers, poly(vinyl chloride) and poly(vinyl acetate) among others. The method differs only slightly from suspension polymerisation, whereby the initiator is soluble as opposed to the monomer, but this dramatically affects the kinetics of polymerisation and the product formed. Emulsion polymerisations are unique in that polymer chain length can be altered without changing the rate of polymerisation, by varying the reaction temperature or concentration of initiator. Water-insoluble monomers are added to a solution of water containing dissolved surfactant at levels well above the critical micelle concentration, (CMC)¹ and vigorously agitated. Three distinct phases are established within the reaction mixture, which are shown in Figure 1.16:

¹ See Chapter 5.2.2 for full discussion of the critical micelle concentration with respect to the surfactant.

- An aqueous phase, in which small quantities of surfactant and monomer are dissolved.
- A micellar phase in which a large number of small monomer-swollen micelles are evident. However, this phase only contains a small amount of the total overall monomer
- Monomer droplets, which are much smaller in number and which are also stabilised by the surfactant.

Water-soluble initiator molecules enter the small micelles and the large monomer droplet. But as the concentration of micelles (10^{21} dm^{-3}) far exceeds that of the droplets ($10^{13}\text{-}10^{14} \text{ dm}^{-3}$), polymerisation occurs almost exclusively in the interior of micelles. The monomer concentration within the micelles is maintained by diffusion of monomer molecules from the larger monomer droplets which decrease steadily in size until total monomer conversion of 50-80 %, by which they have been totally consumed. The rate of polymerisation then decreases until all remaining monomer in the micelle has been converted to polymer.

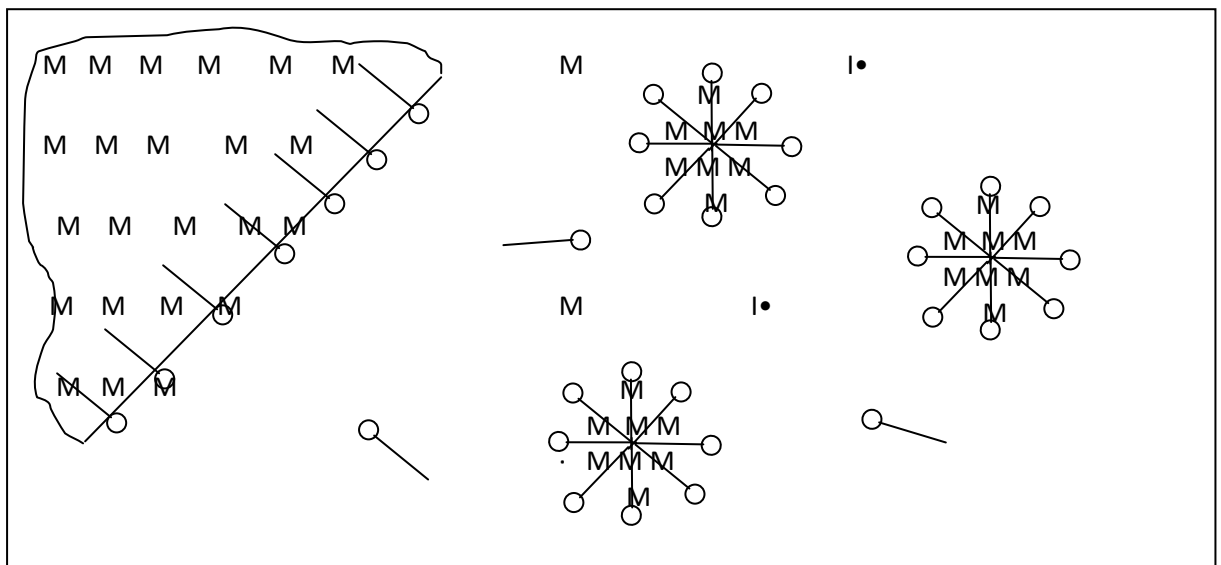


Figure 1.16: Schematic showing the mechanism for emulsion polymerisation showing the three phases (i) the aqueous phase containing surfactant above its CMC, small amounts of dissolved monomer (M) and initiator (I^\bullet); (ii) monomer-swollen micelles stabilised by surfactant and (iii) large monomer droplets shown in part.[29]

Smith and Ewart's [30] and Harkins [31] model can be broken down into three intervals or stages. The first interval involves particle nucleation where the primary free radical formed

from initiator dissociation reacts with molecules of monomer in the aqueous phase to form an oligomer. The oligomer radical continues to propagate in the aqueous phase and can either (a) terminate to produce a surfactant like species, (b) continue to propagate until a critical degree of polymerisation is exceeded upon which they become surface active or (c) undergo further propagation until they reach a further critical degree of polymerisation where they are no longer soluble in the aqueous phase, and hence precipitation occurs.

Harkins proposed method (b) whereupon the oligomeric radicals diffuse into the monomer-swollen micelles, initiating polymerisation. To support polymerisation, continuous replenishment of the monomer is required by the monomer droplets. These formed micelles are considerably larger than the original micelles and so to maintain colloid stability, additional surfactant is required.

Provided the particles remain colloidally stable, the number of particles per volume of latex remains constant at the end of the first interval. In the second interval, the rate of polymerisation remains constant as the reservoir of monomer in the large droplets diffuses into the micelles. Once the supply of monomer is exhausted, the third interval is commenced, the rate of polymerisation decreases continuously until it eventually ceases once all of the monomer is consumed. The final product, known as a latex, is comprised of small polymer particles suspended in water and stabilised against agglomeration by the emulsifying surfactant [32]. The rate of polymerisation can be expressed as:

$$R_p = k_p [M_p] \left[\frac{N_p}{2} \right]$$

where M_p is the concentration of monomer in the micelle and $N_p/2$ the number of active micelles. The rate at which the radicals enter the micelle can be calculated as R_i/N_p and can be viewed as the rate of initiation of the polymer chain (or its termination). The kinetic chain length in the micelle particle can, as a result, be written as:

$$\bar{U} = \frac{k_p [M_p]}{(v_i/N_p)} = \frac{k_p [M_p] [N_p]}{2fk_d [I]}$$

Therefore, increasing the initiator concentration decreases the polymer chain length whilst leaving the rate of polymerisation unaffected. Conversely, for a fixed initiator concentration, the kinetic chain length is dependent on the surfactant concentration so therefore increasing the level of surfactant increases the polymerisation rate and the molar mass of the resulting polymer.

1.4.5 The Polymerisation Process in the Preparation of Porous PMMA Materials

Although the process of making porous PMMA materials is fairly simple, understanding the mechanism behind the system is complex. Discussions around raw materials leads to the assumption that the basic system, before addition of beads, is an oil-in-water emulsion with monomer droplets being suspended in the water phase by mechanical agitation. However, benzoyl peroxide and the surfactant are shown to be dissolved in the monomer phase, suggesting that the reaction is closer in character to that of a suspension polymerisation. Polymerisation occurs around the added PMMA beads, disrupting the micelles and allowing for the formation of bridging ligaments, which once set hold the beads together to form a rigid material (see Figure 1.17). In this case the solvent (water) is evaporated from the block by heating overnight and the surfactant removed by washing the following day. If the block is ineffectively washed, the surfactant remains within the polymer matrix and causes significant plasticisation of the bridging ligaments. In turn, it is unknown whether the reaction goes to full conversion as a large amount of monomer is lost through evaporation with further residual monomer being driven off in the drying process when the material is dried overnight in an oven at 60 °C. Calculations made after drying show residual monomer levels pre-hardening are at approximately 20 %, with levels dropping to 1-5 % in the final specimen [33]. Throughout this report further discussion will be undertaken around the final mechanism of formation of porous PMMA, the final conclusions of which are summarised in Chapter 10.

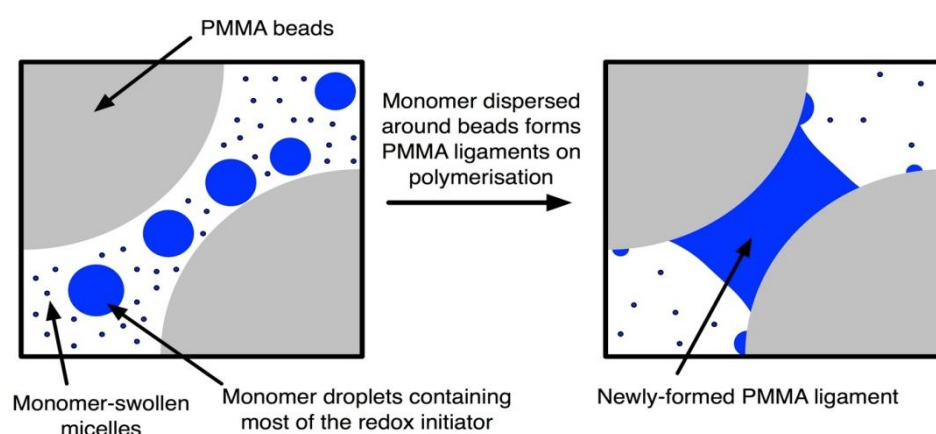


Figure 1.17: Illustration to show the formation of PMMA ligaments between the pre-formed PMMA beads

2. Review of Porosity and Porous Materials

Porous materials, in particular porous polymers, are used in a wide range of applications ranging from filtration membranes to catalyst supports and biomaterial scaffolds. However, achieving high porosity without compromising mechanical strength is a common problem for all applications. To create successful porous materials which balance porosity and mechanical strength, interdisciplinary communication is often required to combine chemical expertise with those of an engineer.

2.1 Porous Materials

Porous materials are defined as any solid which contains cavities, channels or interstices[9]. Thus, most materials can be viewed as porous to some extent; hence a more stringent definition of porosity often is required. The International Union of Pure and Applied Chemistry (IUPAC) classifies porosity into three broad categories; micro, meso and macro. The categories are defined by pore size where micro pores have a pore width smaller than 2 nm, mesopores have widths between 2 and 50 nm and macropores have widths larger than 50 nm[34-35] (see Figure 2.1). The pore-width is defined as the smallest dimension of the pores. Hence, for a cylindrical pore the pore-width is the diameter of the pore not the radius. However, a number of authors have challenged the guidelines, suggesting alteration of the boundaries of these classifications to bring pore size into alignment with SI units to allow for more meaningful values[36].

Pore Size Class									
Nanopore			Micropore			Millipore			
Sub-	Inter-	Super-	Sub-	Inter-	Super-	Sub-	Inter-	Super-	
0.1nm	1nm	10nm	100nm	1um	10um	100um	1mm	10mm	10mm
Micro-			Meso-			Macro-			Current IUPAC Scheme
2nm			50nm						

Figure 2.1: Classification of pores by size[35]

Porosity can also be defined in terms of the pore shape. Most simplistically, pores can be divided into two main categories namely open pores and closed pores, which differ by their accessibility to external fluid. Open pores are “a continuous channel of communication with the external body” [37] and can be open at one end (‘non-penetrating’ pores), or have openings on two sides of the cell, thereby allowing flow of a liquid or a gas through them

(‘penetrating’ pores). Open pores are exploited in filtration and bioreactors due to their permeability to fluid (see Figure 2.2). Closed pores are isolated from the external phase by a solid material. They may contain a trapped liquid or be unfilled. Closed pores influence bulk properties, such as density, mechanical strength and thermal conductivity, and are utilised in thermal and sonic insulators. However, they are inactive to fluid flow being completely isolated from their neighbours.

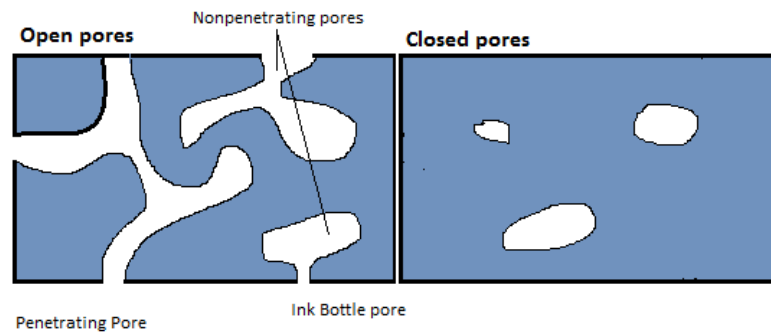


Figure 2.2: Defining porosity by pore type

Alternatively, pores can be classified according to their shape, i.e cylindrical, ink bottle shaped or funnel shaped (see Figure 2.3). It is important to distinguish that a rough surface, as shown in Figure 2.3 (g), is not defined as a pore unless the irregularities are deeper than they are wide.

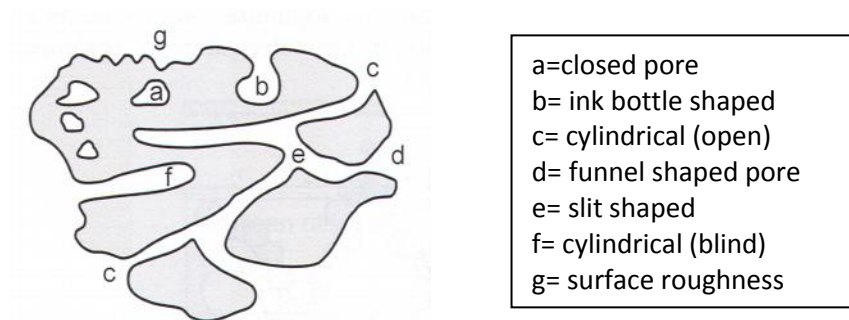


Figure 2.3: Schematic of a porous solid showing variations in pore shape.

Due to the range of pore types (open/closed) and size (nanometres to millimetres), large variations in bulk properties are attainable from porous materials, and hence a wide range of applications are possible (see Table 2.1 for examples).

Table 2.1: Examples of porous materials and their properties[9]

Application Property	Filter	Catalyst	Gas Separation	Foam	Ceramic
Open Porosity/ %	>30	>30	>30	Very high	High
Pore Size Distribution	Narrow	Narrow but may be bimodal	Narrow	Wide	Low
Permeability	High	Variable	High	Low	High
Mechanical Strength	High	Variable	Variable	Low	High

2.2 Measuring Porosity

Quantitatively, porosity can be defined as the fraction of the volume which is attributed to pores, which can be calculated by dividing the pore volume (V_p) by the apparent volume (V)[37].

$$\varepsilon = \frac{V_p}{V}$$

However, the value of porosity (ε) is greatly influenced by the means of measurement. Techniques such as geometrical determination and fluid displacement exclude interparticle voids in the measurement of the apparent volume. Thus, when comparing porosity values both the method of determination and the reported porosity value are important. Similarly, pore size measurement incurs difficulties due to the wide range of pore shapes available. Often a model is used which requires an oversimplification of the pore shape. Thus the reported category used, i.e cylindrical, ink bottle etc., may differ from the true shape of the pores. As pore shape is highly irregular, pore size is also problematic to define. IUPAC loosely states that the pore size is the “the limiting measurement of a pore” notably, the pore width is that of the “smallest dimension in the absence of further precision”[37]. However, the interconnectivity of porous networks leads to yet further difficulties and complications.

Model idealised systems are used to define pore shape, of which there are five shapes: cylinders, prisms, cavities (or windows), slits and spheres. However, a full description of porosity must include shape, size and interconnectivity. Detailed below are several methods used to determine porosity and characterise the pores.

2.1.1 Intrusion Methods

Mercury porosimetry is a common method for the measurement of both the size of pores and the open porosity in a sample. Mercury is a non-wetting liquid which requires a positive pressure to enable entry into a pore of radius r . As the radius of the pore increases, the pressure (P) required to enter it is greater and hence ΔP is inversely proportional to r . Mercury porosimetry enables collection of the volumetric distribution of pore sizes by varying the pressure throughout a run. Therefore, the volume of pores with radii between r and $r + \Delta r$ will equal the volume of mercury (ΔV) intruded between the pressures P and $(P + \Delta P)$, where r can be calculated from the pressure from [9]:

$$r = - \frac{2\sigma \cos\theta}{P}$$

where σ is the surface tension of pure mercury (4.84 mN m^{-1}) and θ the contact angle between the materials and the mercury (assumed to be 141°) [9].

Mercury porosimetry equipment can measure pores with radii between $75 \text{ }\mu\text{m}$ and 3.5 nm by escalating pressure from 0.1 to 2000 bar . However, the technique makes the assumption that all pores are regular cylinders. Hence, irregular-shaped pores with narrow inlets cannot be distinguished between those which have a consistently small radii. Therefore, an ink-bottle shaped pore with inlet radius (r) is seen by the equipment to be the same as a cylindrical pore of radius r and assumed to be able to hold the same volume of mercury [38].

2.1.2 Fluid Displacement

Fluid displacement is a simple way of measuring porosity. A sample is weighed dry (W_1), then weighed fully submerged in a liquid such as water, toluene or alcohol which is contained in a beaker on a zeroed balance (W_2). The sample is then weighted wet after being patted dry with paper (W_3). The fraction of the bulk density to theoretical density (d) and open (P_o) and closed (P_c) porosity can then be calculated as follows.

$$\rho_{bulk} = \frac{W_1 \rho_{liquid}}{W_3 - W_2}$$

$$d = \frac{\rho_{bulk}}{\rho_{th}}$$

$$P_o = \frac{W_1 - W_2}{W_3 - W_2}$$

$$P_c = 1 - d - P_o$$

where ρ_{bulk} is the bulk density of the porous material, d is the fraction of the bulk density to theoretical porosity, ρ_{th} the theoretical porosity and ρ_0 the density of the liquid[9]. The principles behind this method are used for the measurement of porosity in this thesis. The percentage porosity was calculated by obtaining the volume of the liquid adsorbed (V_{ad}) of the sample, assuming a solid material, based upon its mass by subtracting the mass of the sample when wet (M_{wet}) from the mass of the sample when dry (M_{dry}) and dividing by the density of water at room temperature (ρ_{water}). This is then divided by the actual volume of the specimen based upon measurements taken using vernier callipers (V).

$$Porosity (\%) = \frac{V_{ad}}{V} = \frac{(M_{wet} - M_{dry}) \div \rho_{water}}{V} \times 100$$

where V is the volume of the test sample and the ρ_{water} the density of water.

2.1.3 Optical Methods

Optical methods are commonly used for the measurement of porosity, where an image can be segregated into two distinct regions by colour or using greyscale values. Ergun et al. [39] used this technique on polished porous PMMA samples, where the polymer was given a grey value of zero and the pores one. Using software such as ImageJ[40], the percentage of dark to light areas can be calculated. As the specimen for analysis is often very small, particularly when SEM is used, it is important that multiple measurements are taken to gain a statistically significant representation of the material. In this project, SEM images have been taken to gain an insight into the structure, but as a fracture surface must be obtained for analysis, which often involved the fracturing of ligaments adjoining the beads and hence creating an artificial increase in porosity, SEM images have not been analysed for porosity in this work. Computational X-ray tomography measurements were undertaken where segregation has been carried out by hand, based upon setting a threshold greyscale for the ligaments. Below this value, all the voxels (3-D pixels) have been assigned to the pores and above this all have been assumed to be the PMMA. Hence, porosity is derived by dividing the volume of the dark area by the total volume (see Chapter 9 for more details).

2.2.3 Gas Adsorption

Gas adsorption can be used to measure the pore size and its distribution when finer pores are present throughout a material (pore size, 0.2 μm). A gas of a known volume, usually nitrogen, is admitted to a sample and then withdrawn to build up a point-by-point Bruanuer-Emmet-Teller (BET) isotherm. The amount of gas adsorbed depends upon the

microstructure of the sample and the pressure and temperature of the gas. Therefore, the surface area of the porous material can be derived. As no micro-pores were observed in the images of porous PMMA, this technique was not utilised during this project.

2.3 Formation of Porous Polymers/Cellular Materials

Due to the wide range of applications for porous materials, pore size varies widely and, therefore, so does the method of preparing them. Pores can be introduced into a sample in a number of ways, ranging from using differences in the combustion temperature of different components to the compaction of solid spheres. However, all the techniques make two fundamental changes to the material; a reduction in density and an increase in the specific surface area[9].

As a first definition, porous materials can be manufactured as either consolidated or unconsolidated materials. Consolidated materials are rigid structures made from the assembly of particles where the material volume far exceeds that of the pores. Unconsolidated materials are loose, non-rigid aggregates made from the assembly of individual particles[37]. Either of the agglomerates may be made from non-porous particles where interstitial voids between the particles create the porosity, which is therefore a direct result of the size, shape and packing of the particles. In other cases, the particles themselves may be porous and thus both inter-particle and intra-particle voids are present. In most cases, the internal pores are much smaller in both size and volume than the external pores[37]. However, the boundaries between the consolidated and unconsolidated materials can be difficult to distinguish and are sometimes interchangeable, i.e. a material made by grinding is considered consolidated whereas that made by sintering is considered unconsolidated.

With such variation in the size and use of porous materials, there are several different routes to form a porous body, some of which are described below with literature examples. It should be noted that this list is not exhaustive.

2.3.1 Microporous Materials

Materials with pores smaller than 2 nm are defined as microporous and have generated much interest in recent years[41-44]. Starting with aluminosilicon zeolites, the area has spiralled to include covalent organic frameworks (COFs) and mesoporous organic polymers.

Zeolites contain 8 Å pores and are a class of mineral which possess tetrahedrally linked, 3-D frameworks with aluminate and silicate tetrahedra sharing the apexes of the structure as shown in Figure 2.4.

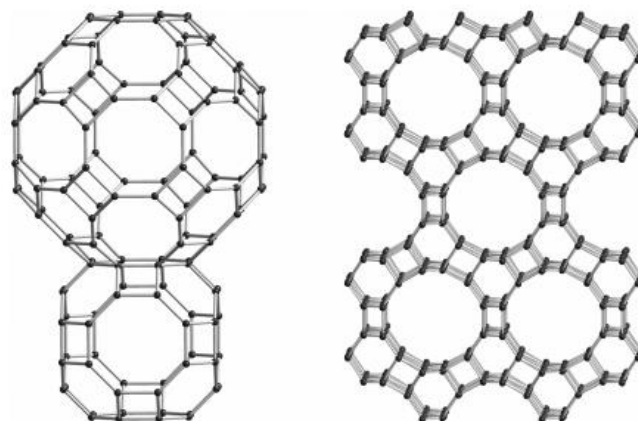


Figure 2.4: Part of the framework structure of naturally occurring zeolites, tschortnerite (lhs) and boggsite (rhs). Only the tetrahedrally coordination framework cations are shown for clarity[45].

Zeolites were observed in 1756 to reversibly adsorb water where on heating, the water is released as steam. Both naturally occurring and synthetic Zeolites are possible, resulting in a wide range of applications from gas adsorption to catalysis in the petrochemical industry[46]. The porosity of Zeolites can be “extrinsic” in nature in which the porosity is a consequence of the packing of the building blocks or “intrinsic” in which the shape of the building blocks gives rise to cavities or windows, an example of which is calixarenes, which is a macrocycle based on the hydroalkylation of p-tert-butyl phenol, see Figure 2.5[47].

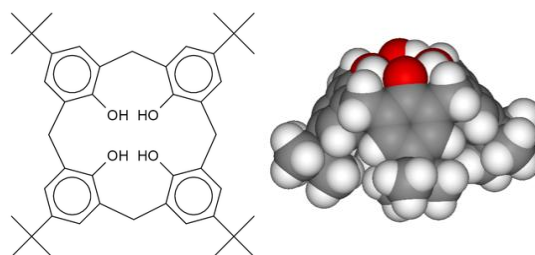


Figure 2.5: Example of a calixarenes with para-ter-butyl substituents showing chemical structure and 3D representation of the cone formed

Covalent organic frameworks (COFs) are porous structures made from the synthesis of extended organic structures which are linked by strong covalent bonds, such as those made between hydrogen, boron, carbon, nitrogen and oxygen[48-49]. The porosity is formed through the adjoining of molecular building blocks which form structure such as the

tetrahedral diamond structure shown in Figure 2.6. This creates lightweight materials which can be used for gas storage, photonic and catalytic applications. The pore size is shown to be in the region of 21.8 Å based upon calculations using the bond lengths[49].

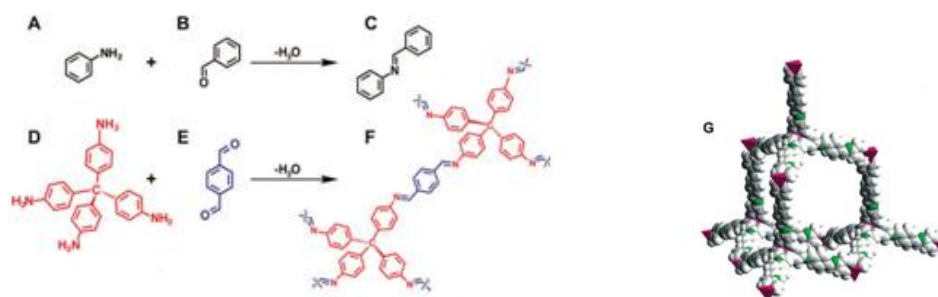


Figure 2.6: Condensation of aniline with benzaldehyde which forms N-benzylidene-aniline. This is then reacted with the product of D and E which join together to produce a tetrahedral structure, G [50]

2.3.2 Compacting

Compacting techniques involve the aggregation and subsequent agglomeration of small particles. Most commonly the techniques consist of applying a pressure to densify a powder which is then pressed into shape. The effectiveness of the final artefact depends on the pre-mixing of the powder or ‘porogen’ with porosity being dependent on the size and shape of the particles. Assuming a set packing structure of the beads and little deformation on densification, simple trigonometry can be used to calculate the pore volume. Below, an example is worked out for one size of PMMA beads assuming a body-centred cubic structure is formed (see Figure 2.7 and subsequent calculations).

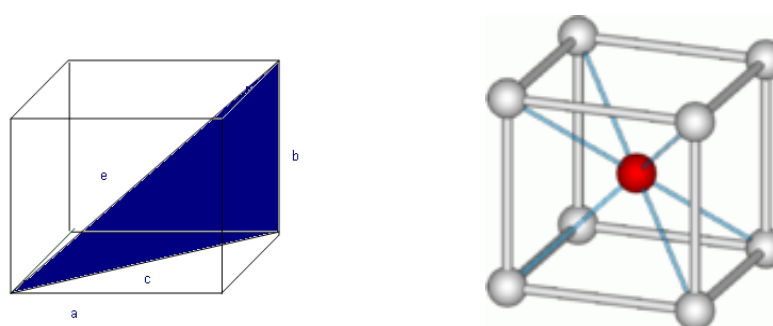


Figure 2.7: Diagrams of a cell indicating nomenclature used and of a body-centred cubic cell

From Figure 2.7, using the Pythagoras theorem:

$$\text{i) } c^2 = a^2 + b^2$$

$$\text{ii) } e^2 = c^2 + b^2$$

Substituting i) into ii)

$$e^2 = (a^2 + b^2) + b^2$$

Rearranging and simplifying since $a = b$

$$a = \sqrt{\frac{e^2}{3}}$$

Using a , the volume fraction of the particles, ϕ_r , in a unit cell can be calculated

$$\phi_r = \frac{\frac{\pi}{3} d^3}{a^3}$$

where d is the diameter of the beads.

The space between beads, τ , on a side of the cubic cell can also be calculated from a where

$$\tau = a - 2r$$

Using the above calculations, spheres with the same density have a volume fraction equal to 0.63 and a porosity equal to 0.37.

Aside from body-centred cubic, face-centred cubic and simple cubic are two alternative packing structures which are based on a cubic unit cell (see Figure 2.8). Using the above principles, the face-centred cubic and simple cubic packing structures have a theoretical volume fraction equal to 0.740 and 0.542 respectively, with porosities of 0.26 and 0.458.



Figure 2.8: Diagrams showing face-centred cubic packing structures

Using the Pythagoras theorem for a face-centred cubic structure:

$$i) c^2 = a^2 + b^2$$

As a cube is the base structure $a = b$, then:

$$c^2 = (2a)^2$$

$$a = \frac{c}{\sqrt{4}}$$

As c is equal to the radius of 4 beads, a can also be written in the form

$$a = 2\sqrt{2}r$$

Therefore in a face-centred cubic cell, each cell contains eight $\frac{1}{8}$ beads on the apex of the cube and six $\frac{1}{2}$ spheres based on the faces. Knowing the volume of a bead, the volume fraction can be calculated based on the equivalent of 4 whole beads being present per unit cell.

$$\phi = \frac{4 * (\frac{4}{3} \pi r^3)}{(2\sqrt{2}r)^3}$$

Powder pressing is used widely in the formation of refractory bricks, and electronic and magnetic ceramics [8], as well as the processing of PMMA for dentistry applications in the 1980's[51]. In most cases, a powder is mixed with a small amount of water to aid lubrication then pressed into shape using a cast. The pressure can be uniaxial (in one direction), or applied in multiple directions surrounding the specimen with liquid to create the pressure. For both procedures, the pressing stage is followed by firing in an oven in which the cast piece shrinks creating both a reduction in porosity and an improvement in

mechanical performance. Known as sintering, the particles in the firing process coalesce to form bridges between adjacent particles, which alter the size and shape of the pores (see Figure 2.9). In excess of 120 °C, the PMMA is above its T_g and hence the bead material softens, creating a bonded link between the particles. In 1976, lightly-sintered PMMA was prepared for use in dentistry applications by compression moulding using a 1 inch die and a pressure of 1000 psi[51]. The success of the technique was found to depend greatly on the temperature of the die, with temperatures in excess of 120 °C resulting in dense non-porous samples due to over-softening of the polymer. Powder pressing is still used widely today in the formation of metals and ceramics[52].

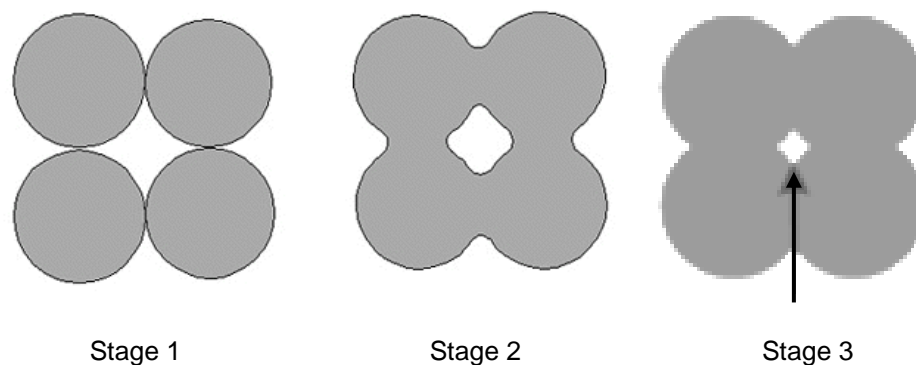


Figure 2.9: Sintering a powder. Stage 1; powder particles after pressing. Stage 2; particle coalescence and pore formation begins. Stage 3; as sintering proceeds, pores change size and shape

Slip casting is a very common method which can be discussed under the heading ‘compacting techniques’. In the slip, clay particles are added to water or a similar liquid to form a slurry. The clay slip or slurry is poured into a mould and left to dry. the drying time depends on the size and shape of the mould, relating to its surface area. The liquid is removed from the slurry by capillary suction through networks of pores in the mould. Once approximately 50 % of the water is removed, the clay particles are consolidated at the mould surface forming a “green body”[53]. As described in Chapter 1, Section 1.2.2, slip casting is still widely used throughout the ceramics industry in the casting of sanitaryware as well as for other applications. The formation of the ceramic is from a densely-packed arrangement of randomly packed spheres, which has a free volume fraction of 36 %.

2.3.3 Subtractive Porosity

Subtractive porosity uses a variety of techniques to selectively remove molecules purposely blended into the material to create pores. The porosity is controlled by the blend formulation where varying the type, level and size of additive changes the porosity.

Combustion is a subtractive technique which burns out additives to create porosity within a sample. In most cases firing of the green article is followed by sintering at elevated temperatures, which induces mechanical strength within the piece as well as porosity. A considerable amount of literature has been published on this topic, with a wide range of fillers being used in materials varying from using PMMA beads in the making of porous metals and ceramics[54-56] to hydroxyapatite particles in ceramics for bone cement[57-58]. In fact, combustion porosity can be used with any combination of materials as long as a distinct difference in combustion temperature between the two materials is apparent. In addition, the components must be able to mix and remain homogeneous whilst setting to ensure an even pore distribution. The technique allows for well distributed pores of well-defined shape and size. Jing et al used a slightly reverse approach where a colloidal crystal template was made using silica microspheres[59]. Irregular packing of the silica spheres creates holes between the spheres. A monomer is introduced to the matrix which is subsequently polymerised, and the silica then removed to create pores by dissolving in 4 % hydrofluoric acid solution. This creates a mesh-like material which can be rigid if formed with PMMA, to more flexible for those made from polyurethanes.

Dispersion techniques utilise the difference in boiling points of liquids, where a liquid with a low boiling point is evaporated from the reaction mixture in the final stages of casting. In 1996, macroporous PMMA was produced using a low molecular weight alcohol dispersed throughout the emulsion. By increasing the alcohol content, the number of pores is increased in the final product [60]. Serrano et al. concluded that 60 %wt ethanol in water is the optimum ratio for maximum porosity and mechanical strength in the final material. Above this percentage, porosity continues to rise resulting in weaker materials which can no longer withstand compressive forces due to poor connections between the spheres.

Salt, (NaCl) was also used to introduce porosity into PMMA in the late 1970s, during the manufacture of PMMA dental implants. Porosity induced the growth of bone tissue through the implant, thereby increasing adhesion to the gum[51]. To create porosity, salt was dissolved in water and added to the MMA and initiator which was subsequently mixed and left to polymerise and cure. On curing, the salt precipitates out as water evaporates

and is removed by a stream of dry compressed air through the sample, which in turn helps to dry the mould. This methodology has been widely used when PMMA is used in surgical applications to enable bone regeneration [61-63]. However, due to the nature of the salt, several washes have to be undertaken before it is fully removed, which was found to be time consuming. However, the porosity of the final material is easily controlled by the particle size and level of the salt particles.

2.3.4 Foaming

Porosity can also be induced by blowing an inert gas, such as nitrogen or carbon dioxide, through a material which causes foaming, often referred to as the 'bubble generation' method. Evolution of this technique led to the finding of materials which foam spontaneously by release of carbon dioxide during a chemical reaction, for example in the production of polyurethane foams[16]. Development of this led to the formation of hydrophilic pores via the addition of water with supplementation of a surfactant or a foaming agent to ensure uniform foaming and stability. The porosity is controlled by the foaming agent and/ or the stirring conditions. It should be noted that foaming often results in a high level of closed porosity where the pores are not connected to one another, which is the desired result for insulating and packing materials. More recently a plethora of literature has been published on the utilisation of supercritical carbon dioxide to form pores in PMMA due to its ease of processing, its non-toxicity, low cost and non-flammability[64-65]. Although the techniques vary, the basic principle behind the use of carbon dioxide as a porogen is similar. On a simplistic level, PMMA is placed in a preparation vessel in which CO₂ is added and the vessel heated to a temperature above the T_g of the polymer. The reaction vessel is rapidly pressured until the adsorbed CO₂ molecules nucleate, therefore forming bubbles in the matrix, see Figure 2.10[64]. The vessel is then slowly depressurised to avoid the collapse of the pores. The pressure of the vessel controls the microstructure and hence pore size of the final material with pore size varying (10-50 microns) depending on reaction conditions[66]. Goel et al updated the technique to use higher pressures (25-35 MPa) in the super-critical region followed by rapidly quenching the material. The cell growth can, therefore, be manipulated by changing the CO₂ pressure resulting in cells from 0.4-20 microns[67].

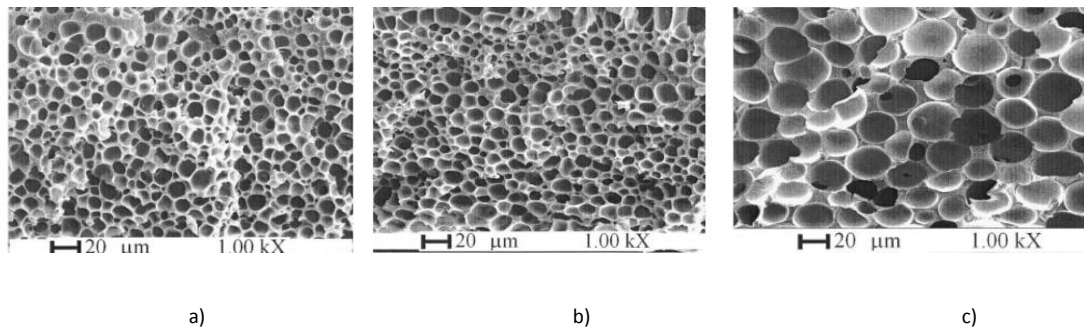


Figure 2.10: Effect of pressure on porous PMMA formed by the super-critical foaming of CO₂ at (a) 25 MPa, (b) 20 MPa and (c) 15 MPa[67].

2.4 Porous PMMA for use as Bone Cement and Surgical Dressings

The objective of this project was to replicate the porous nature of gypsum as a mould material for ceramics by creating a material with a highly-interconnected porous network. However, the new materials must be stronger and more durable to enable more ceramic pieces to be cast from the same mould. Substituting a synthetic replacement for gypsum is not a new idea. In 1962, Götz and Will filed a patent detailing a new material for the preparation of surgical dressings [68]. The novel polymer discussed in the patent has the benefit of being lighter, stronger and permeable to water and X-rays. The resin was prepared *in situ* by mixing a monomer, polymeric beads, water, alcohol and a catalyst suitable for room temperature initiation. During polymerisation the aqueous solvent was expelled, leaving voids in the hardened casting. The authors commented that the solvent must make up no more than 50 % of the overall volume in order to retain an acceptable mechanical strength, with the alcohol being used for faster evaporation. Including water in the blend formation in the making of porous PMMA allows the temperature released on polymerisation to be dissipated by the aqueous medium, thereby allowing the mixture to be applied directly to the skin. Acrylic resins have been utilised in more recent studies where a similar polymerisable mixture is used over a scaffold to bind an open wound[69].

First trialled in the 1960's, acrylic bone cement has been used solely as the "cement" material for attaching a metal implant to bone tissue in hip replacement surgery[70]. Acrylic bone cements are composed of two main components: a liquid and a solid. The liquid part consists of MMA, dimethyl-*para*-toluidiene, (DMPT, an amine catalyst to allow for polymerisation at room temperature) and hydroquinone, used as a reducing agent. PMMA beads, benzoyl peroxide and a radiopacifier make up the solid part of the reaction mixture to allow for visualisation by X-rays [71-72]. Initially, the use of acrylic cements was

limited as without a suitable solvent, the heat released in the exothermic propagation step was well above threshold levels known to damage biological tissues[73]. Pascual et al looked to control the exotherm by changing the size of the PMMA beads, which make up approximately 70 % of the overall volume. By using larger beads with an average diameter of 60 μm , Pascual reduced the peak temperature of polymerisation by approximately 30 $^{\circ}\text{C}$ when compared with smaller counterparts (20 μm) [33]. However, the mismatch of mechanical properties between the strong PMMA and relatively weak bone led to significant wear of the bone tissue. To improve the interface between the plastic and bone, several studies modified the standard acrylic bone cement to include aqueous molecules which evaporate on curing. In turn, this further helps to dissipate the heat of polymerisation[5, 74-75]. De Wijn added a cellulose derivative in the form of an aqueous gel to unreacted acrylic dough as a means to introduce porosity into the material. However, unlike previous studies he did not add a preformed polymer bead, thus no porosity was gained by irregularities in bead packing [5]. Once set, the gel was washed out leaving behind pores. The porosity was shown to increase as the gel volume increased, with the water coagulating to form interconnecting, penetrating pores thereby increasing the permeability of the material. Incorporation of the aqueous gel at 50 % of the total volume led to a decrease in the temperature rise to 40 $^{\circ}\text{C}$. However, the pioneering study was abandoned after the mechanical properties of the material (including fatigue life, ultimate failure stress and stiffness) were found to be considerably weakened. Boger recently repeated a similar study to De Wijn's using cellulose as a pore-forming agent [74]. Again he linked the level of cellulose gel to increasing porosity and to a weakening of the mechanical properties of the material. In addition, Boger noted that inadequate mixing led to the coagulation of the gel, leading to large voids within the material (see Figure 2.11). This additional porosity was removed when mixing time of the gel and polymer was increased to 120 seconds.

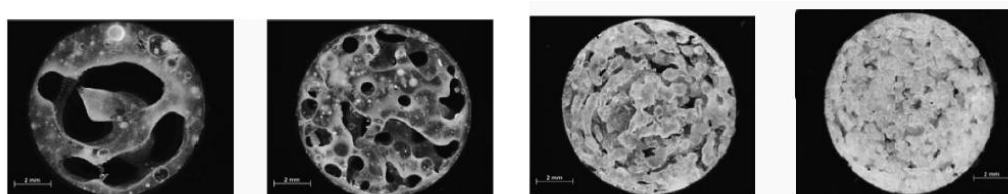


Figure 2.11: Influence of mixing time on porosity (from left to right) 30 s, 60 s, 90 s and 120 s [76] of an acrylic dough with a cellulose gel.

2.5 Porous PMMA in the Making of Ceramics

Porous PMMA was first used for the casting of ceramics in 1966 [77]. The patent claims detail two methods; one similar to that of the surgical dressings where the porous material is formed by the expulsion of water [68], the second differing as the aqueous phase remains in a dispersed state once the polymerisation has finished, resulting in liquid-filled pores. The addition of this non-solvent allows for the tailoring of the porosity of the material. However, it is limited to pores of 50 μm or less. Using different levels of solvent to non-solvent the interconnectivity of the pores can be varied, but again these alterations are limited and the material consists mainly of closed pores. To be able to remove water from a ceramic, open, interconnected pores are desired and hence studies involving liquid-filled pores were abandoned at an early stage[78].

Several studies have identified similar procedures to those described for bone cement [12, 39, 79-80]. In all systems, the basic porosity is derived from the irregular packing of pre-made polymer spheres, which comprise the largest part by weight of the mixture [12]. The beaded polymer is bound together by polymerisation of a monomer (usually MMA, although styrene is commonly mentioned) which is polymerised at room temperature using a redox initiation system. Water is added to the blend mixture to reduce viscosity and allow for improved mixing as well as heat dissipation [12]. The powdered polymers control the pore size through their dimensions, shape and particle size distribution, giving an overall open pore volume of 30 % with pores irregular in shape and distribution [80]. More recent studies have used surfactants to help stabilise the blend mixture and, by increasing liquid volume, decrease the onset of the rise in viscosity. The surfactants (emulsifying agents) vary widely in character from anionic to non-ionic. No inference is given as to why the surfactants are added, but after introduction by Will in 1973 their inclusion continues throughout the literature [80]. Substituting gypsum with the porous polymer allows for pressure casting to be introduced. This rapidly speeds up the drying time of the cast piece by blowing a stream of dry compressed air over the cast body, thereby creating a positive pressure increasing the removal of water from the mould. Utilising low pressure methods of 0.75 bar, the waiting time between moulds is reduced to 15 minutes from a previous waiting time of 230 minutes when slip casting techniques are used[81]. In addition, plastic moulds also have the benefit of being mechanically stronger and therefore can withstand 5,000 cycles as opposed to fewer than 100 cycles with gypsum [12]. The British Ceramic Research company builds upon reducing casting pressures by introducing tubes throughout the casting material [14]. The reduced pressure is applied by sucking fluid from the mould

through sealed pipes spaced evenly throughout the mould which is heated to 40 °C. Once dry, the mould is released by blowing air back through the extended network of pipes. The invention has received little uptake industrially due to the high initial capital outlay needed to implement the system.

In 2004 Ergun et al. made several porous PMMA composites using a two-bead system and evaluated them with respect to their mechanical performance [2]. Difficulties arise, however, when attempts are made to duplicate the data. The experimental conditions given are incomplete, with no amine accelerator mentioned in the text nor any indication of a thermal input to allow for decomposition of the benzoyl peroxide. Nonetheless, this is one of the few published academic studies on porous PMMA materials. Ergun used two beads of diameters of 22 and 150 μm in size. Using simple trigonometry and assuming the larger beads are touching each other in the form set out in a simple cubic structure shown in Figure 2.12 the large variation in bead diameter would enable the smaller bead (yellow) to fit in the interstitial sites between the larger beads (red) (see Section 2.1.3 for details of these calculations). In theory this would decrease the porosity of the material.

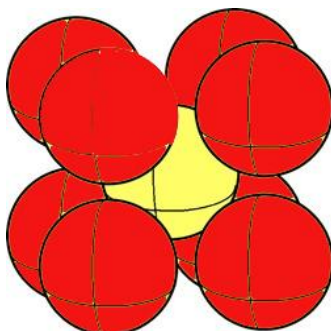


Figure 2.12: Diagram of simple cubic structure of large beads (red) encasing the smaller bead (yellow)

Ergun et al carried out a series of experiments where the overall concentration of water and surfactant were varied between 30-40 % whilst keeping the water:surfactant ratio constant at 1:0.13. He concluded that the water+surfactant concentration significantly affects the pore fraction, morphology and cell connectivity with increased water content forming finer pores with better connectivity. However, the study would have been more convincing had the surfaces not been polished prior to visualisation by SEM from which much of the data is drawn, since this significantly distorts the materials. Polishing creates a significant amount of heat, forcing the polymer above its T_g which softens the polymer which may then flow, resulting in a decrease in the calculated porosity and significantly altering the pore shape. In addition, the paper would appear to be over ambitious with its claims about increased permeability, with little variation observable in the points shown

outside the error margins for the test. Furthermore, the conclusions place significant weighting on one point which is arguably slightly higher than the rest. However, the compression testing results clearly show that increasing the surfactant+water concentration decreases the mechanical properties of the materials. Other papers by the same authors detail investigations into increasing the particle diameter of the PMMA beads [82]. Here, permeability is shown to increase with average particle diameter, albeit without indications of the error levels, whilst no real increase in porosity is observed. In addition, the collapse strength of the material decreases with particle size.

Although little research has been undertaken on the fundamentals of porous PMMA, several authors have conducted studies into toughening procedures with the aim to increase the fatigue life of the moulds [3, 82-85]. Chapter 8 focuses on the toughening of porous PMMA, and hence these papers have been discussed within that chapter.

2.6 Summary

Although the literature on porous PMMA materials is limited, parallels can be made with the more studied fields of bone cement and surgical dressings. Porosity has been introduced to the porous PMMA in a number of ways, including seeding with salt and alcohol. The mechanism of formation of the pores has two possible proposed theories. Conclusions from the literature point towards the porosity being reliant on the inclusion of water during formation, where porosity is formed by the removal of the solvent on drying of the materials[86]. However, calculations on bead packing show that the obtained levels of porosity are similar to that of the random packing of beads, with a pore volume fraction of 0.3 and a density of 0.8 g cm^{-3} (as calculated in Section 2.3.2). This thesis discusses both these methodologies, with the aim of elucidating the mechanism of pore formation in the production of porous PMMA moulds for ceramics processing.

3. Experimental Details for the Synthesis and Characterisation of Porous PMMA

This chapter is divided into three parts: the characterisation of the starting materials; the preparation of porous PMMA materials; and characterisation of the final materials.

Porous PMMA is made from 4 main components: monomer, PMMA beads, surfactant and a redox initiator system. A range of different surfactants, monomers and PMMA beads have been incorporated into the blend formulation (see Table 3.1) to observe their effects on the physical characteristics of the final materials. The surfactants have been characterised using NMR and pendant drop analysis to obtain critical micelle concentrations (CMC) in both water and in an MMA-saturated water solution. NMR has also been used to elucidate the structure of polybutadiene diacrylate (PBDDA), which was used as a toughening agent in the ligaments as detailed in Chapter 8, and the synthesised graft copolymer of MMA-PBDDA. The molecular masses of PMMA beads was obtained using gel permeation chromatography (GPC) at Lucite International.

The synthesis route for porous PMMA involves 3 distinct stages: the dissolution of an initiator, (benzoyl peroxide, BPO), in MMA; the forming of an emulsion through addition of water and surfactant; and the addition of beads and the tertiary redox agent, dimethyl-*p*-toluidene (DMPT). Full experimental details follow in Section 3.2.

Finally, characterisation of the porous PMMA materials is detailed, which includes compression testing, cyclic fatigue testing, residual monomer analysis by gas chromatography (GC), porosity, water permeability, differential scanning calorimetry (DSC), and imaging techniques.

3.1 Characterisation of the Starting Materials

With the exception of “alternative monomers”, all materials used in the making of porous PMMA have been used as received. Their purities, suppliers and brand names are given in Table 3.1. Where applicable, the materials used in the standard blend have been highlighted in bold. Alternative monomers, for example styrene, *t*-butyl methacrylate, and isobutyl methacrylate, were purified by washing with NaOH (2%) to remove the inhibitor and then washed with deionised water prior to being dried over anhydrous calcium carbonate. The monomers were separated from the drying agent by filtration before use.

Table 3.2: Table of materials

CHEMICAL	SUPPLIER	GRADE AND CHARACTERISTICS
Monomer		
Methyl methacrylate (80-62-6)	Lucite International	Colacryl TS1504, 60ppm of hydroquinone inhibitor
t-butyl methacrylate (585-07-9)	Sigma- Aldrich	200 ppm hydroquinone monomethyl ether inhibitor
Isobutyl methacrylate (97-86-9)	Sigma Aldrich	≤15 ppm hydroquinone monomethyl ether as inhibitor
Styrene (100-42-5)	Sigma Aldrich	10-15 ppm 4-tert-butylcatechol as inhibitor
Catalyst System		
Dimethyl-p-toluidene (99-97-8)	Sigma Aldrich	M_n 135.21
Benzoyl peroxide (94-36-0)	Sigma Aldrich	Luperox A75, 75% active (remainder water)
Surfactant		
Triton X100 (9002-93-1)	Sigma Aldrich	Laboratory grade, 100 % active, M_n 647 g mol⁻¹
Lutensol TO3	BASF	100 % active, M _n 340 g mol ⁻¹
Lutensol TO5	BASF	100 % active, M _n 430 g mol ⁻¹
Lutensol TO6	BASF	100 % active, M _n 470 g mol ⁻¹
Lutensol TO7	BASF	100 % active, M _n 500 g mol ⁻¹
Lutensol TO8	BASF	100 % active, M _n 600 g mol ⁻¹
Lutensol TO109	BASF	85 % active, M _n 630 g mol ⁻¹
Lutensol TO129	BASF	85 % active, M _n 750 g mol ⁻¹
Lutensol TO15	BASF	100 % active, M _n 850 g mol ⁻¹
Lutensol TO20	BASF	100 % active, M _n 1000 g mol ⁻¹
Congis Disponil FES32	BASF	30 % active, M _n 432 g mol ⁻¹
Congis Disponil A1080	BASF	80 % active, M _n 632 g mol ⁻¹
PMMA Beads^b		
Colacryl DP300	Lucite International	Mean particle size 93 µm, M_w 1110 kg mol⁻¹
Colacryl TS2082	Lucite International	Mean particle size 92 µm, M _w 447 kg mol ⁻¹
Colacryl DP300U	Lucite International	Mean particle size 93 µm, M _w 2406 kg mol ⁻¹
Colacryl TS1334	Lucite International	Mean particle size µm, M _w kg mol ⁻¹
Colacryl TS1890	Lucite International	Mean particle size 42 µm, M _w 377 kg mol ⁻¹
Colacryl D120	Lucite International	Mean particle size 50 µm, M _w 655 kg mol ⁻¹
Colacryl D80	Lucite International	Mean particle size 68 µm, M _w 778 kg mol ⁻¹
Colacryl D150	Lucite International	Mean particle size 55 µm, M _w 782 kg mol ⁻¹
Colacryl D60	Lucite International	Mean particle size 71 µm, M _w 884 kg mol ⁻¹
Elvacite E2010	Lucite International	MMA/EA mix Mean particle size 155 µm, M _w 92 kg mol ⁻¹
Elvacite E3001	Lucite International	MMA/EA mix Mean particle size 186 µm, M _w 88 kg mol ⁻¹
Colacryl MH254	Lucite International	Mean particle size 482 µm, M _w 137 kg mol ⁻¹
Lucite 47Gi	Lucite International	Mean particle size 142 µm, M _w 822 kg mol ⁻¹
Colacryl TS1352	Lucite International	Mean particle size 45 µm, 4 % crosslinked with allyl methacrylate
Colacryl TS1697	Lucite International	Mean particle size 70 µm, 10 % crosslinked with allyl methacrylate
Toughening Particles		
XC42 toughening particles	University of Manchester, PhD project	A 3 layer toughened particle consisting of a rubber layer of crosslinked poly{(n-butyl acrylate)-co-styrene} and a glassy layer of poly{(methyl methacrylate)-co-(ethylacrylate)}. The particles have a rubber core and outer layer which is separated by a glassy polymer layer graft-linked to the other layers in contact with it. [87]
Polybutyadiene diacrylate (SR307)	Sartomer	M _n 3770 g mol ⁻¹
PMMA-polybutadiene diacrylate	For preparation see Chapter 8.	M _n 4970 g mol ⁻¹

^a M_n is the number average molecular mass defined by $M_n = \sum N_i M_i / \sum N_i$ where N_i is the number of molecules of species i of molar mass M_i.

^b M_w signifies the weight average molar mass defined by $M_w = \sum N_i M_i^2 / \sum N_i M_i$

3.1.1 PMMA Bead characterisation using Gel Permeation Chromatography (GPC)

GPC, or size exclusion chromatography, is a secondary method of determining number average molecular weight (M_n), weight average molecular weight (M_w), and molar mass distribution of a polymer in which analytes are separated on the basis of hydrodynamic

volume (V_h). The dilute polymer solution is injected into a continuously-flowing solvent passing through a densely packed column containing a porous poly(styrene-divinylbenzene) gel [88]. Smaller molecules can penetrate the pores and so explore a larger volume, increasing their retention time on the column giving a larger elution volume (V_e). Molecules larger than the largest pores pass through the column unhindered and therefore are the first to be eluted (see Figure 3.1).

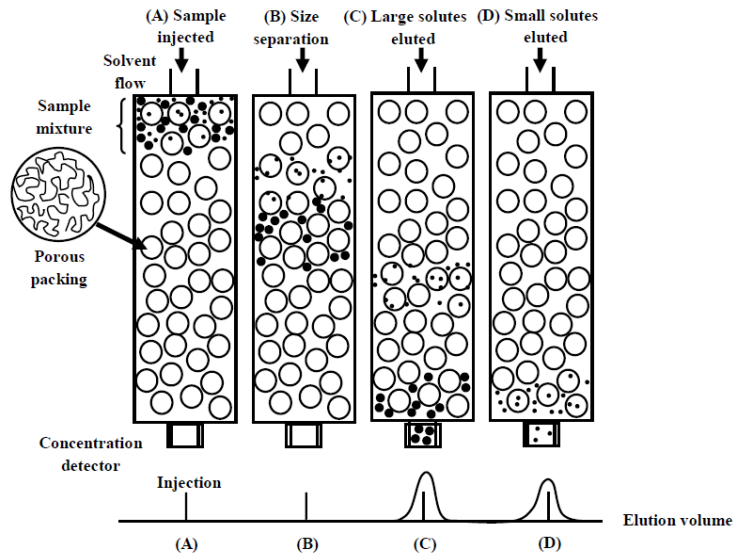


Figure 3.1: Separation in a GPC column by molecular size [89]

The elution volume (V_e) is the amount of solvent which must flow through the system before a molecule of solute is eluted, and is divided into two parts: the interstitial volume (V_o), which corresponds to the volume of the mobile phase located between the packing particles and within the piping, and the pore volume accessed, where K_{se} is the fraction of the pores penetrated by the polymer molecules and V_i is the volume of solvent inside the beads[16]. For very large molecules which are unable to penetrate the pores, K_{se} is equal to zero.

$$V_e = V_o + K_{se} V_i$$

When solute molecules enter small pores, their conformational degree of freedom is limited, resulting in a decrease in entropy (S). Assuming no interaction between the stationary phase and the solute molecules, the relationship between K_{se} and the change in free energy (ΔG^0) can be expressed as[88-89]:

$$\Delta G^0 = -RT \ln K_{se}$$

Given the thermodynamic relationship

$$\Delta G^0 = \Delta H^0 - T\Delta S^0$$

Rearranging and assuming $\Delta H^0 = 0$

$$K_{se} = \exp\left(\frac{\Delta S^0}{R}\right)$$

where R is the gas constant and T the temperature in Kelvin.

Inside the pore, the number of conformations available for a polymer molecule to assume is reduced and thus the entropy change is negative. Various models can be used to assess this loss; however the general result is given below:

$$\Delta S_p^0 = -RA_s \left(\frac{\bar{L}}{2}\right)$$

where A_s is the surface area per unit volume and \bar{L} is the mean diameter.

Therefore, substituting back into the equation for V_e , the elution volume is inversely proportional to the molecular size of the molecule

$$V_e = V_o + V_i \exp\left(\frac{-A_s \bar{L}}{2}\right)$$

To allow for determination of molecular weight, the GPC must be calibrated with polymer standards of known molecular weight. Using a universal calibration procedure, which assumes that hydrodynamic volume is proportional to the product of the intrinsic viscosity ($[\eta]$) and molar mass (M), the separation of molecules is governed only by hydrodynamic volume. Therefore, one calibration curve can be used for multiple polymers as V_e is independent of the polymer being identified. From the GPC data, a plot of $\log([\eta]M)$ versus V_e can be constructed. Most of the curve is linear in the required range and can thus be linked to a slightly altered Mark-Houwink equation ($[\eta]M = KM^{\alpha+1}$)

$$M(V_e) = \left[\frac{([\eta]M_{V_e})}{K} \right]^{1/(1+\alpha)}$$

where α and K are constants which can be readily determined for the polymer and solvent, and $([\eta]M_{V_e})$ can be obtained from the calibration curve at V_e .

In practice, GPC measures the time of elution rather than the elution volume. To enable simultaneous analysis of concentration, viscosity and molar mass, 3 detector systems are possible. These use (a) a differential refractometer to monitor the concentration of the polymer by the change in the refractive index (Δn) of the eluent which is directly proportional to the concentration of the polymer; (b) a differential viscosity detector which measures the specific viscosity of the eluent; and (c) a low-angle laser light scattering detector which measures the weight average molar mass. The analogue signal from the detectors is processed and converted in a computer to allow for analysis of the data. If more than one detector is used in series, a flow rate marker can be used to synchronise the detectors. In this project, a differential refractometer has been used to measure the polymer concentration which was calibrated against PMMA standards to obtain molar mass.

3.1.1.1 GPC Method

GPC analysis was carried out on all the PMMA beads supplied by Lucite International as a means of determining the molecular masses. Dilute solutions were made by dissolving the beads (~10 mg) overnight in tetrahydrofuran (THF, 5 ml) in a sealed vial, before a flow rate marker of diphenyl ether (DPE) was added to the solution prior to injection. The solution was filtered through a 0.2 μm Milipore filter, and 0.5 ml of the solution injected using a hypodermic syringe into the sample injection valve. The GPC system was equipped with three Phenogel columns of 500, 50,000 and 5,000,000 Å (particle size 5 μm , dimensions 300 x 7.8 mm) connected in series to a Shodex RI-101 differential refractometer. The system was eluted by THF at a rate of 1 ml min⁻¹ at room temperature. PMMA standards (600 to 7,700,000 g mol⁻¹) were used to calibrate the GPC as supplied by Polymer Laboratories, see Figure 3.2. The data was collected by a computer and analysed using PSS Win GPC software, unity version (Polymer Standards Service).

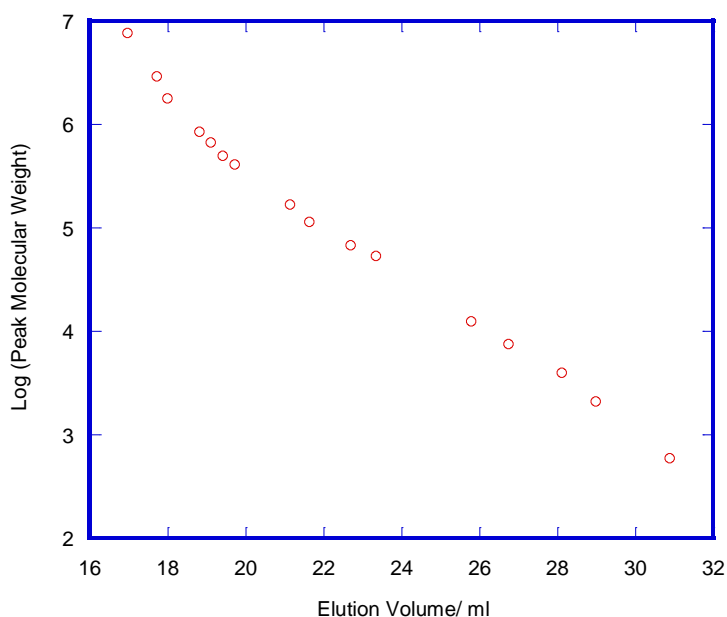


Figure 3.2: Calibration curve for GPC using PMMA standards with known molar mass

3.1.2 Surfactant Characterisation

All surfactants received have been analysed by NMR to elucidate their structure and by the pendant drop method to obtain the critical micelle concentration (CMC).

3.1.2.1 Nuclear Magnetic Resonance (NMR)

NMR spectroscopy involved the detection of the emission and absorption of electromagnetic radiation between discrete energy levels within a system. The energy levels are influenced by the surrounding environment of the nuclei and are related to the chemical structure of the substance being investigated. For the technique to work, the nuclei in question must have a nuclear spin (I) not equal to zero (i.e. have an unequal number of protons and/or neutrons) which on application of a magnetic field acts like bar magnets and can orient $2I+1$ ways. Only ^1H and ^{13}C NMR have been used, so it is these nuclei which shall be focussed on to discuss the technique. Both ^1H and ^{13}C have a spin of $\frac{1}{2}$ and can therefore take up two orientations in an applied field ($+\frac{1}{2}$ and $-\frac{1}{2}$). The difference in energy levels is given by:

$$\Delta E = h\gamma B_0 / 2\pi$$

where γ is the magnetogyric ratio (a proportionality constant which measures the strength of the nuclear magnet), h is Planck's constant, and B_0 is the strength of the applied magnetic field[90]. In the absence of a magnetic field, the magnetic moments of the nuclei

are orientated randomly and therefore, all the spinning nuclei possess the same time-averaged energy. When the spinning nuclei are placed in a strong magnetic field, the moments align resulting in a splitting into two distinct energy levels (see Figure 3.3).

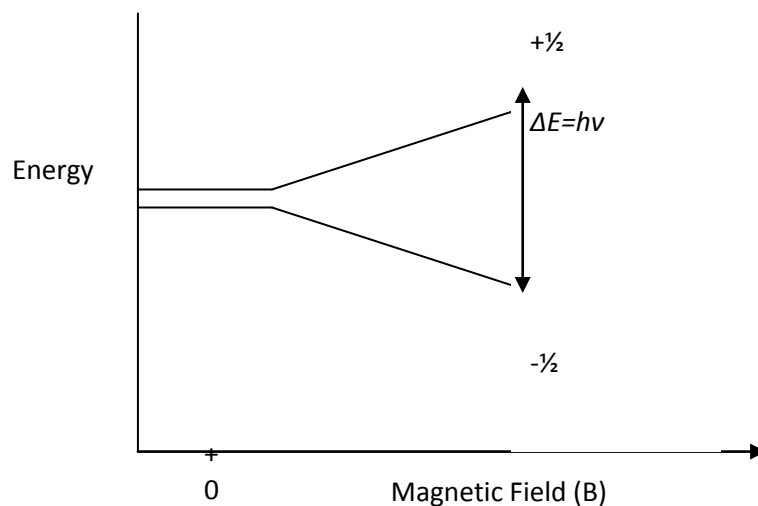


Figure 3.3: Divergence of energy levels on applying a magnetic field

The distribution of nuclei in each of the two states is determined by Boltzmann's distribution

$$\frac{N_{\beta}}{N_{\alpha}} = \exp\left(\frac{-\Delta E}{kT}\right)$$

where N_{β} is the number of nuclei in the higher energy state, N_{α} the number of nuclei in the lower energy state and k , the Boltzmann constant which relates the energy of the particle to its temperature defined by the equation $k = R/N_A$ where R is the gas constant and N_A Avogadro's number. When a specific radio frequency is applied, the nuclei can jump from the lower energy state to that of the higher energy state,

$$\nu = \gamma B_0 / 2\pi$$

Calculating for ^1H , a frequency of 100 MHz is obtained for ^{13}C , a frequency of 25.41 MHz when $B_0 = 2.35$ Tesla[90]. As the population difference of the two energy states differs with the field strength B_0 , it is desirable to operate at higher field strengths (and corresponding higher frequencies) to improve sensitivity.

Two measurement techniques are possible in NMR spectroscopy, continuous wave and Fourier transform. Fourier transform is used almost exclusively due to faster analysis times and smaller sample sizes. Fourier transform spectroscopy applies a radio frequency in a

single powerful pulse which covers a large frequency range in a few microseconds. The pulse excites all the nuclei into their higher energy states simultaneously. As the nuclei relax over time back to the lower energy state, they lose energy of specific frequencies. It is the sum of these frequencies during the decay back to the ground states which is measured as the free induction decay (FID) can be converted to the NMR spectrum by Fourier transform.

If all the nuclei in a molecule were in the same environment, the NMR resonance would occur at one value corresponding to the field strength. However, even in a simple molecule, the field strength felt by the nuclei differs depending upon the density of the electron cloud surrounding the nucleus (see Figure 3.4). These electrons induce electric currents that produce local magnetic fields which oppose the applied magnetic field. The higher the electron density around the nucleus, the higher the induced field and therefore the greater the extent of the shielding. The effective field can be expressed as:

$$B_{eff}=B_0(1-\sigma)$$

where σ is the screening constant which is the magnitude to which the nucleus is shielded. It is often therefore referred to as the chemical shift[91]. In practise, defining shifts by their frequency is inconvenient as each machine differs and variations are observed on a daily basis. Therefore, the difference in the shift of the sample peak (ν_s) is compared to an internal standard; nearly exclusively tetramethylsilane (ν_{TMS}); which is then divided by the operating frequency (ν_0). The result is a dimensionless parameter which is expressed as a fraction of the applied field (parts per million, ppm).

$$\delta = \frac{\nu_s - \nu_{TMS}}{\nu_0}$$

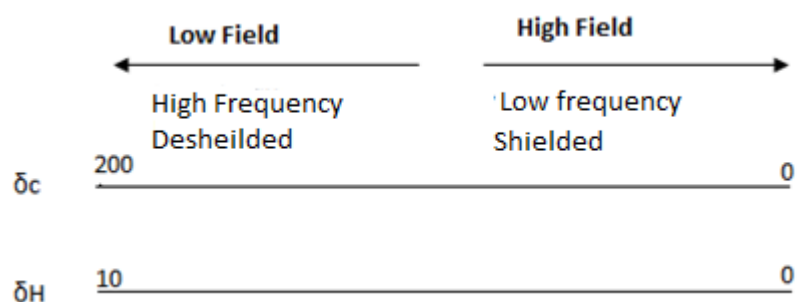


Figure 3.4: Visualisation of frequency shift due to shielding[90]

In summary, electropositive groups such Li and Si shift signals up-field whereas electronegative groups for example N, O and Cl shift signals down-field, as they donate and withdraw electrons respectively. In turn chemical bonds are regions of high electron density and can set up anisotropic magnetic fields. π bonds are especially effective at influencing the chemical shift of nearby atoms and therefore shift the signal downfield when compared with saturated counterparts. A selection of chemical shifts for CH_3X is given in Table 3.2 as an illustration.

Table 3.1: Chemical shifts on CH_3X

X	δ_{C}	δ_{H}
Li	-14.0	-1.94
H	-2.3	0.23
Me	8.4	0.86
Et	14.5	0.91
OH	5.2	3.39
Cl	24.9	3.06

NMR Method

NMR spectra were recorded on a Bruker Avance III 400 MHz spectrometer at ambient temperature equipped with an auto-tuning multi-nuclear direct observation probe able to measure among others, ^{13}C and ^1H spectra. A pulse angle of 30° and a pulse length of $8\ \mu\text{s}$ with 16 transients were employed. ^1H NMR spectroscopy was used to identify the structure of the Lutensol TO and Disponil A1080 and FES32 surfactants. Solutions for ^1H NMR analysis were prepared by dissolving the sample ($\sim 1\ \text{ml}$) in deuterated dimethyl sulphoxide (DMSO) to give a concentration of approximately $10\ \text{mg ml}^{-1}$. MestRe-C software (Magnetic Resonance Companion NMR Data Processing, Version 3.5.1.7) was employed to Fourier transform the free induction decay (FID) data. The NMR spectral data were analysed using the resonance of the deuterated solvent (DMSO 2.50 ppm) as the internal standard. For the surfactants, the peaks were integrated with respect to the terminal alcohol hydrogen.

3.2.2.2 Surface Tension

Surface tension is a measurement of a surface to resist change. Practically, a drop is formed at the end of a needle, which is then measured and a fit of the drop undertaken.

Theoretically, a pressure difference (ΔP) is observed between two points on a curved interface such as a drop. The pressure difference is found to equal the mean curvature of the surface at point $(1/r_2 + 1/r_1)$, where r_1 and r_2 are the principle radii of curvature and γ the surface tension.

$$\Delta P = \left(\frac{1}{r_1} + \frac{1}{r_2} \right) 2\gamma$$

The radius of curvature is the radius of a circular arc which best approximates the curve at that point[92].

For a hanging drop, the pressure difference within the drop between any two vertical positions is

$$\Delta P = \Delta \rho g z$$

where $\Delta \rho$ is the difference in density of the fluids, g the gravitational acceleration constant and z the vertical distance between the two positions A and B (see Figure 3.5).

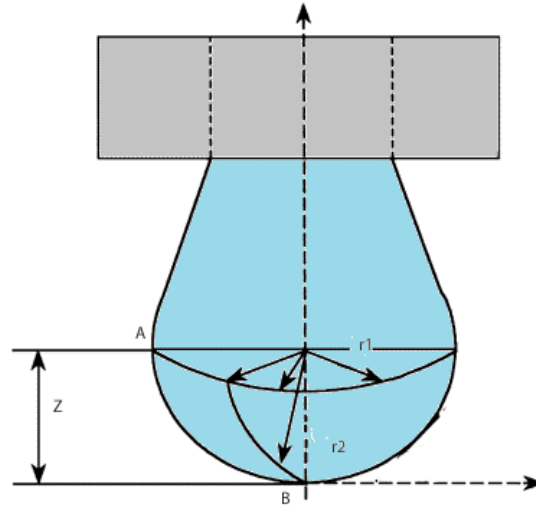


Figure 3.5: Diagram showing the parameter in the Laplace equation for pendant drop analysis

Equating the pressure equations, the surface tension (γ) can be resolved

$$\Delta \rho g z_{\text{between A and B}} = \left[\left(\frac{1}{r_1} + \frac{1}{r_2} \right)_{\text{at A}} - \left(\frac{1}{r_1} + \frac{1}{r_2} \right)_{\text{at B}} \right] 2\gamma$$

Within a few seconds, the software takes hundreds of pairs of points on a single drop, allowing a curve fit as close as possible to the drop shape. As the software analysis is

automated, no further details will be discussed here but further information can be found in the textbook by Miller & Liggieri and in the paper by Nguyen et al[93-94].

Pendant Drop Method

Pendant drop analysis was undertaken on a Krüss DSA-100 drop size analyser using a 1 ml disposable syringe to which a needle of diameter 1.833 mm was affixed. Solutions containing different concentrations of surfactant were tested and analysed using DSA1 v1.9 drop analysis software (Krüss). A drop was formed at the end of the needle which was attached to a syringe plunger assembly on a stepped motor and illuminated using a light source and diffuser. The motor was controlled by a computer so that the drop volume, and hence surface area of the drop, could be changed to obtain the maximum surface area before the drop detaches from the needle under the action of gravity. Prior to the drop detaching, a static photograph is taken on which axi-symmetric drop shape analysis (ADSA) is undertaken. ADSA analyses the drop using differences in grey scale of both the drop and the surrounding interface, in this case air. The software fits a curvature to the droplet based upon the Laplace equation for capillaries, which is linked to the profile coordinates

Critical Micelle Concentration Calculations

The critical micelle concentration (CMC) of a surfactant is the concentration at which micelles spontaneously form in a solution and can be seen experimentally by a discontinuity in a plot of surface tension against $\log(\text{surfactant concentration})$, as shown in Figure 3.6[95]. At surfactant concentrations below the CMC, the surfactant molecules exist independently in solution and also pack at the air-water interface, thereby forming a monolayer and reducing the surface tension of the solution. In the region of the CMC, a compact monolayer exists at the interface and the surfactant molecules begin to build up micellar structures in the bulk liquid, thereby decreasing the free energy of the system through shielding the hydrophobic parts of the surfactant from the water molecules. Above the CMC, further addition of surfactant only leads to the formation of additional micelles.

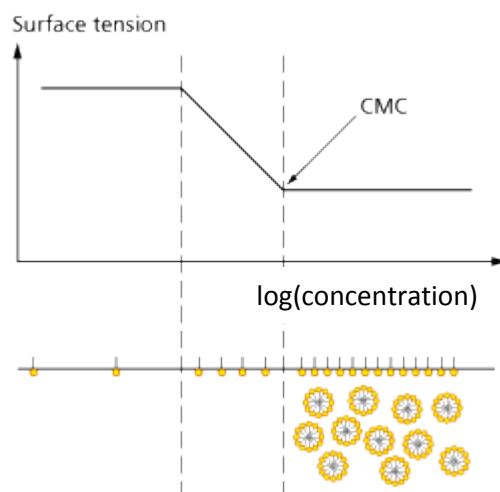


Figure 3.6: Surface tension against log[concentration] for a surfactant in water highlighting detection of the CMC[96]

To determine the CMC of surfactants used in this study, a pendant drop experiment was undertaken to measure the surface tension at different concentrations of surfactant in water and an MMA saturated water solution. Table 3.3 compares values found in literature to those obtained experimentally. In addition to literature values, calculated values of the CMC have been estimated using the Huibers three-parameter model the constants $cKHO$, represents the size of the hydrophobic fragment (8.778 for C12 and 9.485 for C13), AIC , represents the complexity of the hydrophobic fragment, and $RNNO$, which represents the hydrophilic fragment and accounts for the increase of CMC with EO number[97].

$$\log_{10}cmc = -1.80 - (0.567 cKHO) + (1.054 AIC) + 7.5RNNO$$

Table 3.2: Literature values for CMC of Triton X100, Lutensol TO109, Lutensol TO6, and Lutensol TO3 compared to experimental data

Surfactant	Calculated values for CMC/ mmol dm ⁻³	Literature values for CMC/ mmol dm ⁻³	Observed CMC/ mmol dm ⁻³
Triton X100	0.204 [98]	0.20 [99]	0.38
Lutensol TO109	0.824	0.378 [100]	0.37
Lutensol TO6	0.274 ^a	0.31 [100]	0.33
Lutensol TO3	0.195 ^a	0.075 [97]	0.23
Disponil A1080	1.131 ^a	1.24 [100]	0.63
Disponil FES32	0.5170	17.13 [97]	0.85

The measured CMCs differ from calculated values, but the pattern seen with increasing CMC with EO number was observed and are reproducible. Due to the log term in the equation, even a small discrepancy in the line of best fit which yields the discontinuity in the plot of surface tension against log(concentration) can cause a very large change in the quoted concentration value. The structure elucidated from NMR has been used in deriving the calculated values of the CMC for Lutensol TO surfactants. As shown by the change from Lutensol TO109 (C13) to Disponil A1080 (C12) a difference of one carbon unit in a hydrophobic chain can alter the CMC dramatically.

3.2 Preparation of Porous PMMA

The methodology was provided by Lucite International[101] and is based upon patent literature[12]. The system has been scaled-up to allow for informative analysis with the final dimensions of the materials being approximately 230 x 230 x 30 mm. Slight amendments to the blend framework were made in the very early stages of the work to improve the reproducibility of process and are included in the now denoted standard method detailed below, as referred to throughout the thesis.

MMA (146.66 g, 10 wt %), water (439.33 g, 29.96 wt %) and surfactant (Triton X100, 73.22 g, 4.99 wt %) were pre-conditioned in a water bath at 25 °C. Meanwhile an atmospherically controlled box was equilibrated at 24 °C.

BPO (1.22 g, 75% active, 0.08 wt %) was dissolved in MMA (146.66 g, 10 wt %) in a 2 L beaker using a mechanical overhead stirrer at 150 rpm. Surfactant (Triton X100, 73.22 g, 4.99 wt %) was added to the solution and the mixture was stirred for 3 minutes. Water (439.31 g, 29.96 wt %) was poured into the solution to form an emulsion which was stirred for an additional 3 minutes. DMPT (1.46 g, 0.09 wt %) was added to the emulsion followed by the PMMA beads (Colacryl® DP300, 805.41 g, 54.92 wt %) and the viscous mixture was stirred for 3 minutes before being poured into a heavy duty baking tray (230 mm x 230 mm x 40 mm). The polymer was left to cure for 40-60 minutes and after 2 hours was placed into an oven at 60 °C overnight. The next day the set material was removed from the mould and washed with water at high pressure to remove excess surfactant. The sample was dried in an oven at 60 °C overnight before being cut into various sizes of specimen for testing.

Throughout the work various components and conditions were varied from that of the standard blend, examples of which are the oven temperature of the final cure, the PMMA

bead size and the level of surfactant. The changes will be discussed briefly at the beginning of each chapter to avoid confusion.

3.3 Characterisation of Porous PMMA Materials and their Emulsions

The characterisation of porous PMMA can be divided into two parts: (i) characterisation of the emulsion and (ii) characterisation of the final material. Emulsion characterisation has been undertaken on a simplified blend involving water, MMA and surfactant. This enabled insight into the partitioning of components, thereby allowing for development of the mechanism behind the formation of porous PMMA. Characterisation of porous PMMA facilitated comparison between blend formulations and can be subdivided into residual monomer measurement, mechanical testing, thermal properties, porosity, permeability testing, and visualisation of ligaments.

3.3.1 Characterisation of the Emulsion

Intricate analysis of the emulsion stage of the reaction has been undertaken using a simplified blending procedure. To water (100 mL), surfactant (3-7 %wt) and MMA (43-12 %wt) were added. The emulsion was stirred (350 rpm) for three minutes before being transferred to a sealed separating funnel where it was left to split into distinct layers overnight. Once separated, the layers were isolated and weighed. Gas chromatography (GC) analysis was undertaken on the lower water layer to determine levels of dissolved MMA. Simultaneously, the surfactant in the top MMA layer was analysed by either UV spectroscopy (Triton X100) or refractometry (Lutensol TO surfactants) depending on the surfactant type.

3.3.1.1 UV/ Visible spectroscopy

UV/Vis light is used to excite electrons from a low energy state to a high energy state, usually that of an unfilled non-bonding orbital or anti-bonding orbital. The wavelength of the absorption is characteristic of the orbitals concerned and therefore can be linked back to the chemical structure of the molecule. In particular electronic transmission of p, d and π orbitals are studied.

The absorption intensity can be calculated using the Beer- Lambert law which assumes that the absorption is proportional to the number of adsorbing molecules and the fraction of absorption by the incident light is independent of the source intensity, and has the form

$$A = \log_{10} \frac{I_0}{I} = \epsilon \times l \times c$$

where A is the absorbance, I_0 is the intensity of the incident light, I is the intensity of the absorbed light, l is the path length, c is the concentration of the solution and ϵ is the molar absorptivity.

UV/Vis Method

UV/vis spectroscopy was undertaken on diluted samples of Triton X100 samples on the MMA phase of the suspension on a Perkin Elmer Lambda45 UV/Vis spectrometer with UV WinLab software (Perkin Elmer). A UV spectrum was taken of the diluted solution between the wavelengths 190 nm and 1100 nm for which the dilution of the solution was known. An aliquot of the solution was transferred into a quartz cell with a path length equal to 1 cm. An identical cell was filled with the pure solvent used as the diluent and placed in the reference cell of the machine. The incident beam is split to form two beams of equal intensity which are then passed through the cells; one through the sample and one through the reference cell. The intensity difference was recorded at each wavelength.

Triton X100 contains a 1,4 substituted benzene ring. In hexane, benzene has 3 absorption peaks at 184 nm, 203.5 nm and 254 nm which corresponds to ϵ values of 60,000, 7400 and 204 respectively[90]. The latter band, referred to as the B band, is a forbidden band due to the loss of symmetry of the ring due to molecular vibrations so is often difficult to observe. Conjugation of the benzene ring causes the K band (203.5 nm) to shift to a longer wavelength. As the B band (254 nm) moves to a lesser extent, the bands overlap and can in extreme cases swap places. In disubstituted benzenes, there are two noteworthy situations when electronically complementary groups are positioned para to each other, a shift of the main adsorption band to a longer wavelength is observed. When the para groups are not complementary or when two groups are meta or para, the spectrum is closer than that observed by non interacting chromophores. For Triton X100, the substituents are uncomplementary as both are electron donating; therefore the transitions are less than predicted by separate chromophores. In turn, as the ring is conjugated only one band is observable within the limits of the machine which corresponds to the red shifted K band. To gain the concentration of Triton X100 in the unknown solutions, a calibration curve was undertaken on samples with a known concentration using the absorption at 254 nm (see Figure 3.7).

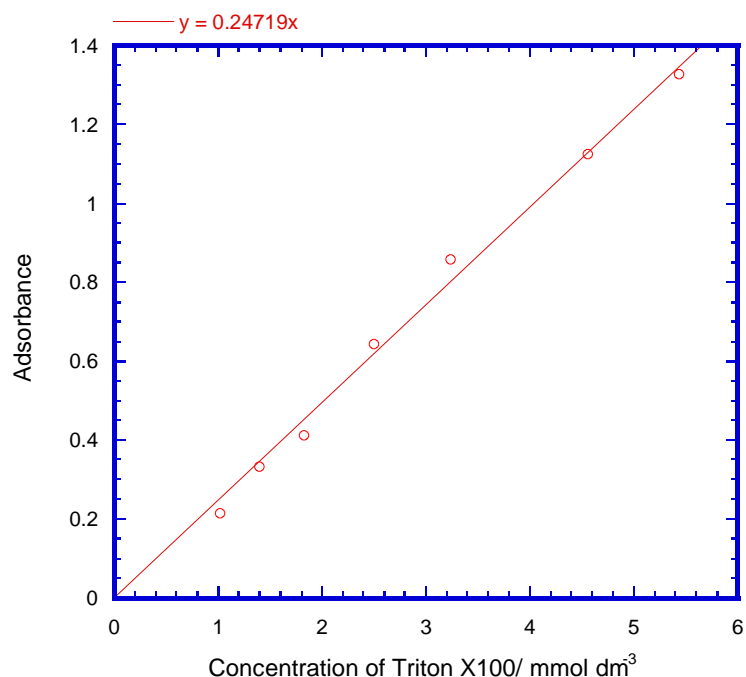


Figure 3.7: UV calibration for Triton X100 in MMA for absorption at 254 nm

3.3.1.2 Refractive Index

An Abbe refractometer has been used to measure the refractive index of monomer-surfactant solutions. Once calibrated the refractive index of a solution can be linked to the solute concentration. Refraction is the change in the direction of a light wave when moving from one medium to another, caused by a change in speed of the wave. When light enters a medium at an incidence angle of α , a portion of the light is reflected back whilst the remainder propagates into the second medium at an angle β . The angles are defined by the gap between the light ray and the line normal to the interface, see Figure 3.8.

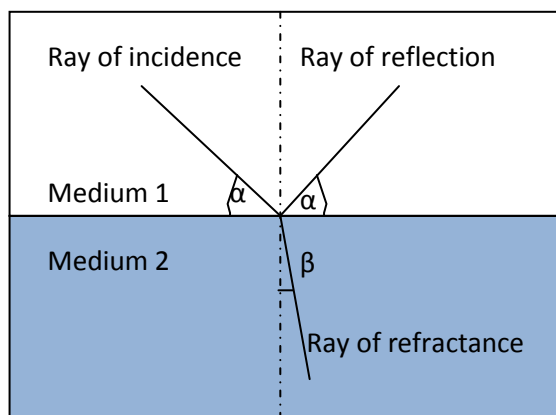


Figure 3.8: Diagram showing light ray passing through two different mediums

The angle of refractance is determined by Snell's law [102-103]

$$n_1 \sin \alpha = n_2 \sin \theta$$

where n_1 is the refractive index of medium 1, and n_2 is the refractive index of medium 2.

The refractive index n of an unknown sample can also be calculated using the ratio of angles

$$\frac{\sin \alpha}{\sin \theta} = n = \frac{\text{velocity of light through medium 1}}{\text{velocity of light through medium 2}}$$

In turn it is also important to note that the refractive index is dependent upon the density and hence temperature of the medium, where the refractive index increases as the temperature decreases. This is defined by the equation

$$n(20) = n(T) + (T - 20) \times 0.00045$$

where n is the refractive index at 20 °C and $n(T)$ the refractive index at temperature T [104].

In an Abbe refractometer, a small aliquot of the sample is pipetted onto a prism which is split into two halves, an illuminating prism and a refracting prism. The refractive prism is made up of glass with a high refractive index i.e 1.75 of which all samples must be less than for the technique to work [104]. A sodium light source is projected through the roughened illuminating prism, ensuring a precise wavelength and multitude of light rays travelling in all directions. As shown in Figure 3.9, the maximum angle of incidence, (θ_i) depicted by light travelling from point A to B, gives the largest angle of refraction (θ_r). Any other ray of light entering the prism will have a smaller refraction angle and hence lie to the left of point C. Hence, the detector, which is placed on the back side of the refracting prism, shows a dark region to the right of point C and a light region to the left.

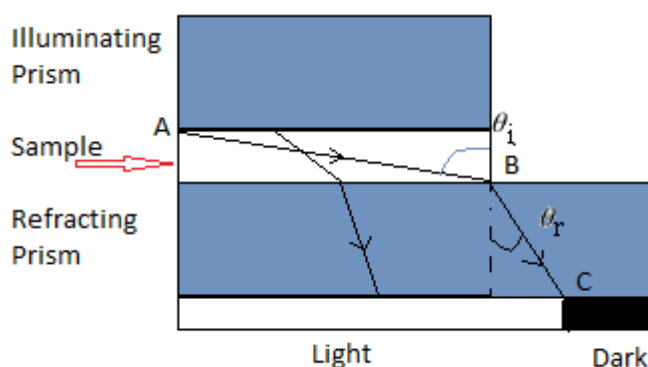


Figure 3.9: Diagram showing key parameters for determination of refractive index in an Abbe Refractometer

If a solution has a different refractive index, then a different angle of refraction will be produced and hence the boundary between the light and dark region will move. This shift can be calibrated with known solutions and the concentration of a component determined. When a sodium light source is used, n can be measured to $\pm 0.1\%$ [91].

Refractive Index Method

The sodium lamp was turned on and left for 30 minutes to obtain full strength. Meanwhile, the water heater was also switched on, allowing water to circulate around the prism equilibrating the cell at a temperature of $25\text{ }^{\circ}\text{C}$. A small aliquot of sample was pipetted between the double prism and the dial adjusted until a clear interface is observed between the illuminated and dark regions meeting on the crosshairs, as shown in Figure 3.10. A reading is then taken off the large and fine scales to obtain the refractive index. The procedure was repeated 5 times for each solution and an average taken.



Figure 3.10: Diagram of Abbe refractometer reading with illuminated and dark regions dissecting the crosshairs

The Abbe refractometer was calibrated with solutions of known concentration of Lutensol TO109, Lutensol TO6 and Lutensol TO3 in MMA (see Figure 3.11,) from which the refractive index of MMA can also be deduced from the y intercept which is deduced as 1.411 ± 0.0005 .

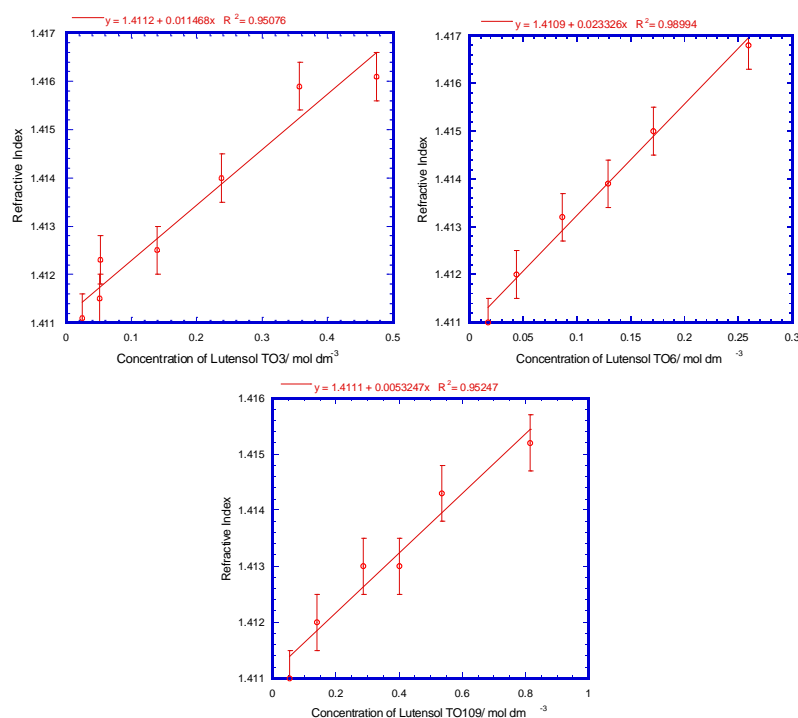


Figure 3.11: Abbe calibration curves for refractive index of Lutensol surfactants dissolved in MMA

3.3.2 Characterisation of Porous PMMA

The following techniques have been used to characterise porous PMMA materials to examine the effects of different blend formulations on properties.

3.3.2.1 Residual Monomer

Levels of residual monomer have been measured using gas chromatography.

In gas chromatography a sample is injected and vaporised onto the head of the chromatographic column before being transported through the column by the flow of an inert gas, the mobile phase. The column itself contains a liquid stationary phase which is adsorbed onto the internal surface of the capillary column. As the carrier gas sweeps the analyte molecules through the column, the analytes interact with the walls on the column and therefore have different retention times depending on the strength of interaction,

which allows for identification and separation. At the end of the column the effluent is mixed with hydrogen and air and ignited to allow identification in a flame ionisation detector. When burnt, organic compounds form electrostatically charged species which can conduct electricity through the flame and produce a current which is measured using a large electrical potential applied at the burner tip. This signal is fed into a computer which plots the signal strength against retention time on the column. The software integrates the curve to obtain the area of each peak.

Evaluation of the GC results was undertaken using the internal standard method, where a known amount of internal standard (butan-1-ol) was added to each sample. The area under the GC peak can then be calculated, where A_i is the peak area, k_i the response factor, c_i the concentration of the internal standard and v the injected volume of solution.

$$A_i = k_i c_i v$$

Similarly the area under the sample peak can be expressed by

$$A_s = k_s c_s v$$

where A_s is the peak area, k_s the response factor and c_s the concentration of the sample.

The injected volume is the same for both the internal standard and the sample; therefore the unknown concentration of sample can be calculated by combining the two equations

$$c_s = \frac{A_s}{A_i} c_i \frac{k_i}{k_s}$$

For MMA,

$$\frac{A_{MMA}}{A_i} = K \times \frac{c_{MMA}}{c_i}$$

where A signifies the areas of the peaks obtained respectively from the GC trace for MMA and butan-1-ol (the internal standard), K is the calibration constant obtained from the plot of A_{MMA}/A_{IS} against C_{MMA}/C_{IS} for samples of known concentration (see Figure 3.12).

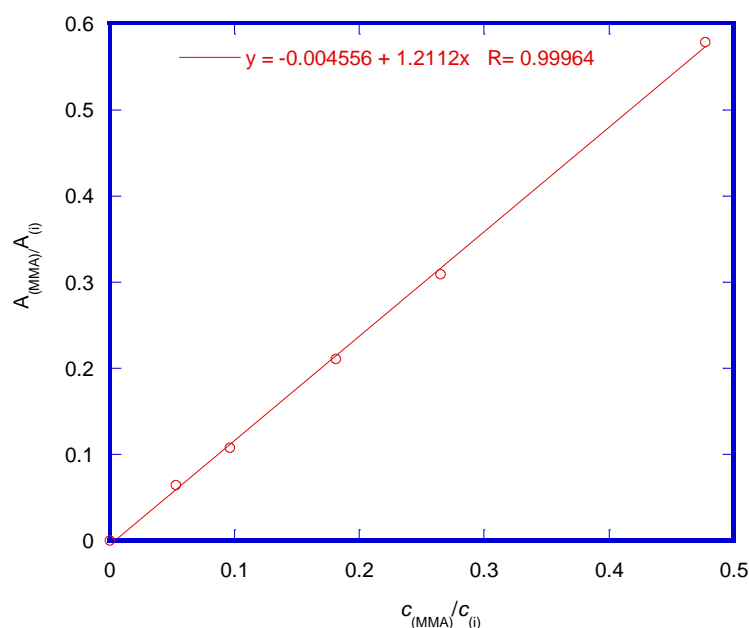


Figure 3.12: Determination of K for MMA using butan-1-ol as an internal standard

GC Method

Gas chromatography measurements were undertaken using an automatic injection Perkin-Elmer Clarus 500 with an injection volume of 1.00 μL Hewlett- Packard HP-FFAP column, (length 10 metres, bore size 0.532 mm) and helium as the carrier gas (flow rate 30 mL min^{-1} , pressure 80 psi). The column was held at 28 $^{\circ}\text{C}$ for 5 minutes before being heated to 160 $^{\circ}\text{C}$ at 10 $^{\circ}\text{C}$ per minute. Once at 160 $^{\circ}\text{C}$ the temperature was maintained for 20 minutes to ensure full elution of the sample.

A sample of known weight of porous PMMA (~ 0.15 g) was dissolved in acetone (~ 4.5 g) using a sonicator in 2 minute bursts followed by a 5 minute rest period (to stop evaporation) until dissolved. Approximately 1 g of the resulting solution was precipitated in a solution of butan-1-ol in methanol ($0.122 \text{ mol dm}^{-3}$) and placed back in the sonicator for 1 minute before being left for one hour at room temperature. The mixture was filtered through a 0.2 μm Millipore filter and the solution placed in a vial on the autosampler ready for analysis. The software (TotalChrom, Perkin Elmer) integrates the area under the curve and the previously discussed calculations can be undertaken manually to obtain the concentration with respect to an internal standard and calibration curve for that component.

3.3.2.2 Mechanical Characterisation

The strength of porous PMMA materials is relevant to the moulding pressure used and the number of cycles the mould can withstand before collapse. Two different techniques have been used to quantify the materials' strength: compressive testing and cyclic fatigue testing.

Compression Testing

Compression testing is a means of calculating the engineering stress (σ) and engineering strain (ϵ). The experimental data gives a force (F) as a function of time which as the crosshead descends at a set speed and also to the change in height of the sample ($l_t - l_o$)

$$\sigma = \frac{F}{A_o}$$

where F is the instantaneous load applied perpendicular to the specimen cross-section and A_o is the original cross-sectional area[8].

Engineering strain, ϵ is defined

$$\epsilon = \frac{l_t - l_o}{l_o} = \frac{k_t}{l_o}$$

where l_t is the instantaneous length, l_o is the original length, k_t is the rate of compression at time t [105]. In compression testing, engineering strain is negative but is expressed as a percentage throughout this thesis.

Values of maximum compressive stress, bulk modulus, transition stress and strain at maximum stress were calculated as detailed in Figure 3.13. The maximum compressive stress is defined here as the point at which a maximum is observed in the stress-strain curve, which may also correspond to the yield point[105]. Porous PMMA materials show compression curves characteristic of brittle materials, with the initial portion having a linear elastic nature, before a region of non-linearity in which there is a significant increase in strain with only a slight increases in stress, and ultimately the material fails.

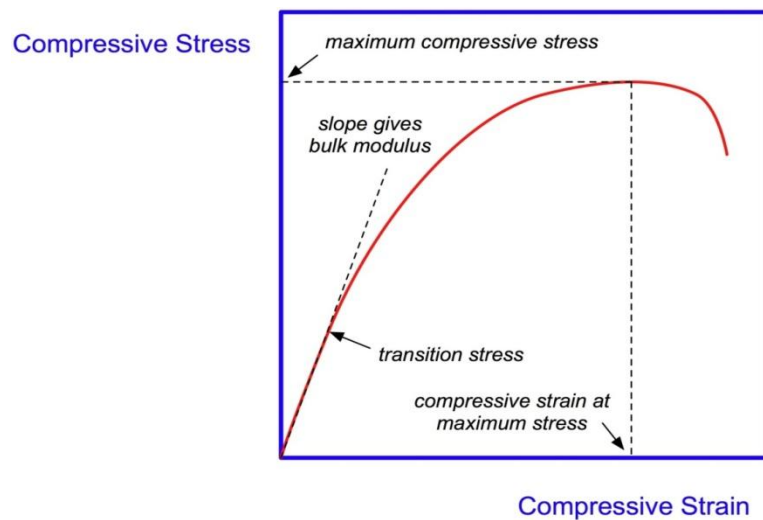


Figure 3.13: Diagram showing key points along the stress-strain curve

The bulk modulus (K_B) can be calculated from the initial linear portion of the graph where at point L

$$K_B = \frac{\sigma_L}{\epsilon_L}$$

The point at which the materials deviated from linear elasticity is denoted throughout as the transition stress.

Compression Testing Method

Compression testing was undertaken on an Instron 5569 universal testing machine using a 10 kN load cell with compression plates of 15 mm diameter and a crosshead speed of 1.3 mm min⁻¹ using rectangular sized samples of 10 mm x 10 mm x 20 mm. Calibration of an extensometer (MTS 52-251-905) and the crosshead was undertaken prior to measurement to allow for accurate measurement of displacement and force. Five specimens from each blend were tested from different points in the material (see Appendix 1) onto which an extensometer is clipped with gauge length 10 mm. The specimens were deformed to fracture by gradually increasing the compressive load uniaxially along the long axis of the specimen at a constant rate, with the applied load and contraction of the sample being measured simultaneously. The Instron testing machine provides two means of measuring the compressive behaviour of the material: crosshead displacement and an extensometer. The crosshead performs two functions. Firstly, through a movable top plate, it exerts a force on the specimen which is monitored by a computer. Secondly, the crosshead measures the displacement of the crosshead from the zero position as a force is applied, thereby measuring the height of the test piece. In addition, as a secondary measure to ensure accuracy, an extensometer has been used to measure the strain by monitoring the

change in height of the specimen as defined in B2782 and ASTM D1621. The displacement of the top arm of the cantilever of the extensometer is uploaded into a computer which calculates the strain on the material (Bluehill software version 2, Instron).

Fatigue Testing

Materials frequently fail by fatigue due to the cyclic application of stresses[106]. The materials may fail at stresses below that of the maximum stress obtained from compression testing as cyclic loading creates microscopic cracks that generate stress concentrations that propagate with time, leading to eventual failure. In fatigue testing a sinusoidal varying stress was applied to the materials which can be represented by[107].

$$\sigma = \sigma_o \sin \omega t$$

where ω is the angular velocity which can also be written $2/\pi T$ where T is the period of oscillation.

Three different tests were run to distinguish between the fatigue life of the different materials based upon their performance in previous compression testing:

- 80% of the transition stress. Below the transition stress all samples should be within the linear elastic region of the material and therefore should not fail. Once the 10,000 cycles are completed, the piece should return to its original dimensions.
- 14 kN. This value was chosen as a middle value to allow for ranking of the samples with respect to fatigue performance, since a 14 kN load corresponds to a point beyond the transition stress for most materials.
- 70 % maximum stress. This is 70% of the maximum compressive stress and should be beyond the linear elastic region of the material. It was hoped that all the materials would fail, therefore enabling separation and ranking of materials.

Application of cyclic stress aims to initiate microscopic cracks around centres of stress in the material. These cracks propagate through the sample on cycling leading to eventual failure of the sample. All materials tested were un-notched so no distinction can be obtained between crack initiation and propagation[106]. However, the tests allow for the materials to be quantified with respect to fatigue. To avoid adiabatic heating which can lead to subsequent thermal failure of the sample, a low frequency of 1 Hz was used.

Porous PMMA for the use in the pressure casting of ceramics has a large number of pores, which in terms of mechanical testing can be equivalent to geometric discontinuities around which an increase in stress is apparent caused by the re-distribution of force lines (see Figure 3.14). The magnitude of stress at the tip of an elliptical defect can be calculated using the equation[107].

$$\sigma_c = \sigma \left(1 + 2 \sqrt{a/r} \right)$$

where σ_c is the local stress, σ the applied stress, $2a$, is the length of the defect and r the radius of the curvature at the tip of the spherical defect. For a hole $a=r$ and hence the stress concentration is 3 and therefore stresses around the edges of the hole are three times as great as the applied stress.



Figure 3.14: Variations in stress concentration around defects[108]

Once initiated, the crack propagates through the sample through micro-defects, or pores and, in the case of porous PMMA the ligaments, since they are observed to be weaker than the beads. The cyclic force causes the crack to grow until the remainder of the cross-section can no longer support the load causing rapid, catastrophic failure. The samples used were moulded and machined to create appropriately sized cylinders. Therefore, in addition to the pores and features made in the moulding process (air pockets etc), there are also machine flaws on the surface of the materials which may be capable of propagation. However, although noteworthy, faults and defects from porosity are inherent in porous PMMA, and thus the technique is still a good guide to the cyclic fatigue ability of the materials.

Fatigue Testing Method

Fatigue measurements were undertaken on an Instron 8869 using an extensometer with a gauge length of 10 mm. Each block was individually moulded to create a cylinder 40 mm in diameter by 45 mm in height. To reduce disparities between the samples, 6 blocks were moulded from each blend.

The load required for a particular test was calculated from previous compressive testing and an oscillation of ± 2 kN of the mean load applied at a frequency of 1 Hz up to a

maximum of 10,000 cycles. Single Axis MAX (SAX) software with Wavemaker For 5800 Series Test System (Instron) was used to build the test programme with the load being ramped over a 15 second period prior to cycling. The electrical signal from the extensometer and crosshead was collected using Wavemaker runtime software (Instron) linked to a computer as described above. Specimens were monitored for differences in strain and height from the initial sample to the final

Not all samples collapsed within the 10,000 cycles and so to differentiate between samples, the stress across the materials and the material height was considered. The reduction in height has been calculated as the % of the original height of the block and strain has been calculated as a ratio between the final height and the original height as measured by the extensometer over a 10 mm area of the sample.

3.3.3 Thermal Properties

3.3.3.1 Differential Scanning Calorimetry

Differential scanning calorimetry (DSC) is a measurement of the thermal changes of a sample as it is heated or cooled when compared to an inert reference. The sample and the reference are located inside a cell which is controlled by an external computer. There are two classes of instrument: power compensation and heat-flux DSC. In power-compensation DSC, the sample and inert reference are heated independently with separate furnaces and temperature sensors. The differential heat input is monitored and is altered to ensure the sample and the reference pans are at the same temperature throughout the cycle. In heat-flux DSC, both sample and reference pans are heated in the same furnace and the temperature difference between the two pans measured by thermocouples. Both pans sit on a calibrated heating block with a known resistance, K_c and the temperature of the block is raised linearly with time. The pans are heated by conduction with the flow of heat into the filled pan being larger than that of the empty pan due to differences in heat capacity (C_p). The difference in heat flow rates induces a small temperature difference between the sample and the reference, ΔT from which the heat capacity, C_p of the sample can be calculated[109].

$$\Delta T = K \frac{\delta q}{\delta t} = K C_p \beta$$

When heat is absorbed by the sample, the signal will exhibit a change in the baseline which can be integrated to give the change in temperature. On a heat-flux DSC, a plot of the temperatures difference of the two pans against the temperature of the heating block is

obtained. When the sample undergoes an exothermic event, the temperature of the sample (T_s) is increased above that of the reference (T_r) resulting in a positive ΔT and therefore an upward displacement of the baseline is observed. For an endothermic event such as melting, T_s is below that of T_r resulting in a negative ΔT and a downward displacement in the baseline. At the T_g , a step in the baseline is observed until a new steady state value of ΔT is obtained (see Figure 3.15). This is because as the specific heat capacity of a rubbery state polymer is higher than that of glassy state.

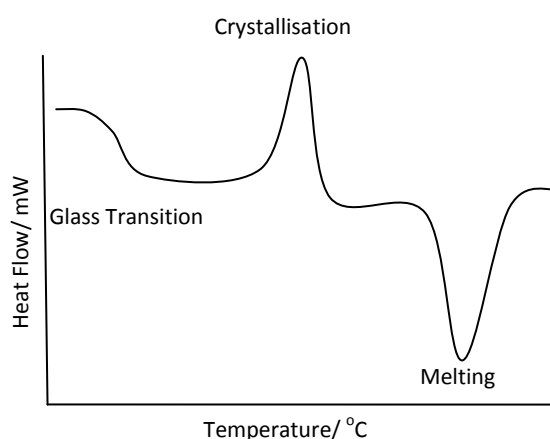


Figure 3.15: Features of a DSC trace for an amorphous sample of a crystalline polymer

3.3.3.2 DSC Method

Differential scanning calorimetry (DSC) has been used to measure the glass transition temperature (T_g) of the polymers. The T_g is a reversible transition in an amorphous polymer where the material goes from a hard brittle state to a rubbery one[110]. A powdered sample of known weight (~10 mg) was dried overnight in a vacuum oven at 120 °C before being placed in an aluminium DSC pan, sealed with an aluminium lid which was punctured with a small hole to allow for the emission of any volatiles. The pan was cycled through 3 heating and cooling runs heating from 10 °C to 160 °C at a rate of 10 °C min⁻¹ using a heat-flux TA instruments Q100 DSC with a refrigerated cooling system.

The data was analysed using TA universal analysis software (TA Instruments) and the onset temperature is reported as the T_g . A typical DSC trace is shown in Figure 3.16 focussing on a change in the baseline step which indicates the glass transition and location of T_g .

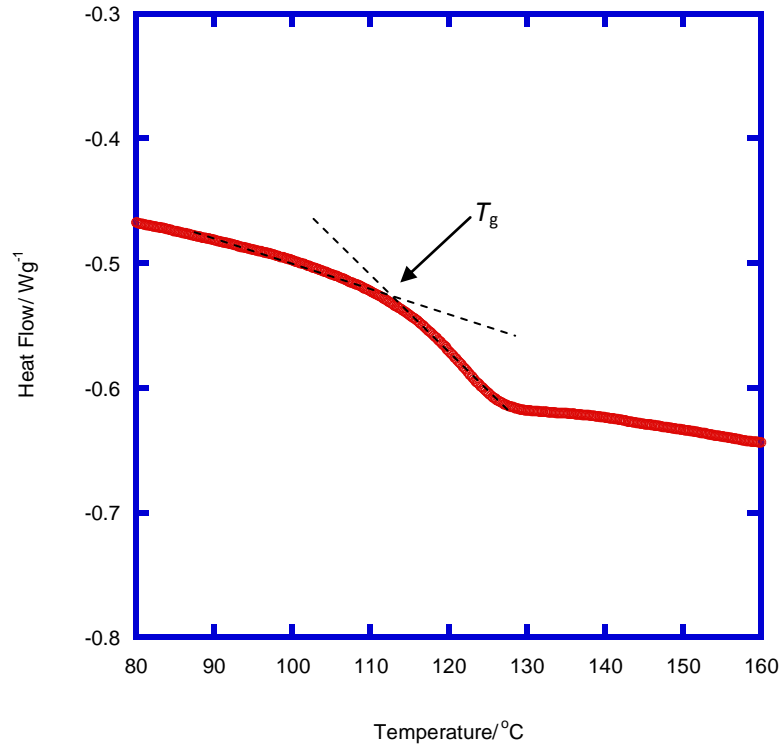


Figure 3.16: Example of a typical DSC trace

3.3.4 Porosity and Permeability

Porosity, ϕ , is a measure of the volume of the voids (V_{void}) or spaces in a material usually expressed as a fraction (or percentage) of the total volume (V_{total}) of the material.

$$\phi = \frac{V_{\text{Void}}}{V_{\text{Total}}}$$

Porosity was calculated on five specimens measuring 10 x 10 x 20 mm cut from different depths of the original block. The test pieces were weighed dry (M_{dry}) then left to soak in distilled water for one week, whereupon they were weighed wet (M_{wet}) to obtain the pore volume. The percentage porosity was calculated as below.

$$\text{Porosity (\%)} = \frac{(M_{\text{wet}} - M_{\text{dry}}) \div \rho_{\text{water}}}{V} \times 100$$

where V is the volume of the test sample and the ρ_{water} the density of water.

Water permeability is a measure of the flow of water through a material. For highly porous materials there is no standard methodology, with previous literature indicating a plethora of in-house methods all with various techniques and theoretical foundations. Prior to

commencement of this work, the literature on techniques for the measurement of permeability (K_p) was reviewed, including industrial standards for permeability measurements on “like” materials, i.e. concrete and sand[2, 79]. In addition a large amount of background research was undertaken on the technique for permeability measurement to ensure the best possible design of apparatus.

Overall there are three general types of testing for permeability in porous materials[111]:

- Constant head method: A pressure gradient is imposed across opposite faces of a sample saturated with water. The flow is assumed to be under steady- state conditions and thus is in accordance with Darcy’s Law (see below).
- Transient (pulse decay) applicable for small samples. A test piece is subject to a small pressure differential and the pressure decay and rise is monitored in response to a pressure pulse. Rapid results are possible with this design of apparatus however, if permeability is greater than 10 nanoDarcy’s, establishing an equilibrium pressure is increasingly difficult[112].
- Constant flow rate method: forces water through the sample under a constant pressure difference.

For porous PMMA materials produced in this work the latter methodology has been used.

Fluid flow through microporous materials usually follows Darcy’s law. As the water passes through the porous material, the flow velocity (v) is proportional to the pressure difference across the material (ΔP). In its simplest form for linear unidirectional flow Darcy’s law is:

$$v = \frac{Q}{A} = \frac{K_p}{\eta} \frac{\Delta P}{l}$$

where Q is the volumetric flow rate, A the cross-sectional area, ΔP the pressure drop across the sample, η the viscosity of the liquid and l , the thickness of the material.

The following dimensional analysis has been used to determine the units (x) of K_p :

$$\frac{m^3 s^{-1}}{m^2} = \frac{x \cdot kg \cdot m^{-1} s^{-2}}{kg \cdot m^{-1} s^{-1} m}$$

Rearranging to obtain x, the units of K_p

$$x = \frac{kg\ m^3\ s^{-2}}{m^2\ kg\ m^{-1}\ s^{-2}}$$

$$x = m^2$$

Often x is converted into Darcy where a medium with permeability of 1 Darcy permits a flow of $1\ cm^3\ s^{-1}$ of a fluid with viscosity $1\ mPa\ s$ under a pressure gradient of $1\ atm\ cm^{-1}$ acting across an area of $1\ cm$. Using this definition, dimensional analysis of K_p in terms of Darcy has been undertaken

$$K_p \equiv \frac{cm^3\ s^{-1}}{cm^2} \times \frac{MPa\ s}{atm\ cm^{-1}}$$

$$1\ Darcy = 1cm^2\ mPa\ atm^{-1}$$

$$1\ Darcy = \frac{10^{-3}\ N\ m^{-2}}{101,325\ Nm^{-2}}$$

$$1\ Darcy = 9.87 \times 10^{-9}\ cm^2$$

Converting to SI units, 1 Darcy is equivalent to $9.869233 \times 10^{-13}\ m^2$ [113].

Considerable discussions were undertaken with workshop staff and Lucite to establish the design of a rig suitable for differentiating between the permeability of highly porous materials. Key concepts were (i) the use of stainless steel to avoid rusting, (ii) a test cell to allow for a single transducer to be used (the open face being at atmospheric pressure), and (iii) a run-in period to ensure complete wetting of the sample. A schematic of the final rig design is shown in Figure 3.17.

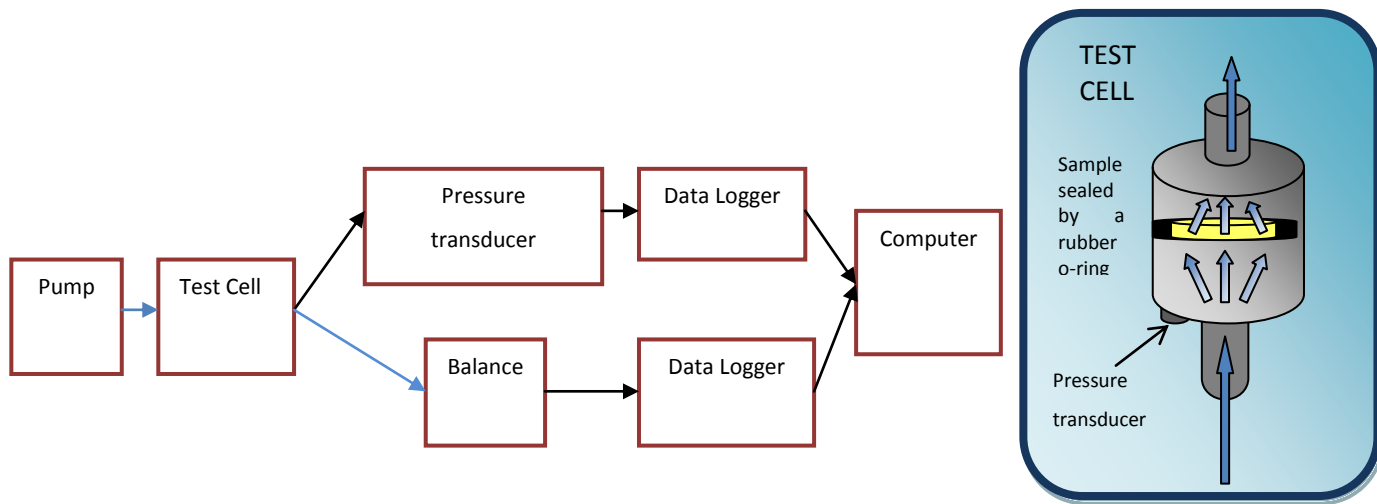


Figure 3.17: Schematic of the permeability rig designed and built at the University of Manchester

Initially an HPLC pump was used to allow for a constant, controlled flow rate of water through the sample, but the flow rate was too low. Therefore, a fish tank pump was used which allowed for a considerably higher flow rate. However, in order to achieve a constant flow rate the pump requires a ballast tank (see Figure 3.18).



Figure 3.18: Photographs of (a) the permeability rig and (b) the test cell

Permeability Test Method

Discs of height 10 mm by 60 mm diameter were cut from the porous PMMA blocks and then immersed in water overnight. Two rubber O-rings were forced around the disc which was then pushed into the test cell so a water-tight seal was achieved. Water was then run through the test cell for 10 minutes after which the water outflow pipe was placed above the beaker and the data logger started (custom made data logging software, Mettler Toledo). The computer then collected data from the pressure transducer (Custom Written Excel Macro, Windows) and balance. Once the 5 L beaker was full or 20 minutes has surpassed (whichever was sooner), the pump was turned off, the temperature of the water taken using a thermometer and the rig reset. For each different material, at least 4 discs were measured and an average permeability taken. From the data collected by the computer the volumetric flow rate (Q) is calculated by taking the gradient of a graph of mass of water against time, and the change in pressure (ΔP) by smoothing and averaging output from the pressure transducer. As the area (A) and length (l) are constant, K_p can be

calculated by converting the water temperature to a viscosity using data tables found in the Handbook of Chemistry and Physics[114].

3.3.5 Visualisation Techniques

A selection of visualisation techniques have been used throughout this work including optical microscopy, scanning electron microscopy (SEM), confocal fluorescence microscopy and X-ray tomography.

3.3.5.1 Optical Microscopy

Optical microscopy uses light and a system of lenses to magnify images of a sample. In the study of porous PMMA, both transmission and reflective modes were tried with transmission microscopy having the greatest success. In transmission microscopy, a thin slice of sample is lit from below thereby stopping the reflectance from the beam. Optical microscopy samples were prepared by cutting slim samples from the material (~2 mm thick) using a band saw. The sample was positioned over a cover slide and light shone through the material using an Olympus BX41 microscope with colorview camera attachment.

3.3.5.2 Scanning Electron Microscopy Theory

An SEM consists of a narrow monoenergetic beam of electrons produced from a heated tungsten “V” filament. To enable better resolution a lanthanum hexaboride source can be used, though these are expensive. The electron beam is accelerated by holding the filament next to a large negative potential and the anode along with the specimen at earth potential. The beam passes through a hole in the anode and is focussed using a system of mirrors. Once the beam hits the specimen three interactions can occur (see Figure 3.19)[91]:

- Electrons can be backscattered due to the electrostatic attraction between the negatively charged free electrons in the incident beam and the positively charged nucleus of the specimen (a).
- Primary beam electrons can interact directly with electrons in the specimen knocking them free, this is known as SEI mode and is the most common imaging mode used (b).
- After a secondary electron has been removed from an inner shell, an electron from an un-bound state can fall into the inner shell via an emission of a photon (c).

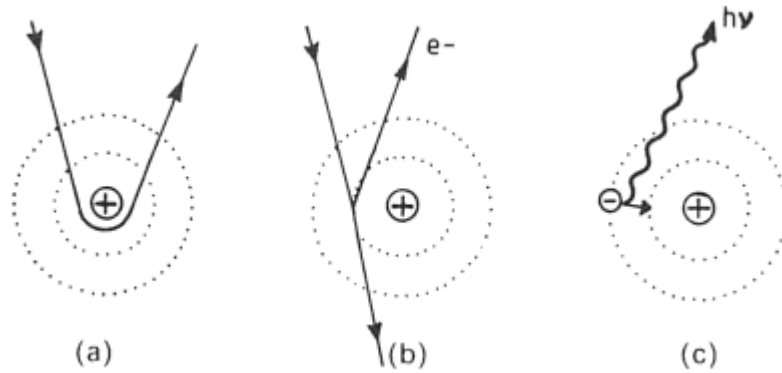


Figure 3.19: Interaction of a high velocity electron atoms[115] (a) backscattered electrons, (b) secondary imaging mode, (c) emission of a photon.

The high electron beam can penetrate up to 1 μm into the sample depending on the energy; however the probability of the electron escaping diminishes with depth. Various detectors are arranged in the specimen chamber to pick up the signals from the interactions above. The electron beam can be moved across the surface of the specimen using a variable magnetic field provided by current-carrying coils scanning a rectangle in a line by line movement. As the beam moves, different characteristic signals are produced enabling contrast. The signal measured by a detector is amplified and is used to control the brightness of the spot using a cathode ray tube. The electron path must be entirely within a vacuum. Surface topography can be seen in the SEM by use of shading. At point A in Figure 3.20, the incident beam strikes in a trough; therefore the secondary electrons emitted by the specimen collide with the surrounding material and are thus absorbed. Consequently the signal is low and is displayed as a dark patch in the resulting images. Conversely, at point B the electrons easily escape the specimen and are drawn towards the positively charged detector and appear as light patches in the images.

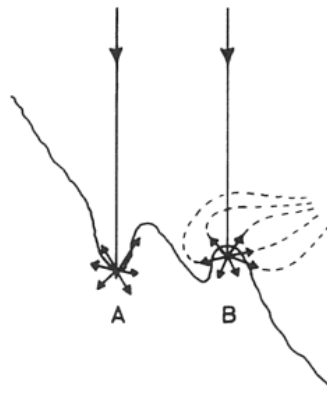


Figure 3.20: Effect of surface topography on the secondary electron signal showing a) dark regions and b) light regions[116]

Polymers are often damaged by the electron beam causing artefacts or burning of the sample. To limit this damage low accelerating potentials are required, but, these limit resolution and contrast. At high magnifications, the PMMA samples became damaged in the beam as greater electron intensity is used on the viewed area to enable sharp focus; the beam is focussed on a nearby area and then moved to a neighbouring area to allow for an undamaged picture of the surface. This is particularly apparent in pictures when going to back to lower magnifications where dark artefacts appear in the images (see Figure 3.21).

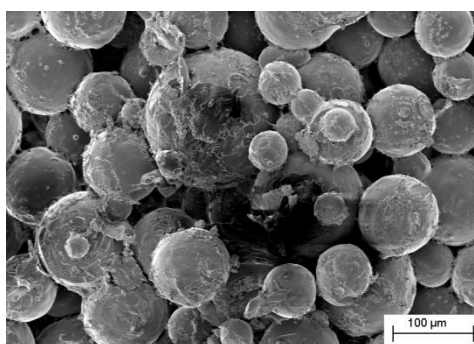


Figure 3.21: SEM micrograph showing dark artefacts in the image

3.3.5.3 SEM Method

Scanning electron microscope (SEM) pictures were taken of a fracture face using a Zeiss EVO60 V PSEM in secondary electron imaging (SEI) depth mode using a 9 carousel fitting. The Zeiss EVO60 uses a tungsten filament which has a high vacuum capability allowing for larger samples than those used within this study to be accommodated. In addition, the Zeiss has a variable acceleration voltage of 0.2-30 kV, magnification from 5 to 1,000,000 x with a 6 mm field of view at the analytical working distance[117]. Although it is not strictly necessary to coat the samples when using SEM, polymers are poor conductors of electricity and therefore a charge readily builds up on the surface which distorts the image. To reduce this effect, the specimens were coated with a thin layer of gold using an Edwards S150B sputter coater.

3.3.5.4 Fluorescent Confocal Microscopy

Used extensively throughout the literature to view biological polymers with a fluorescent chromophore [118-120], confocal-fluorescence microscopy is an optical imaging technique which increases the optical resolution of a micrograph by using point illumination combined with a spatial pinhole to exclude out-of-focus light in specimens thicker than the

focal plane. By scanning through different heights, the confocal microscope reconstructs three-dimensional images from the structures viewed. The samples are illuminated using light of a specific wavelength which is absorbed by the fluorophore. The fluorophores are promoted into an excited state where energy is lost causing them to emit a photon of a longer wavelength of discrete energy and hence colour. The illuminated light is separated from the weaker emitted light, known as fluorescence, by use of a filter. The filter allows for images to be obtained where only the fluorescence is observed as opposed to the sample, allowing for selective illumination of areas which are stained by the fluorescent moiety.

Confocal microscopy measurements were undertaken using a Leica TCS SP5 confocal microscope with Leica application suite (LAS-AF) software using an excitation wavelength of 521 nm to visualise porous PMMA samples copolymerised with fluorescein- σ -methacrylate.

3.3.5.5 X-ray computational Microscopy

X-rays are produced when fast moving electrons decelerate and interact with the target material. A beam of electrons is accelerated and passed through a molybdenum target from which electrons are ejected producing X-rays. The X-rays pass through the sample and the extent to which they are attenuated by the object is measured at the detector. The beam can be attenuated in two ways: either by photoelectric absorption, or Compton scattering. Photoelectric absorption occurs when an X-ray loses all its energy to a tightly bound inner electron in the atom resulting in the release of a free electron once the binding energy is overcome. Compton scattering by contrast is the interaction of an X-ray photon with an outer shell electron which deflects the photon from its original course resulting in a decrease in the energy of the photon. Assuming a monoenergetic beam for simplicity

$$N_{out}=N_{in} \exp \left[- \int \mu(x,y) ds \right]$$

where N_{out} is the total number of photons which have passed through the object, N_{in} is the number of photons which enter the object, ds is the path length from source to detector and μ the attenuation coefficient through the space (x,y) then [121-122]:

Equivalently:

$$\int \mu(x,y) ds = \ln \frac{N_{in}}{N_{out}}$$

However, in practice, an energy beam is polychromatic and therefore an incident photon number density $S_{in}(E)$ is introduced which allows for a range of different energy photons (E) where $S_{in}(E)dE$ is the total number of incident photons in the range E and $E+dE$ [123].

$$N_d = \int S_{in}(E) \exp \left[- \int \mu(x, y, E) ds \right] dE$$

In practice the detector measures the difference in attenuation or S_{exit} [124]

$$S_{exit}(E) = S_{in}(E) \exp \left[- \int \mu(x, y, E) dS \right]$$

There are three types of detector: a count-type detector, which outputs the proportion of the total number of photons detected on it; a scintillation-type detector, in which the output is proportional to the total photon energy; and an ionization detector, in which the response is the energy collected per unit mass[125]. For this work, an ionization detector has been used to measure the attenuated X-ray for which the data is stored on a computer. The denser the material, the more attenuated are the X-rays. The total scan time takes approximately 40 minutes for each sample, however the reconstruction of the micrographs can take up to 3 days before computer modelling can be undertaken. The individual radiographs contain a projection of a 3D object on a 2D area which when combined can be reconstructed using VG Studio Max 2.0 software to build a 3D image. In addition, as the 3D structure is built up slice-by-slice orthogonal to the rotation axis, planar sections, termed 'orthoslices', can be built upon the x, y and z coordinates. Further analysis has been undertaken using Avizo 6.3 (VSG) and Avizo Fire software (VSG) which allows for the visualisation and manipulation of the data to obtain qualitative and quantitative information on structural images of the materials.

3.3.5.6 X-ray Tomography Method

X-ray tomography was undertaken on selected samples measuring 5 mm diameter by 20 mm length using a Nikon Custom Bay 320 kV Scanner (irradiation energy 45 kV, current 171 μ A) with a molybdenum source. The stage rotates by 360° enabling 2001 projections of the material to be recorded. The transmission micrographs are then reconstructed into 3-D volumes using VG Studio Max 2.0 software and later reconstructed in Avizo 6.3.

4. Establishing Experimental Methodologies

4.1 Introduction

Lucite International produces materials for synthesis of porous PMMA moulds for use in the pressure casting of ceramics based upon a patent filed by AG fur Keramische Industrie Laufen in 1970[12]. The patent details the invention of a plastic material with fine open pores in which a pourable mixture comprising of a beaded polymer, monomer, surfactant, water and an accelerator (able to initiate polymerisation at room temperature) polymerises to form a rigid polymer within a few minutes. The water is later removed by drying to form an open porous structure with pores of 5 to 20 microns.

The industrial blend methodology supplied by Lucite (as detailed in Section 4.2), when replicated on a laboratory scale, formed a small cylinder of material measuring approximately 74 mm in diameter and 80 mm in height. To enable full characterisation of each cylinder, a broad range of tests was devised which required larger volumes of material. To avoid batch variation between blends, the blend mixture size was increased and blocks of material produced in baking trays measuring 230 mm by 230 mm. Initial repeatability was poor, and hence a substantial amount of work was required to standardise the blend procedure for academic purposes and minimise batch variation. This chapter details preliminary work undertaken on various aspects of the blend methodology, including external and internal factors aiming to increase the homogeneity of the blends and increase the blend size.

4.2 Evolution of the Standard Blend Methodology

The Lucite International blend methodology as used at the start of the project is given below.

Triton X100 (10 g) was added to a solution of DMPT (0.2 g) dissolved in MMA (20 g) and mechanically stirred for 3 minutes at a speed of 160 rpm. To this solution, water (110 g) was added and the emulsion mixed for 3 minutes. PMMA beads (110 g, Colacryl® DP300) and BPO (0.25 g, 50 % active) were added to the emulsion and the resulting viscous mixture stirred for 1 minute before being poured into a mould. The mould was left to harden for 40 minutes at room temperature prior to being placed into an oven at 60 °C to finish the polymerisation process. After 24 hours the hardened blend was washed using water from a tap at full pressure to remove the excess surfactant whence it was then returned to a 60

°C oven to drive off the remaining water. The materials used in a scaled- up version of this blend methodology were shown to be poorly mixed, with high levels of standard deviation in properties obtained between samples taken from the same block, see Table 4.1.

The above synthesis mixed the powdered benzoyl peroxide (BPO) into the emulsion alongside a large quantity of PMMA beads in the latter stages of blending, creating a highly viscous mixture. It was apparent that the BPO was not dissolving sufficiently in MMA and was thus inadequately distributed throughout the mixture, leading to observable discolouration in the final material. To increase dissolution of the powered catalyst, BPO was combined with the monomer in an initial mixing stage prior to the formation of the emulsion. The liquid dimethyl-*para*-toluidene (DMPT) was then added in the final step of the synthesis just prior to addition of the PMMA beads. Premixing the BPO in MMA facilitated a reduction in the standard deviation observed between samples and enabled a more efficient, repeatable synthesis of porous PMMA materials (see Table 4.1). However, both methods gave materials with similar properties, indicating that there is no change in the inherent nature of the porous PMMA when the order of addition of the initiator and catalyst is varied. This slightly altered method was therefore used throughout the research and is referred to as the “Standard Methodology”.

Table 4.1: Comparison of methodologies for the formation of porous PMMA (standard deviation given in parenthesis)

Sample Code and Method	Compression Testing:				H ₂ O porosity measurements, f / %
	Maximum Compressive Stress / MPa (Standard Deviation)	Compressive Strain at Maximum Stress / %	Transition Stress / MPa	Bulk Modulus / MPa	
Lucite method (KA010)	13.4 (3.55)	12.34 (3.01)	11.15 (2.19)	281.28 (78.36)	32
Repeat of Lucite method (KA010)	15.02 (3.23))	11.96 (4.56)	8.04 (1.09)	290.48 (61.15)	29
Method alteration 1a (KA008)	13.98 (0.99)	9.61 (2.08)	8.55 (0.51)	315.23 (43.75)	29

To gain an insight into the nature of failure of the materials and their behaviour under compression, SEM images were taken of the materials both pre- and post-compression (see Figure 4.1). The images clearly show that as the sample is compressed, and that the crack propagates through the sample by dissecting the ligaments as supposed to the PMMA beads.

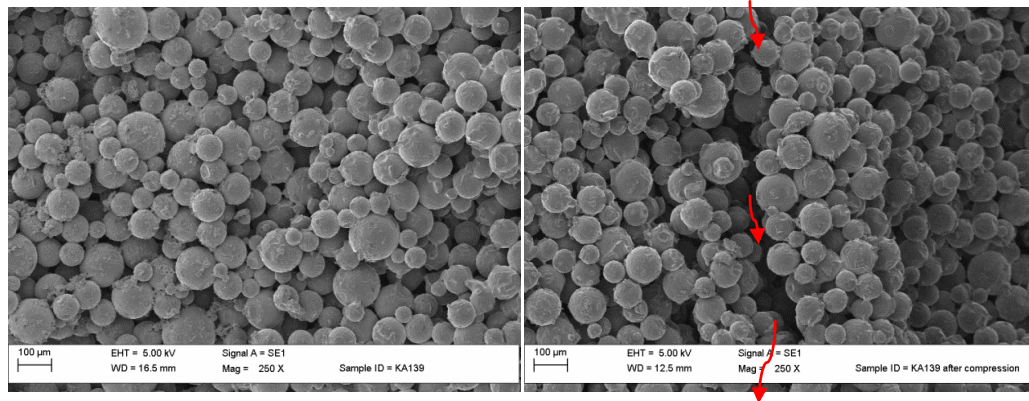


Figure 4.1: Pre- and post-compression testing of porous PMMA material after 30 minutes stirring of the emulsion. The red arrows highlight the propagation of the crack through the ligaments

This phenomenon was previously reported by Hoey and Taylor in which the fatigue behaviour of bone cement and sheet acrylic are compared[126]. Both bone cement and sheet acrylic are made from the monomer, MMA, but, sheet acrylic differs from porous PMMA as it is made using a bulk polymerisation process and so there is no solvent in the synthesis. MMA is added to an initiator and the polymerisation left to proceed either by heating or at room temperature with a redox initiator. The lack of solvent results in a uniform clear polymer which has distinct brittle properties. Bone cement uses a very similar manufacturing method to porous PMMA, but, again there is no water in the process though the pre-formed PMMA beads introduce porosity into the polymer due to the random packing of the beads. The technical paper showed that cracks grow around the individual beads, thereby indicating that the failure is taking an indirect route. Therefore, the mechanical properties of the materials depend strongly on the polymer in the ligaments between beads rather than properties of the beads. In sheet acrylic, the crack formed by stressing the material grows in a straight line with little or no deviations from its path, see Figure 4.2.

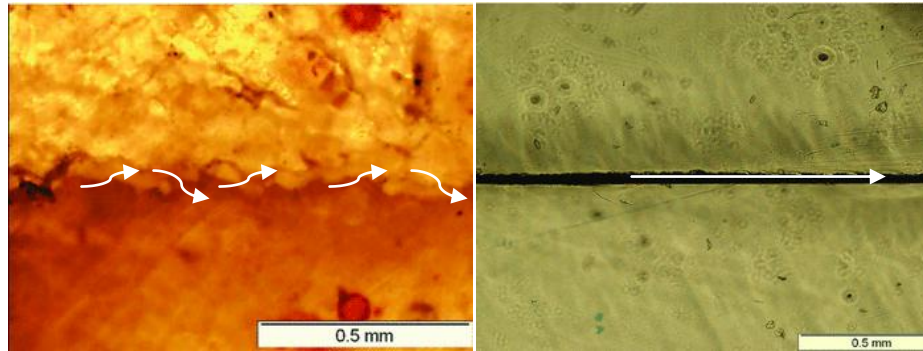


Figure 4.2: Micrographs of fatigue crack paths in bone cement (on the left) and acrylic glass (on the right). Taken from D.Hoey & D. Taylor[126]. The white arrows signify the crack propagation through the sample

This deviation around the beads for samples of bone cement is thought to be due to the significant differences in the strength of the polymer beads and the polymer in the ligaments, with failure occurring in the weaker material. Consequently, it is the composition of the ligaments which is vital in controlling the mechanical properties of porous PMMA.

4.3 Effect of Surface Area: Volume Ratio

Initially, the blend formulation present by Lucite allowed blocks of material to be cast in a plastic beaker (diameter 74 mm and height 80 mm). This volume was insufficient to undertake the testing required to fully characterise each batch. However, in increasing the blend size to 230 mm x 230 mm x 20 mm, the surface area to volume ratio was considerably altered. To see if this had an effect on the material properties, a selection of different blocks with varying surface area to volume ratio were cast using the standard methodology. To eliminate variation between batches, a number of materials were cast using the same mixture as indicated by the batch number (see Table 4.2.)

Table 4.2: Comparison of maximum temperature and compressive stress at different surface area to volume ratios for the production of porous PMMA (standard deviation given in parenthesis)

Sample Code	Batch	Dimension ^a / mm	Surface area: volume /mm ⁻¹	Set time/ min	Compressive Testing			
					Maximum Compressive Stress / MPa (Standard Deviation)	Compressive Strain at Maximum Stress / %	Transition Stress / MPa	Bulk Modulus / MPa
KA018	K	D=69.0, h=74.5	0.013	58	18.37 (1.25)	13.72 (1.42)	10.14 (0.85)	295.13 (22.71)
KA021	K	D=82.0, h=50.0	0.019	56	19.07 (2.09)	13.45 (1.09)	11.74 (0.66)	295.21 (54.74)
KA019	K	216.0 x 215.5 x 6.0	0.100	69	14.14 (2.26)	9.40 (2.94)	8.86 (0.50)	282.82 (7.91)
KA020	K	176.5 x 176.5 x 10.0	0.100	70	16.75 (1.39)	12.03 (1.39)	8.78 (1.30)	298.33 (5.75)
KA026	L	D=56.8 h=86.2	0.012	36.5	12.62 (0.34)	7.22 (0.33)	9.53 (0.27)	295.95 (29.05)
KA025	L	D=72.3, h=72.2	0.014	38	12.62 (0.34)	9.25 (1.10)	8.34 (0.43)	264.00 (19.13)
KA024	L	D=117.0, h=65.0	0.015	40	12.18 (0.38)	9.16 (0.06)	7.70 (0.49)	244.14 (1.18)
KA028	L	D= 29.5, h=31.5	0.029	43	13.45 (2.30)	10.89 (1.45)	9.45 (0.47)	304.74 (48.94)
KA032	M	D=117.3 h=30	0.033	60	8.82 (1.50)	6.98 (1.57)	7.39 (0.76)	174.25 (50.87)
KA034	M	230 x 230 x 5.0	0.171	66	16.79 (3.69)	13.68 (2.37)	9.07 (0.69)	347.49 (48.97)
KA035	M	230 x 230 x 10	0.112	70	27.14 (6.95)	17.49 (3.05)	11.07 (0.35)	396.02 (58.66)

a) Baking trays except for diameter (D) and height (h) for cylindrical pots.

b) K, L, and M are the batch numbers for the blends, i.e materials KA019-KA020 were made from the same blend of which the contents was divided into the individual containers to create the sample. Similarly KA026-KA028 and KA032-KA035 are made from the same batch of material.

For each material, five rectangular samples (10 mm x 10 mm x 20 mm) were cut from different areas of the block (see Appendix 1) and compression tested as detailed in Section 3. A standard deviation for the compressive stress can then be derived from the results which are reported in brackets after each value. In this work, an average percentage error of 11.24 % is observed on average maximum compressive stress, 14.29 % in strain at maximum stress, 6.53 % in transition stress and 10.66 % in bulk modulus. However, between batches, a considerable difference can be observed in the percentage errors where the error in maximum stress rises to 30 %, strain at maximum stress to 27 %, transition stress, 12 % and bulk modulus to 15 %. Therefore, the methodology as it stands does not produce a homogeneous or a reliably repeatable mixture. Despite this, a trend can be seen in rising set times as the surface area increases. Additional studies were

undertaken to increase the reliability of the standard methodology for the formation of porous PMMA.

4.4 Effect of Oxygen

Dioxygen is known to retard radical reactions[16], as it reacts with the propagating radical chain to form a peroxy radical, as shown in Figure 4.3.

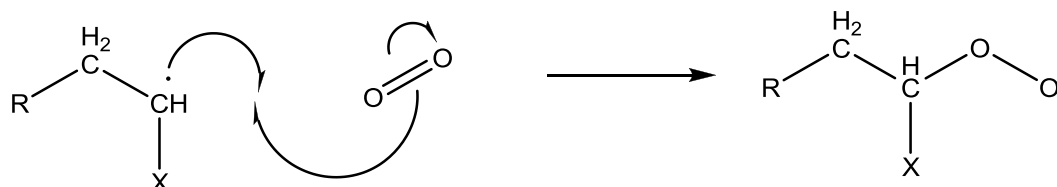


Figure 4.3: Formation of a peroxy radical

The peroxy radical is much less reactive than a carbon based radical, but it can reinitiate polymerisation, albeit slowly. If reinitiation does occur weak peroxide bonds are formed in the polymer backbone, which can act as sites for bond scission and hence premature degradation of the resulting polymer.

Within the Lucite blend methodology, there is no precaution for the exclusion of oxygen. There are two points during the reaction where the blend may potentially be exposed to oxygen:

- i. Dissolved oxygen, found in the components prior to polymerisation
- ii. Surface oxygen due to the porous PMMA block being formed in the open air

Dissolved oxygen was removed from the liquid components by degassing them prior to use for 2 hours with nitrogen. Surface oxygen was eliminated by undertaking the experiment in a sealed glove box filled with nitrogen. The set time of the porous PMMA materials was monitored using a K-type thermocouple and the resulting blocks tested to obtain compressive strength. The results are shown in Figure 4.4.

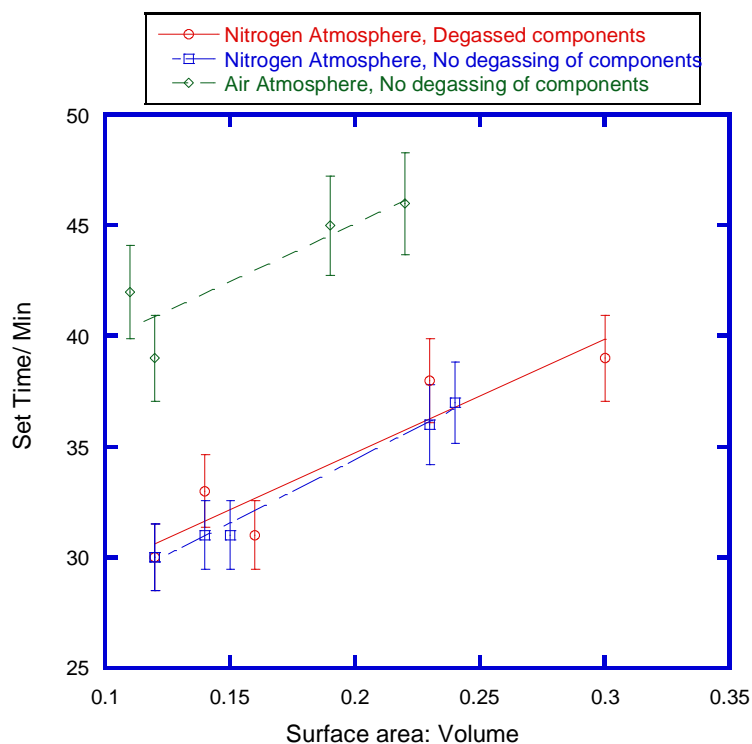


Figure 4.4: Effect of oxygen on the set time at different surface area to volume ratios

Dissolved oxygen, as tested by the degassing of liquid components, was shown to have no visible effect on the set time of the materials with little observable difference between the red and blue data sets in Figure 4.4. Surface oxygen, which was tested by changing the atmosphere from nitrogen (as indicated by the blue points) to air (green points) which shows a noticeable shift to slower set times indicating a retardation of the reaction rate. This finding clearly shows that the presence of oxygen does inhibit the radical reaction.

Compression testing and porosity measurements were undertaken on the materials. However, little difference is observed between those made in air, nitrogen or when the components are pre-treated to remove oxygen. This confirms previous data showing that, although set time is increased with increasing surface area to volume ratio, the final properties of the materials are comparable. Hence, within the limits tested, scaling up the formulation to create large blend sizes is plausible and will have little to no difference on the materials manufactured. Interestingly, in testing the materials the glove box proved beneficial in controlling the external temperature of polymerisation during the room temperature hardening phase, enabling a reduction in the percentage variation between batches from over 30 % to ± 10 % in the average maximum compressive stress. Improvements were also observed in variations in the transition stress which was reduced from 27 % to 20 % and porosity from 32 % to 8 %.

For production purposes, it was concluded that carrying out the polymerisation in an oxygen free environment was impractical and not cost effective for the gains obtained in set time and therefore the reactions continued to be carried out in the presence of air. However, benefits observed by controlling the external temperature and environment by using a temperature-controlled purpose-built sealed chamber (see Figure 4.5) were implemented in further development of the standard methodology. In addition, as temperature control was shown to be key in the formation of porous PMMA, it was decided that all liquids be pre-heated to 25 °C in a water bath to eliminate further variations and improve repeatability of results.



Figure 4.5: Photograph of the purpose-built temperature controlled chamber

4.5 Oven Temperature

The effect of oven temperature on the porous PMMA materials was investigated by heating two identical blends at 25 °C and 60 °C, respectively, see Table 4.3.

Table 4.3: Results of changing oven temperature (standard deviation given in parenthesis)

Sample Name	Temperature of cure/ °C	Set time/ min	Compressive Properties				Max residual monomer /%
			Average Max Stress / MPa (Standard Deviation)	Strain at maximum stress/% (Standard Deviation)	Transition Stress/ MPa (Standard Deviation)	Bulk modulus / MPa	
DP300 standard (KA053)	25	35.5	9.2 (1.76)	7.50 (1.09)	4.4 (0.76)	280	11.0
DP300 standard (KA052r)	60	25.0	16.3 (2.64)	12.07 (1.02)	6.4 (1.43)	500	0.7

Heating the PMMA material at 25 °C resulted in the incomplete conversion of monomer to polymer, as denoted by comparably higher levels of residual MMA. Residual monomer is known to plasticise PMMA, with increasing amounts resulting in poorer performance under compression. The MMA has been shown to diffuse into the polymer under the control of Fick's Law which reduces the T_g of the PMMA[127-131]. Hopfenberg used extreme measures to highlight the effect of plasticisation by treating hooked PMMA rods with MMA. The monomer slowly dissolved the polymer which resulted in the polymer fully detaching from the support as it deformed[127]. Further details of plasticisation are given in Chapter 5.

At 60 °C, a small amount of residual monomer is still evident in the materials, but, the compressive properties are significantly improved. The levels of residual monomer remain unchanged pre- and post-washing, indicating that the washing process mainly removes excess surfactant rather the residual monomer. It would, therefore, appear that at levels below 1 %, the unreacted monomer is trapped within the PMMA and cannot be removed by further drying at 60 °C. Drying above the glass transition temperature of PMMA would facilitate its removal, but is not practical on either a laboratory or an industrial scale.

4.6 PMMA Bead Properties

PMMA beads are the major component by weight of porous PMMA, making up approximately 55 % of the blend formulation. The PMMA beads can be characterised by (i) their molecular weight, and (ii) their diameter. The following subsections detail the effect of both these parameters on the final properties of porous PMMA materials.

4.6.1 Diameter of the PMMA Bead

Kevin Xiao, a Masters student who studied at the University of Manchester in 2011, generated the following data presented in Table 4.4 by varying the diameter of the PMMA beads. His experimental results are interpreted within this section to enable a complete overview of porous PMMA materials with respect to the blend components.

Table 4.4: Results of varying the PMMA bead size on the properties of porous PMMA (standard deviation given in parenthesis)

Bead Name (Lab code)	Bead diameter/ μm	Compressive Properties			Water Porosity (%)
		Average Max Stress / MPa (Standard Deviation)	Strain at Maximum Average Stress/ %	Bulk Modulus/ MPa (standard Deviation)	
TS1890 (XX05)	42	10.7 (1.02)	10.5 (1.09)	266.5 (16.9)	32.5
D120 (XX06)	50	11.9 (5.16)	9.3 (5.19)	263.4 (8.5)	31.0
D80 (XX08)	68	16.4 (1.86)	16.0 (3.31)	281.7 (74.5)	33.2
DP300 (XX02)	93	21.1 (3.72)	16.1 (6.12)	351.5 (41.2)	36.4

Figure 4.6 shows that as the diameter of the bead increases, the average maximum compressive stress increases. This trend also is evident in bulk modulus and strain at maximum stress.

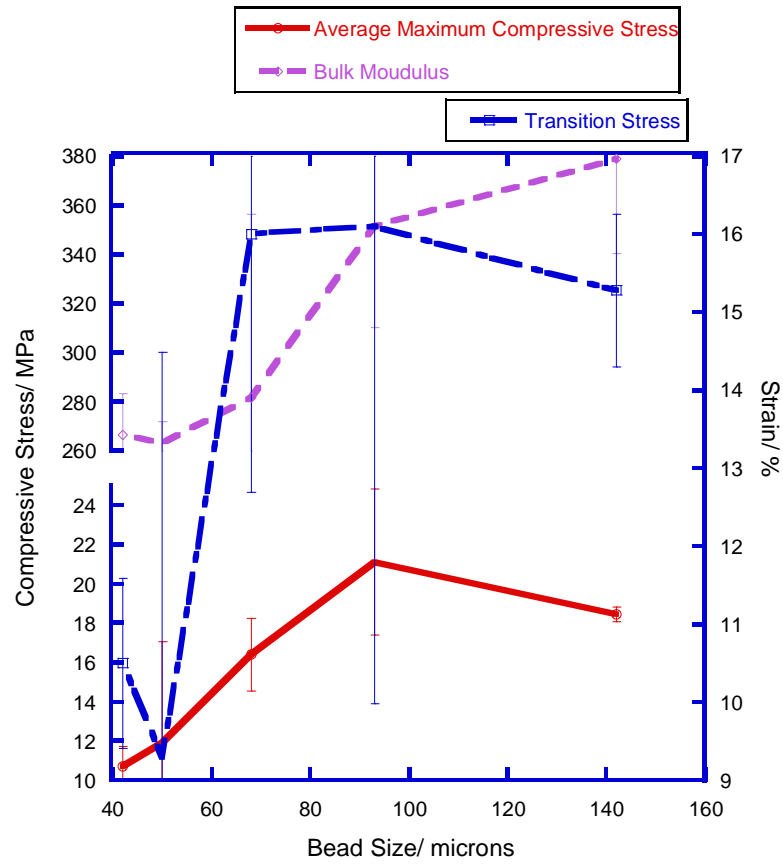


Figure 4.6: Plot showing how the PMMA bead size affects the compressive properties of porous PMMA materials

Diffusion of MMA into a sphere is determined by the surface area of the sphere and the concentration of the external MMA, as established by Fick in 1855, where the rate of diffusion is inversely proportional to the radius of the PMMA sphere[132].

$$\text{Rate of Flux (single particle)} = 4\pi r D [MMA]$$

$$\text{Rate of Flux (per unit surface area)} = \frac{4\pi r D [MMA]_{ext}}{4\pi r^2}$$

$$\text{Rate of Flux (per unit surface area)} = \frac{D [MMA]_{ext}}{r}$$

where D is the diffusion coefficient, r the particle radius and $[MMA]_{ext}$ is the concentration of MMA external to the particles[8].

The total surface area of the beads is given by

$$\text{Total Surface Area} = N_B 4\pi r^2$$

$$N_B = \frac{M_b}{m_b}$$

where N_B is the total number of beads, M_b is the total mass of PMMA beads, and m_b is the mass of an average PMMA bead.

Therefore,

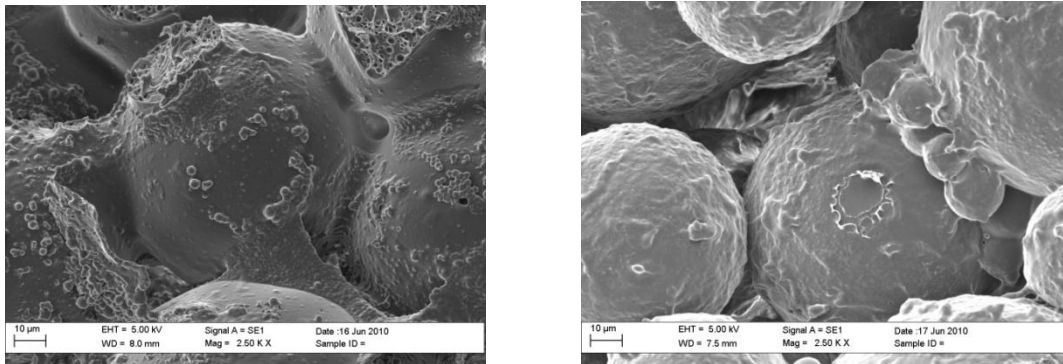
$$N_B = \frac{M_B}{\frac{4}{3}\pi r^3 \rho}$$

$$\text{Total Surface Area} = \left(\frac{3M_B}{\rho} \right) \left(\frac{1}{r} \right)$$

Hence

$$\text{Total Rate of Diffusion} \propto \frac{1}{r^2}$$

Diffusion is therefore inversely proportional to the radius of the beads squared. Hence, as the bead size decreases, the rate of diffusion of MMA increases. As more MMA is entering into the beads, less is available to form the ligaments, which it was previously concluded control the compressive properties of the materials. Conversely with larger spheres, a larger amount of MMA is “free” to form the ligaments and hence they are more substantial in volume. This can be observed in SEM pictures. (see Figure 4.7).



a)

b)

Figure 4.7: SEM pictures showing a) samples made with 93 μm diameter beads and b) samples made with 42 μm diameter beads highlighting the difference in connectivity

A considerable volume of literature has been published on the diffusion of small molecules into polymers[128-131, 133-134]. In particular, MMA is well known to diffuse into PMMA. As the surface of the PMMA bead swells, diffusion is possible of both the MMA into the

bead and PMMA out[135]. The rate of diffusion is governed by the size of a molecule, with smaller molecules, such as MMA, diffusing faster than larger molecules such as PMMA. In glassy polymers such as PMMA at room temperature, the effect of monomer diffusion can be observed by the decrease in glass transition temperature (T_g) which shows a linear decrease as the concentration of monomer into the particle increases[136]. Therefore, heat cured polymer beads have a higher T_g (117-122 °C) than T_g s obtained after the curing of porous PMMA (97-100 °C)[137]. Reis et al noted that increasing the bead diameter influenced the curing parameters of PMMA, with larger bead diameters increasing the set time of the materials but decreasing the temperature of curing[138]. This can also be explained by the difference in diffusion due to the size of the PMMA spheres.

4.6.2 Molar Mass of PMMA Beads

Four beads with differing molar masses but similar radii were incorporated into the synthesis of porous PMMA. The results are shown in Table 4.5.

Table 4.5: Effect of PMMA bead molecular weight on the porosity and compressive properties of porous PMMA (standard deviation given in parenthesis)

Bead Name (Lab code)	Molar Mass/ kg mol ⁻¹	Set Time / min	Compressive Properties				Water Porosity/ %	Residual MMA/%
			Average Max Stress/ MPa	Strain at Maximum Average Stress/ %	Transition Stress/ MPa	Bulk Modulus / MPa		
TS2082 (KA119)	447.4	35	19.53 (1.75)	20.64 (3.27)	6.85 (1.38)	291.11 (99.05)	30.42 (2.46)	2.59
DP300 (KA055)	1110.4	25.5	18.2 (4.73)	16.0 (3.00)	6.7 (1.46)	384.61 (166.9)	29.63 (3.33)	2.60
TS1338 (KA137)	1400.0	21.0	9.99 (0.77)	7.90 (3.84)	5.71 (0.92)	274.82 (39.74)	32.67 (3.23)	8.21
DP300U (KA120)	2406.0	24	9.01 (0.78)	8.28 (0.28)	5.95 (0.67)	163.13 (9.3)	30.46 (4.90)	2.36

As the molar mass increases from 447.4 kg mol⁻¹ to 1110.4 kg mol⁻¹ very little difference is seen in the compressive performance within the error margins for the tests. Similar results were obtained by Morejon where, within the molar mass limits of 230 kg mol⁻¹ and 850 kg mol⁻¹ tested, no difference was observed in the mechanical properties [139]. However, as shown in Table 4.5, when the molar mass was increased to 1400 kg mol⁻¹, there is a large decrease in the overall compressive performance above which no further decline is observed. This can be related to the high viscosity seen when mixing in the beads in the second stage of the reaction. The rapid rise in viscosity causes the mixture to be difficult to pour, therefore on transfer to the baking tray large air bubbles are likely to become

trapped in the mixture, resulting in large voids which compress readily under testing leading to weak, brittle samples. Although the best possible efforts were made to obtain beads with similar diameters, it should be noted that the above beads range in size from approximately 74-93 μm . However, extrapolating the data from Section 4.7.1, the reduction observed in compressive properties with the larger molecular weight beads is greater than that resulting from the reduction in diameter. Theoretically, if the molar mass effect was negligible, a bead size of 74 μm would have a predicted average maximum stress of about 17 MPa. Similarly, bead sizes of 87 μm and 93 μm would give compressive failure stresses of about 20 MPa. Therefore, it can be concluded that the molar mass of the beads is significant in determining the compressive properties of the materials.

A high mixing viscosity signifies that the beads have swollen in the MMA/surfactant mixture and gained highly “tacky” surfaces which impede their flow past each other. At this stage it is believed that two processes are occurring simultaneously. Firstly, the penetration of MMA into the particles by diffusion can be expected to be greater when the molar mass is smaller. Secondly, the PMMA is dissolving in the monomer. As the molecular weight decreases, the rate of dissolution increases creating a viscosity rise[138].

Two types of crosslinked PMMA beads supplied by Lucite International which have different levels of crosslinking with a comonomer allyl methacrylate at level of 4 % and 10% have been tested. Crosslinked beads cannot dissolve in MMA, but can undergo limited swelling. When crosslinked beads are used in the making of porous PMMA, the materials are very weak and perform poorly in compressive testing with an average maximum compressive stress of approximately 1 MPa. A low viscosity was retained throughout the mixing process even on addition of PMMA beads and no thickening on standing. With the 10 % allyl methacrylate crosslinked beads a temperature rise associated with an exothermic polymerisation process was observed, but the material retained a spongy consistency and did not form a rigid block, enabling layers of beads to be removed by light hand rubbing of the material.

The results indicate that two processes are taking place within the setting stages of the polymerisation. Firstly, the MMA is rapidly diffusing into the PMMA beads which causes swelling and a tacky bead surface, leading to a viscosity rise. This phenomenon is well documented throughout the literature where the molar mass of the beads influences the

rate of diffusion. As the molar mass increases, the rate of diffusion is reduced creating a high concentration of MMA around the edges of the bead. Secondly, the dissolution of the PMMA beads in the monomer was shown to be key in controlling the final properties of porous PMMA. As the beads dissolve, the viscosity of the mixture rises rapidly. This was observed by Pascal et al where the dissolution of PMMA beads in MMA reduced the set times of the materials[33]. Soxhlet extraction of the crosslinked beads was performed by refluxing pre-weighed beads (2 g) with methyl ethyl ketone (MEK) for one week before the beads were reweighed and the molecular weight of any polymer in the sol fraction obtained. The results correlated well with expectations, indicating a very small mass loss from the beads averaging 8 % wt, thus reaffirming the lack of dissolution of the crosslinked beads in MMA. The MEK solution of the soluble PMMA was concentrated on a rotary evaporator and the resultant viscous liquid dissolved in tetra hydro furan (THF) and analysed by GPC to determine the molecular weight of the sol fraction. The 4 % crosslinked beads resulted in a bimodal distribution of molecular weight with maxima at M_n 472 kg mol⁻¹ and 26.5 kg mol⁻¹. The 10 % crosslinked beads resulted in a sol fraction with a single peak at M_n 249 kg mol⁻¹ likely to be from polymer which was not fully bound by the crosslinking process.

4.7 Monomer Droplet Size

The stability of the emulsion is dependent on, but not limited to, the monomer droplet size, the concentration of the surfactant and the solubility of the monomer in water[140]. This subsection looks at the effect of the monomer droplet size on the emulsion by varying the length and intensity of mixing of the emulsion stage of the reaction prior to the addition of PMMA beads. It was assumed that increasing the intensity of stirring would decrease the droplet size, where intensity increases in the order manual stirring < mechanical stirring < high shear mixing < sonication. The porosity and compression results are presented in Table 4.6 with comparison to the standard stirring time of 3 minutes. It should be noted that the level of the surfactant, Triton X100, is half that of the standard blend methodology for all blends used in the analysis of monomer droplet size and, therefore, the results presented here cannot be directly compared with previous results outside of this section.

Table 4.6: Effects of the stirring intensity on the properties of porous PMMA (standard deviation given in parenthesis)

Sample Code (Lab book No)	Set Time/ Min	Compressive Performance				Water Porosity (Standard Deviation)/ %
		Average Max Stress / MPa (Standard Deviation)	Strain at Maximum Average Stress/ %	Transition Stress/ MPa (Standard Deviation)	Bulk Modulus (Standard Deviation)/ MPa	
Normal Stirring 3 mins (KA068)	21.0	17.35 (2.84)	14.36 (3.40)	9.92 (2.30)	254.39 (118.05)	30.60 (1.71)
Normal Stirring 10 mins (KA091)	25.5	21.29 (2.03)	14.12 (2.74)	12.92 (1.70)	363.03 (97.86)	28.44 (2.41)
High Shear Mixing 10 mins (KA093)	24.5	25.30 (1.50)	14.16 (1.11)	14.28 (0.42)	424.37 (157.41)	26.66 (3.39)
Sonication 10 minutes (KA082r)	22.0	26.22 (3.29)	15.52 (2.81)	15.52 (2.81)	527.93 (90.97)	28.82 (5.24)

For the standard blend methodology, increasing the mechanical stirring time of the emulsion improves the maximum compressive stress from a value of 17.3 MPa with 3 minutes stirring to 21.3 MPa after 10 minutes. Transition stress and bulk modulus also increase. Therefore, improving the mixing of the emulsion improves materials in terms of compressive properties. This is due to improved distribution of the monomer and the initiator throughout the mixture. Therefore, it can be concluded that the current stirring time of the emulsion in the standard methodology is insufficient for full homogenisation of the blend mixture. However, this inference was made in January 2011, approximately 18 months into the project, and so, for consistency, 3 minutes mixing remains the standard for all materials describes in the thesis to allow for comparison between materials.

With the apparent benefit of increasing the emulsion mixing time from 3 to 10 minutes using an overhead mechanical stirrer, a second study was undertaken in which the length of mixing of was varied from 1-30 minutes (See Figure 4.8, Results table given in Appendix 2.9).

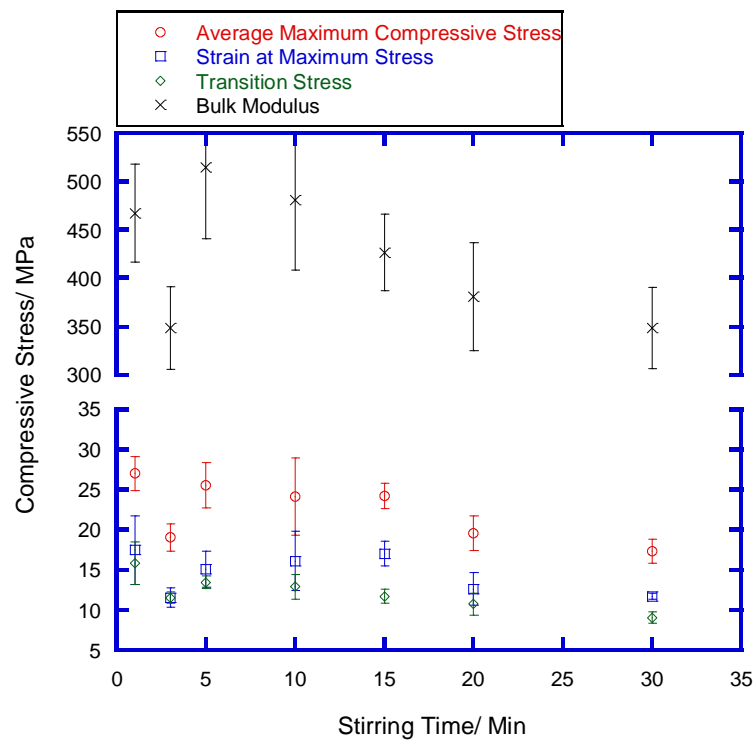


Figure 4.8: Effect of stirring time on the compressive performance of porous PMMA.

Figure 4.8 indicates that increasing the mixing time from 3 to 5 minutes gives an advantageous outcome in terms of compressive properties by increasing the average maximum compressive stress, the transitions stress and bulk modulus, demonstrating significantly stronger materials. However, this increase comes at the expense of porosity which is reduced by approximately 3 %. SEM highlights that the pores within the samples mixed for 5 minutes are better distributed, with fewer large voids being evident. This observation is reinforced by the permeability results which indicate little or no reduction in permeability as stirring time is increased, see Figure 4.9

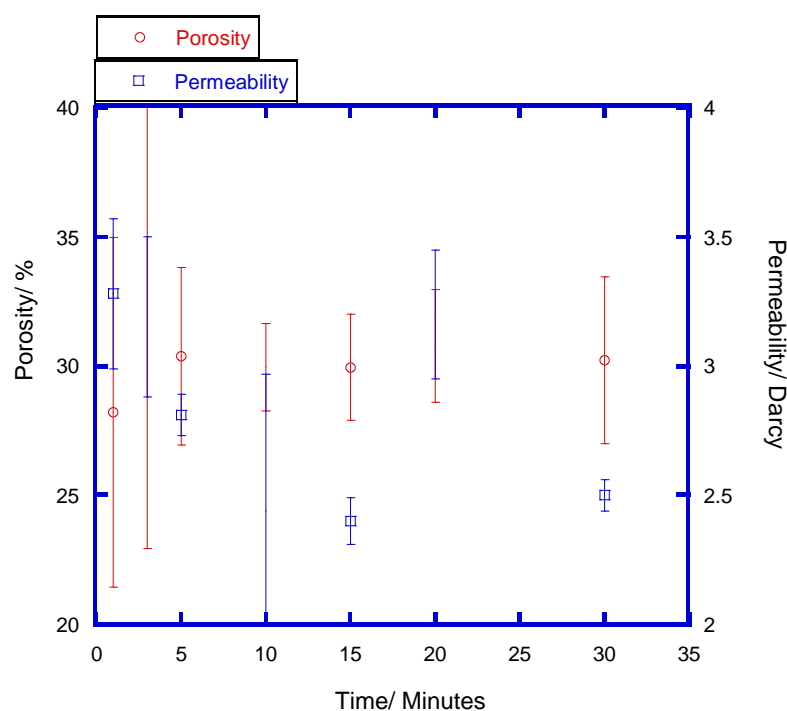


Figure 4.9: Effect of stirring time on porosity and permeability

Increasing the stirring time loses its initial benefits once 15 minutes has been surpassed, after which a reduction is observed in the average maximum compressive stress, strain, transition stress and bulk modulus, which rapidly declines after 30 minutes stirring. Since MMA is volatile, and the reactions are carried out in a sealed glove box at 25 °C, it is believed that the MMA is vaporising into the surrounding environment as the sample is being stirred. Therefore as the stirring time is increased, more MMA is being lost into the surrounding atmosphere. The loss of MMA results in an overall decrease in the volume of the ligaments hence the beads are less strongly bound resulting in a decrease in compressive performance.

The loss of monomer is evident in SEM pictures of the final materials (see Figure 4.10) where the volume of ligaments in the sample stirred for 30 minutes is significantly less than stirred for 3 minutes.

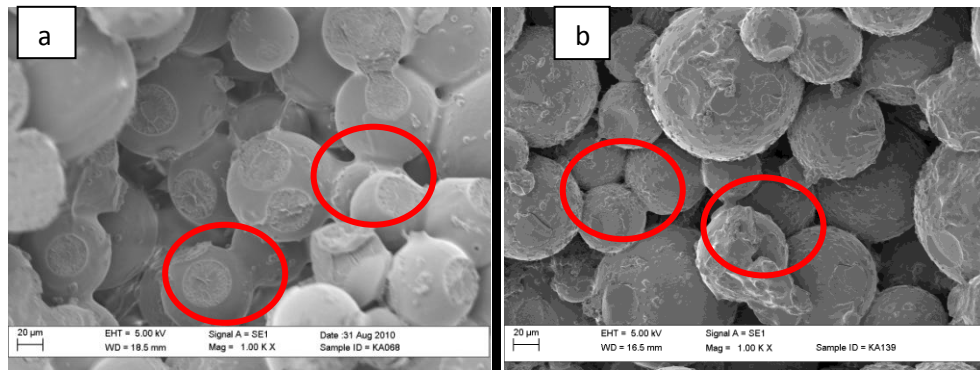


Figure 4.10: SEM of porous PMMA at 1 kX after a) 3 minutes stirring and b) 30 minutes stirring. Highlighted are regions showing differences in ligament volume

Increasing the intensity of mixing from mechanical stirring to sonication has very little effect on the properties of the materials, indicating that the intensity of mixing is unimportant within the limits used (see Figure 4.11). More important is the mixing time, where similar trends were observed with both sonication and mechanical stirring. Therefore it can be concluded that the distribution of the monomer is the dominant factor in improving the properties of porous PMMA as supposed to the droplet size.

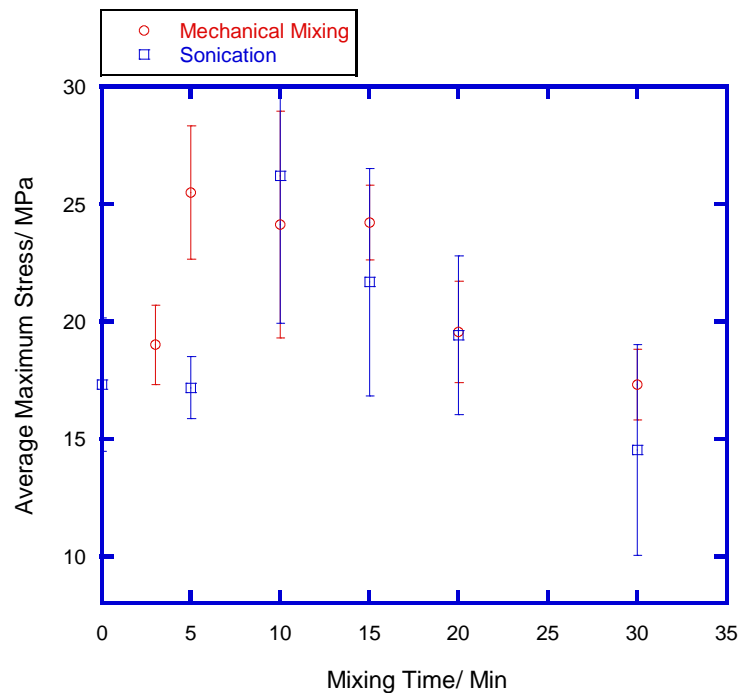


Figure 4.11: Comparing the effects of sonication and mechanical mixing on the average maximum compressive stress of porous PMMA samples

4.8 Summary

This chapter has established important experimental alterations from the initial blend methodology provided by Lucite International on which the project was based. Most importantly, the research has shown the importance of having a stable temperature environment that is free from draughts to prepare the samples and that the reaction is highly temperature sensitive with a few degrees variation having a significant impact on the set time and the average maximum compressive stress of the materials. The temperature has, therefore, been controlled by utilising a purpose built chamber which can be heated to 23 °C and excludes draughts, as well as by the pre-heating of the liquid starting materials to 25 °C prior to use. This control of the temperature enabled blends made throughout the three years of research to be compared and the reproducibility improved with a decrease in the standard deviation between samples.

This chapter also highlighted the importance of heating the samples to 60 °C in the final stage of the reaction to complete the polymerisation process. Without this stage, the materials were observed to be significantly weaker as the residual monomer was not removed from the ligaments which failed more readily due to increased plasticisation.

Initial experiments suggest that the PMMA bead size and molar mass controlled the diffusion of monomer into the beads and hence the properties of the final materials. Decreasing the diffusion of monomer led to improvements in the properties of the materials as more monomer is available to form the ligaments. SEM pictures indicate that it is the ligaments which are central in controlling the final properties of the materials with stronger ligaments forming more robust materials. Dissolution of the PMMA beads was also shown to be fundamental to the ligament formation by generating a viscous solution which enables the monomer droplets in the emulsion to coalesce, thereby creating ligaments which as polymerisation occurs, bind the beads together. Further work on visualisation of the ligaments is discussed in Chapter 9.

5. Effect of Surfactant on the Properties of Porous PMMA

5.1 Introduction

Surfactants are compounds which lower the surface tension of a liquid or alter the interfacial tension between two liquids. They are amphiphilic, meaning they contain both hydrophobic and hydrophilic groups, i.e both oil and water soluble components[141]. Surfactants can be subdivided into three categories based upon the nature of their hydrophilic group:

- Anionic, in which the hydrophilic group has a negative charge
- Cationic, in which the hydrophilic group has a positive charge
- Non-ionic, in which the hydrophilic group has no electrostatic charge

A surfactant molecule is not fully compatible with either a polar or a non-polar medium and therefore there will always be a conflict of affinity for either the head group or the tail group in polar and non-polar media respectively[142]. The size and shape of the relative parts affect the affinity and ability of the surfactant to adsorb at the interface.

Anionic surfactants have a negatively-charged counter-ion as a head group, usually consisting of a carboxylate (COO^-), a sulphate (SO_4^{2-}), a sulphonate (SO_3^-) or a phosphate (PO_4^{3-}) group. They are widely used in the production of household and personal care items due to their detergency and emulsification capabilities. Sulphated anionic surfactants have been shown to exhibit a synergistic effect with non-ionic surfactants which has proved to be particularly beneficial to their application[143]. Synergism occurs when a mixture of surfactants has superior properties when compared to the properties of the single components alone[144]. Idealistically, for maximum solubilisation, the surfactant should be at the interface between the oil/water layer as supposed to dissolved in either of the phases. Mixtures of anionic and non-ionic surfactants have been reported to increase the interaction at the boundary, enhancing the solubilisation of water in an oil-in-water microemulsion[145].

Non-ionic surfactants have no inherent charge on the head group. The hydrophilic part of the molecule is provided by polar functional groups, e.g hydroxyl groups ($-\text{OH}$) or an ethylene oxide chain (denoted EO; $-\text{OCH}_2\text{CH}_2-$). Increasing the number of EO groups increases the water solubility of the surfactant molecule, allowing for a longer chain hydrocarbon tail group to be used. If only one EO group is present, a maximum of 6-8

carbon atoms is permissible in the hydrophobic chain before the surfactant becomes insoluble in water[146]. Non-ionic surfactants are used exclusively in literature for the preparation of porous PMMA and hence are the focus of the work undertaken herein.

The preparation of standard porous PMMA materials, as made by Lucite International customers using a one bead system, contains a significant proportion by weight of an octyl phenol ethoxylate surfactant (Triton X100, 5 wt%). Manufactured by DOW, Triton X100 has an aromatic hydrophobic tail group and is widely used as a household or industrial cleaner or as an emulsifier in paint manufacture[99]. NMR analysis of the surfactant reveals 11 ethoxylate units to each phenyl group corresponding well to reported values[99]. To help aid the derivation of the mechanism for the formation of porous PMMA, detailed studies investigated the partitioning of components in the initial emulsion stage of the reaction prior to the addition of PMMA beads.

This chapter will further discuss the effect of the surfactant with respect to the structure of the tail group (aromatic/aliphatic), the hydrophilic-lipophilic balance (HLB), the level of the surfactant used in the synthesis, and the nature of the hydrophilic head group (non-ionic/anionic).

5.2 Characterisation of Surfactants

A large variety of surfactants have been sought to allow for the effective perception of their function and resulting properties of porous PMMA materials.

The Lutensol TO surfactant range was sourced from BASF to analyse the effect of the head to tail ratio (HLB) of the surfactant. The series is based around a fixed saturated iso-C₁₃ alcohol-based terminal alkyl group with variable ethoxylate chain length. The generic structure of this family of surfactants is shown in Figure 5.1.

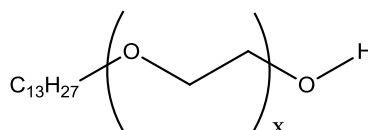


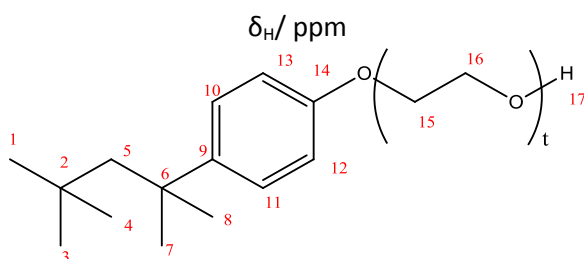
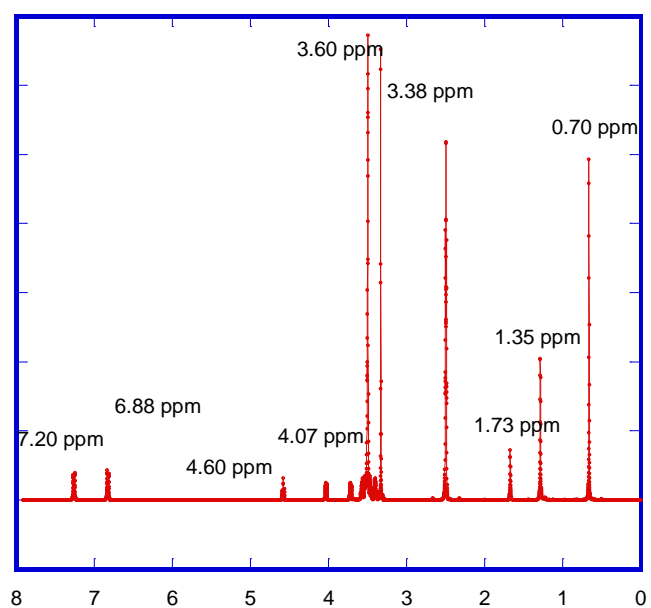
Figure 5.1: Structure of a Lutensol TO surfactant where x signifies the ethylene oxide chain length

Disponil FES32, an anionic surfactant, was also sourced from BASF, along with its non-ionic equivalent which is similarly based upon a linear chain alcohol with an ethylene oxide as the head group (see Figure 5.5).

5.2.1 NMR Structure Elucidation

Triton X100 and Lutensol TO surfactants were subjected to NMR to elucidate their structure, using the process detailed in Section 3.2.1. For Triton X100, the number of hydrogens in the repeat unit (t) was derived by dividing the integral obtained for hydrogen in the repeat unit (I_{OCH_2} , 3.60-3.44 ppm) by that obtained from the terminal alcohol (I_{OH} , 4.64 ppm) over 4 (the number of Hs in the repeat unit). See Figure 5.2 for NMR elucidation and integrals.

$$t = \frac{I_{OCH_2}}{4 I_{OH}}$$

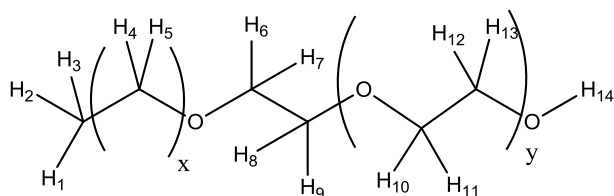
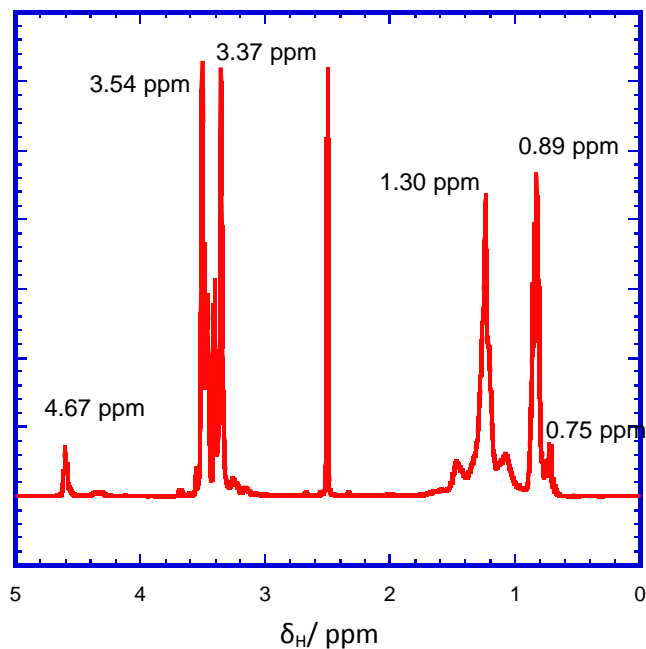


δ_H / ppm	Integral	Assignment
0.70	4.60	Terminal methyl, H1, H3, H4
1.35	4.00	Alkyl chain methylene, H5
1.72	1.0	Methylene adjacent to benzene H7, H8
4.07-3.38	22.09	Polyether repeat unit, H15, H16
4.64	0.50	Terminal alcohol, H17
6.88	1	Benzyl hydrogens meta to ether group, H10, H11
7.27	1	Benzyl hydrogens ortho to ether group, H13, H12

Figure 5.2: NMR structure elucidation and peak analysis of Triton X100

From NMR, the chain length (t) of Triton X100 was calculated to be 11 which compares with the manufacturer's nominal quoted value of 10[99].

The basic peak patterning for all the Lutensol TO surfactants are identical, but, the ratio of the integral of CH₂ to OCH₂ peaks decreases as the ethylene oxide (EO) length increases. The spectra and peak analysis for Lutensol TO3 is shown in Figure 5.3.



δ_H / ppm	Integral	Assignment
0.75	2.75	Terminal methyl, H1, H2, H3
0.89	12.78	Alkyl chain methylene, H4, H5
1.30	10.85	Alkoxy methylene H4, H5
3.37-3.54	13.56	Polyether repeat unit, H6, H7, H8, H9, H10, H11, H12, H13
4.69	1.00	Terminal alcohol, H14

Figure 5.3: NMR structure elucidation and peak analysis of Lutensol TO3

To calculate the ethylene oxide chain length (y), the integral of the polyether repeat unit, (I_{OCH_2} , 3.37-3.54 ppm) was divided by 4x the integral of the terminal alcohol peak (I_{OH} , 4.69 ppm) because there are 4 H atoms per EO unit and only one OH end group.

$$EO \text{ chain length} = \frac{I_{OCH_2}}{4I_{OH}}$$

Similarly, the length (n) of the methylene chain was derived by dividing the ratio of the integrals of the methylene chain (I_{CH_2} 0.89-1.30 ppm) and terminal alcohol (I_{OH} 4.69 ppm) by 2 because there are 2 methylene atoms to each OH end-group. Where an overlap was observed, the three hydrogens from the terminal methyl group were subtracted before division.

$$Alkyl \text{ chain length} = \frac{I_{CH_2}}{2I_{OH}}$$

The structures derived by NMR for the Lutensol TO surfactant range are given in Table 5.1

Table 5.1: Structure derivation for Lutensol surfactants from NMR where the integrals for each region is given.

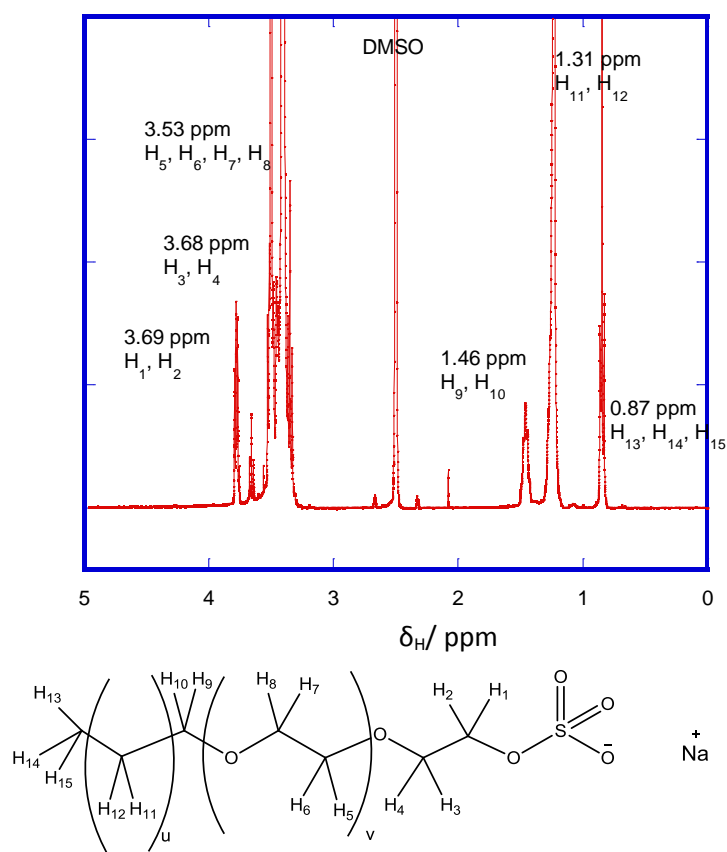
δ_H / ppm	Terminal methyl, H1, H2, H3 (0.75 ppm)	Alkyl chain methylene, H4, H5 (0.89 ppm)	Alkoxy methylene H4, H5 (1.30 ppm)	Polyether repeat unit, H6, H7, H8, H9, H10, H11, H12, H13 (3.37-13.34 ppm)	Terminal alcohol, H14 (4.69 ppm)	Structure
Surfactant						
Lutensol TO3	2.75	12.78	10.85	13.56	1.00	$CH_3(CH_2)_{12}(OC_2H_4)_3OH$
Lutensol TO5	2.54	12.95	10.51	19.61	1.00	$CH_3(CH_2)_{11}(OC_2H_4)_5OH$
Lutensol TO6	1.35	10.77	14.62	23.95	1.00	$CH_3(CH_2)_{12}(OC_2H_4)_6OH$
Lutensol TO7	2.40	10.00	13.94	28.79	1.00	$CH_3(CH_2)_{13}(OC_2H_4)_7OH$
Lutensol TO8	3.82	10.11	15.77	43.37	1.00	$CH_3(CH_2)_{13}(OC_2H_4)_{10}OH$
Lutensol TO109	-	14.08	15.61	49.74	1.00	$CH_3(CH_2)_{13}(OC_2H_4)_{12}OH$
Lutensol TO129	-	11.70	12.82	56.15	1.00	$CH_3(CH_2)_{11}(OC_2H_4)_{14}OH$
Lutensol TO15	1.50	11.55	11.41	65.63	1.00	$CH_3(CH_2)_{11}(OC_2H_4)_{16}OH$
Lutensol TO20	0.62	10.68	13.77	68.42	1.00	$CH_3(CH_2)_{11}(OC_2H_4)_{17}OH$

Disponil FES32 and Disponil A1080 were also subjected to NMR analysis (see Figure 5.4 and 5.5). Disponil A1080 was analysed as for Lutensol TO surfactants by comparing the integrals to the terminal hydrogen. As FES32 does not have a terminal OH hydrogen, the EO chain length and alkyl chain length was accessed from the ratio of their integrals together with the integral for the terminal methyl group in the alkyl group.

$$EO\ chain\ length\ (v) = \frac{I_{OCH_2}}{4} \times \frac{3}{I_{CH_3}}$$

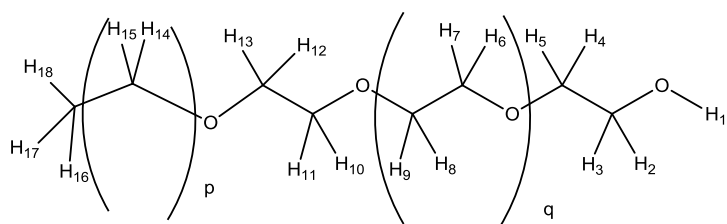
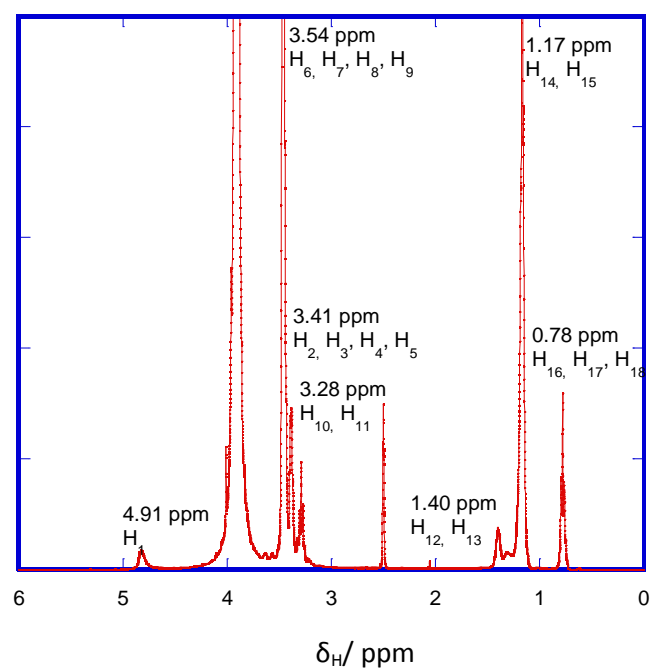
$$Methylene\ chain\ length\ (u) = \frac{I_{CH_2}}{2} \times \frac{3}{I_{CH_3}}$$

Table 5.2 gives a summary of the NMR findings.



δ_H / ppm	Integral	Assignment
0.87	1.00	Terminal methyl, H13, H14, H15
1.31	6.31	Alkyl chain methylene, H11, H12
1.46	0.68	Alkoxy methylene H9, H10
3.53	5.10	Polyether repeat unit, H5, H6, H7, H8
3.68-3.69	0.65	Terminal alkoxy methylene, H1, H2, H3, H4

Figure 5.4: NMR spectra of Disponil FES32 and assignment of resonances



δ_H / ppm	Integral	Assignment
0.78	3.55	Terminal methyl, H16, H17, H18
1.17	21.73	alkyl chain methylene, H14, H15
1.40	1.64	Alkoxy methylene, H12, H13,
3.28	2.61	Alkoxy methylene, H10, H11
3.41	4.32	Terminal alkoxy methylene, H2, H3, H4, H5
3.54	40.31	Polyether repeat unit, H6, H7, H8, H9
4.91	1.00	H1, Terminal hydrogen

Figure 5.5: NMR spectra of Disponil A1080 and assignment of resonances

Table 5.2: Structure derivation for Congis surfactants from NMR where the integral for each region is given

δ_H / ppm Surfactant	Terminal alkoxy methylene H1, H2, H3, H4 (3.68-3.69 ppm)	Polyether repeat unit H5, H6, H7, H8 (3.53 ppm)	Alkoxy methylene H9, H10 (1.46 ppm)	Alkyl chain length methylene H11, H12 (1.31 ppm)	Terminal methyl, H13, H14, H15 (0.87 ppm)	Structure
Disponil FES32	0.65	5.10	0.68	6.31	1.00	$\text{CH}_3(\text{CH}_2)_{10}(\text{OC}_2\text{H}_4)_3\text{O}$ $\text{C}_2\text{H}_4\text{OSO}_3^-\text{Na}^+$
	Terminal methyl H16, H17, H18 (0.78 ppm)	Alkyl chain methylene H14, H15 (1.17 ppm)	Alkyloxy methylene, H6, H7, H8, H9, H10, H11, H12, H13 (3.41, 1.40/ 3.28 ppm)	Polyether repeat unit, H2, H3, H4, H5 (3.4 ppm)	Terminal alcohol, H1(4.91 ppm)	Structure
Disponil A1080	3.55	21.73	4.32/ 1.64/ 2.61	40.31	1.00	$\text{CH}_3(\text{CH}_2)_{11}(\text{OC}_2\text{H}_4)_5\text{O}$ H

Results gained from NMR data differ slightly from that stated in the manufacturer's data sheet, as can be seen from the information given in Table 5.3[99, 147].

Table 5.3: Structure comparison of data obtained from NMR and supplier data sheets

Surfactant	Supplier	Supplier Data	NMR Elucidation
Lutensol TO3	BASF	100 % active, EO length 3, Mn 340 g mol ⁻¹	EO length 3, Mn 332 g mol ⁻¹
Lutensol TO5	BASF	100 % active, EO length 5, Mn 430 g mol ⁻¹	EO length 5, Mn 406 g mol ⁻¹
Lutensol TO6	BASF	100 % active, EO length 6, Mn 470 g mol ⁻¹	EO length 6, Mn 464 g mol ⁻¹
Lutensol TO7	BASF	100 % active, EO length 7, Mn 500 g mol ⁻¹	EO length 7, Mn 552 g mol ⁻¹
Lutensol TO8	BASF	100 % active, EO length 8, Mn 600 g mol ⁻¹	EO length 10, Mn 654 g mol ⁻¹
Lutensol TO109	BASF	85 % active, EO length 10, Mn 630 g mol ⁻¹	EO length 12, Mn 742 g mol ⁻¹
Lutensol TO129	BASF	85 % active, EO length 12, Mn 750 g mol ⁻¹	EO length 14, Mn 802 g mol ⁻¹
Lutensol TO15	BASF	100 % active, EO length 15, Mn 850 g mol ⁻¹	EO length 16, Mn 890 g mol ⁻¹
Lutensol TO20	BASF	100 % active, EO length 20, Mn 1000 g mol ⁻¹	EO length 17, Mn 934 g mol ⁻¹
Congis Disponil FES32	BASF	30 % active, EO length Mn 430 g mol ⁻¹	EO length 4, Mn 449 g mol ⁻¹
Congis Disponil A1080	BASF	80 % active EO length 10, Mn 630 g mol ⁻¹	EO length 10, Mn 626 g mol ⁻¹

Calculated and experimental values may differ for a number of reasons. Firstly, those stated in the supplier data sheets are often rounded to the nearest ten, this accounts for the majority of the difference above. Higher EO length Lutensol surfactants may also have reduced solubility in the solvent used for NMR. For experimental analysis, the surfactant was dissolved in deuterated DMSO and left to dissolve whilst stirring for 6 hours. The supplier methodology is not stated, however a different solvent may result in slight differences in the EO length if the surfactant is dissolved to a different extent. For all remaining calculations, the measured EO length from NMR will be used through the thesis with the corresponded calculated molar mass.

5.2.2 Critical Micelle Concentration (CMC)

Surfactants solutions were subjected to measurement of surfactant tension by pendant drop analysis to obtain the critical micelle concentration (CMC) both in water and in an MMA-saturated aqueous solution (see Table 5.4 and Figure 5.6).

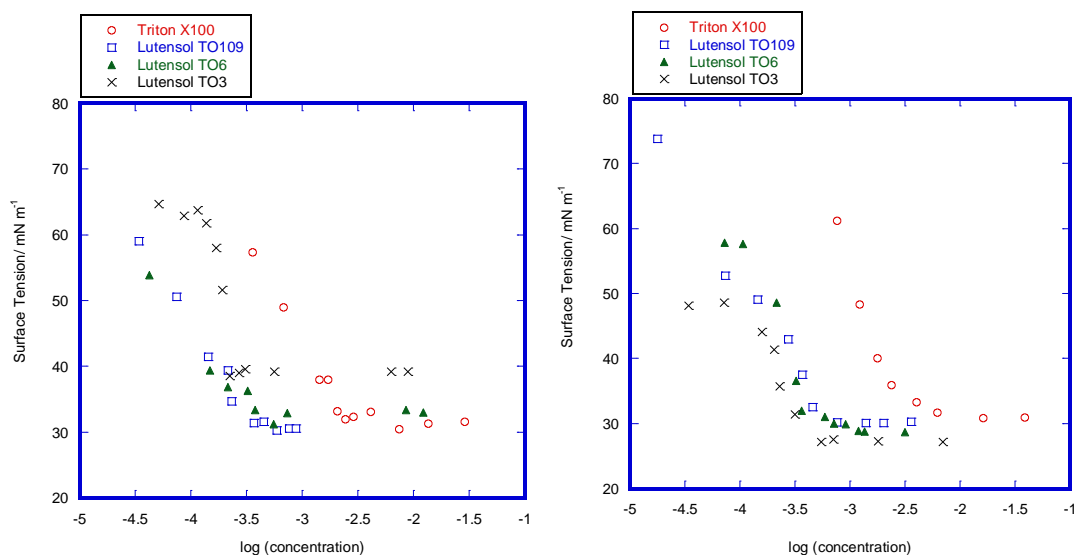


Figure 5.6: CMC of Triton X100, Lutensol TO109, Lutensol TO6, Lutensol TO3 in a) water and b) an MMA-saturated aqueous solution

The critical micelle concentration (CMC) of a surfactant is the concentration at which micelles spontaneously form in solution and is seen experimentally by a discontinuity in a plot of surface tension against log(surfactant concentration) [95]. At surfactant concentrations below the CMC, the surfactant molecules exist independently and pack at the air-water interface, thereby forming a monolayer and reducing the surface tension of the solution. In the region of the CMC, a compact monolayer exists at the surface and the surfactant molecules begin to build up micellar structures in the bulk liquid, thereby decreasing the free energy of the system through shielding the hydrophobic parts of the surfactant from the water molecules (see Figure 5.7). Above the CMC, further addition of surfactant only leads to the formation of additional micelles.

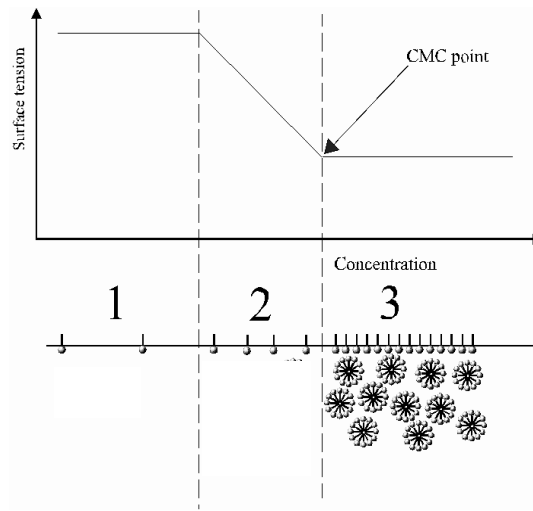


Figure 5.7: Surface tension against concentration for a surfactant in water highlighting the CMC value[148]

Density profile experiments indicate that surface active agents tend to pack at the interface thereby favouring an expansion of the air-water interface. This counteracts the tendency of the surface to contract under normal surface tension forces. If Π is the expanding pressure or surface pressure exerted by the adsorbed surfactant then

$$\Pi = \gamma_o - \gamma$$

where γ_o is the surface tension of the pure solvent and γ is the surface tension of the solution.

The Gibbs adsorption isotherm relates the change in surface tension with the chemical potential (μ) of the components (J). The surface tension describes the ease at which the surface area of a substance can be distorted. It is affected by the composition of the surface so is heavily influenced by surfactants which pack at the interface. By increasing the concentration of surfactant, more surfactant molecules are available, creating a positive surface excess concentration (Γ) and increasing the chemical potential, which reduces the surface tension.

$$d\gamma = - \sum_J \Gamma_J d\mu_J$$

The chemical potential of the components in this case specifically the surfactant (μ_s) can be calculated from the activity coefficient of the surfactant (a_s) where μ^0 is the standard chemical potential, R the molar gas constant and T the temperature in Kelvin. Giving

$$\mu_s = \mu^0 + RT \ln a_s$$

For dilute solutions, the activity coefficient is approximately equal to 1 hence a_s can be approximated by using the molar concentration of the surfactant, c [149]. Therefore,

$$d\mu_s = RT d \ln c$$

At a constant temperature [150]

$$\left(\frac{d\gamma}{dc}\right) = \frac{-RT \Gamma'_s}{c}$$

Analysis of the CMC plots using this equation enables the surfactant surface excess concentration (Γ_s) to be calculated, and hence the area occupied per molecule (see Table 5.4) where N_A is Avogadro's constant.

$$\Gamma'_s = \frac{c}{-RT} \left(\frac{d\gamma}{dc}\right)_T$$

$$\text{Area occupied per molecule} = \frac{1}{\Gamma'_s} \times N_A$$

Table 5.4: Details of experimentally obtained CMC and N_A/Γ_s for Triton X100, Lutensol TO109, Lutensol TO6, and Lutensol TO3

Surfactant	CMC(H ₂ O) / mmol dm ⁻³	Literature values for CMC(H ₂ O) / mmol dm ⁻³	CMC(aq MMA) / mmol dm ⁻³	N_A/Γ_s water / \AA^2 molecules ⁻¹	N_A/Γ_s aq MMA / \AA^2 molecules ⁻¹
Triton X100	0.38	0.20 [99]	0.56	14.76	11.32
Lutensol TO109	0.37	0.378 [100]	0.46	14.03	11.60
Lutensol TO6	0.33	0.31 [100]	0.37	20.56	12.19
Lutensol TO3	0.23	0.075 [97]	0.55	6.50	18.15
Disponil A1080	0.63	1.24 [100]	1.36	8.13	12.50
Disponil FES32	0.85	17.13 [97]	1.06	16.36	15.21

The results gained by these tests differ slightly from literature values, however the pattern seen with increasing CMC with EO number is observed [99, 151]. Due to the logarithmic

term in the equation, even a small discrepancy in the line of best fit which yields the discontinuity in the plot of surface tension against $\log(\text{concentration})$ can cause a very large change in the value of Γ_s .

As the EO chain length increases the CMC increases due to the EO constituent increasing the solubility of the surfactant in water. This increased interaction with the aqueous phase increases the amount of energy needed to dehydrate the material which is to be incorporated into the micelle, and therefore the CMC will move to higher concentrations. Similar findings have been observed by Cox et al. in studies of linear alcohol ethoxylates[152]. In addition, the EO chain length increases the molecular size of the surfactant which causes steric interactions when the surfactant packs at the interface and therefore the ability to lower the surface tension is reduced.

MMA is soluble in water at a concentration of 1.6 g per 100 ml[153] and therefore values of the CMC for MMA saturated water have also been obtained. When MMA is dissolved in the water, the CMC moves to slightly higher values, indicating that molecular dissolution of the surfactant is enhanced. It should be noted that in the formation of porous PMMA, all surfactants are used at levels well above the critical micelle concentration, so most of the surfactant molecules are found in micelles in which the non-polar monomer (MMA) can be found to reside. Hence, MMA can be considered to have been “solubilised” in the water, as shown in the schematic in Figure 5.8.

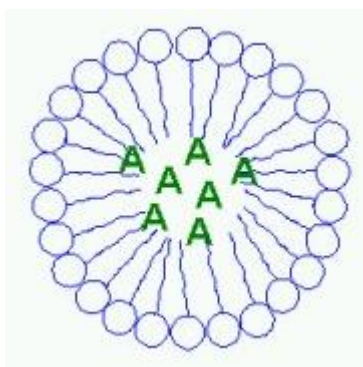


Figure 5.8: Cartoon of a micelle in water showing the formation and how a hydrophobic substance A can become solubilised by dissolution in the central core.

5.2.3 Solubility Constant

The dissolution of a polymer in a solvent is controlled by the change in the Gibbs free energy, ΔG_m on mixing[154]

$$\Delta G_m = \Delta H_m - T\Delta S_m$$

where T is the temperature, ΔH is the enthalpy change and ΔS the entropy change on mixing. A negative value of ΔG indicates that spontaneous mixing will occur. If positive, two or more phases will result from the mixing process. Solubility parameters were derived to provide a simple guide to the enthalpy of mixing of liquids and have since been extended to include polymers and polar solvents. For polymers, entropy (S) can be assumed to be negligible as it is dwarfed by the enthalpy (T) of termination. Scatchard, Hildebrand and Scott proposed the term “like dissolves like” which related the enthalpy of mixing to the cohesive energy density (E/V) and defined the solubility parameter δ as:

$$\delta_i = \left(\frac{\Delta E_i}{V_i} \right)^{1/2}$$

where E_i is the molar energy of vaporisation and V_i the molar volume for component i in the mixture. The solubility parameter therefore describes the attractive strength between the molecules of the materials. This can be related back to the enthalpy term of mixing given by

$$\Delta H_m = V_m (\delta_1 - \delta_2)^2 \varphi_1 \varphi_2$$

where φ is the volume fraction[27]. For simple liquids, the solubility parameter can be calculated directly from the enthalpy of vaporisation. However, polymers are non-volatile and hence the Hildebrand parameters and heat of vaporisation data cannot be obtained. Therefore, indirect methods have to be used to calculate δ [154]. Most commonly used is the Group Contribution method derived by Hoy[155], van Krevelen[156], Hoftyzer[157] and Small[158]. The group contribution technique assumes that the overall properties of a substance can be derived from the addition of the contributions of different functional groups present in the repeating polymer unit. The solubility parameter can therefore be calculated from the summation of the molar attraction constant (F), the density (ρ), of the compound and its molar mass (M_i)[154].

$$\delta = \left(\frac{\Delta E_i^v V_i}{V_i^2} \right)^{1/2} = \frac{\sum_j F_j}{V_i} = \frac{\rho_i \sum_j F_j}{M_i}$$

Small first tabulated values of F_j which was later developed by Hoy. However, the concept was most comprehensively investigated by van Krevelen. In this work, F_j values developed by van Krevelen have been used as the tables are self-consistent [159]. It should be noted

that all the values obtained for each solubility occurrence are simplified estimates due to the complexities involved in the derivation of solubility parameters. In this case no secondary bonding has been taken into account so contributions from van der Waals forces and hydrogen bonds have been excluded. Therefore, the values obtained will be used only as a guide to aid in the reasoning of material properties and miscibility of the surfactant. Table 5.5 has the derived solubility parameters with differences to PMMA (19.23 MPa^½) and MMA (14.01 MPa^½).

Table 5.5: Derivation of solubility parameters for Triton X100 and Lutensol TO surfactants

Surfactant Name	Molecular Weight	Length of Ethylene Oxide Chain	Hydrophilic-Lipophilic Balance	Solubility Parameter/ δ MPa ^½	Difference in Solubility Parameter to MMA/ δ MPa ^½	Difference in Solubility Parameter to PMMA/ δ MPa ^½
TX100	647	10	13.4	20.26	6.25	1.03
TO3	340	3	9	19.10	5.09	0.14
TO5	430	5	10.5	19.23	5.22	0.00
TO6	470	6	11	19.46	5.45	0.23
TO7	500	7	12	20.08	6.07	0.85
LutTO8	536	8	13	20.84	6.83	1.61
LutTO109	630	69	13.5	20.55	6.54	1.32
LutTO129	780	12	14.5	19.10	5.09	0.13
LutTO15	805	15	15.5	20.84	6.83	1.60
LutTO20	1000	20	16.5	21.27	7.26	2.04

In Table 5.5, if the solubility parameter is within ± 1 of either PMMA or MMA, it would be expected that the surfactant is miscible in the material. The above data indicates that the smaller chain surfactants are highlight miscible with PMMA, the difference in solubility parameters being in general <1 . The difference in solubility parameter to MMA is significantly greater, indicating that the surfactants are less miscible in MMA. This indicates that there is a strong driver for the surfactant to end up in the polymer and therefore cause plasticisation and lower the materials' overall T_g .

5.3 Partitioning of the Emulsion

The synthesis of porous PMMA can be divided into 3 main stages: the dissolution of BPO in monomer, the making of a stable emulsion and the addition of PMMA beads and DMPT. The emulsion stage was found to be key in controlling the final properties of the materials. Current literature is greatly lacking in the mechanistic understanding of this stage and the formation mechanism of porous PMMA, with authors differing in the mechanism from emulsion polymerisation followed by elimination of the water post polymerisation[77, 84] to the adsorption of monomer by the beads[79]. To aid in elucidation of the mechanism, simplistic blends of water, surfactant and MMA were prepared and, once settled, were analysed by GC to obtain levels of monomer in the water layer and water in the MMA layer. Ultraviolet spectroscopy (UV) or the refractive Index (RI) was used to obtain the surfactant concentration in each layer for Triton X100 and Lutensol surfactants, respectively, using the analytical procedures discussed in Section 3.3.1.

The water phase was found to contain small amounts of dissolved MMA and surfactant. Similarly, the monomer layer was found to contain a small amount of dissolved water; however, a considerable amount of surfactant was also present.

The main role of the surfactant in the synthesis of porous PMMA is to form a stable emulsion. Above the CMC, the surfactant in the water layer arranges in micelles with their hydrophilic head groups in contact with the water and the hydrophobic tail facing inwards thereby forming a hydrophobic core in which monomer can reside[16]. Three phases in the emulsion are evident:

- An aqueous phase in which dissolved monomer and surfactant are present
- Monomer droplets which are maintained in suspension in which it was found a considerable amount of dissolved surfactant and small amount of dissolved water
- Surfactant stabilised micelles in which monomer is contained.

GC revealed that in a solution of MMA and water, a concentration of $0.016 \text{ mol dm}^{-3}$ of MMA is found molecularly dissolved in water. If Triton X100 is present, the concentration of MMA found in water increased to $0.0545 \text{ mol dm}^{-3}$, indicating that the surfactant enhanced the molecular dissolution of MMA. In addition, from pendant drop analysis, the CMC of Triton X100 can be obtained both in water and an MMA saturated water solution. Table 5.6 gives a summary of the constants used in calculating the partitioning of the surfactant in the making of porous PMMA.

Table 5.6: Data used in the calculation of phase partitioning

Saturation Concentrations	Value/ mol L ⁻¹
Concentration of water in MMA ^a , [water] _{MMA}	0.765
Concentration of MMA in water ^a , [MMA] _{water}	0.016
Concentration of MMA in water with Triton X100 present just below its CMC ^a [MMA] _{water+X100}	0.0545
Concentration of Triton X100 in MMA ^b , [X100] _{MMA}	0.198
CMC of Triton X100 in water ^c , [X100] _{water}	3.80 x 10 ⁻⁴
CMC of Triton X100 in water saturated with MMA ^c [X100] _{water+MMA}	5.60 x 10 ⁻⁴
Additional Data	Values
Molar Mass of MMA [160], RMM _{MMA}	100.12 g mol ⁻¹
Molar Mass of water [161], RMM _{water}	18.02 g mol ⁻¹
Molar Mass of Triton X100 [99], RMM _{X100}	646.85 g mol ⁻¹
Density of MMA [162] ρ _{MMA}	0.94 g ml ⁻¹
Density of water at 25 °C [163] ρ _{water}	0.997 g ml ⁻¹
Density of Triton X100 [99] ρ _{X100}	1.061 g ml ⁻¹
Triton X100 Micellular aggregation number[164], Ag _{X100}	128
Molecules of MMA per Triton X100 micelle	212

^a Measured by GC

^b Measured by UV

^c Measured by pendant drop analysis

Three further assumptions have been made to allow for estimation of the partitioning of Triton X100 between the MMA layer and the aqueous phases. Firstly, the amount of water and MMA always correspond to the water:MMA ratio that exceeds the saturation solubility of water in MMA. Secondly, the amount of water and MMA always corresponds to a MMA:water ratio that exceeds the saturation solubility of MMA in water. Finally it is assumed that

$$\frac{[X100]_{water}^{below\ saturation}}{[X100]_{MMA}^{below\ saturation}} = \frac{[X100]_{water}^{saturation}}{[X100]_{MMA}^{saturation}}$$

Since:

$$\frac{[X100]_{water}^{below\ saturation}}{[X100]_{MMA}^{below\ saturation}} = \frac{m_{water}^{X100}/v_{water}}{m_{MMA}^{X100}/v_{MMA}}$$

where m_y^x denotes the mass of the component x in the layer y, i.e m_{water}^{X100} is the mass of Triton X100 in the water layer and v_y is the volume of y, then:

$$m_{water}^{X100} = \frac{m_{MMA}^{X100} \times v_{water} \times [X100]_{water}^{saturation}}{v_{MMA} \times [X100]_{MMA}^{saturation}}$$

and so:

$$\frac{m_{water}^{X100}}{m_{MMA}^{X100} + m_{water}^{X100}} = \frac{v_{water} \times [X100]_{water}^{saturation}}{(v_{MMA} \times [X100]_{MMA}^{saturation}) + (v_{water} \times [X100]_{water}^{saturation})}$$

Inputting the quantities used in the standard blend formulation for MMA (146.66 g), water (439.33 g) and Triton X100 (73.22 g) the amounts of components transferred to the relative phases can be calculated (see Table 5.7). The first line of the table uses the quantities in the standard blend formulation. Taking the phases in turn and assuming that the input values for MMA and water remain throughout, the amount of MMA transferred to the aqueous phases (m_{MMA}^{water}) can be calculated where RMM_{MMA} is the molar mass of MMA (100.12 g mol⁻¹), $[MMA]_{water+X100}$ is the concentration of MMA in water when Triton X100 is present just below its CMC and calculated from pendant drop analysis, m_{MMA}^{aq} is input mass of water and ρ_{water} the density of water

$$m_{MMA}^{water} = RMM_{MMA} \times [MMA]_{water+X100} \times \left(0.001 \times \frac{m_{MMA}^{aq}}{\rho_{water}} \right)$$

Similarly the amount of water transferred to the MMA (m_{water}^{MMA}) phase can be calculated.

$$m_{water}^{MMA} = RMM_{water} \times [water]_{MMA} \times \left(0.001 \times \frac{m_{MMA}^{MMA}}{\rho_{MMA}} \right)$$

where RMM_{water} is the molar mass of water (18.02 g mol⁻¹), $[water]_{MMA}$ is the concentration of water in the MMA phase as obtained from GC, m_{MMA}^{MMA} is the input mass of MMA and ρ_{MMA} the density of MMA (0.94 g ml⁻¹).

The total concentration of Triton X100 to MMA in the solution phase ([X100]:[MMA]) is derived by:

$$[X100]:[MMA]=1000\times\left(\frac{m_{X100}^{input}}{RMM_{X100}}\right)\div\frac{m_{MMA}^{MMA}}{\rho_{MMA}}$$

where m_{X100}^{input} is the input mass of Triton X100, for the standard formulation 73.22 g. If this value is greater than 0.198 mol L⁻¹ then the concentration of surfactant is above the CMC hence micelles will form. If less than 0.198 mol L⁻¹ no surfactant micelles will form hence all the MMA will be either dissolved in the water layer or in the MMA layer. Ideally, to minimise the effects of plasticisation, the value of [X100]:[MMA] would be as close to than 0.198 mol L⁻¹ as possible whilst still allowing for a stable emulsion to form.

Where the value of [X100]:[MMA] exceeds 0.198 mol L⁻¹, the partitioning of Triton X100 between the water and MMA can be calculated. The level of Triton X100 transferred to the MMA solution (m_{X100}^{MMA}) is:

$$m_{X100}^{MMA}=RMM_{X100}\times[X100]_{MMA}\times\left(0.001\times\frac{m_{MMA}^{MMA}}{\rho_{MMA}}\right)$$

where RMM_{X100} is the molar mass of Triton X100 (646.85 g mol⁻¹), $[X100]_{MMA}$ the concentration of X100 in the MMA phase. Similarly, the ratio of the concentration of Triton X100 to water can be calculated, which if greater than the calculated critical micelle concentration when water is saturated with MMA $[X100]_{water+MMA}$ then the partitioning of Triton X100 into the water layer (m_{X100}^{aq}) can also be obtained.

$$[X100]:[water]=1000\times\left(\frac{m_{X100}^{input}-m_{X100}^{MMA}}{RMM_{X100}}\right)\div\frac{m_{water}^{aq}}{\rho_{water}}$$

$$m_{X100}^{aq}=RMM_{X100}\times[X100]_{water+MMA}\times\left(0.001\times\frac{m_{MMA}^{aq}}{\rho_{MMA}}\right)$$

All the above calculations are based on the input levels of Triton X100, water and MMA. However, the calculations show that in fact some water is present in the MMA phases, some MMA in the water phase and the Triton X100 is present in both layers. Thus the

output values from the 0th iteration are now used as the input values as shown by columns k, l and m. The same process is then repeated to gain the partitioning of the components based on the new inputs. Through each iteration, the difference between the input and output values diminishes. For Triton X100 five iterations are required before the numbers converge (see Table 5.7).

Table 5.7: Partitioning calculations and results for Triton X100 in a standard blend formulation

Iteration Number	Amounts in Solution Phases			Calculation of Amounts Transferred							Micellar Phase		
	MMA in MMA / g	Water in Aqueous / g	X100 in X100 / g	MMA transferred to Aqueous Solution Phase / g	Water transferred to MMA Solution Phase / g	Total X100 to MMA Concentration / mol/L	X100 transferred to MMA Solution Phase if the concentration is below saturation in MMA / g	X100 transferred to MMA Solution Phase/ g	Total X100 to Water Concentration / mol/L	X100 transferred to Aqueous Solution Phase / g	Residual X100 in micelles / g	Number of Micelles	MMA in Micelles / g
0	146.66	439.33	73.22	2.4044	2.1508	0.7255	Exceeds Saturation Conc.	19.9826	0.187	0.1596	53.078	3.860E+20	13.61
1	130.64	437.18	0.00	2.3927	1.9160	0.8144	Exceeds Saturation Conc.	17.8011	0.197	0.1588	55.26	4.019E+20	14.17
2	130.10	437.41	0.00	2.3939	1.9080	0.8178	Exceeds Saturation Conc.	17.7265	0.196	0.1589	55.33	4.025E+20	14.18
3	130.08	437.42	0.00	2.3940	1.9077	0.8180	Exceeds Saturation Conc.	17.7237	0.196	0.1589	55.34	4.025E+20	14.19
4	130.08	437.42	0.00	2.3940	1.9077	0.8180	Exceeds Saturation Conc.	17.7236	0.196	0.1589	55.34	4.025E+20	14.19
5	130.08	437.42	0.00	2.3940	1.9076	0.8180	Exceeds Saturation Conc.	17.7236	0.196	0.1589	55.34	4.025E+20	14.19
Calculations	k	l	M	a	B	c	d	e	f	g	h	i	J

$$\begin{aligned}
 \text{a) } m_{MMA}^{water} &= RMM_{MMA} \times [MMA]_{water+X100} \times \left(0.001 \times \frac{m_{MMA}^{aq}}{\rho_{water}} \right) & \text{b) } m_{water}^{MMA} &= RMM_{water} \times [water]_{MMA} \times \left(0.001 \times \frac{m_{MMA}^{MMA}}{\rho_{MMA}} \right) & \text{c) } [X100]:[MMA] &= 1000 \times \left(\frac{m_{X100}^{input}}{RMM_{X100}} \right) \div \frac{m_{MMA}^{MMA}}{\rho_{MMA}} \\
 \text{d) If (c) } > 0.198 \text{ mol L}^{-1} & \text{ then exceeds surfactant concentration will show} & \text{e) if (c) } > 0.198 \text{ mol L}^{-1} & \text{ then } m_{X100}^{MMA} &= RMM_{X100} \times [X100]_{MMA} \times \left(0.001 \times \frac{m_{MMA}^{MMA}}{\rho_{MMA}} \right) & \text{f) } [X100]:[water] &= 1000 \times \left(\frac{m_{X100}^{input} - m_{X100}^{MMA}}{RMM_{X100}} \right) \div \frac{m_{water}^{aq}}{\rho_{water}} \\
 \text{g) if f) } > [X100]_{water+MMA} & \text{ then } m_{X100}^{aq} &= RMM_{X100} \times [X100]_{water+MMA} \times \left(0.001 \times \frac{m_{MMA}^{aq}}{\rho_{MMA}} \right) & \text{h) if f) } > [X100]_{water+MMA} & \text{ then } m_{X100}^{micelles} &= m_{X100}^{input} - m_{X100}^{MMA} - m_{X100}^{aq} & \text{i) Number of micelles} &= N_A \times \frac{\frac{m_{X100}^{micelles}}{RMM_{X100}}}{Ag_{X100}} \\
 \text{j) } m_{MMA}^{micelles} &= \text{Number of micelles} \times \left(\frac{\text{molecules of MMA per X100 micelle}}{Av} \right) \times RMM_{MMA}
 \end{aligned}$$

Table 5.8 Output for partitioning calculations for Triton X100

OUTPUT		
Final Amounts in Phases After Partitioning:	Mass / g	Concentration in Phase / wt%
MMA in MMA Solution Phase	130.08	86.89
MMA in Aqueous Solution	2.39	0.54
MMA in Micelles	14.19	20.41
<i>Total Partitioned MMA</i>	<i>146.66</i>	–
<i>Total Final MMA Phase</i>	<i>149.71</i>	–
Water in Aqueous Solution Phase / g	437.42	99.42
Water in MMA Solution Phase/ g	1.91	1.28
<i>Total Partitioned Water / g</i>	<i>439.33</i>	–
<i>Total Final Water Phase</i>	<i>439.97</i>	–
X100 in MMA Solution Phase / g	17.72	11.84
X100 in Aqueous Solution Phase / g	0.16	0.04
X100 in Micelles/ g	55.34	79.59
Total Partitioned X100	73.22	–
<i>Total Final Micellar Phase</i>	<i>69.53</i>	–

The partitioning of the emulsion highlights that in the standard blend, a considerable excess of surfactant is used above and beyond the amount which is needed to stabilise the emulsion, with a considerable proportion being present in the MMA layer and in micelles. The remainder of this chapter will discuss the effects of this excess surfactant on the properties of porous PMMA. However, already it can be observed that a considerable amount resides in the polymerisable monomer due to the similarity in solubility constants. In addition, approximately 7.86 % of the monomer in the standard formulation is found trapped in surfactant stabilised micelles. As polymerisation occurs in the larger monomer droplets, as is typical with suspension polymerisation, the monomer in micelles is not being used to form ligaments and, in this respect, is wasted.

Reducing surfactant concentration reduces the level of monomer in micelles. Changing the surfactant type would also change this as the aggregation number and number of MMA molecules in each surfactant micelle would change.

Similar studies were undertaken with Lutensol TO3, Lutensol TO6 and Lutensol TO109. The constants used in calculations and the final outputs are given in Tables 5.9 and 5.10 respectively.

Table 5.9: Constants for Lutensol surfactants

	Lutensol TO3	Lutensol TO6	Lutensol TO109
Saturation Concentrations	Value/ mol L ⁻¹	Value/ mol L ⁻¹	Value/ mol L ⁻¹
Concentration of water in MMA ^a , [water] _{MMA}	0.765	0.765	0.765
Concentration of MMA in water ^a , [MMA] _{water}	0.016	0.016	0.016
Concentration of MMA in water with surfactant present just below its CMC ^a [MMA] _{water+ Lut}	0.082	0.083	0.086
Concentration of surfactant in MMA ^b , [Lut] _{MMA}	0.6697	0.3145	0.540056
CMC of surfactant in water ^c , [Lut] _{water}	2.30E-04	3.30E-04	3.70E-04
CMC of surfactant in saturated with MMA) ^c [Lut] _{water+MMA}	5.50E-04	3.70E-04	4.60E-04
Additional Data	Values	Values	Values
Molar mass of MMA[160], RMM _{MMA}	100.12 g mol ⁻¹	100.12 g mol ⁻¹	100.12 g mol ⁻¹
Molar mass of water [161], RMM _{water}	18.02 g mol ⁻¹	18.02 g mol ⁻¹	18.02 g mol ⁻¹
Molar mass of surfactant [99], RMM _{xLut}	332 g mol ⁻¹	464 g mol ⁻¹	742 g mol ⁻¹
Density of MMA [162] ρ _{MMA}	0.94 g ml ⁻¹	0.94 g ml ⁻¹	0.94 g ml ⁻¹
Density of water at 25 °C [163] ρ _{water}	0.997 g ml ⁻¹	0.997 g ml ⁻¹	0.997 g ml ⁻¹
Density of surfactant [99] ρ _{Lut}	0.93 g ml ⁻¹	0.97 g ml ⁻¹	1.02 g ml ⁻¹
Surfactant micellular aggregation number[164], Ag _{Lut}	116	118	107
Molecules of MMA per surfactant micelle	128	128	128

^a Measured by GC, ^b Measured by R.I, ^c Measured by pendant drop analysis

The Lutensol surfactants were added to porous PMMA formulation at equal molar levels, therefore, Lutensol TO3 was added into the formulation at levels of 18.70 g, Lutensol TO6 at 26.25 g and Lutensol TO109 at 40.66 g.

Table 5.10: Output from partitioning calculations for Lutensol surfactants

Final Amounts in Phases After Partitioning:	Lutensol TO3		Lutensol TO6		Lutensol TO109	
	Mass / g	Concentration in Phase / wt%	Mass / g	Concentration in Phase / wt%	Mass / g	Concentration in Phase / wt%
MMA in MMA Solution Phase	137.52	97.18	137.13	97.83	136.87	96.31
MMA in Aqueous Solution	3.60	0.82	3.65	0.83	3.78	0.86
MMA in Micelles	5.54	24.97	5.89	18.98	6.02	13.90
<i>Total Partitioned MMA</i>	146.66	–	146.67	–	146.67	–
<i>Total Final MMA Phase</i>	141.51	–	140.17	–	142.11	–
Water in Aqueous Solution Phase / g	437.31	99.17	437.32	99.15	437.32	99.11
Water in MMA Solution Phase/ g	2.02	1.43	2.01	1.43	2.01	1.41
<i>Total Partitioned Water / g</i>	439.33	–	439.33	–	439.33	–
<i>Total Final Water Phase</i>	440.99	–	441.05	–	441.25	–
Surfactant in MMA Solution Phase / g	1.97	1.39	1.03	0.73	3.23	2.27
Surfactant in Aqueous Solution Phase / g	0.08	0.02	0.08	0.02	0.15	0.03
Surfactant in Micelles g	16.65	75.03	25.14	81.02	37.28	86.10
<i>Total Partitioned Surfactant</i>	18.70	–	26.25	–	40.66	–
<i>Total Final Micellar Phase</i>	22.19	–	31.03	–	43.30	–

Table 5.10 indicates that when the Lutensol surfactant range is utilised considerably less of the surfactant (0.73-2 wt %) resides in the MMA phase when compared with Triton X100 where approximately 12 wt % of the surfactant was found to be present. This suggests that the ligaments formed would be stronger in these materials, as less plasticisation by the

surfactant should be occurring. However, in the acquisition of these results two different techniques were employed: UV spectroscopy and RI. UV is a substantially more accurate method than refractometry in which human errors are greater. In addition, although the RI is sensitive, it requires a significant difference between the background level and that of the surfactant, i.e. a significant change in the refractive index must be observed between different surfactant concentrations. Calibrating the RI with Lutensol TO3 from a molar concentration of 0.02 mol dm^{-3} to 0.50 mol dm^{-3} changed the refractive index by only 0.005 units from 1.411 of water saturated MMA to 1.416 when 0.5 mol dm^{-3} of surfactant is present. Similarly, over the same range Lutensol TO109 changed the refractive index by 0.0003 and Lutensol TO6 by 0.012 units. Even between the three surfactants tested, the RI is shown to vary in sensitivity. This variation causes errors in the value obtained for the concentration of the surfactant in the MMA layer particularly when Lutensol TO109 is studied. Thus comparison between the data for Triton X100 and the Lutensol surfactants should be undertaken with caution.

Crucially, all the surfactants investigated are shown to be highly soluble in MMA with significant amounts of surfactant present in the MMA. The dissolution of the surfactant in MMA results in considerable plasticisation of porous PMMA ligaments which greatly reduces the mechanical strength of the materials. In addition, the emulsion partitioning results indicate that in the standard formulation, a considerable excess of surfactant is used above and beyond the amount which is needed to stabilise the emulsion, with a considerable proportion being present in the MMA droplets and in micelles. This work has been highly informative for the formation of porous PMMA with clear indications of the phases formed and the mechanism of formation of the ligaments. Three phases have been shown;

(i) The water phase, in which small amounts of monomer are dispersed. This phase is purely used to distribute the components evenly throughout the mixture and reduce the viscosity once the PMMA beads are added. It plays no part in the polymerisation process.

(ii) The monomer phase which was shown to be key in the formation of ligaments. The monomer phase contains considerable amount of dissolved surfactant which plasticises the ligaments once formed, hence weakening them when compared to PMMA made in a bulk polymerisation process. Therefore, the overall

polymerisation can be described as being most similar to a suspension polymerisation.

(iii) The micellular phase, comprising of MMA-swollen surfactant micelles. The calculations show that this phase contains a very small proportion of monomer compared to the other two phases.

5.3 Varying the Tail Group of the Surfactant

Throughout the research, a number of different surfactants have been used in the standard formulation given in Section 3.1.2. In this section two surfactants will be focused on, Triton X100 which is a octylphenol ethoxylate surfactant containing 11 ethylene oxide units (from NMR), and Lutensol TO109, a linear alkyl ethoxylate with an ethylene oxide chain length of 12 (from NMR). The structures of both are shown in Figure 5.9.



Figure 5.9: Structures of Lutensol TO109 and Triton X100 as derived from NMR

Both surfactants have similar EO lengths of 11-12 units but differ in tail group structure with Triton X100 having an aromatic ring present and Lutensol TO109 having a linear alkyl chain. Both surfactants were added to the blend formulation at a total weight percentage of 2.56 % for Triton X100 and 2.83 % for Lutensol TO109 to gain molar equivalents of surfactant. Once made, the blocks were sectioned (see Appendix 1 for the cutting plan) and tested for compressive performance, porosity, permeability and residual monomer. In addition, the T_g of the blocks was obtained from DSC data. The results are shown in Table 5.11.

Table 5.11: Comparison of materials made using Triton X100 and Lutensol TO109 as a surfactant (numbers in parenthesis are standard deviations)

Sample Name	Set Time/ Min	Compressive Properties				Porosity/ %	Permeability / Darcy	Residual Monomer /%	$T_g/ ^\circ\text{C}$
		Average Max Stress / MPa	Strain at Maximum Stress/ %	Transition Stress/ MPa	Bulk Modulus / MPa				
TX100 (0.5) (KA068)	21	17.33 (2.84)	14.36 (3.40)	9.92 (2.30)	254 (118.05)	30.60 (1.71)	3.19 (0.31)	5.76	111 (2.40)
LutTO109 (0.5) (KA086)	17	30.84 (3.25)	19.75 (2.45)	16.11 (2.44)	450 (55.40)	29.82 (1.11)	3.46 (0.378)	3.28	107 (2.56)

The results highlight a significant difference in the compressive properties of the materials with the linear alkyl chain ethoxylate Lutensol TO109 material far outperforming that from aryl-alkyl ethoxylate Triton X100 surfactant. The solubility of the DMPT may be different in the respective surfactants; however, if the MMA goes to 100% conversion, this factor becomes irrelevant. In addition, due to slight differences in molar mass of the surfactant the effective concentration of DMPT is slightly altered. If the concentration of DMPT changes, the rate of initiation is higher resulting in a lower molar mass. But molar mass studies indicated that the molar mass of the polymer is not critical unless very high. Thus the only explanation between the above materials is the solubility of the surfactant in PMMA.

Fernandez and Lebbanema looked at the solubilisation of monomers in surfactant micelles [165]. Solubility calculations (see Table 5.4) indicate that both surfactants are highly miscible with PMMA. However, Triton X100 is more miscible in PMMA ($\delta_{\text{X100}} - \delta_{\text{PMMA}} = 1.03$) than Lutensol TO109 ($\delta_{\text{X100}} - \delta_{\text{PMMA}} = 1.32$) and hence a higher proportion of the surfactant will reside in the polymer and thus is likely to plasticise the ligaments reducing their ability to withstand compressive forces. In addition, calculations undertaken when evaluating the partitioning of the emulsion using different surfactants indicate that only 2.27 wt% of Lutensol TO109 is present in the MMA layer. Comparably, 11.84 wt% of Triton X100 was found in the MMA layer. Higher levels of surfactant again increases the extent of plasticisation thereby further weakening the ligaments. Both factors result in Lutensol TO109 material being stronger in compression testing than Triton X100. No difference is observed in T_g which is dependent upon overall surfactant volume as the ligaments and PMMA beads gave one combined change in baseline.

An additional benefit to changing from an octyl phenol surfactant to a linear alkyl chain surfactant is to reduce the environmental impact, with particular reference to degradation products. Environmental agencies across the world have started to limit the use of octyl phenol dispersants due to their persistence in the environment and toxicity to aquatic life[166-167]. Triton X100 has been shown to have a significant resistance to oxidative degradation with a half life in excess of 60 days. In addition, it has the potential to degrade into even more hazardous substances, including octyl phenol[166]. Environmental agencies have, therefore, suggested limiting the use of octyl phenol surfactants, with the aim being to replace them entirely within the next few years. Linear alkyl chain ethoxylate surfactants, although more toxic initially, have little persistence in the environment and degrade into carbon dioxide, water and mineral salts and hence have little to no effect on aquatic organisms. This study indicates a straight swap would provide some benefit to the final properties of porous PMMA with little change to the production process being required.

5.4 Varying the Hydrophilic-Lipophilic Balance

The Hydrophilic-Lipophilic Balance (HLB) is a measure of the degree to which a surfactant is hydrophilic or lipophilic. Using the Griffin methodology, HLB is given by the ratio of molar mass of the hydrophilic portions of the molecule is divided by the total molar mass of the molecule multiplied by twenty[168].

$$HLB=20 \times \frac{M_h}{M}$$

A value between 0 and 20 is obtained, where less than 10 indicates a molecule which dissolves readily in oils (lipophilic) and anything greater than 10 is water soluble. A detergent usually has an HLB within the range 12-15[169].

To assess which surfactants form the best materials when included in the synthesis of porous PMMA, the Lutensol TOx range of surfactants was tested, for which the hydrophilic head group varies in term of the number of ethoxylate units (x) whilst the tail remains unchanged, based upon an iso-C₁₃ alcohol. The standard blend procedure was followed, adding surfactants at molar levels equal to Triton X100=36.61 g, 2.56 total wt %, 0.057 moles (see Appendix full data table).

The set time is denoted as the time it takes for polymerisation to reach a critical level so that the mixture solidifies in the baking tray observable by a rapid rise in temperature. As

the HLB increases, the set time was observed to decrease (see Figure 5.10). An rise in set time indicates that the viscosity of the mixture is increasing. A short set time, although desirable to reduce preparation time, can result in the trapping of air during the blend formation due to the rapid increase in viscosity, as shown by a rise in the permeability once the HLB exceeds 15 (see Figures 5.11 and Figure 5.12). Interestingly, porosity remains constant within the experimental errors.

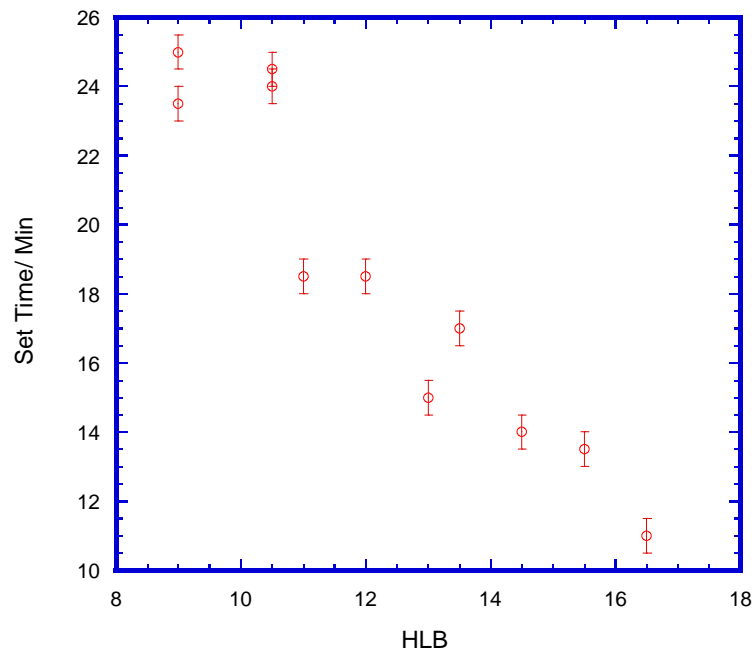


Figure 5.10: Effect of surfactant HLB on the set time of porous PMMA

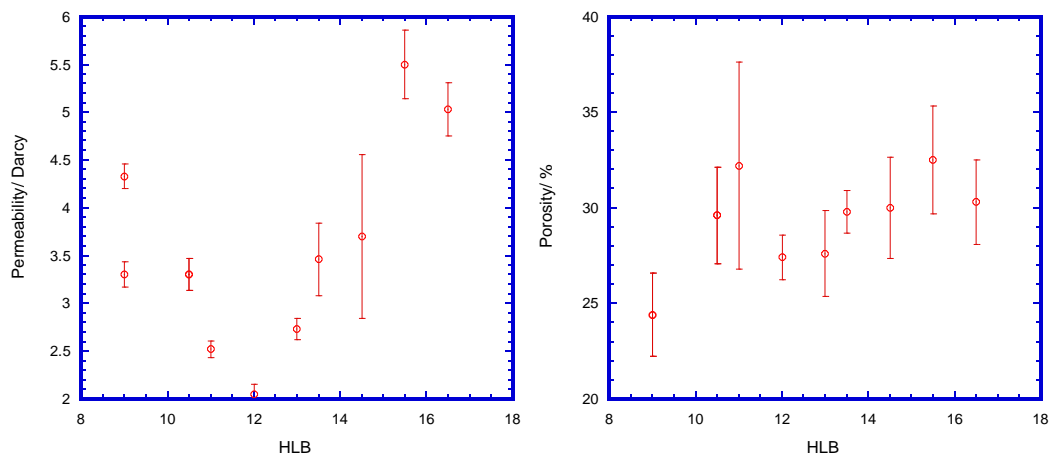


Figure 5.11: Effect of HLB on permeability and porosity

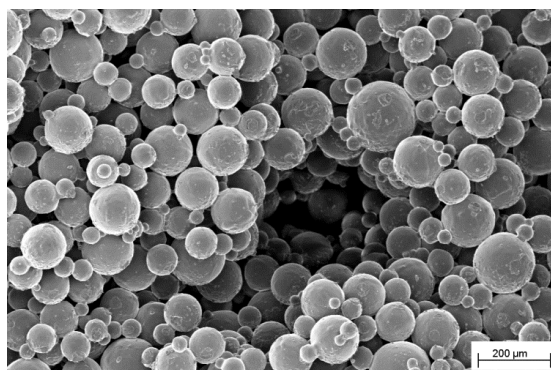


Figure 5.12: SEM image of void left by trapped air bubble for a materials made with Lutensol TO20

Incorporation of larger air voids due to the rise in viscosity forms weak materials in compression testing if greater than 12 ethylene oxide units are present in the surfactant. (see Figure 5.13). Cox studied similar linear alcohol ethoxylates and concluded that initially increasing the EO chain length reduces the viscosity of the fluid as the surfactant is solubilised by the water[152]. However, at high levels of EO content (>80 molar wt%), as found in Lutensol TO15 and Lutensol TO20, increasing the EO content increases the viscosity as considerable hydrogen-bonding occurs to water, therefore increasing the effective volume of the surfactant in the solution. This in turn is documented in other papers by Schonfeldt[170] and Mitchell et al.[171] where alternative ethoxylates were used and by comparison the length of the alkyl chain was studied. At the same EO level, increasing the alkyl chain increases the viscosity of a water/surfactant mixture. This is due to the hydrophobic nature of the alkyl chain[171]. Mitchell et al. also went on to document that at very low EO levels (chain length less than 5), the nature of the micelles changes from a spherical to a lamella structure; however, no evidence of this has been found in our studies.

Compression testing indicates that these air pockets create nucleation sites for the fracture of the materials from which cracks readily propagate through the PMMA ligaments (see Figure 5.13).

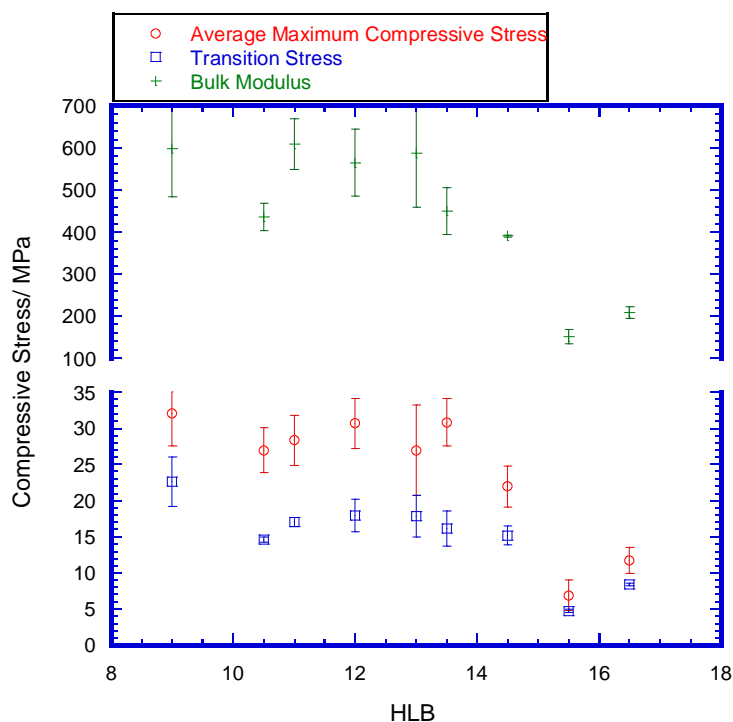


Figure 5.13: Effect of changing the HLB of the surfactant on the compressive properties of the materials

Little change is observed in residual monomer levels or T_g of the materials. Residual monomer is expected to be fairly constant in all the blends as all contained the same starting level of monomer and initiator and underwent the same post-polymerisation washing and drying processes. Therefore, it can be expected that the monomer was polymerised to the same extent and any residual monomer was either washed out in the preparation process or trapped in the beads. Similarly, as the levels of surfactant used are constant through, the T_g is unchanged with HLB.

In conclusion, the properties of the porous PMMA materials are comparable when a surfactant of HLB in the range 8-14 is used. If an ethylene oxide chain length of 12 is exceeded (HLB=15), a large rise in viscosity is observed resulting in a decrease in set time and apparent trapping of large air pockets in the blend mixture. Once set, the air pockets create large voids which act as nucleation sites and the materials collapse readily under compression.

5.5 Varying the Level of Surfactant

The partitioning studies revealed a considerable amount of excess surfactant is evident in the standard blend formulation. This section details work undertaken on varying the level of surfactant and the effects observed on the materials. As Triton X100 was the surfactant used in the formulation provided by Lucite International, Section 5.5.1 focuses solely on

this surfactant and its effects. Section 5.5.2 develops the study to include the Lutensol TO range of surfactants with specific focus on Lutensol TO3, Lutensol TO6 and Lutensol TO109.

5.5.1 Triton X100

Triton X100 is an octyl phenol ethoxylate used as the standard surfactant in the making of porous PMMA at levels of 5 %wt. The beads make up a considerable proportion of the total weight. In the standard blend formulation, the surfactant is at 50 wt% (73.22 g) when compare to monomer (146.66 g), significantly higher than required. The level of the surfactant was, therefore, lowered and the porous PMMA materials assessed with respect to compression performance, porosity, permeability and T_g (see Section 2.1 in Appendix 2 for a full results table).

Immediately, it was noticeable that as the level of surfactant was reduced from the standard formulation (5 wt%) to lower levels, a significant improvement was observed in compressive properties (see Figure 5.14). Figure 5.15 focuses on the average maximum compressive stress of the materials which can be shown to correlate to the fatigue performance of the materials with higher stress capability resulting in an increased number of cycles to failure. At lower surfactant levels, the material is more elastic with little change observed in either the height or the strain across the sample after 10,000 cycles. At higher Triton X100 levels, the materials are less elastic with considerable damage being evident after 10,000 cycles and a significant change in the shape of the block indicated by an increase in strain and loss of height.

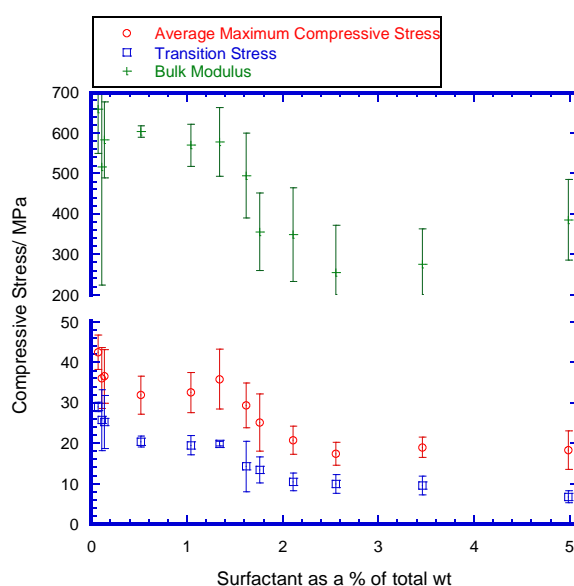


Figure 5.14: Effect of surfactant concentration as a percentage of the total wt on the compressive performance of porous PMMA

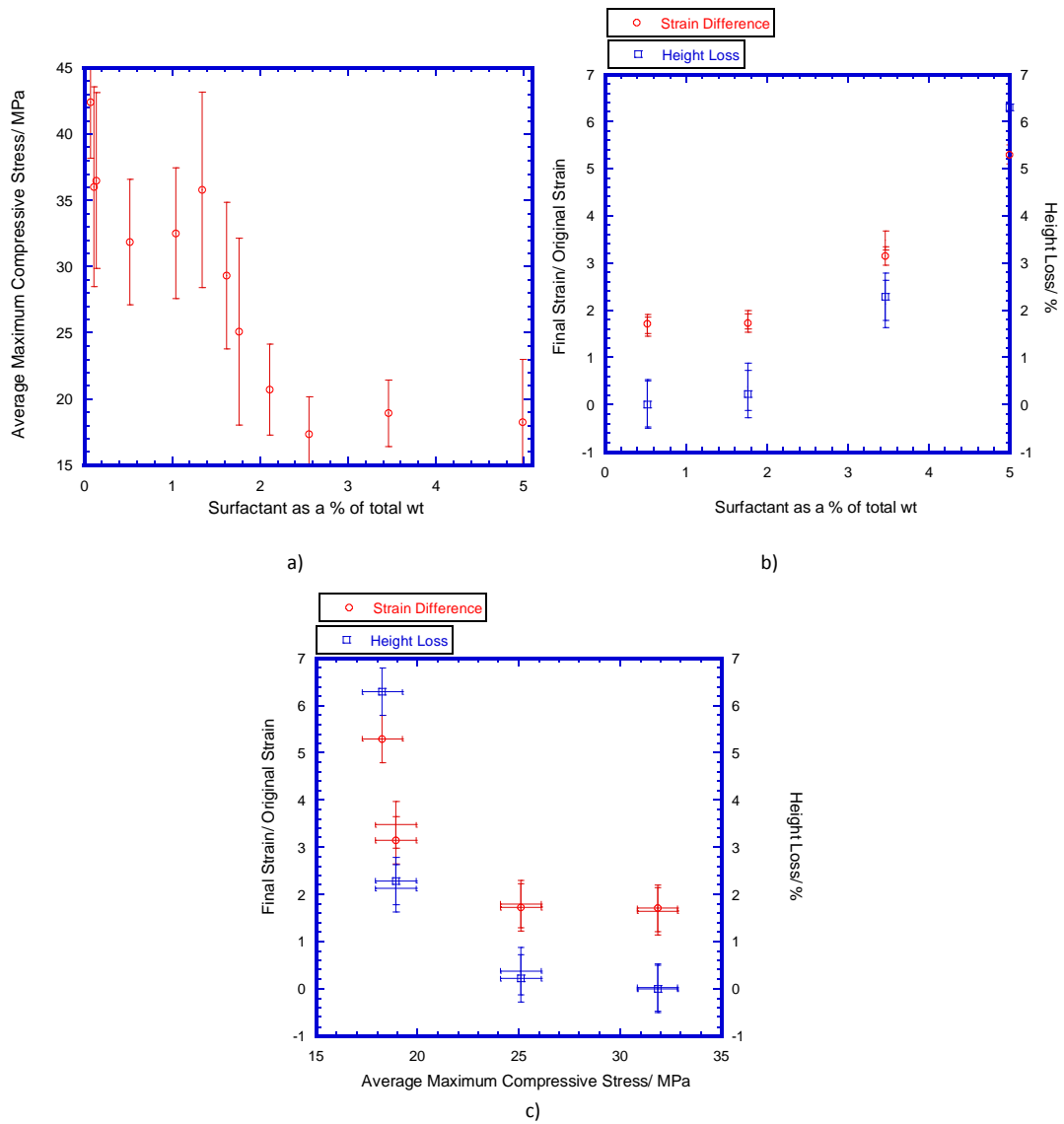


Figure 5.15: Effect of Triton X100 levels on the fatigue performance of porous PMMA showing a) effect on the average maximum compressive stress, b) strain difference and height loss after 10,000 cycles at 14 kN and c) the correlation of fatigue against compressive stress.

The correlation between surfactant level and average maximum compressive stress is not linear. In fact, the average maximum compressive stress is shown to be unchanging with surfactant concentration until levels of 1.34 total wt% are exceeded. In excess of this amount, a sharp decline is seen in performance until a level of 2.56 wt % is surpassed upon which a minimum level of performance is reached. This decline in compressive performance can be related to a drop in T_g (see Figure 5.16) whereby it can be concluded that the excess surfactant plasticises the ligaments which binds the beads together, therefore weakening the materials.

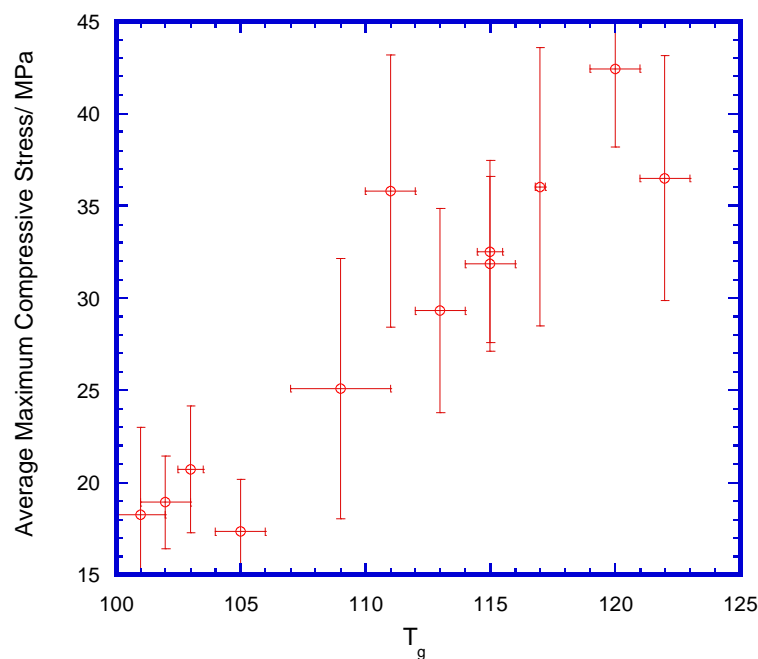


Figure 5.16: Effect of T_g as measured by DSC on average maximum compressive stress for materials made with Triton X100

Porosity and permeability are key factors in the making of porous PMMA with high levels of permeability being required to efficiently remove the excess water from the clay slip. Materials made with Triton X100 indicate that at high levels of surfactant the porosity and permeability are unchanged as the surfactant concentration is varied. However, at very low levels of surfactant the porosity is reduced by approximately 8 % from 29.60 % to 21.09 % and permeability is significantly reduced (see Figure 5.17). Observations made in the making of these materials indicate that at very low concentrations, the surfactant level is insufficient to stabilise the blend resulting in breaking of the emulsion which forces the water out of the materials resulting in a compaction of the material once agitation has ceased. This phase separation, although not affecting the polymerisation, significantly reduces the porosity of the porous PMMA resulting in a decline in the porous network, thereby reducing permeability. In turn, at very low surfactant levels the viscosity of the blend mixture rises rapidly within the stirring time, which although not problematic on a small scale, would limit the commercial scale-up of the formulation. The level of surfactant can, therefore, be significantly reduced from that of the current formulation. However, care must be taken to select a surfactant level which does not affect the pouring ability of the materials to ensure the reacting mixture can effectively fill the mould. No trend was observed on residual monomer concentration or set time as the level of surfactant was varied.

A considerable amount of literature has been published on the effects of plasticisers on polymers[105, 172-174]. The addition of plasticisers is particularly evident in melt extrusion processes to render improved flexibility at lower temperatures by softening the plastic e.g. in the manufacture of PVC without which the polymer is unprocessable[174]. In porous PMMA it is evident that excess Triton X100 acts as a plasticiser, reducing the T_g of the ligament material which in turn reduces the resistance of porous PMMA to cyclic loading at low stresses and reducing the ability to withstand high pressures in compressive testing.

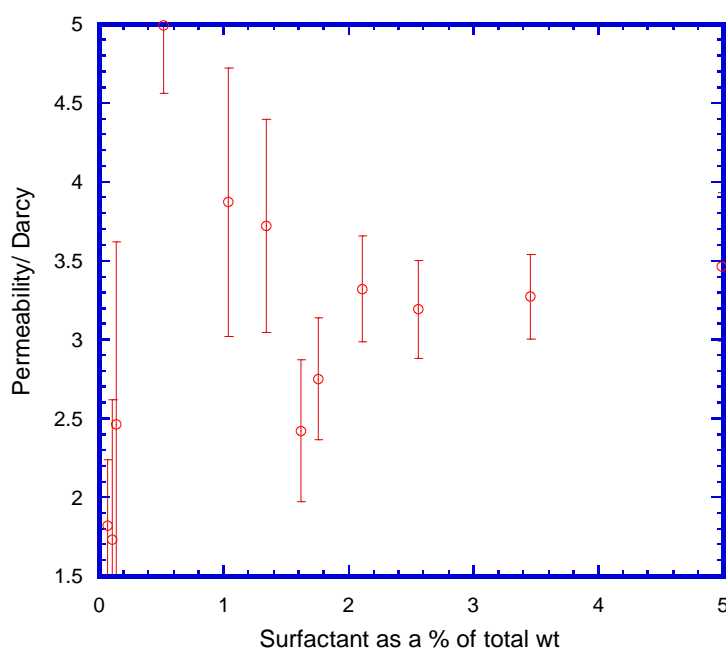


Figure 5.17: Effect of surfactant level on permeability

5.5.2 Lutensol TO Surfactant Range

In order to assess the effect on performance of surfactant on porous PMMA, the Triton X100 study was repeated on formulations using Lutensol TO3, Lutensol TO109 and Lutensol TO6. The surfactants have a tail group of $C_{13}H_{27}$, with varying EO lengths, where Lutensol TO3 nominally has 3 EO units, Lutensol TO6 has 6 EO units and Lutensol TO109 has 12 EO units, as shown in Figure 5.18 .

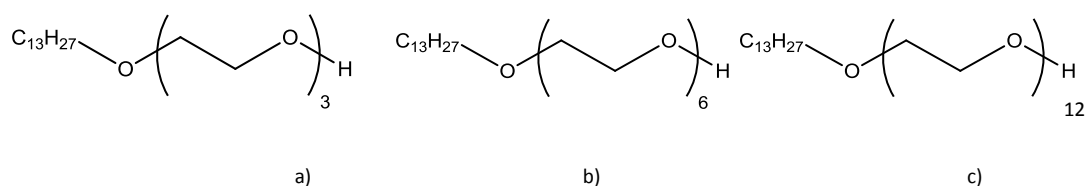


Figure 5.18: Structures of a) Lutensol TO3, b) TO6 and c) TO109 as derived from NMR (see Section 5.2.1)

For the purpose of analysis, the average maximum compressive properties of the materials will be focused on as a means of assessing the effect of the surfactant on the materials. A full data table for all the different levels used and surfactants is shown in Sections 2.3, 2.4 and 2.5 in the Appendix.

Figure 5.19 compares the reduction in compressive properties as the level of the surfactant is reduced.

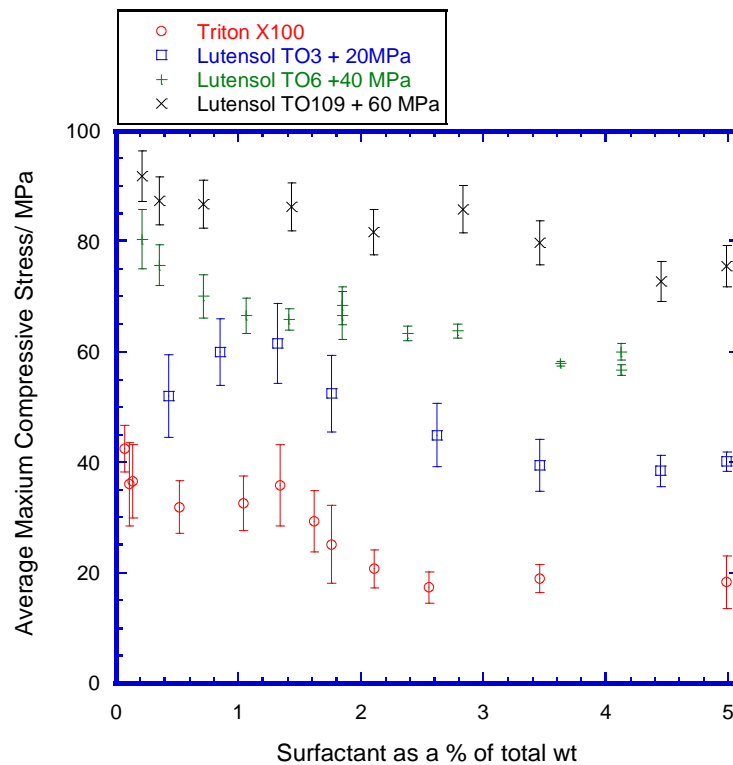


Figure 5.19: Effect of surfactant treat rate on average maximum compressive stress

Lutensol TO3 most closely mimics results seen using Triton X100 with little variation in compressive performance evident within the error margins of the test until a level of 1.5 wt% is exceeded. Above this, a measureable decrease is observed in compressive stress until a level of 3.5 wt % where the curve levels out. Lutensol TO6 does not show an initial plateau region with a reduction in compressive performance being evident from very low levels. Porous PMMA is less sensitive to changes in the level of Lutensol TO109 with the variation of compressive performance being significantly less over the range of the surfactant levels than the other surfactants. However, a decrease in the compressive stress is evident as the surfactant level is increased, albeit smaller than when alternative surfactants are used.

Figure 5.20 presents the results of fatigue testing where the level of surfactant is varied. Fatigue testing or dynamic loading aims to recreate the pressure cycles of the mould materials in the manufacture of ceramic artefacts. A standard pressure across a mould in the dewatering process is 40 bar. However, to differentiate between moulds on a shorter timescale, a pressure of 1400 bar has been used at a cyclic rate of 1 Hz for a maximum of 10,000 cycles. It can be observed that as the concentration of surfactant increases, the ability of the samples to withstand multiple cycles under compression decreases. This is shown by an increase in the loss of height of the test piece with samples at 5 wt% for both Lutensol TO109 and Lutensol TO3, which ultimately fails completely. The strain difference is also seen to increase as the wt% of surfactant to PMMA+MMA increases

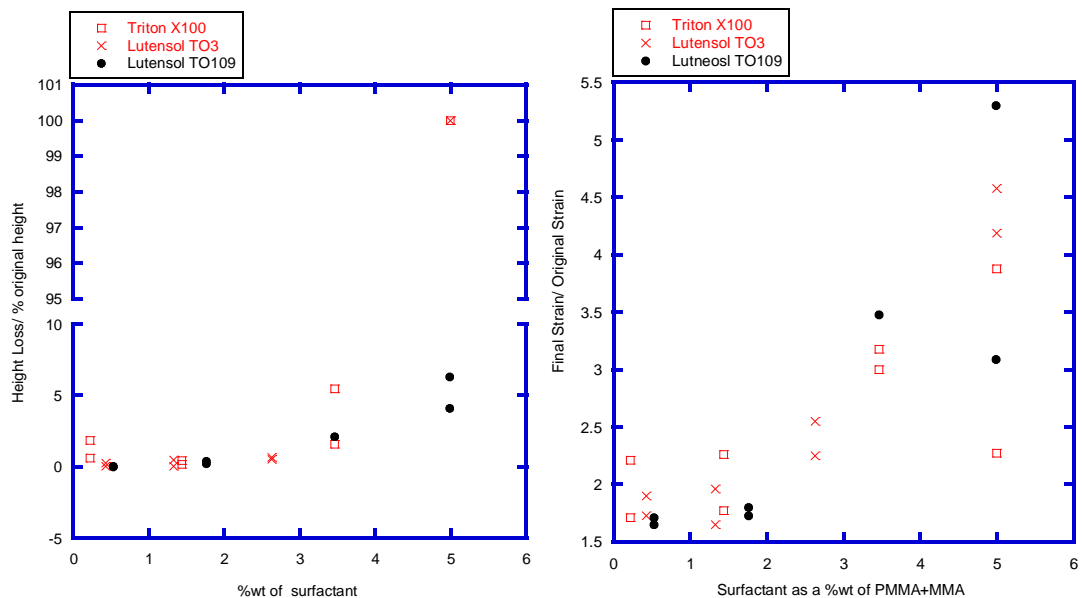


Figure 5.20: Fatigue results at 14 kN ± 2 kN varying the surfactant level for Triton X100, Lutensol TO109 and Lutensol TO3 showing a) height loss after 10,000 cycles and b) strain difference

Increasing the surfactant concentration has a direct effect on the glass transition temperature of the material, with a similar trend being reproduced in the comparison between surfactants, as can be seen from Figure 5.21.

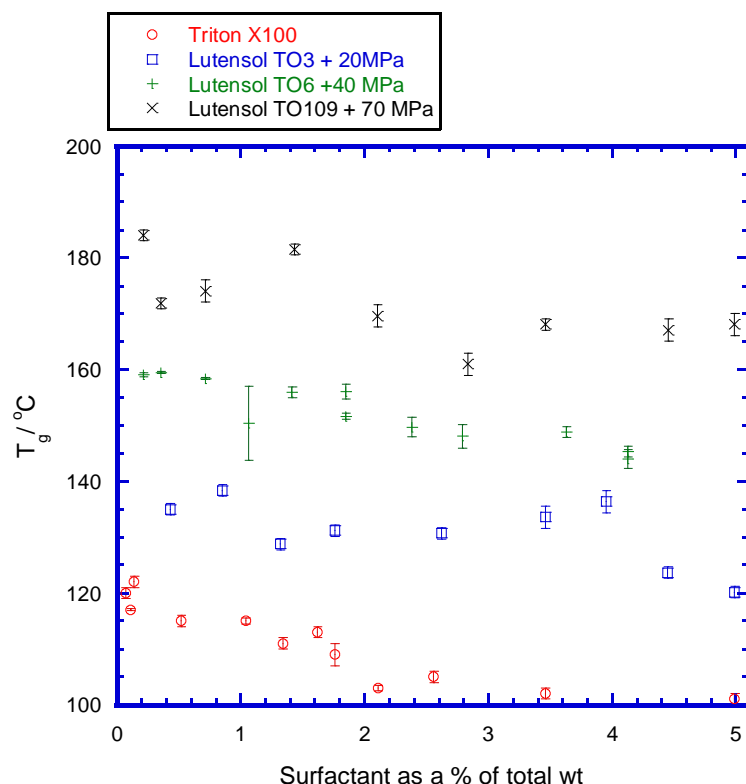


Figure 5.21: Effect of surfactant level on T_g

Small molecules have been used to change the flow properties of a polymer in melt extrusion processes[172] by lowering the melt viscosity, making fabrication more facile. In addition, plasticisers can be added to plastics to soften them by dissolving the polymer and lowering its glass transition temperature [105, 173, 175]. The lower the T_g of the plasticisers, the more effective it is at lowering the T_g of the polymer-plasticiser materials, as long as the solubility parameter is close to that of the polymer. At low concentrations, the reduction in glass transition temperature is an approximately linear function of the volume fraction of the two components. However, it has been observed that small amounts of plasticiser are more effective in lowering the T_g than amounts at higher concentrations, creating a curvature in the data. In turn, the surfactant can reach a solubility limit above which an additional amount of plasticiser is ineffective in the lowering of T_g [176].

Neilsen et al. observed that the addition of plasticisers was analogous to increasing temperature on the stress-strain curve with increasing plasticiser concentration reducing the modulus, yield stress and compressive strength [177]. Wu found similar results when polyol was used as a plasticiser in poly(vinyl alcohol) films with the elasticity of the material being increased, creating an elongation in plastic deformation as supposed to a brittle fracture[172].

The solubility parameters of the surfactants is given in Table 5.5 which indicates that all of the surfactants should be highly miscible with both MMA and PMMA. Therefore, the surfactant can be carried into the beads by the diffusion of MMA and in turn can dissolve in the polymer thereby reducing the overall T_g of the materials. Lutensol TO109 should be the least miscible with PMMA and MMA which may explain why the T_g is less affected by the surfactant. However, this would not help to explain the compressive results, see Appendix 2.6 for graphical split. It is thought that all the plasticisers would interact via intermolecular forces with the polymer chains which dilute and weaken the cohesive interactions in the PMMA matrix. This reduces the friction and entanglement of the PMMA molecules by increasing the free volume in the materials, as described by Ghebreemeskel in experiments using different solid active materials utilised throughout the pharmaceutical industry [178]. This implies that it is not only the miscibility which affects the ability of the surfactant to interact with the PMMA but also the viscosity, the molecular weight (or size) and the atoms present which will affect the chemical interactions, i.e. hydrogen, oxygen and nitrogen which lead to strong polar bonds.

Unlike Triton X100, no trend is observed in the permeability or the porosity of the porous PMMA with all the materials having an approximate porosity of 29.42 ± 1.81 % and permeability of 3.42 ± 0.67 Darcy. Comparing the permeability data, it is interesting to note that on average, samples made using Lutensol TO6 have on average a 36 % lower permeability than their TO3 or TO109 counterparts. However, within the margins of the test, no trend can be distinguished across the range of surfactant levels.

Overall it can be concluded that lowering the surfactant level significantly improves the properties of the porous PMMA mould by increasing the compressive performance and hence the fatigue life of the materials by reducing plasticisation with little to no difference in the permeability of the materials.

5.6 Anionic Surfactants

Throughout the literature non-ionic surfactants have been used exclusively in the making of porous PMMA. However, research undertaken at Manchester and discussed in previous sections indicates that non-ionic surfactants are soluble in both PMMA and MMA resulting in plasticisation of the ligaments. Plasticisation weakens the ligaments, therefore causing

premature failure in compressive testing. Reducing or eliminating the plasticisation should strengthen the materials.

Anionic surfactants have the benefit of being able to be used at lower levels than non-ionic surfactants and are insoluble in MMA, therefore plasticisation is unlikely to occur.

Two anionic surfactants were investigated for use in the preparation of porous PMMA, sodium dodecyl sulphate (SDS) and Disponil FES32 obtained from Congis and used as obtained (see Figure 5.22). The anionic surfactants have been substituted into the formulation for Triton X100 at an active content of 27.90 g (1.96 total wt %), 10.00 g (0.71 wt %) and 5.00 g (0.36 wt %) which has shown to be a key region for compressive properties in previous studies².

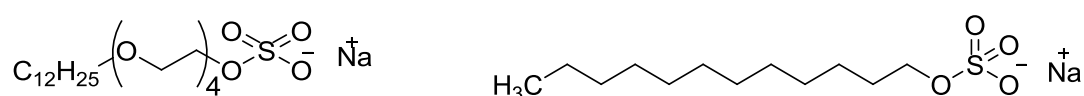
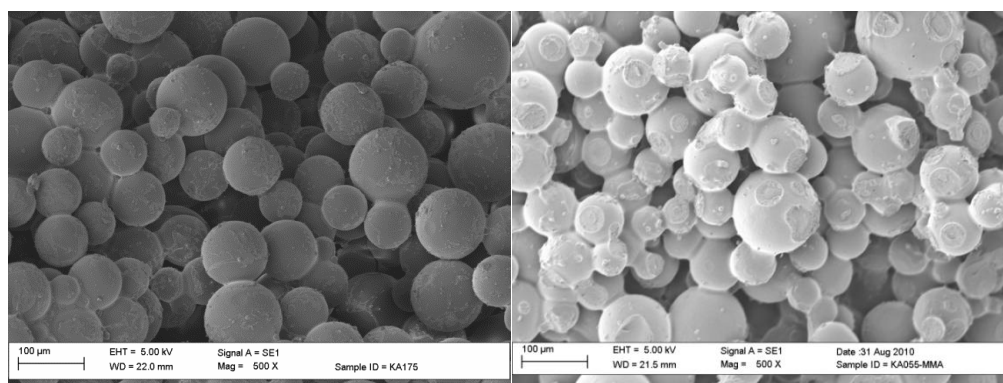


Figure 5.22: Structure of FES32 (derived from NMR, see Section 5.2.1) and SDS

At the higher levels of surfactant, foaming was observed on stirring which stopped upon addition of beads. All blends were very low in viscosity compared with the standard blend and took longer to set (approximately 30 minutes in comparison to 24 minutes). However, on trying to release the materials from the mould for washing after 12 hours in an oven at 60 °C, the materials crumbled. On further observation, little bonding had occurred between the beads, and they remained mostly unbound to adjacent beads (see Figure 5.23). No further testing could be undertaken on the materials.

² The treat rate of X100 in the standard blend formulation is 73.22 g (4.99 wt%)



a)

b)

Figure 5.23: SEMs of a) Disponil FES32 based materials and b) materials made using the standard formation

Sodium dodecyl sulphate (SDS) was tested at a surfactant level of 10.00 g (0.71 total wt %) to assess if this phenomenon was specific to Disponil FES32 or a general issue for anionic sulphate surfactants. The blend made using SDS was significantly lower in viscosity than the standard blend with a longer set time of 34 minutes. As with Disponil FES32, the block disintegrated back into its constituent beads when trying to release it from the mould after overnight heating at 60 °C.

Given that Disponil A1080 (the non ionic equivalent to Disponil FES32) gave materials with similar properties to those prepared with Lutensol TO109 (see Appendix 3), the suggestion is that it is the $\text{SO}_4^- \text{Na}^+$ moiety that is responsible for the low extent of polymerisation when Disponil FES32 is used. Lower levels of FES32 were, therefore, tried using similar to levels usually used in emulsion polymerisation (0-5 wt% monomer)[16]; see Table 5.12. Materials prepared using the equivalent levels of Triton X100 were tested for comparison (see Table 5.13).

Table 5.12: Results for lower concentrations of Disponil FES32 (numbers in parenthesis are standard deviations)

Sample Name	Total wt % surfactant	Set Time / Min	Compressive Properties				Porosity/ %	Permeability/ Darcy	Residual Monomer /%	$T_g / ^\circ\text{C}$
			Average Max Stress / MPa	Strain at Max Stress / %	Transition Stress/ MPa	Bulk Modulus / MPa				
FES32 0.93 (KA189)	0.07	46	31.93 (6.32)	20.48 (5.48)	16.57 (1.02)	536 (104.78)	29.12 (2.55)	5.28 (0.23)	6.31	112 (1)
FES32 1.55 (KA201)	0.11	37	10.67 (2.24)	6.64 (2.73)	9.55 (1.61)	248 (24.82)	31.68 (1.85)	5.62 (0.37)	5.62	117 (1)
FES32 1.99 (KA190)	0.14	>2hrs	14.07 (3.69)	14.28 (4.56)	14.82 (1.00)	358 (21.65)	30.87 (1.38)	5.59 (0.24)	9.05	110 (2)

Table 5.13: Results for the comparative Triton X100 study at low levels (numbers in parenthesis are standard deviations)

Sample Name	Total wt % surfactant	Set Time / Min	Compressive Properties				Porosity/ %	Permeability/ Darcy	Residual Monomer/ %	T _g / °C
			Average Max Stress / MPa	Strain at Max Stress / %	Transition Stress/ MPa	Bulk Modulus / MPa				
TX100 0.93 (KA199)	0.07	19.0	42.43 (4.25)	25.76 (6.60)	28.89 (1.14)	659 (109.20)	21.09 (2.26)	2.46 (1.16)	3.91	119 (1)
TX100 1.55 (KA202)	0.11	16.5	36.03 (7.54)	16.34 (2.29)	25.67 (7.50)	515 (290.92)	26.99 (1.91)	1.73 (0.89)	1.08	120 (1)
TX100 1.99 (KA200)	0.14	19.0	36.4 (6.64)	20.99 (6.55)	25.20 (6.60)	582 (94.08)	29.39 (4.76)	1.82 (0.42)	3.87	121. (1)
TX100 73.22 (KA055)	4.99	25.5	18.20 (4.73)	15.70 (2.72)	6.71 (1.46)	385 (166.90)	29.63 (3.33)	3.39 (0.55)	1.15	101 (1)

Comparing the two tables it can clearly be seen that at all weight percentages, the materials made with Triton X100 are superior to those made with Disponil FES32, although the porosity and permeability is significantly reduced when a surfactant level of 0.07 wt% was used when compared to the standard formulation (ca. 30 % porosity). The reduction in porosity can be explained by considering the phase separation which was evident as the blend was setting, during which the aqueous phase was forced to the surface. Phase separation observations indicate that at very low surfactant concentrations, the emulsion is unstable. In turn, the breakdown of the emulsion creates large voids that cause the large variation between blend samples tested, with high standard deviations being obtained.

Considering Disponil FES32 and DMPT in molar terms, at the lowest level of FES32 (0.07 wt%), 0.20×10^{-2} moles of surfactant are present in the formulation. Comparably, 1.08×10^{-2} moles of DMPT are also in the formulation. Assuming the Disponil FES32 surfactant reacts in a 1:1 molar ratio with DMPT, as the surfactant level increases more, DMPT is being consumed in a side reaction with the surfactant resulting in a lower effective concentration of DMPT. Reducing the effective DMPT concentration will result in a smaller molecular weight polymer in the PMMA ligaments which would in turn indicate a weaker ligament. In addition, the rate of the reaction will decrease as shown by the increase in set time shown in Table 5.12 where the set time is 46 minutes whereas that with Triton X100 at the same weight level (0.07 wt%) is 19 minutes. Increasing the mass of Disponil FES32 to >5 g increases the number of moles 1.08×10^{-2} which is equivalent to the moles of DMPT. At this level above, all of the DMPT is consumed thus any polymerisation of the MMA is purely due to the thermal initiation of BPO when the sample is put in the oven. This

explains why some polymerisation is observed in the initial samples however the majority of the monomer remains un-polymerised.

Although the anionic surfactant FES32 does not plasticise the surfactant through dissolution in the monomer, the T_g s are reduced from PMMA (120 °C). This is due to the high levels of residual monomer in excess of 5 %. This indicates incomplete polymerisation of the MMA in the blending process. A considerable amount of literature has been published on the diffusion of monomers into polymers, including extensive studies on the diffusion of MMA into PMMA. Although the papers differ on the mode of diffusion and whether it is controlled by Fick's law, all papers indicate that MMA will diffuse into PMMA which therefore reduces the T_g of the polymer [128-131, 179]. Significantly Hopfenberg, although using extreme measures, highlighted that the solubility of PMMA in MMA results in extreme plasticisation so much so that the sample being measured "dropped off the supporting hook"[179]. The plasticisation effect was directly related to the concentration of MMA by the equation

$$T_{g12} = \varphi_1 T_{g1} = (1 - \varphi_2) T_{g1}$$

where T_{g12} is the glass transition temperature of the plasticised film, T_{g1} is the glass transition temperature of the dry polymer, and φ_1 and φ_2 are the volume fractions for the polymer and monomer, respectively. Using this equation, it can be calculated that a 6 % level of residual monomer will give an approximate reduction of 7 °C in the T_g of the PMMA beads, similar to that observed experimentally.

Model polymerisations of MMA (49.10 g, 23.32 wt%) were performed in the presence of surfactant (active content 13.383 g, 6.36 wt%), water (147.13 g, 69.89 wt%) BPO (0.41g, 0.19 wt%) and DMPT (0.49 g, 0.23 wt%) to assess the extent of polymerisation in the presence of Triton X100 and FES32. Samples were removed periodically and monitored by gas chromatography for unreacted monomer and by precipitation, by weighing the dried precipitated product. The results are shown in Figure 5.24.

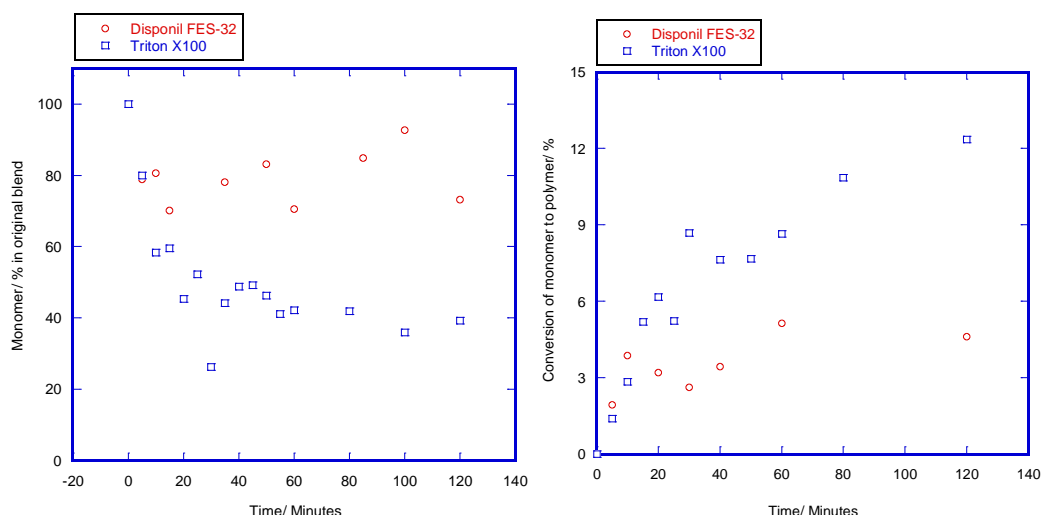


Figure 5.24: Extent of polymerisation of MMA using Triton X100 and FES-32 as a surfactant as monitored by a) GC b) precipitation

Overall, it can be seen that the reaction does not go to 100 % conversion for either surfactant, but the conversion attains substantially higher values with Triton X100 than with Disponil FES32. It is also interesting to note that all solutions containing FES32 had a purple colouration which was not observed when Triton X100 was used.

It is documented that conversion of aniline to an anilinium cation results in a blue shift in the UV spectra moving peaks from wavelengths of 251 nm and 299 nm closer to that of benzene at 203 nm and 254 nm[180] which may cause the discolouration evident in the blends. DMPT is known to be in its protonated form when in acidified water. Analysis of a simplified blend of DMPT, FES32 and MMA indicates that a large proportion of the DMPT is found in its protonated form trapped in the water layer. Some DMPT is evident in the MMA in its non-protonated form, albeit in much lower concentration than the control (see Figure 5.25).

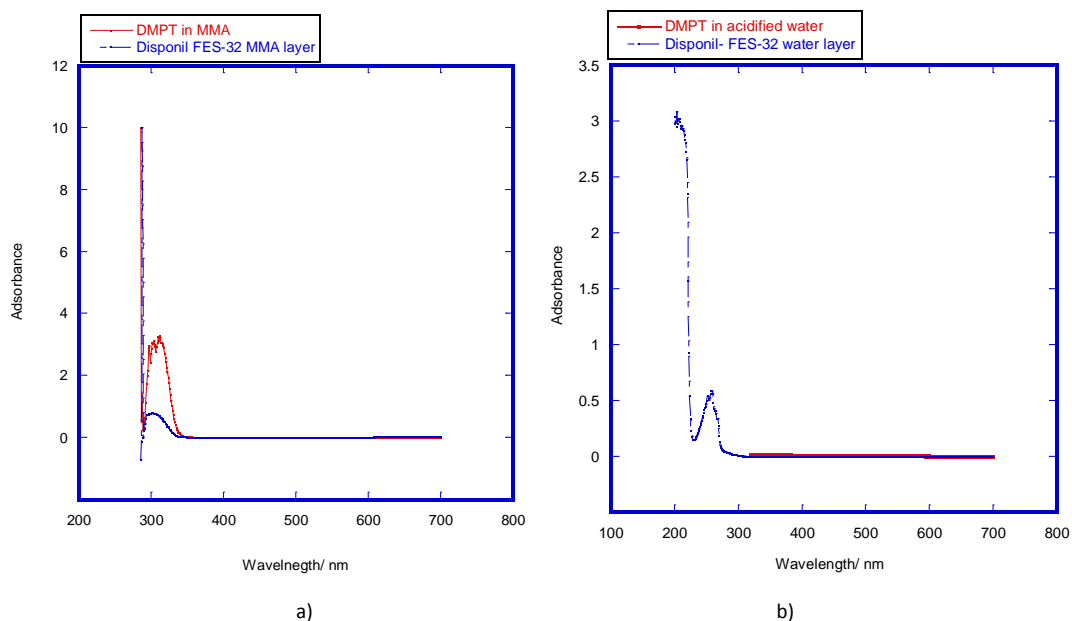


Figure 5.25: UV spectra of DMPT in a) the presence of FES32 (blue) against a control where no surfactant is present (red) and b) in the presence of FES32 in water (blue) and a control of acidified water (red)

For initiation to occur, the amine nitrogen in DMPT must donate an electron to the peroxide bond in benzoyl peroxide to create a free radical species (see Figure 5.26).

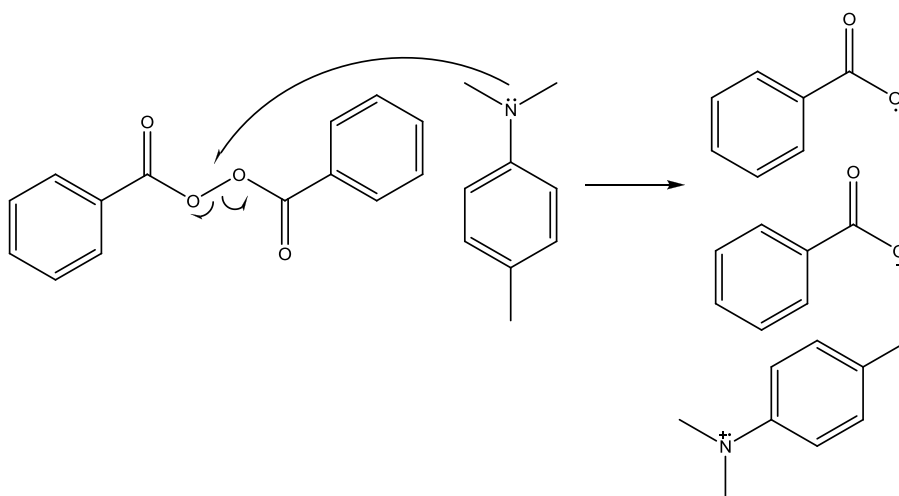


Figure 5.26: Mechanism for redox initiation of benzoyl peroxide with DMPT

However, in the presence of SO_4^- , the nitrogen of the DMPT becomes protonated, which stops the initiation reaction with peroxide as the nitrogen atom is no longer able to donate an electron to the peroxide bond (see Figure 5.27). This could simply be a counter-ion exchange where the tertiary ammonium ion from DMPT replaces Na^+ in the FES32 surfactant.

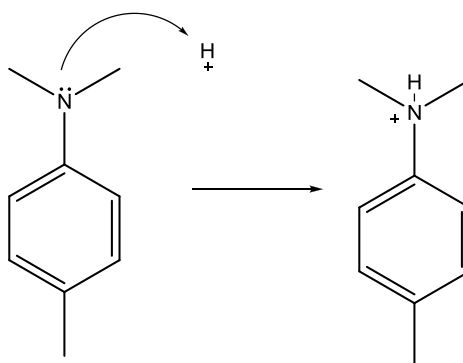


Figure 5.27: Protonation of DMPT in more acidic media

In the model polymerisation reaction, Disponil FES32 is at the level of 2.88×10^{-3} moles and DMPT at 3.64×10^{-3} moles. This indicated that all of the DMPT would have been consumed in the reaction with the surfactant hence no polymerisation is observed when Disponil FES32 is used as a surfactant.

In summary, the anionic surfactant could be used as a suitable substitute for Triton X100 in the blend procedure only when significantly lower levels were used. However, levels of residual monomer are significantly higher, which in turn causes plasticisation of the ligaments due to incomplete polymerisation. Alternatively, higher levels of DMPT could be utilised, to bring the molar level to above that of the surfactant thereby taking into account the side reaction. There is potential for a mixed surfactant system to be used in the preparation of porous PMMA, but this has not been explored in this work.

5.7 Effect of Surfactant on the Glass Transition Temperature (T_g)

Significant evidence has been collected on the effect of surfactants on the T_g of porous PMMA. However, both residual monomer and surfactant contribute to the reduction of T_g . This model study aimed to quantify the effect of just the surfactant for Triton X100, Lutensol TO109, Lutensol TO6 and Lutensol TO3.

PMMA beads (8.75 g) were dissolved in acetone (140.00 g) with varying amounts of surfactant (0 g, 0.11 g, 0.22 g, 0.44 g, 0.65 g and 0.88 g). The samples were dried in a vacuum oven and analysed by DSC (see Figure 5.28). The ratio of surfactant:beads is comparable to standard blends where the standard formulation has a mass ratio of surfactant: beads of 0.09.

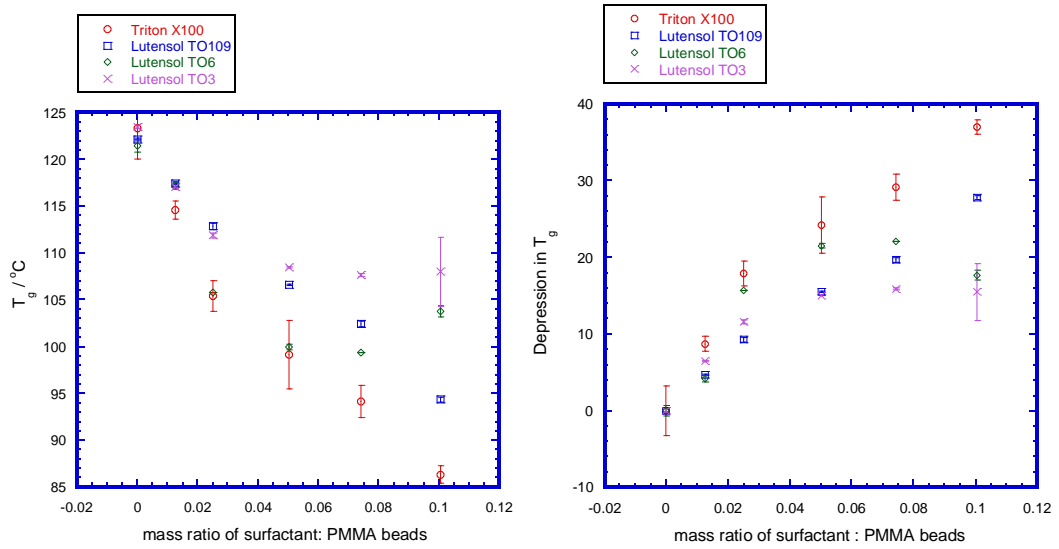


Figure 5.28: Depression of T_g as the concentration of surfactant increases

T_g is reduced most by Triton X100, followed by Lutensol TO109, both of which gave nominally linear reductions in T_g as the level of surfactant increased. However, the reduction in T_g diminishes as the amount of surfactant increases for Lutensol TO6 and Lutensol TO3.

Jenckel and Heusch demonstrated that a little as 10 % solvent could reduce the T_g of a polymer by up to 50 °C[181]. When plotting T_g against the weight fraction of the polymer, a convex curve was obtained in which as long as the T_g of the pure diluent is known (T_{gd}), the T_g of the plasticised polymer can be predicted using the equation derived by Gordon-Taylor [182] and Fox[183], (see Figure 5.29). Where, w_1 and w_2 are the weight fractions of the polymer and diluents respectively, T_{g1} is the glass transition temperature with respect to the polymer, T_{g2} the glass transition temperature of the diluents and k is the ratio of the changes in thermal expansion ($\Delta\alpha_2/\Delta\alpha_1$) or the change in heat capacity ($\Delta c_{p2}/\Delta c_{p1}$)[184]. Therefore, it is an adjustable parameter which can be derived from the fitting of experimental data[185].

$$T_g = \frac{w_1 T_{g1} + k w_2 T_{g2}}{(w_1 + k w_2)}$$

Kwei expanded the equation to include a second adjustable parameter q , to increase the flexibility of use, allowing for increased coverage to all polymer blend systems where 1 and 2 are two different components[186].

$$T_g = \frac{w_1 T_{g1} + k w_2 T_{g2}}{(w_1 + k w_2) + q w_1 w_2}$$

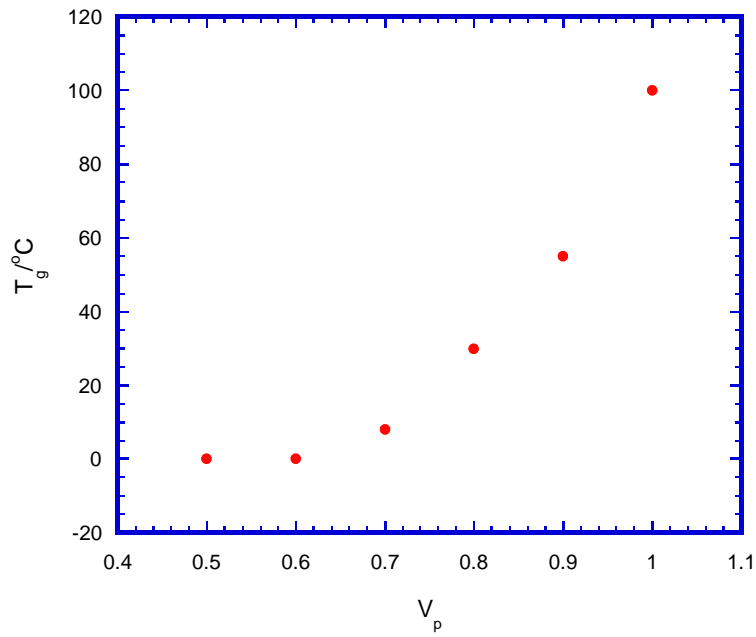


Figure 5.29: Effect of changing the volume fraction of the polymer (V_p) to solvent on the T_g of MMA [181]

Applying this theory to different volume fractions (V_p) of Triton X100 where the constants, $T_{g2} T_{g2} = -58.5$ °C and $k = 4.8 \times 10^{-4}$ K⁻¹ [187](see Figure 5.30).

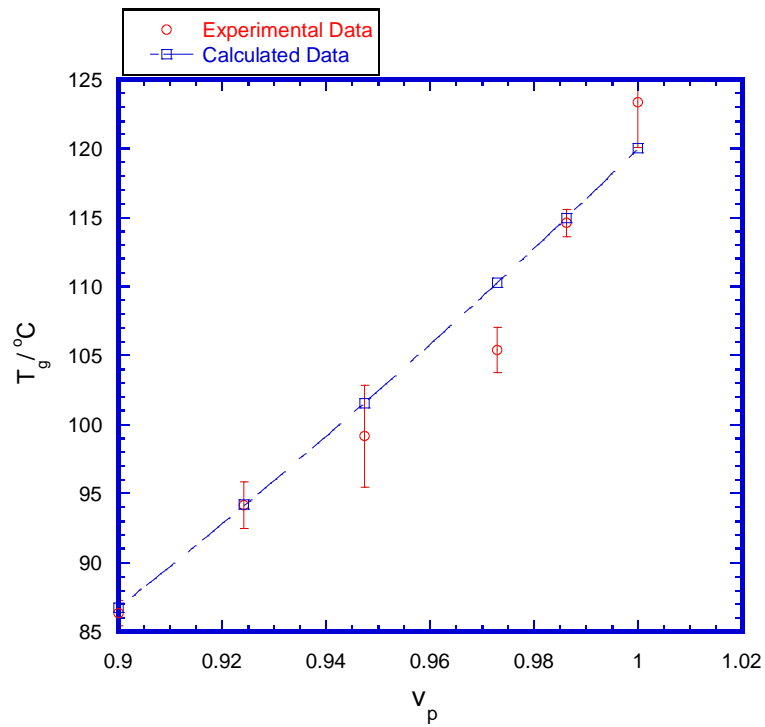


Figure 5.30: Comparison of experimental T_g s and calculated T_g at different volume fractions of PMMA

The theoretical calculation provides a linear relationship between T_g and the volume fraction of polymer, whereas the experimental data has a curvature, which is evident from Figure 5.30. The calculation does not take into account the effect of intermolecular forces, including hydrogen bonding or the chemical structure of the diluents with respect to the polymer. However, the calculation does allow for a rough estimate of T_g to be obtained and it can clearly be shown that even a small volume of plasticiser has a significant effect on the plasticisation of PMMA.

Solubility parameters were calculated using the group contribution method using values published by van Krevelen and are given in Table 5.5 [159]. The values indicate that all the surfactants should be miscible with PMMA. Plasticisation by the surfactant is evident by a decrease in T_g which can be linked to a decrease in the compressive properties of the materials, as shown in Figure 5.31.

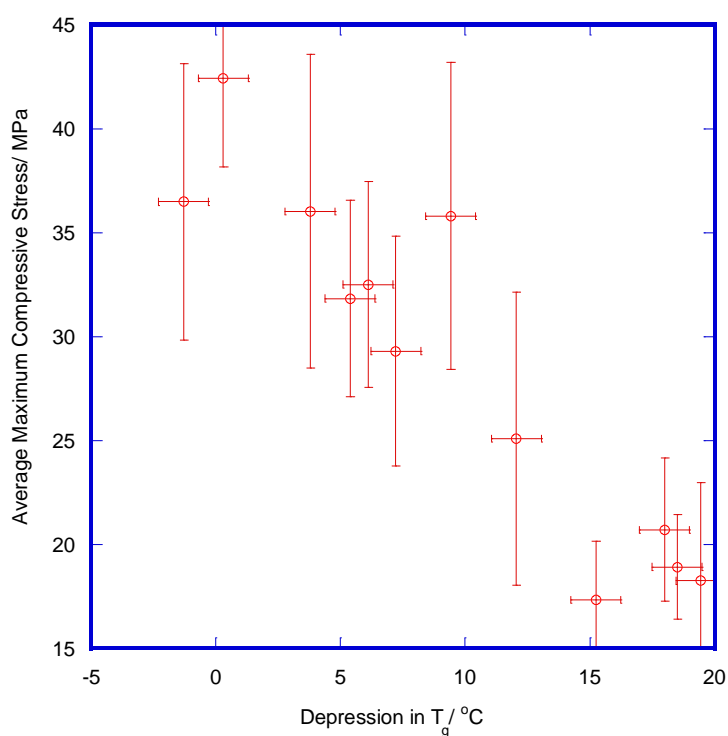


Figure 5.31: Effect of T_g on compressive properties for porous PMMA made using Triton X100

To assess the validity of the model, the T_g s from the model blend results were compared to T_g s obtained from porous PMMA materials made using Triton X100 (see Figure 5.32). The correlation between the model mixtures and the samples is good up to a mass ratio of surfactant:beads of 0.04. Above this level, significant deviation occurs where the model mixtures continue on a linear trend whereas the porous PMMA materials made using Triton X100 show a smaller reduction in T_g than predicted. This is not unexpected as only

some of the surfactant is in the PMMA beads. A small amount of surfactant will be lost, as shown in the work on partitioning of the emulsion and as is known from the observed loss of excess surfactant when washing the porous PMMA blocks during preparation of the materials. It is expected that these losses are more considerable at higher levels of surfactant, hence the deviation from the predicted model.

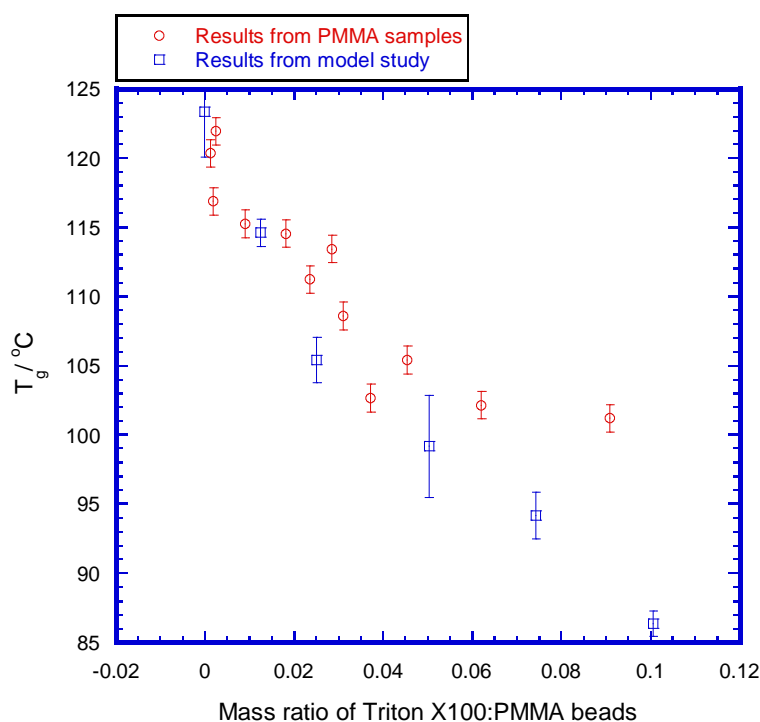


Figure 5.32: Comparison of model study to actual results obtained from PMMA samples

Linking this to the compressive data discussed above, decreasing the level of surfactant to the lowest possible levels in order to decrease plasticisation but ensuring levels stay above that required for a homogeneous emulsion which remains at a low viscosity throughout the mixing process should significantly improve the lifetime of porous PMMA moulds.

5.8 Summary

Porous PMMA materials are used in the pressure casting of sanitaryware. Current formulations are not competitive in the market when compared to gypsum due to the high material cost and start-up capital required to obtain the equipment. To justify the higher material cost, it is vital that porous PMMA is comparably stronger and can withstand more cycles, hence the higher mould cost can be spread over more ceramic articles, i.e more articles per mould unit. Throughout this work, the strength of ligaments has been found to

define the compressive properties of the material, with stronger ligaments resulting in more loading/unloading cycles. This chapter focussed on the effect of the surfactant with respect to the ligament strength and overall material properties.

Fundamental studies were undertaken to understand the partitioning of the emulsion. The results highlight that a considerable amount of the surfactant is found in the MMA layer and thus will end up in the PMMA ligaments resulting in plasticisation. Detailed calculations were made from simple inputs including: CMC of the surfactant in water, the concentration of MMA in water, the concentration of water in MMA, and the CMC of the surfactant in an MMA saturated solution. They enabled the amounts of the components in each phase to be derived. Thus, for any formulation, the actual level of MMA forming the ligaments can be found, and similarly the levels of surfactant can be tailored. This enables a prediction of the final properties of the porous PMMA materials to be obtained prior to making the materials, allowing for the screening of formulations, surfactants and inevitable reduction of waste. In particular, the studies highlighted the gross overuse of Triton X100 in the original formulation provided by Lucite International which in turn caused a weakening of the ligaments by plasticisation.

Three regions were found in the emulsion if the surfactant is above its CMC:

- An aqueous phases in which dissolved monomer and surfactant are present
- Monomer droplets containing some dissolved surfactant and water which are maintained in suspension by adsorbed surfactant
- Surfactant stabilised micelles in which a small amount of monomer is contained

Below the CMC, no micelles are present. In an ideal formulation, the surfactant levels are equal to the CMC thus no monomer is wasted in unused stabilised micelles.

Experimental work looked in detail at the level of non-ionic surfactants. They have been shown to readily plasticise porous PMMA materials due to a high solubility in both PMMA and MMA. The surfactant is readily dissolved by the MMA and transported into the beads, which it can then subsequently plasticise. This reduces the compressive properties of the materials, which has been shown to be a good guide to the fatigue behaviour. Current levels of surfactant (5 %wt) have been shown to be in vast excess of the required amount needed to obtain a low viscosity and homogenous mixture, so by reducing the surfactant concentration to 1 %wt, the performance of these porous PMMA materials improves. Most importantly excess surfactant was shown to plasticise the PMMA ligaments formed in

between the beads. Ligament plasticisation greatly reduced the compressive properties of porous PMMA reducing the number of cycles the material can withstand. This is particularly significant for industry where it is essential that porous PMMA materials undergo a large number of cycles to be economically competitive and efficient thereby allowing for the higher investment cost to be spread over the greatest number of artefacts.

In addition to the level of surfactant, the tail group and HLB of the surfactant has been investigated. Changing the tail group from an aromatic to an aliphatic carbon chain led to an improvement in the properties of porous PMMA. The defining property of the surfactant is its miscibility with PMMA. Triton X100 was shown to be highly miscible with PMMA with a difference in solubility parameter of $1.03 \text{ MPa}^{1/2}$. Lutensol TO109 was slightly less miscible ($1.32 \text{ MPa}^{1/2}$) thus plasticised the ligaments less resulting in stronger materials. In addition, the change to a linear chain ethoxylate would improve the environmental bearing of porous PMMA, creating a greener chemistry which upon degradation of the surfactant provides clean by-products.

Anionic surfactants, which are insoluble in MMA, were therefore investigated to stop the plasticisation effect. After initial difficulties in which the anionic surfactant was found to protonate the nitrogen in the DMPT, hence it was unable to donate electrons to the peroxide bond and initiate polymerisation, lower surfactant levels were tried. At very low levels, the molar fraction of DMPT is greater than that of the anionic surfactant enabling some DMPT to remain unprotonated and hence limited polymerisation occurs. The materials gave a significant improvement in properties compared to the standard blend, but dropping levels of Triton X100 to these very low levels also gave similar results. Therefore, it can be concluded that anionic surfactants at very low levels are a suitable substitute for Triton X100 with the benefit of creating a more stable emulsion at lower surfactant levels and keeping reasonable mixing viscosities. Alternatively, the level of DMPT can be increased to take into account this side reaction. As anionic and non-ionic surfactants are compatible, it may be possible to mix the two systems to create a more optimum surfactant formulation depending on the final properties required in the mould material.

Overall it was found that the miscibility of the surfactant with PMMA is the key parameter in determining the final properties of porous PMMA. The surfactant is also important in forming a stable emulsion and enabling the homogenous distribution of water and MMA. Using the predictions set out by the emulsion partitioning spreadsheet should enable the

screening of surfactants with different properties and ensure that the highest volume of MMA is present in the MMA phase to enable the greatest volume of ligaments to be made. In addition, choosing a surfactant which is not miscible with PMMA should reduce plasticisation resulting in stronger materials.

6. Varying the Monomer to Water Concentration

6.1 Introduction

Early investigations indicated that the ligaments between the beads control the compressive properties of porous PMMA. By varying the size, volume and construction of the ligaments, it should be feasible to accurately control the properties of the material.

Hoey and Taylor compared the fatigue crack behaviour between acrylic glass and bone cement[126], where acrylic glass is made using bulk polymerisation of MMA and bone cement is the bulk polymerisation of MMA around PMMA beads. In the micrographs they observed that fatigue cracks propagate around the preformed PMMA beads, indicated by an irregular path shown in Figure 6.1, implying that the mechanical properties of porous PMMA depend strongly on the polymer in the ligaments between beads rather than properties of the beads themselves.

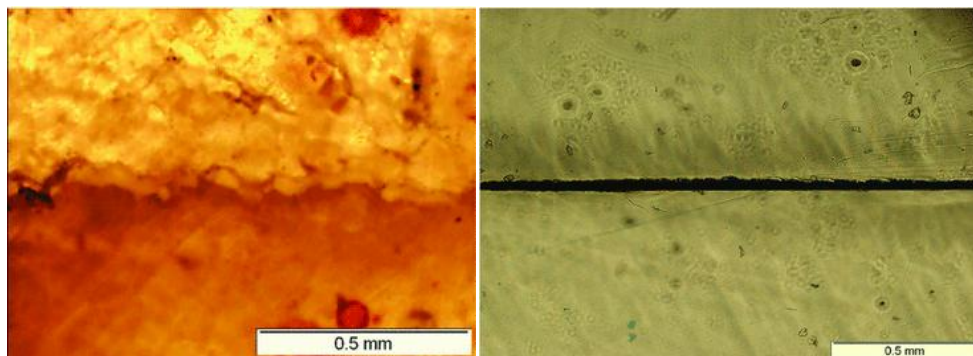


Figure 6.1: Micrographs of fatigue crack paths in bone cement (on the left) and acrylic glass (on the right).
Taken from Hoey and Taylor[188]

Therefore increasing the amount of monomer should, in theory, increase the volume of the ligaments, thereby producing stronger materials.

The following chapter discusses experimental work undertaken on varying the MMA:water ratio. Previous research by Ergun et al varied the water and surfactant content between 30-40 % of the overall weight of the mixture, whilst keeping the surfactant:water mass ratio constant at 1:3[82]. Their results highlighted that increasing the water/surfactant content increased the porosity and permeability of the samples as measured from SEM images of polished specimens and using an in-house permeability apparatus. The same results were released in a 2004 paper[2], where the authors reported that the macroporous structure was defined by the water droplets within the emulsion stage of the

reaction where again water is observed to be the key driver in the formation of porosity and permeability[2]. A patent written in 1966 reported that the amount of water added is of considerable importance in the production of porous PMMA. The patent states that levels ranging from 45-95% by volume changed the nature of the materials from foam-like materials with isolated non-intercommunicating pores at low water percentages to sponge-like materials with intercommunicating pores at high water concentrations[77].

As part of the project developing the understanding into porous PMMA materials, the monomer:water concentration was varied to clarify and aid interpretation of the above observations.

6.2 Varying the MMA:Water Ratio with Triton X100

Initially the level of MMA was increased in the formulation from 8.74 wt % to 12.01 wt % where the mass level of water was fixed and the MMA:bead mass ratio kept constant at 0.182. The results indicate that increasing the MMA concentration with respect to water increases the compressive performance of the porous PMMA materials; see Figure 6.2. For the full set of results see Appendix 2.7.

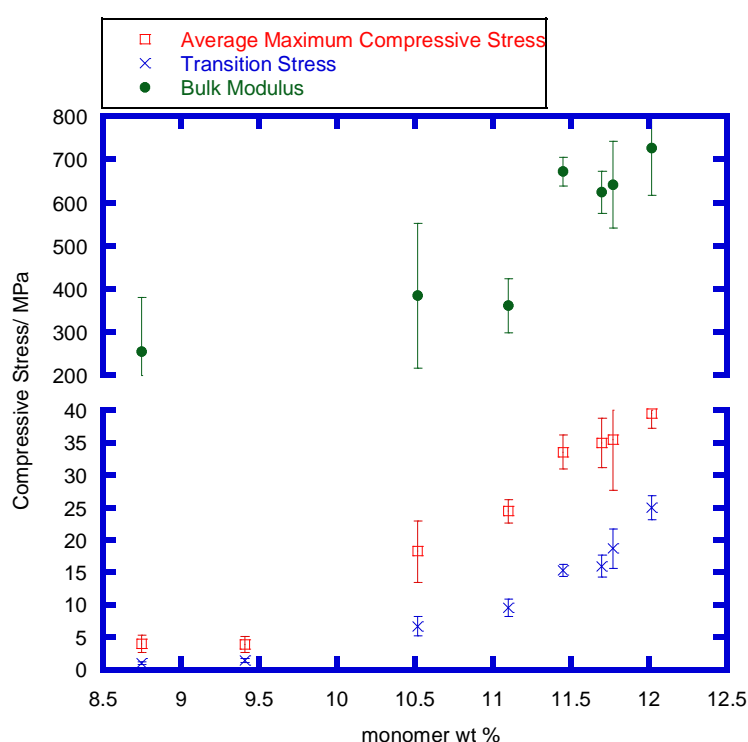


Figure 6.2: Effect of increasing the monomer %wt on the compressive properties of porous PMMA

Figure 6.2 indicates that as the volume of MMA increases in the formulation, the more stress the material can withstand before failure. SEM images (see Figure 6.3) identify the

formation of thicker ligaments between the beads, resulting in a higher overall ligament volume. Assuming all other parameters are equal, in this case the observation of thicker ligaments indicates a greater volume of PMMA material being formed, which would require more energy to break and lead to stronger materials.

However, introducing higher levels of MMA decreases the porosity and permeability of the material (see Figure 6.4). Using calculations detailed in Section 2.1.1, the close packing of beads with the same diameter with no additional materials gave a theoretical maximum porosity of 37 %. The porosity and permeability are key factors in the formulation of porous PMMA to allow for the drainage of water from the clay slip. If the permeability is reduced, the time for the removal of water from the clay slip is lengthened and the pressures within the mould are increased. This results in longer drying times, reducing the efficiency of the process. In addition, large pressures can build up inside the mould, which if too great can lead to failure of the mould. Therefore, reduction in open porosity and permeability can be viewed as detrimental to the properties of porous PMMA.

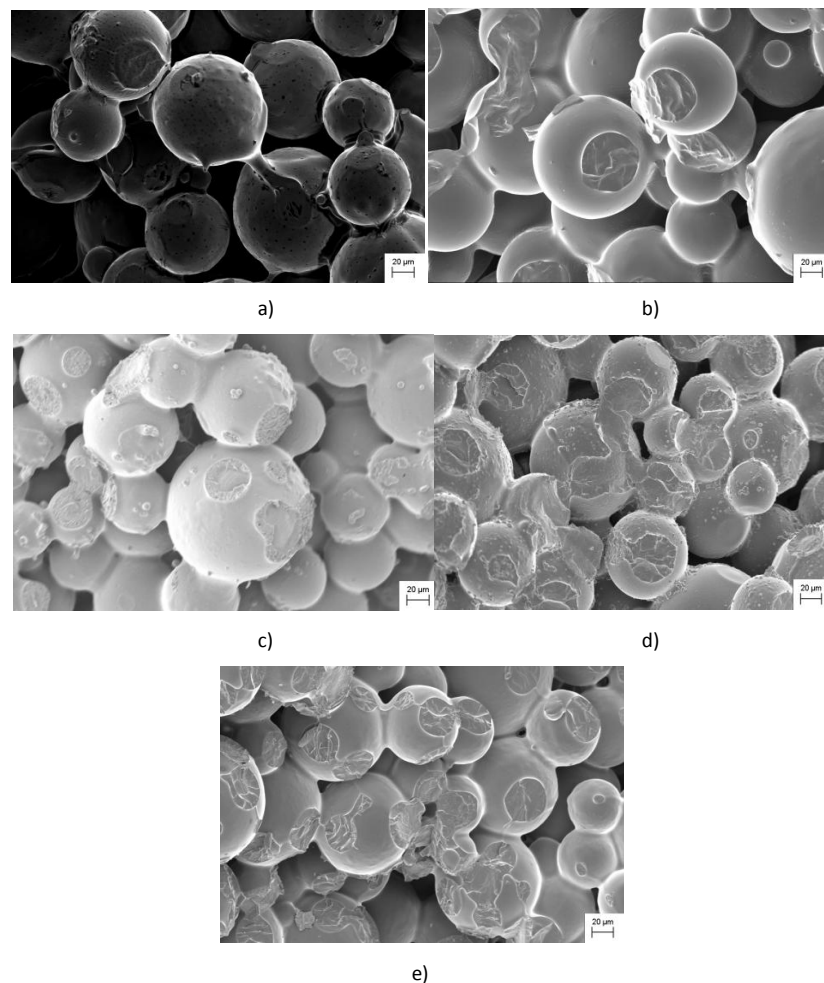


Figure 6.3: SEM images for materials made with a) 8.75 b) 9.41 c) 10.52 d) 11.10 e) 12.02 monomer %wt of the total mass of components

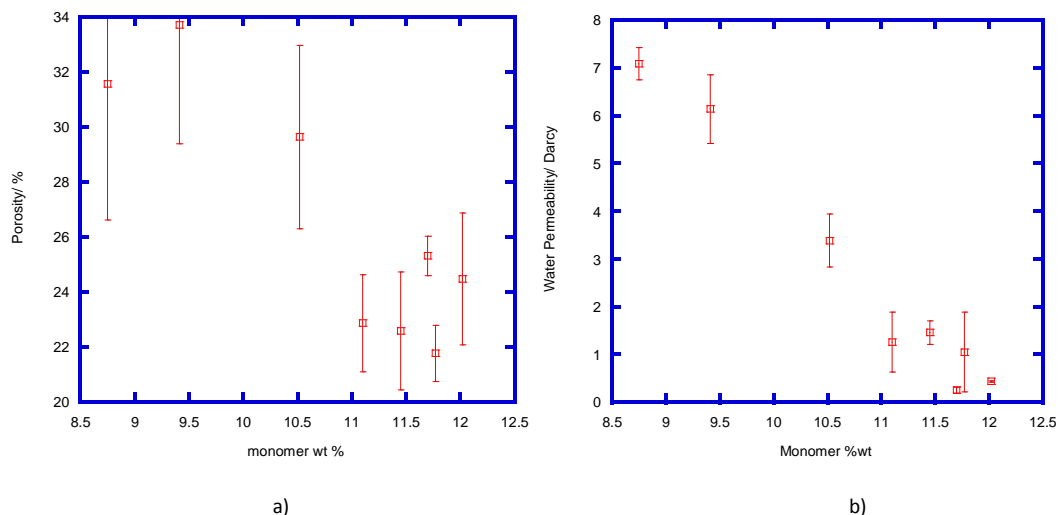


Figure 6.4: Effect of monomer level on a) porosity and b) permeability

As the amount of MMA increases the set time lengthens, see Figure 6.5. This is due in part to a volume effect, with larger volumes of MMA taking longer to completely polymerise. In addition, as the level of DMPT in the formulation was unchanged from that of the standard (1.44 g), there is effectively less DMPT in the mixture as the concentration of MMA increases, hence decreasing the effective concentration of DMPT. As the rate of polymerisation is dependent upon the concentration of initiator to the power one half, this effectively means the set time is increased.

$$R_p \propto [I]^{1/2}$$

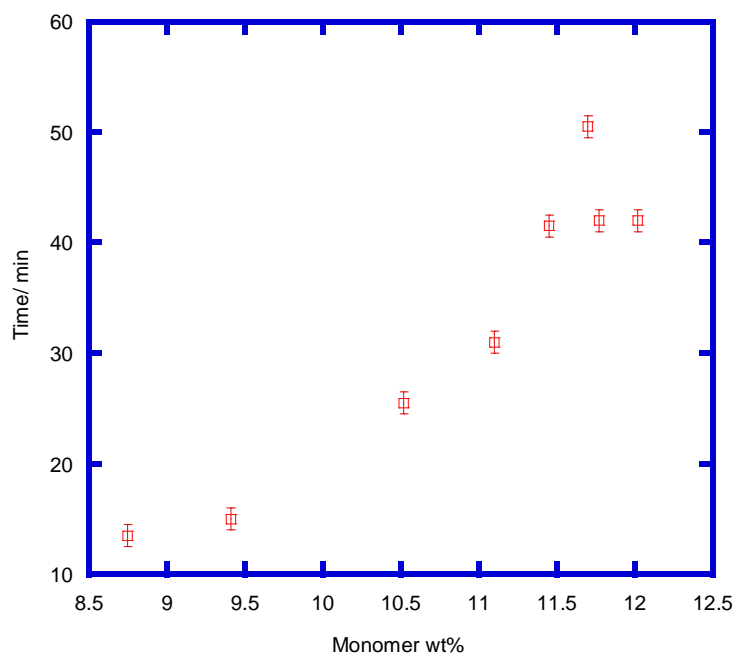


Figure 6.5: Amount of MMA and its effect on set time

6.3 Varying the MMA:Water Ratio with Lutensol TO3 and Lutensol TO109

Similar studies were undertaken with Lutensol TO3 and Lutensol TO109 as surfactants using the same wt % of surfactant. The materials had similar compressive properties (see Figure 6.6) and permeability (see Figure 6.7). Structural details for these surfactants can be found in Section 5.

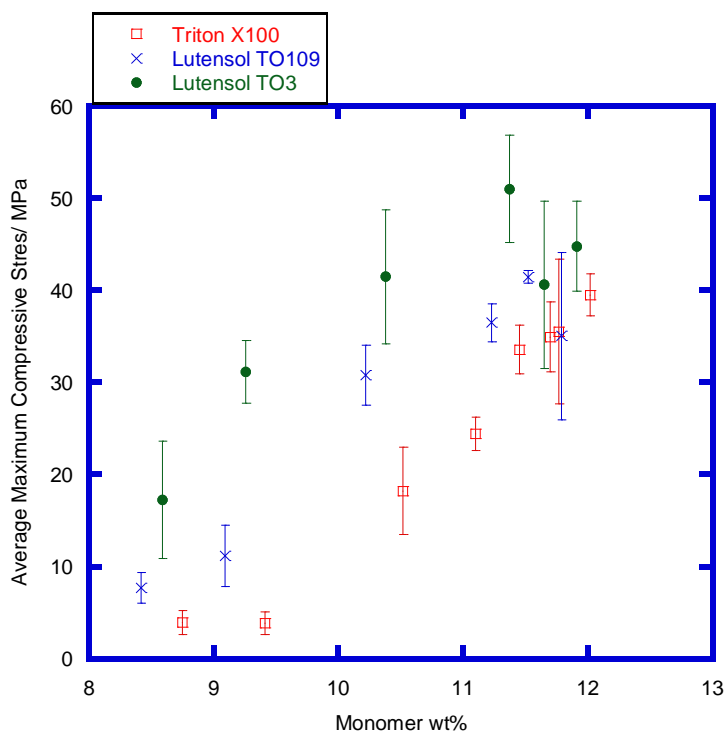


Figure 6.6: Effect of changing the monomer wt% compared to the total wt % of components on the average maximum compressive stress with Lutensol TO109, Lutensol TO3 and Triton X100

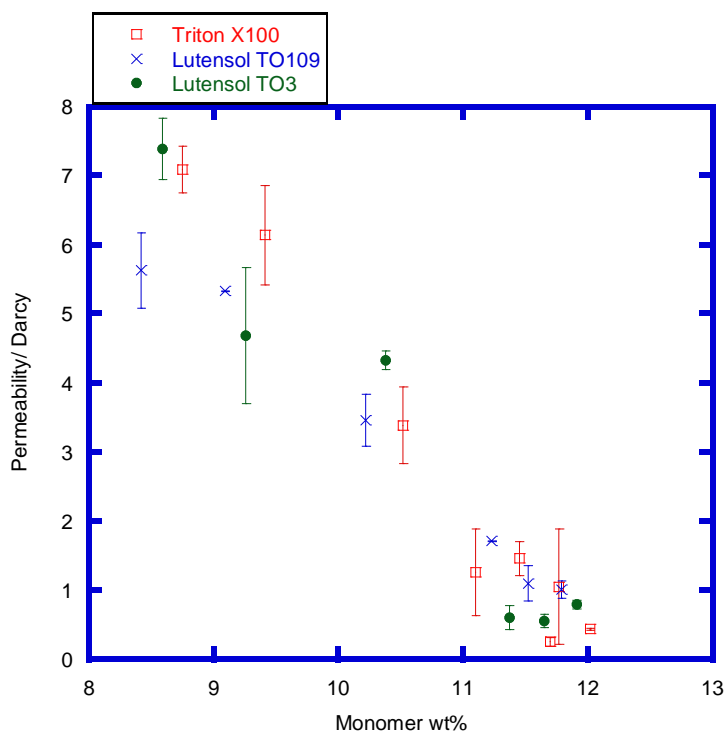


Figure 6.7: Effect of changing the wt % of monomer compared to the total wt % of components on the permeability for Triton X100, Lutensol TO109 and Lutensol TO3

As observed in Chapter 5, slightly different compressive results are obtained at each monomer level, due to structural differences in the surfactant which alter the CMC and the solubility in MMA and PMMA. However, the overall trend of increasing compressive performance with MMA level remains unchanged.

SEM images obtained of the materials made with Lutensol TO3 and Lutensol TO109 are shown in Figures 6.8 and 6.9 respectively. The images clearly show a narrowing of the pore channels between beads as the MMA level increases which is consistent with the results gained where Triton 100 is used as a surfactant.

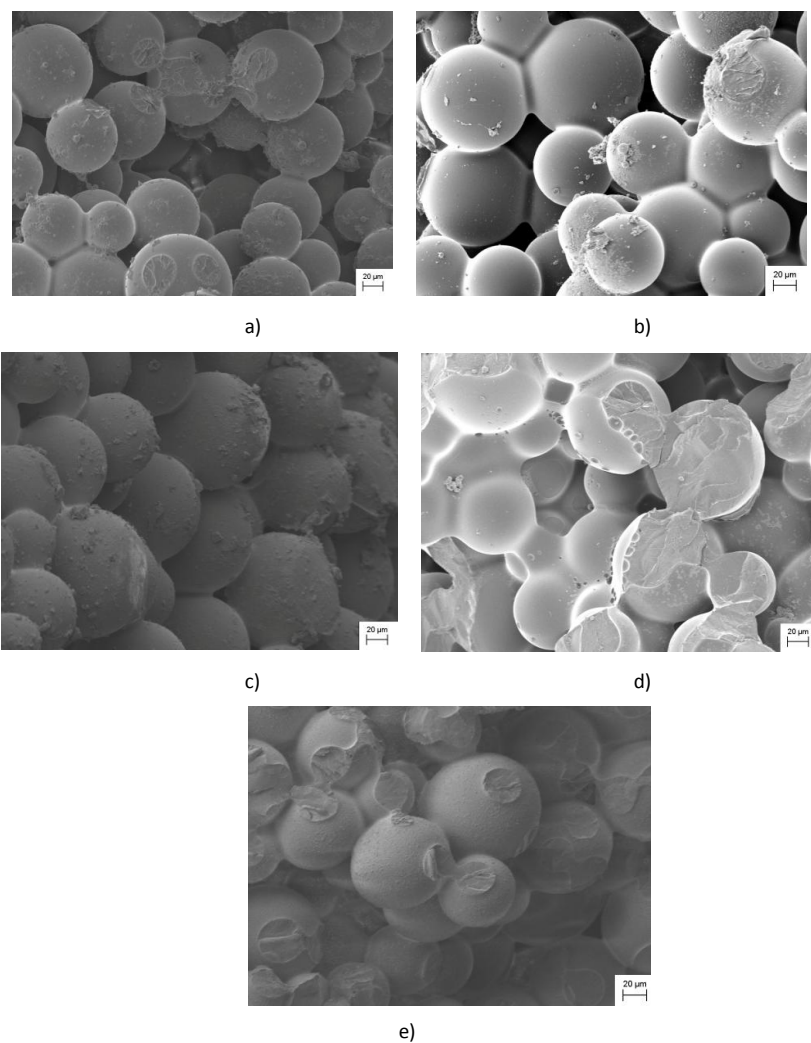


Figure 6.8: SEM images for materials made with Lutensol TO3 using a)8.59 b)10.38 c)11.37 d)11.65 e)11.91 monomer wt% compared to the total wt % of components

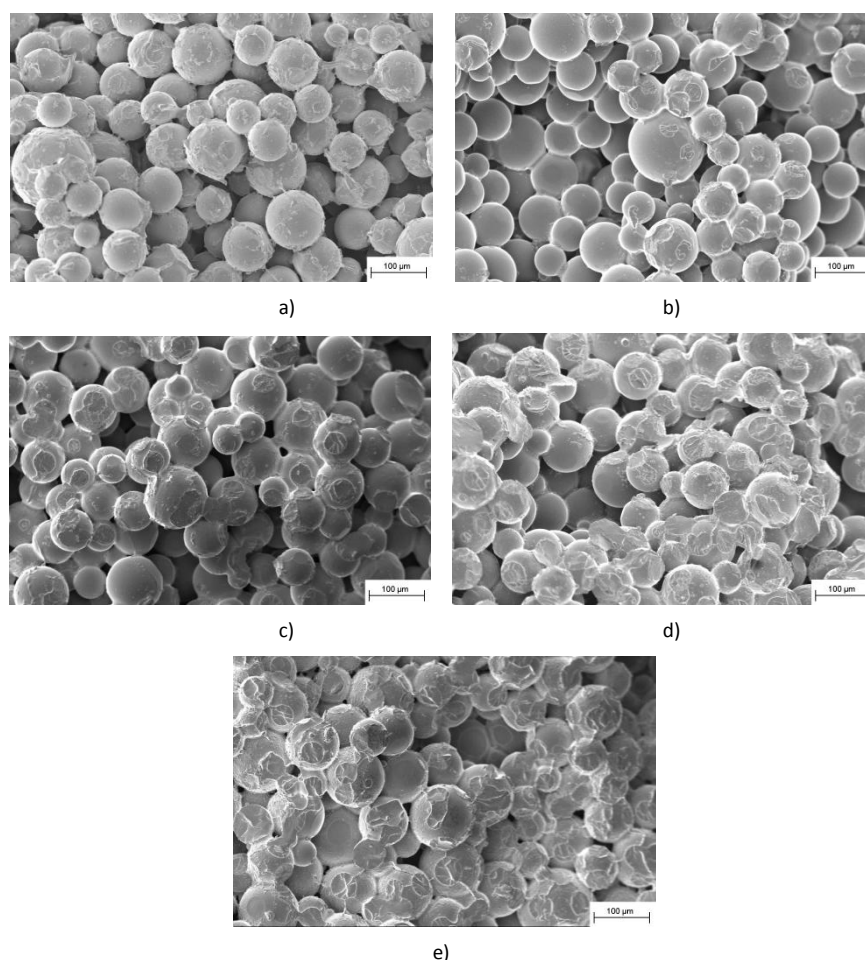


Figure 6.9: SEM images for materials made with Lutensol TO109 using a)8.42 b)9.09 c)11.23 d)11.52 e)11.79 wt % of monomer compared to the total wt % of components

Fatigue measurements undertaken on selected samples of porous PMMA are shown in Figure 6.8 for samples made with Lutensol TO3 and Triton X100 surfactants at different weight percentages of MMA to the total weight of components. Materials made with low levels of monomer were observed to deform readily whilst under stresses of 14 kN, which is particularly evident for the material made using 9.25 wt % MMA with Triton X100, which fails catastrophically after 900 cycles. The same materials made with the equivalent levels of MMA and Lutensol TO3 do not fail completely, although significant changes in the structure are observed, namely compacting and bulging, resulting in an overall height loss and increased strain across the material. The results reinforce previous observations that the results of compression testing are a good indicator as to how the materials will perform under cyclic loading of 14 kN. As observed with compression testing, the failure of porous PMMA occurs through the ligaments which join the beads together (see Figure 6.11), and hence the crack is shown to propagate through these areas and not through the beads themselves.

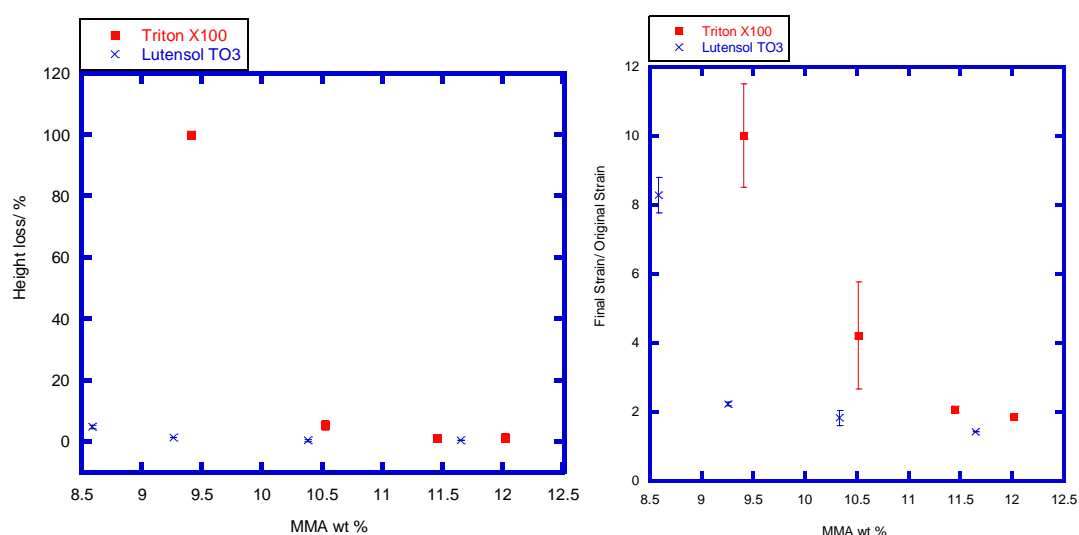


Figure 6.10: Fatigue results for porous PMMA materials made with different wt % of monomer compared to the total wt % of components using Triton X100 and Lutensol TO3 as a surfactant

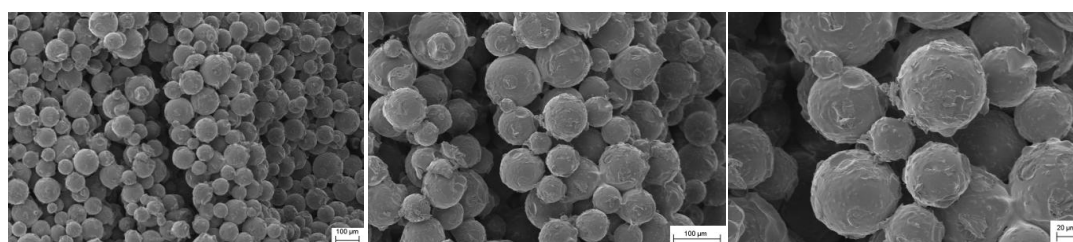


Figure 6.11: SEM images highlighting crack propagation through ligaments at 250x, 500x, and 1k x magnification. The images show the beads are undamaged by compression testing, however, a lack of ligaments branching the gap indicates they have been severed

An inverse relationship is evident between fatigue life and porosity. Prior studies mentioned that clear trends can be observed, despite large scattering being obtained in the data from the inherent nature of the materials, indicating that as porosity increases, the fatigue life decreases [189]. Hoey went on to model the correlation using a novel fracture mechanics theory, TCD (the theory of critical distances). The theory demonstrated that two pores of equal diameter in close proximity reduces the fatigue strength of a material by the same extent as if a singular pore was present. In addition to porosity, parameters such as the size distribution of pores and the number density are considered allowing for a more accurate prediction of fatigue strength. However, deviation from the model was still apparent due to errors between samples which can be attributed to slight deviations in the pore structure. Pores were highlighted as microcrack nucleation sites in work undertaken

by Topoleski et al [190], and so increasing the porosity of the materials increased the propagation of the crack and expanded the damage zone, see Figure 6.12.

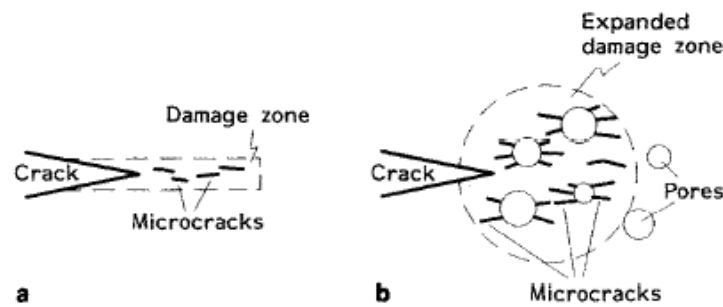


Figure 6.12: Schematic of expansion of fatigue crack zone due to the presence of porosity where a) no pores are present and b) pores are in the vicinity of the crack[190]

It can clearly be seen that a compromise has to be gained between compressive performance and permeability. Therefore, dependent upon the application, the properties of the porous PMMA can be tailored to obtain a superior material. Contrary to previous research, the main porosity is not obtained by the stabilised water particles but by the packing of the beads which is evident from SEM micrographs[82]. This may have been overlooked in previous research i.e. that undertaken by Ergun et al, as the SEM images were taken on polished samples which alter the appearance and properties of the materials. The water in the formulation is simply a means of distributing the components throughout the mixture and allowing for increased fluidity of the mixture prior to setting. Isolated pores are evident if the viscosity of the mixture is too high prior to setting, which is also evident in SEM images. In this project, porosity has been measured by water uptake which excludes closed porosity as water cannot penetrate the closed pores and hence these are excluded from the analysis. Later in the thesis, a comparison with X-ray tomography has been undertaken in which closed porosity is included (see Chapter 9). Porosity from air inclusion has been measured by Hoey and Taylor in the mixing of bone cement where levels from 4-13% porosity arises from trapped air and monomer evaporation[189]. They suggested the use of vacuum mixing or centrifugation to remove such porosity.

6.4 Summary

Contrary to previous studies, porosity was found to be derived from the close random packing of the PMMA beads. The polymerisation process introduces ligaments which form around the beads and it is these ligaments which control mechanistic properties. The thicker the ligaments, i.e. the more MMA is included in the formulation, the stronger the material and hence the longer the materials last under cyclic testing with little to no deformation of the material and little change in the stress or strain. However, thicker ligaments result in a loss in permeability and porosity of the material, making the drying process of the mould less efficient and increasing the overall casting time of ceramic bodies. Therefore, a compromise must be achieved between materials high in compressive properties with high MMA levels and good permeability, with larger pore channels made by reducing the MMA content.

7. Alternative Monomers

7.1 Introduction

There is a broad base of literature regarding the formation of porous PMMA-based copolymer materials, utilising a number of different comonomers in order to change specific properties[12, 68, 79]. Early patent literature included acrylic acid[68] and styrene[12] as co monomers, however no change was noted in the properties of porous PMMA at the levels of comonomer used when pore size and open porosity was considered. In 1973, Will included a large number of variables with regards to the monomer component, comprising polymerisable water-immiscible ethylene (=) monomers of general structure $\text{CH}_2=\text{CR}_2$ [79]. Examples given are aromatic monovinyl hydrocarbons which include styrene and alkylated styrene, aliphatic vinyl and vinylidene halides, α - β olefin unsaturated monomers, and α - β olefin unsaturated carboxylic acids. However, aside from mentioning that a water-in-oil emulsion is desired, little else is stated as to preferential monomer incorporation or to the benefit to the product of adding different monomers.

The objective of the work described in this chapter was to investigate the effect upon the final materials of using different monomer and comonomer systems for the synthesis of porous PMMA- based materials.

7.2 Substitution of MMA by Styrene

Styrene was substituted for MMA in the standard formulation to clarify the coverage found in the patent (EU 3763056 [79]) and all subsequent patents since[4, 81]. In addition, the effect of styrene on the mechanical properties was also to be observed. As initial experiments with styrene indicated a very slow rate of polymerisation, the inhibitor was removed from styrene and all alternative monomers in the preparation of the porous materials discussed in this chapter. Inhibitor was removed by adding the monomer as supplied to an equal volume of sodium hydroxide (2 mol dm^{-3}) in a separating funnel. The mixture was shaken vigorously, then allowed to separate before running off the excess sodium hydroxide. The process was repeated again with sodium hydroxide before being repeated with water to remove the excess sodium hydroxide. The washed monomer was then left to dry over anhydrous calcium chloride to remove excess water and stored in the refrigerator until needed.

The effect of removing the inhibitor from MMA was also assessed, see Figure 7.1, using a bulk polymerisation with the residual monomer measured using GC. An induction period of approximately 5 minutes is observed when an inhibitor is present, which reflects the time taken for the inhibitor to react with the radicals and become consumed. Once all the inhibitor is reacted, new radicals formed will start the initiation of MMA and hence a curve is observed[27]. The rate of the reaction as shown by the gradient of the data is unchanged whether the monomer is washed or unwashed. In all work contained in this thesis, the inhibitor has not been removed from MMA in the synthesis of porous PMMA. However it has been removed from other comonomers prior to synthesis.

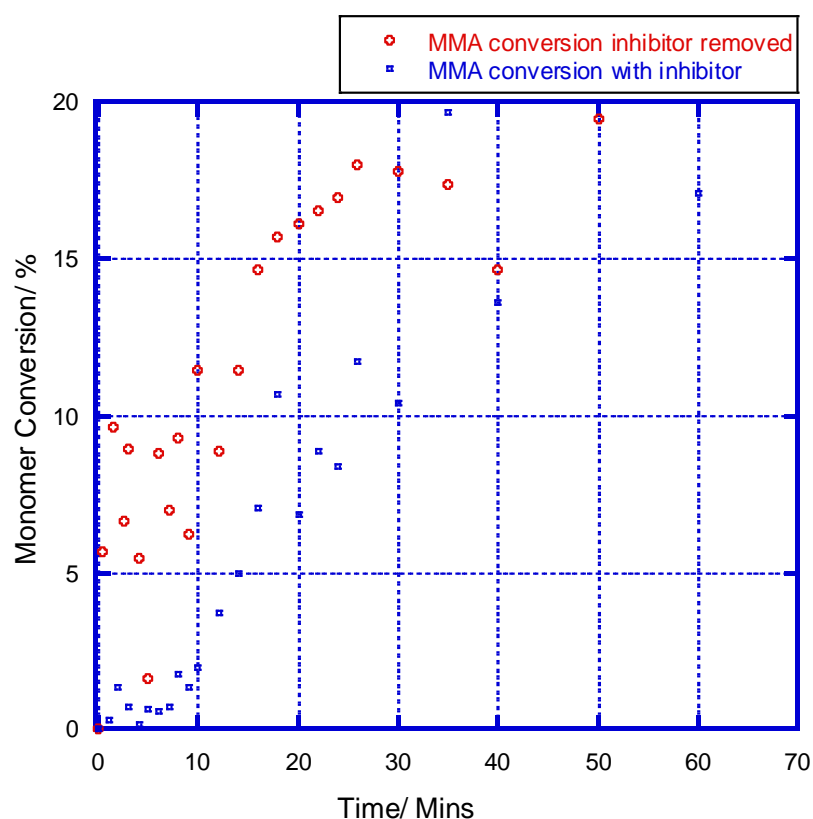


Figure 7.1: MMA conversion to polymerisation with time

Styrene was used as a direct substitute for MMA in the synthesis of porous PMMA-based material at the same weight percentage, see Table 7.1.

Table 7.1: Results of exchanging MMA for styrene in the standard formulation with Triton X100 (numbers in parenthesis are standard deviations)

Monomer (Sample Name)	Set time / min	Compressive Properties				Water porosity (f) / %	Permeability / Darcy	Residual Monomer/ %	T _g / °C
		Average Max Stress/ MPa	Strain at max stress/ %	Transition Stress	Bulk Modulus / MPa				
Styrene (KA071)	>2h	19.33 (3.10)	16.5 (1.99)	14.91 (2.66)	410 (157.37)	31.97 (5.27)	5.37 (0.46)	1.72	100 (0.71)
MMA (KA055)	25.5	18.25 (4.73)	16.0 (3.00)	6.701 (1.46)	385 (166.90)	29.63 (3.33)	3.39 (0.55)	2.60	109 (0.69)

Replacing MMA with styrene has very little effect on the final compressive properties of the materials, with similar results being obtained for both materials. Permeability is increased when styrene is used, most probably due to the hydrophobic nature of the monomer. The most marked difference in properties is in the set time of the materials, with styrene not being observed to polymerise at room temperature within 2 hours of transferral to the mould. However, overnight in an oven at 60 °C, the materials set resulting in a hard block similar to that made using MMA.

The difference in the rate of reaction is related to the difference in the rate of polymerisation for MMA and styrene. The Arrhenius equation, given below, is a means of calculating the rate coefficient for propagation, k_p .

$$k_p = A_p \exp\left(\frac{-E_p}{RT}\right)$$

where A_p is the pre-exponential factor for propagation, E_p is the activation energy for propagation, R is the gas constant and T is the absolute temperature.

Using this equation with reliable literature values of E_p and A_p , it can be calculated that at 25 °C MMA has a k_p of 321 dm³ mol⁻¹ s⁻¹ whereas styrene has a k_p of only 85 dm³ mol⁻¹ s⁻¹ [191].

The rate coefficient for propagation can be substituted into the equation given below to obtain the overall rate of polymerisation, signified by R_p . For full derivation see Chapter 1. Section 1.3.2.

$$R_p = k_p \left(\frac{fk_d}{2k_t} \right)^{0.5} [M][BPO]^{0.5}[DMPT]^{0.5}$$

Assuming that the initiator concentrations and efficiency are the same in both reactions this can be simplified to

$$R_p \propto k_p k_t^{-1/2} [M]$$

For bulk monomer (as effectively used in the formulations), $[M]_{t=0}$ is defined by the monomer density. Hence it is possible to calculate $k_p [M]_{t=0}$ with confidence. This gives $k_p [M]_{t=0}$ values of 30100 s^{-1} for MMA and 7400 s^{-1} for styrene.

When $[M]_{t=0}$ is high there is often a sharp increase in R_p as the conversion of monomer increases, referred to as auto-acceleration or the Trommsdorff-Norrish effect, beyond which there is rapid formation of polymer. Auto-acceleration occurs due to the increase in viscosity arising from the polymer that slows the termination stage of the reaction as the mobility of the long polymeric radicals reduces. Free-radical reactions are exothermic, and so auto-acceleration is further driven by the release of heat energy. If the heat source is removed, auto-acceleration can be controlled[192]. The reduction in k_t is known to occur earlier and be more significant for MMA than styrene. Thus, both $k_p [M]_{t=0}$ and the reduction in k_t are expected to give rise to much higher values of R_p for MMA than for styrene.

To investigate R_p experimentally, bulk polymerisations of MMA and styrene have been carried out at 25°C using BPO and DMPT at the concentrations employed in the porous PMMA formulation. Samples were removed from the polymerisations and added to a solution of methanol to form a precipitate. The mass of the precipitate was weighed after being removed by filtration and measured to obtain the percentage monomer conversion. Residual monomer analysis was also undertaken on these solutions by GC (see Figure 7.2).

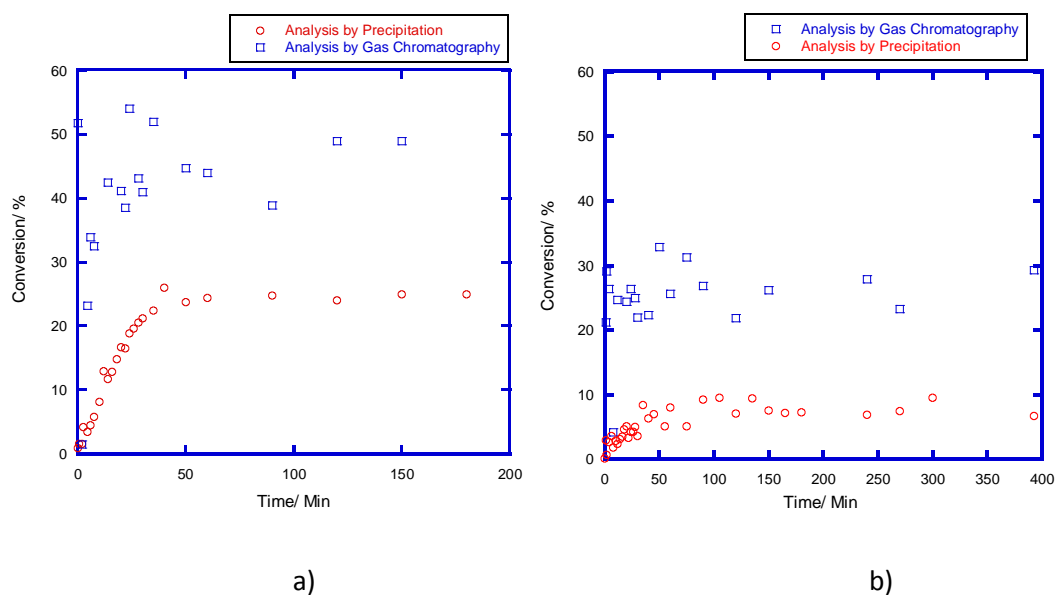


Figure 7.2: Data from bulk polymerisation a) conversion of MMA with time b) conversion of styrene with time

At the monomer levels detected very little difference is observed between samples for analysis by GC, therefore in this case it can be concluded that precipitation is the more accurate measure of conversion. Bulk polymerisation of PMMA did not reach the point for auto-acceleration, which usually occurs at approximately 25 % conversion at room temperature[193]. Both analyses highlight that maximum conversion is reached after 50 minutes, after which the reaction ceases. Free radical initiation is very quick at room temperature hence at the start of the reaction radicals are generated quickly. After 50 minutes, the initiation system is exhausted hence not all the monomer is converted into polymer. Both monomer systems cease at approximately the same point as the concentration of the BPO and DMPT is the same in both reactions. This further indicates the importance of post-heating porous PMMA materials after the reaction ceases at room temperature. Without this post-heating, only 50 % of the MMA has been converted to PMMA resulting in incomplete conversion leading to weaker materials. Post-heating the sample to 60 °C thermally activates the excess BPO which converts the remaining monomer to polymer, as shown by relatively low residual monomer amount when analysed by GC.

Chapter 4.5 clearly shows the effect of not post-heating materials with the compressive stress decreasing by 43 % when the temperature of the oven is reduced from 60 °C to 25 °C. The rate of formation of radical species can be given as

$$\frac{d[R\cdot]}{dt} = f k_d [DMPT] [BPO]$$

Therefore, the monomer has a negligible effect on the rate of initiator consumption. However, the conversion of styrene to polystyrene is slower than that of MMA to PMMA, as expected from the differences in $k_p[M]$. To obtain the initial rate of polymerisation, the gradients of the graphs shown in Figure 7.2 a) have been analysed. MMA was observed to have a polymerisation rate 5.29 times faster than that of styrene, which is relatively close to the theoretically value obtained above whereby PMMA was expected to polymerise 4.07 times faster based on $k_p[M]$ values.

This work clearly indicates that styrene may be added to the blend formulation to reduce the viscosity of the mixture prior to transferral to the mould, to allow for increased ease of handling and better flow characteristics. Styrene was, therefore, substituted for MMA at levels of 10 % and 20 % using an optimised formulation with reduced Triton X100 levels (1.04 total wt %). The resulting data are shown in Table 7.2.

Table 7.2: Substitution of MMA by styrene at 10 %, and 20 % in an optimised blend formulation (standard deviation given in parenthesis)

Monomer (Sample Name)	Set time/ min	Compressive Properties				Water porosity, f/ %	Permeability/ Darcy	Residual Monomer/%	T _g / °C
		Average Max Stress/ MPa	Strain at max stress/ %	Transition Stress	Bulk Modulus/ MPa				
20% Styrene (KA158)	51.5	26.49 (2.37)	15.54 (1.32)	14.52 (1.86)	466 (71.95)	33.14 (1.58)	3.90 (0.26)	6.45	112 (1)
10% Styrene (KA157)	33	28.15 (2.83)	18.15 (1.32)	15.03 (0.93)	527 (33.79)	33.12 (1.76)	3.28 (0.38)	3.35	113 (2)
MMA optimised (KA070)	27.5	32.51 (4.94)	19.46 (9.12)	19.45 (2.39)	569 (51.91)	33.24 (2.28)	3.87 (0.85)	5.98	114 (1)

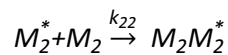
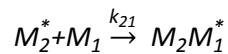
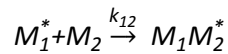
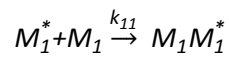
Increasing the levels of styrene increases the set time of the materials, which as the polymerisation is slower reduces the viscosity of the blending mixture to allow for improved pouring ability when transferring into the mould. Table 7.2 indicates that there is a slight decrease in the compressive properties when styrene is used, leading to the idea that using an alternative monomer may allow for further reductions in Triton X100 concentration, which will reduce plasticisation. Unlike when 100 % styrene is used, no benefits are apparent in the permeability and porosity when a MMA-styrene copolymer is used.

Analysis of the reactivity ratios for copolymerisation of MMA with styrene can be undertaken to understand the final composition of the material using the Mayo equation

$$\frac{dm_1}{dm_2} = \frac{M_1(r_1M_1+M_2)}{M_2(r_2M_2+M_1)}$$

where m_x is the number of moles of monomer x entering the copolymer, M_x the number of moles of monomer x in the monomeric mixture and r_1 and r_2 are the monomer activity ratios which can be obtained from literature[194-195].

The monomer reactivity ratios are derived from the four propagation reactions shown below[154]



The reactivity ratios, r_1 and r_2 , are:

$$r_1 = \frac{k_{11}}{k_{12}}$$

$$r_2 = \frac{k_{21}}{k_{22}}$$

From literature[154], the r_1 (MMA) and r_2 (styrene) are similar with values ranging from both approximately equal to $r_1 = 0.46$ and $r_2 = 0.52$. For calculations shown here, $r_1 = 0.46$ and $r_2 = 0.52$ have been used.

Using the equations above with these reactivity ratios, the material containing 10 % styrene has an initial copolymer composition $\frac{dm_1}{dm_2} = 5.03$ where MMA is monomer 1 and styrene, monomer 2. Therefore MMA is 5 times more likely to be in the polymer backbone than styrene. Similarly, the material containing 20 % styrene has an initial copolymer composition $\frac{dm_1}{dm_2} = 2.5$.

Similar reactivity ratios of approximately 0.5 indicate that the styrene is as likely to be in the final polymer as the MMA, indicating that all of the styrene will be incorporated within the final material hence forming a copolymer.

The experimental T_g of the materials reported in Table 7.2 has been further analysed using DSC, whereby the differential of the heat flow curve is used to detect small changes in the gradient. From literature, the peak for polystyrene would be expected at 100 °C [196] and for PMMA at 105 °C [174, 197-199]. The DSC graphs show just one base line shift with a broad peak at approximately 110 °C. Analysing the differential of the heat flow indicates that this is a composite peak, however the bands cannot be clearly defined. However, as the styrene content is reduced, the shape of the differential curve changes (see Figure 7.3).

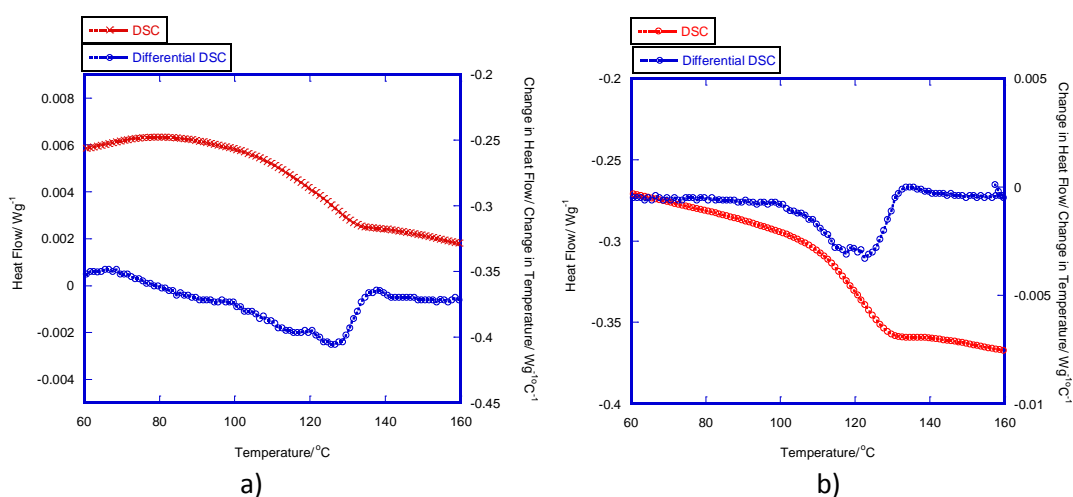


Figure 7.3: Differential analysis of DSC data with styrene as a comonomer using a) 100% styrene and b) 20 % styrene

7.3 Substitution of MMA with Isobutyl Methacrylate and Tert-butyl Methacrylate

PMMA is a brittle material and rapid brittle failure is observed in both compressive and fatigue testing. To reduce the brittle fracture nature, 100% of the MMA was substituted with (i) isobutyl methacrylate (homopolymer $T_g = 64$ °C [200]) and (ii) tert-butyl methacrylate (homopolymer $T_g = 107$ °C[201]). However, neither of the formulations set overnight in the oven, resulting in crumbling blocks. This was unexpected as the propagation rate coefficients for the monomers are similar, with a k_p for MMA of $321 \text{ dm}^3 \text{ mol}^{-1} \text{ s}^{-1}$ at 25 °C, tert-BMA of $350 \text{ dm}^3 \text{ mol}^{-1} \text{ s}^{-1}$ and iso-BMA of $369 \text{ dm}^3 \text{ mol}^{-1} \text{ s}^{-1}$ [154].

Firstly, it was checked that the catalyst system was compatible with the new monomers. Iso-BMA and tert-BMA were miscible with DMPT and dissolved BPO, albeit significantly

slower than MMA. This is confirmed by the similarity in solubility parameters (δ) as calculated using the group contribution method with constants from van Krevelen[202]. As detailed previously, the solubility parameter can be calculated from the summation of the molar attraction constants (F) and the density (ρ), of the liquid[154].

$$\delta = \left(\frac{\Delta E_i^v V_i}{V_i^2} \right)^{1/2} = \frac{\sum_j F_j}{V_i} = \frac{\rho_i \sum_j F_j}{M_i}$$

Using the above equation, the solubility parameter for MMA is 14.01 MPa^½, iso-BMA is 14.53 MPa^½, and tert-BMA 14.35 MPa^½.

Secondly, bulk polymerisations were undertaken where all three monomers (iso-BMA, tert-BMA and MMA) polymerised after approximately two hours with agitation at room temperature, indicating that both monomers are compatible with the initiator system and should result in polymerisation when in the porous PMMA reaction.

Finally the emulsion stability was assessed. Both iso-BMA and tert-BMA formed poor, non-homogenous emulsions when Triton X100 was used as a surfactant, with obvious phase separation being evident even under light agitation. Ceasing agitation causes the emulsion to break into distinct layers, with the monomer making up the majority of the top layer and water the bottom layer with dissolved surfactant in both layers. In comparison, MMA formed a cloudy stable emulsion which did not split on standing.

To improve the emulsion stability with isobutyl methacrylate and tert-butyl methacrylate the surfactant was changed to Lutensol TO3. Lutensol TO3 enabled a stable emulsion to be formed with all three monomers (MMA, tert-BMA and iso-BMA) which split approximately 12 minutes after agitation ceased. It was observed that the butyl methacrylate monomers had a more definitive phase separation than MMA, which showed a gradual discolouration through the test-tube to a clear MMA layer. Table 7.3 gives the results for materials made with different monomers using Lutensol TO3 as a surfactant.

Table 7.3: Substitution for MMA of tert-BMA and iso-BMA, styrene using Lutensol TO3 as a surfactant (standard deviations are given in parenthesis)

Monomer (Sample Name)	Set time / min	Compressive Properties				Water porosity, f/ %	Permeability / Darcy	Residual Monomer/ %	T _g / °C
		Average Max Stress/ MPa	Strain at max stress/ %	Transition Stress	Bulk Modulus / MPa				
Styrene TO3- (KA194)	>2h	41.4 (6.21)	18.19 (1.31)	35.89 (3.92)	830.28 (98.32)	14.67 (1.84)	1.77 (0.05)	4.23	Peak 1:103 (0.3) Peak 2:121 (0.4)
MMA TO3 (KA109)	43.5	24.89 (5.73)	14.29 (3.21)	16.55 (3.91)	466.41 (150.73)	26.21 (1.41)	0.96 (0.33)	3.23	111 (0.5)
tert-BMA TO3 (KA193)	>3h	4.82 (0.59)	2.47 (0.49)	4.62 (0.50)	246.42 (26.48)	29.39 (1.64)	1.48 (0.33)	5.66	119 (0.5)
iso-BMA TO3 (KA192)	>2h	3.51 (0.35)	12.01 (0.68)	2.23 (0.28)	57.87 (10.72)	28.31 (1.22)	1.32 (0.23)	4.89	118 (0.5)

Materials made using styrene, tert-BMA and iso-BMA did not set at room temperature. However, hardening was apparent when left overnight in an oven at 60 °C. On releasing from the moulds, iso-BMA and tert-BMA based materials were observed to be considerably weaker than those made with styrene, which is particularly evident in compression testing where the butyl methacrylate blocks crumble readily under small pressures. The T_gs do not shift as much as predicted and it is believed that the ligament shift is masked by that of the PMMA beads. Therefore, the results were reanalysed using the differential of the heat flow curve to detect small changes in the gradient of the curve, see Figure 7.4.

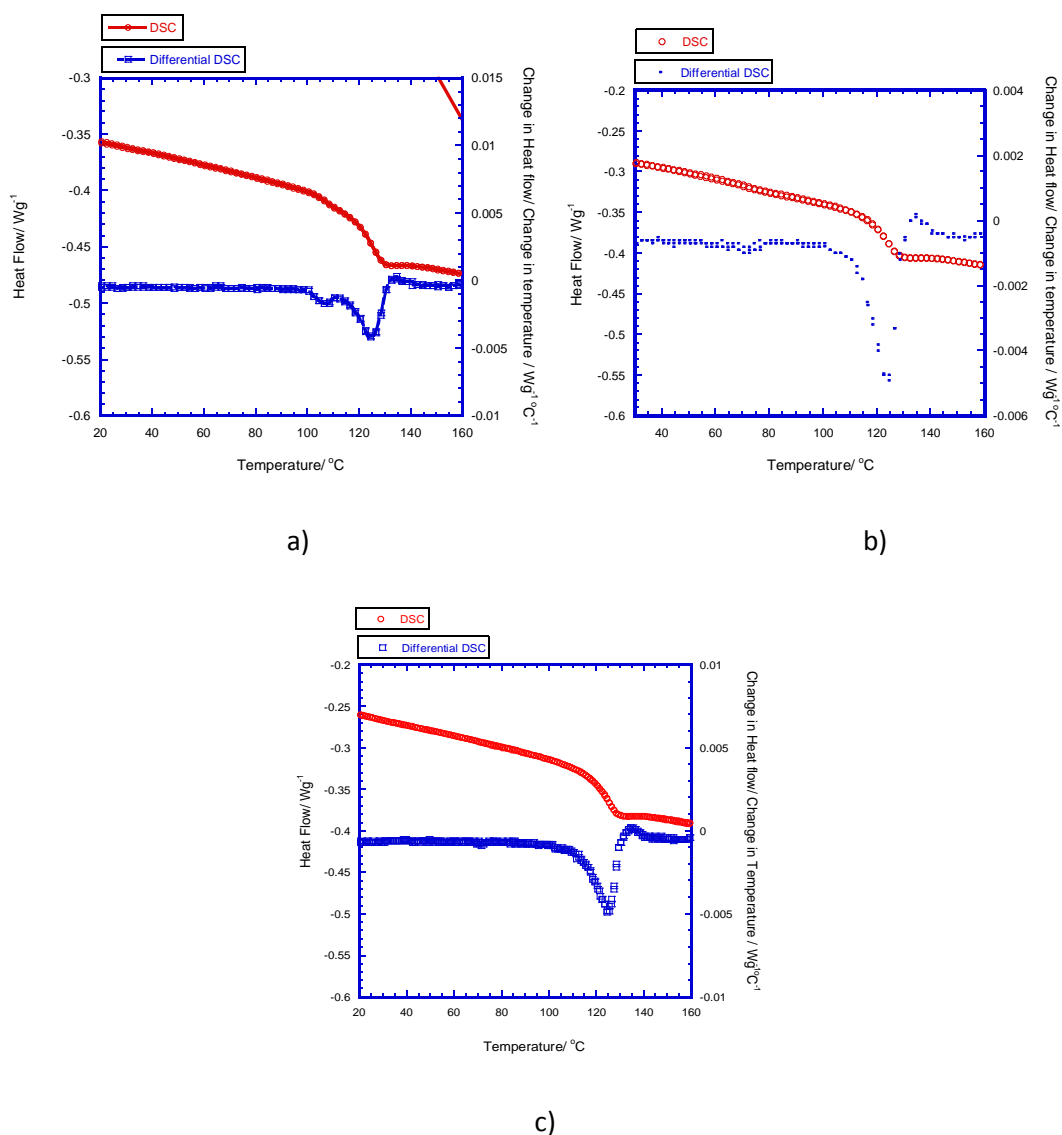


Figure 7.4: DSC data for a porous PMMA-based materials prepared from a) styrene and b) iso-BMA c) tert-BMA (see Table 7.3)

The differential heat flow plots reveal a previously hidden transition at 70 °C for the iso-BMA based materials and at 110 °C for the styrene based material. No additional peak was observed for the tert-BMA based materials. Comparing to literature, polystyrene has a T_g of 100 °C, poly (tert-BMA) 107 °C and poly (iso-BMA) 64 °C [154].

SEM images of the materials are shown in Figures 7.5 and 7.6, which show an incomplete coating around the beads when tert-BMA and iso-BMA are used. The images also indicate that the emulsion stability was poor, with discrete droplets of materials being evident on particle surfaces in the SEM micrographs.

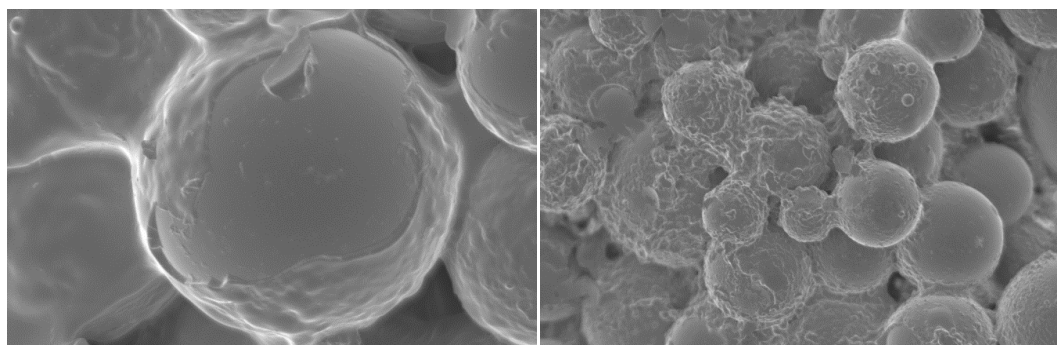


Figure 7.5: SEM images of materials made with iso-butyl methacrylate

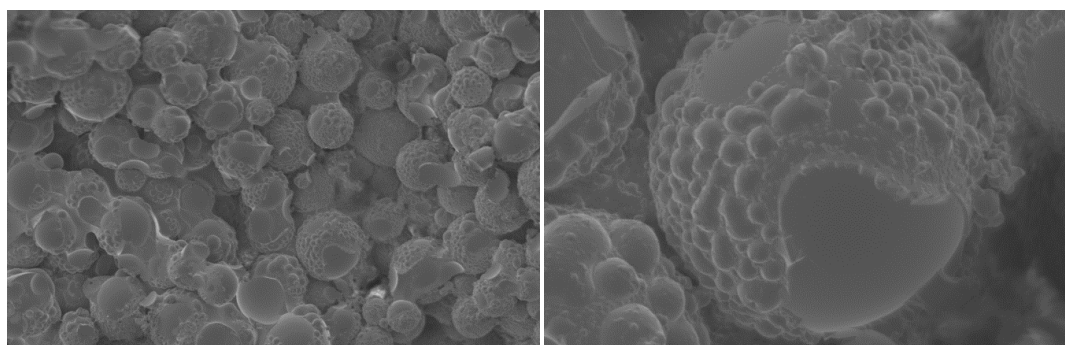


Figure 7.6: SEM images of materials made with tert-butyl methacrylate

7.4 Summary

The substitution of MMA, in part or entirely, by other monomers gave mixed results depending on the stability of the monomer emulsion containing water, monomer, initiators and a surfactant. The butyl methacrylate monomers tested form an unstable water-in-oil emulsion even when alternative surfactants are used, resulting in exceptionally weak materials. Although in part this was expected, as the T_g of butyl methacrylate is lower than that of MMA, the lack of bonding between beads was unexpected with SEM images highlighting incomplete coverage of beads by the polymerised butyl methacrylate.

Substitution with styrene was more successful, with particular achievements when Lutensol TO3 was utilised as a surfactant. However, due to the slower rate of polymerisation the production time for making the mould is considerably longer and a significant increase in set time was observed. However, this could be beneficial as the viscosity of the mixture is considerably lower over a longer period of time. Therefore, pouring the mixture into a mould is easier, thus allowing for smaller more detailed articles to be cast.

8. Toughening of PMMA Ligaments

8.1 Introduction

Currently, the industrial uptake of porous PMMA moulds is limited due to the high capital cost of specialist equipment and comparatively higher cost of starting materials. To reduce the unit cost, toughening can be used to increase the number of cycles that the mould can withstand which allows for the expenditure to be distributed over a greater number of artefacts, therefore reducing the cost per unit.

Conventional polymer composites incorporate inorganic fillers, namely calcium carbonate, glass beads and talc to enhance the materials' mechanical properties utilising changes in the filler volume fraction, shape and size to control the final properties[203]. Increasing the aspect ratio by changing from glass beads to glass fibres provides reinforcement enhancements. Fracture toughness benefits have also been recognised[204]. More recent filler materials include fibres and nanoparticles to further reduce the aspect ratio in order to gain material enhancements. This chapter aims to provide a brief overview of the literature found in the field of polymer toughening, followed by experimental attempts to toughen porous PMMA ligaments using (i) addition of rubber-toughening particles, (ii) liquid polybutadiene and (iii) the grafting of polybutadiene chains to PMMA.

8.2 Overview of Literature on the Toughening of Brittle Plastics

The properties of brittle polymers can be manipulated in a number of ways, including the incorporation of rubber phases, the introduction of hard particles, such as silica or the inclusion of fibrous material. The following section is a brief overview introducing toughening mechanisms and some examples with reference to PMMA and where possible porous PMMA.

8.2.1 Toughening of Brittle Plastics by Using a Rubber

The introduction of a secondary phase containing rubber particles aims to compensate for the often brittle nature of plastics, by helping to absorb and dissipate energy through the polymer matrix over a range of temperatures[174]. There are two ways to add this secondary phase: (i) through copolymerisation of initially-compatible monomers with phase separation of the rubbery phase during the reaction and (ii) the introduction of an incompatible rubbery polymer, usually in the form of particles, through blending[16]. However, the overall aim of rubber-toughening is to increase toughness, whilst minimising

loss in other aspects of mechanical performance (i.e. stiffness) to retain or gain a competitive advantage for the manufacturer[204].

Rubber toughening was first established as a method for increasing the fracture resistance of thermoplastics in 1942 when PVC was mixed with natural rubber[204-205]. Later that same year, Dow Chemicals released blends of polystyrene with added polybutadiene creating high-impact polystyrene (HIPS). this approach to rubber-toughening involves the formation of toughening particles *in-situ* by phase separation from the matrix material. However, difficulties arose in trying to simultaneously control the matrix properties and those of the rubber filler due to the delicate balance required between thermodynamic, kinetic and rheological parameters. An alternative approach is to incorporate sub-micron sized particles which are pre-prepared before blending into a polymer matrix. In the early 1980s epoxy resins were toughened by the addition of a rigid polymer (such as poly(ethersulfone) which was shown to be beneficial[206].

8.2.1.1 Mechanism of Deformation in Brittle Plastics

Before discussing toughening, a brief discussion on the deformation of plastics is useful. Polymers are often described as brittle however it is not the chemical structure which designates the method of fracture but the ability of the material to undergo yielding when a stress is applied. There are two principle deformation mechanisms in brittle polymers: (i) shear yielding and (ii) crazing.

Shear yielding occurs when a materials is put under stress causing molecular alignment in the plane of orientation to the sheared region. Shear yielding occurs at constant volume and can therefore occur when the material is both in tension and under compression. The structure of the shear bands is dependent on the polymer type and can range from fine well-defined bands to a broad deformation zone. In addition, for a given polymer, shear bands are determined by the temperature and the strain rate[207]. Although theoretically shear bands occur at a 45 ° angle to the tensile axis, a simultaneous dilatation process result in shear bands ranging between 30-60 ° to the motion of deformation.

Crazing involves a local change in volume of the material resulting in the formation of fine fibrils. The fine orientated fibrils span the void space composed of orientated polymer chains resulting in a directionally strong fibre stabilizing the craze gap. Crazes are typically 0.1-1.0 µm thick with polymer fibres approximately 5-20 nm in diameter filling a volume of 50 %. The remaining 50 % volume is void space[208].

In brittle polymers, the volume of deformation of both of the above mechanisms is tiny, resulting in highly localised stress concentrations. The mechanical energy supplied by the deformation mechanism, is therefore focussed into a very small volume resulting in rapid brittle fracture as the material has a low resistance to crack propagation. The start of deformation can occur either due to molecular factors but more likely due to scratches or dust particles incorporated into the matrix in blending. These foreign bodies act as stress concentrators focussing the energy in small area.

Rubber-toughening increases the plastic deformation by distributing the applied energy at multiple sites throughout the polymer. Number–rubber-concentrations are in the range 10^8 - 10^{14} per gram of material, therefore greatly increasing the volume of material undergoing deformation. The toughening particles initially accelerate shear yielding by acting as stress concentrators causing initial deformation of the polymer matrix. If a certain level of stress is applied, the rubber-toughening particles cavitate, or rupture internally, relieving the stress in the matrix facilitating local shear yielding[209-210]. Both mechanisms greatly increase the total energy required for fracture.

8.2.1.2 Mechanics of Fracture

Glassy polymers such as PMMA and polystyrene show brittle fracture. Griffith developed a brittle fracture theory to explain the fracture behaviour of glass[211]. Crack growth is initiated from pre-existing flaws in the polymer which can be in the form of scratches or cracks. The flaws cause an increase in the local stress at the crack tip which is greater than that of the material as a whole which causes the crack to propagate through the material. The effect of a crack in a body can be determined by considering an elliptical shaped crack as shown in Figure 8.1 where $a \gg b$.

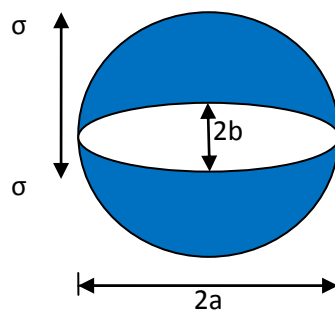


Figure 8.1: An elliptical crack of length $2a$, width $2b$ with a stress σ at the crack tip. The blue-shaded area represents a stress-free zone above and below the crack.

Griffiths theorised that for fracture to occur, the energy required to produce a new surface must be equivalent to the decrease in the stored elastic energy in the stressed body, which is concentrated around the flaws found in the material. If the stress at a large distance from the crack is σ_0 , the stress at the crack tip (σ) is defined as

$$\sigma = \sigma_0 \left(1 + \frac{2a}{b} \right)$$

The stress-concentrating effect of the crack is defined by the ratio σ/σ_0 and for a circular hole, where lengths a and b are equivalent, is equal to 3. For an ellipse, the radius of curvature ρ is a more convenient function where

$$\rho = \frac{b^2}{a}$$

Hence

$$\sigma = \sigma_0 \left[1 + 2 \left(\frac{a}{\rho} \right)^{1/2} \right]$$

A sharp crack will cause a stress concentration at the tip of the crack, which is from where the crack propagates. The crack creates an area in which the stress is reduced or relieved (shaded blue in Figure 8.1). The crack will propagate through the material if the energy gained by relieving the stress is greater than that to create a new surface[29]. Griffith suggested that in plane strain, the fracture stress (σ_f) of the material is based upon the size of the flaws present, a .

$$\sigma_f = \left[\frac{2E\gamma}{\pi(1-\nu^2)a} \right]^{1/2}$$

where E is the Young's modulus, γ the surface energy of the material and ν the Poisson ratio. Hence reducing the size of the flaw will toughen the material, but a critical level is obtained upon which further reducing flaws makes no difference to σ_f , which for PMMA at room temperature is at a flaw size of 0.07 mm [29].

Commonly, 2γ is replaced in the equation with the critical strain-energy-release-rate, G_c . Hence,

$$\sigma_f = g \left[\frac{EG_c}{\pi(1-\nu^2)a} \right]^{1/2}$$

When a material is in plane stress, E^* the effective tensile modulus is equivalent to the Young's modulus (E), or in plane strain E^* is equivalent to $E/(1-\nu)$. Thus the equation can be simplified and rearranged for a material under plane strain to give:

$$G_I = \sigma_f^2 \pi a / E^*$$

For an elastic material, the strain energy release rate (G_I) and the stress intensity factor (K_I) are related by the Young's modulus so that[212-213]:

$$G_I = K_I^2 / E^*$$

The stress intensity factor defines the stress field in the vicinity of the crack. It is dependent upon the geometry, size and location of the crack as well as the magnitude and distribution of the stress throughout the sample. Assuming one mode of fracture K_I can therefore be written

$$K_I = \sigma Y a^{0.5}$$

where Y is a dimensionless function of the crack length and specimen width.

The fracture of PMMA has been investigated by several authors under a range of temperatures, strain rates and loading conditions[214-215]. At temperature below 80 °C, the PMMA crazes prior to fracturing. In turn it was found by Marshall et al. that as the molecular weight increases, the fracture resistance increases[216]. For brittle plastics, the stress is concentrated at a specific site, the crack tip. Introducing rubber-toughened particles distributes this energy over a number of sites thereby creating deformations through out the material. However for the work contained herein, no fracture toughness measurements were undertaken. To compare the toughness of the materials, the energy per unit volume has been calculated by differentiating the area under the stress-strain curve.

8.2.2 Examples of the Rubber-Toughening of Brittle Plastics

Rubber-toughening aims to induce plastic deformation within a larger volume of the material than would otherwise occur. Rubbery particles modify the local stress state experienced by the matrix which initiates local yielding around the particles[217]. A number of authors have utilised this idea with mixed levels of success.

Both the matrix material and that of the incorporating toughening material influence fracture toughness. Kramer noted that the crazing can be observed in the matrix if the

entanglement density is low[208]. However, using the incorporation of rubber-filler particles as supposed to *in situ* formation allows for the particle influence to be measured independent of the matrix material. The rubber-toughening particles properties can be varied in terms of size, composition and concentration. A number of authors have investigated varying the rubber particle size [218-219]. Particles over 5 microns were deemed too large to interact with the stress field under the crack tip whereas particles of size <100 nm were too small to cavitate effectively. Without cavitation, the matrix material is still constrained and unable to change in volume to form crazes and therefore unable to relieve the stress in the material. The effect of rubber concentration has also been studied. At high rubber content, the toughness decreases as the rubber particles concentrate which stops the matrix from shear yielding or crazing. At high concentration levels, the rubber is ineffective as the stress levels required for cavitation are not reached, hence as before, the matrix material is constrained and brittle fracture occurs.

Kennedy et al. synthesised a series of polyisobutylene (PIB) toughened PMMA networks in which the PIB domains were covalently bonded to the PMMA matrix[220]. Different molecular weights of the trifunctional macromonomer PIB(MMA)₃ (see Figure 8.2) were synthesised to obtain different variations of PIB to PMMA phases.

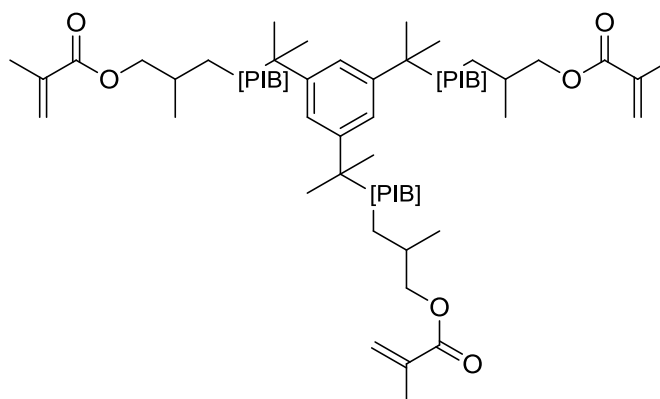


Figure 8.2: Structure of trifunctional macromonomer PIB(MMA)

PIB(MMA)₃ polymer (M_n 18500) incorporated at 20 % weight was found to be the optimum formulation to toughen the PMMA matrix and increase the area under the stress-strain curve. Increasing the rubber to 30 %wt resulted in the semi-continuation of the PIB phase, suggesting an overfilled material. Conversely, at 5 %wt incorporation, little elastic deformation behaviour was observed. Kennedy et al. went on to include the methacrylate-capped PIB in bone cement using a copolymerisation technique[221]. A significant increase

in viscosity was observed when PIB (M_n 18000) was added to the formulation resulting in a loss of pouring ability and the trapping of air in the mould, rendering the materials weaker than the original PMMA material. Increasing the mixing time or decreasing the amount of PIB reduced the size of these voids but, only a slight improvement was observed at a PIB content of 9.2 wt% with stress whitening evident. The paper indicates an array of problems associated with the incorporation of rubber into PMMA, including the lack of bonding between the matrix and the rubber additives.

Alternatively, instead of using monomer incorporation to form a copolymer, rubber particles have been added into the polymerisation process to aid in the dissipation of the fracture energy. Rubber-toughened polymers are made by dispersing pre-formed toughening particles either directly into the polymer via extrusion or mixing with the monomer prior to polymerisation. So as not to change the physical properties of porous PMMA, only the latter method is feasible and is discussed herein, though both methods are used widely throughout the plastics industry.

Lovell et al. made rubber-toughened acrylic sheet (RTAS) by dispersing 3-layer rubber toughening particles in methyl methacrylate monomer, which was subsequently polymerised in sheet moulds[87]. The toughening particles have 3 layers: a core and outer layer made from a glassy polymer and a rubber phases sandwiched between the two (see Figure 8.3)

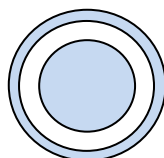


Figure 8.3: Schematic of a 3-layer rubber-toughened particle as used by Lovell et al[217].

The glassy shell made from poly[methyl methacrylate)-co-(ethyl acrylate)] stops coalescence and aids interaction with the matrix material, in this case PMMA. Stress transfer to the rubber layer, made from cross-linked poly[*n*-butyl acrylate)-co-styrene] is also crucial in the ability of the particle to toughen the matrix[217]. Five different weight fractions of rubber-toughening particles were used to assess the effect on mechanical properties. As the weight fraction of rubber-toughening particles increased, a linear decrease was observed in the yield stress and Young's modulus in tensile testing. The fracture stress remained unchanged as the weight fraction of particles increased, until a pronounced drop was seen when 8 % particles was exceeded, highlighting significant yielding with strain softening. During the tensile testing, the RTAS materials stress-

whitened, with an increase observed in whitening when both strain and the weight fraction of rubber-toughening particles increased. In addition, there is some evidence that crazing may make a small contribution to the toughening abilities of the materials, although it is believed that the dominant mechanism of deformation is by shear yielding. In later work, it was found that the method and rate of fracture was important in dictating the failure method[217]. At low rates of tensile shear, particle cavitation occurred which led to stable shear yielding. At high rates of shear, crazing occurs and is the dominant mechanism of failure. TEM pictures show that the rubber particles sit in voids, and that it is these voids which dominate the switch in deformation from a brittle crack to a plastic yielding. The images also show the clustering of toughening particles into aggregates spanning 5-10 μm in size, resulting in larger errors and a less distinctive trend than their melt extrusion counterparts. Overall, the addition of rubber toughening particles to the acrylic matrix decreases the brittle nature of the sheet plastic creating a more ductile material which deforms by shear yielding. This is stabilised and enhanced by the formation of voids around the particles through which the energy of the crack dissipates. From the rest of the paper, it can be concluded that the overall toughness of the material is dependent on the size, morphology and chemistry of the toughening particles. It can be shown that increasing the size of the glassy core can increase the yield stress and Young's modulus of the overall material without compromising toughness.

Danielsson et al. modelled the inclusion of rubber-toughening particles in polycarbonate[222]. The simulations similarly concluded that addition of the particles allowed for the plastic deformation of the matrix, which was initiated in the equatorial region of the voids. The particles were depicted as voids with similar conclusions to Lovell et al., where low concentrations were deemed to reduce the brittle nature of the matrix creating a toughening effect.

Both forms of rubber toughening induce plastic deformation in a larger volume of the material than would otherwise occur[217]. The rubber particles provide stress concentration sites in which either crazing occurs (when localised yielding results in the formation of interconnected macrovoids[8]), or shear yielding occurs (in which shear is highly localised in deformation bands). The stress sites consume the energy of the propagating crack, resulting in a substantial increase in the energy required for failure of the overall material and therefore toughening it.

8.2.3 Toughening of Brittle Plastics by Using Rigid Particles

A number of rigid particles have been added to polymer matrixes with the aim to enhance the material properties, most notably silicon dioxide (nanosilica). An excellent review paper has been written by Tjong[223]. Below is given a summary of key areas with particular reference to PMMA composites.

Silica particles toughen polymers by the crack pinning method. As the crack propagates, in the material, it is first pinned by the filler. As the energy is increased, the crack bows around the particles (see Figure 8.4) until eventually it separates leaving an undulating crack through the length of the matrix. The concentration of the filler is highly important in the toughening process[224]. Too much filler results in a reduction in the properties of the matrix where there is ineffective crack bowing. However, up to this critical value, the fracture toughness, G_c increases as the concentration of filler increases as for each particle, energy is required to form a new surface. Most authors suggest that the filler size, concentration and distribution are key in controlling the region of the polymer matrix affected by the filler [224-226] whilst the actual chemistry of the particles dictates the intensity of the interaction with the matrix material[227-228].

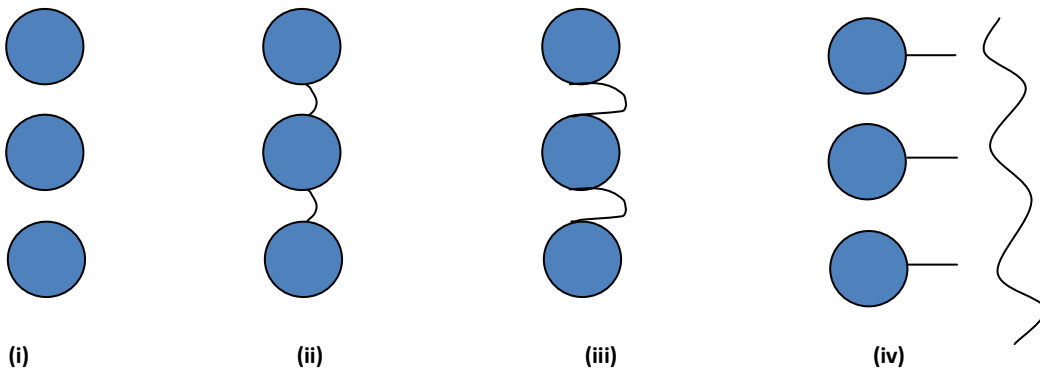


Figure 8.4: Schematic of crack pinning mechanism where (i) is the materials prior to fracture (ii) the pinning stage (iii) bowing and (iv) break-away[16]

Modification of PMMA with clay particles has become increasingly popular, with the main aim being to improve the thermal stability of the materials. Although PMMA has relatively good mechanical properties at room temperature, a rapid deterioration in mechanical strength is observed as the temperature is increased[174]. The addition of clay particles which have greater oxidation stability, redresses the mechanical failures of PMMA at

elevated temperatures. However, as with all additives, the success of the filler depends on its ability to interact with the matrix, whether via mechanical or chemical forces.

Clay minerals are hydrous aluminium silicates. Therefore to interact with the polymer matrix, the clay surface has to be modified. This can be done in a number of ways, although ion-exchange is the most common method with the inorganic cations being exchanged with alkyl ammonium. This gives rise to an increase in the interlayer spacing between clay layers that depends upon the alkyl chain length[229-230]. Once modified the organoclay can be incorporated in two ways, either by the intercalation of polymer chains which extend into the clay network structure, or by an exfoliated structure where individual clay sheets disperse as platelets through the polymer matrix[231]. However, obtaining a fully-exfoliated structure is rare and mostly a mixture of intercalation and exfoliated structures are observed. Organoclays are now commercially available through Southern Clay Products in the US (Cloisite® and Nanofil®[232]) and Lamosa Chimica Mineraria in Italy (Dellite®[233]), amongst others which render the clays compatible with specific monomers. For example, Cloisite 10A contains a benzyl moiety to promote intercalation with styrene derivatives. Melt intercalation can be utilised with certain polymers to distribute the particles through the polymer, examples of which are the mixing of organoclay with polystyrene at 165 °C before being pressed into a pellet[234].

Mechanical properties of the polymer-clay composite are derived from the incorporation of the clay platelets in the polymer. If the dispersion is good, the matrix will have improved tensile strength and Young's modulus but lower impact strength and ductility when compared to the neat polymer[235-236]. Park et al. incorporated Cloisite 30B into PMMA using a melt blend process at 200 °C[237]. Their results indicate that the tensile stiffness of the material increases as the loading of clay increases, from 925 MPa with no clay to 1225 MPa with 3.8 %wt clay. However, impact strength and ductility was lost which was due to the poor dispersion of the clay in the PMMA matrix. Therefore, the process was deemed a failure as the properties of the materials were not desirable. Unnikrishnan[238] had more success using a melt intercalation process with organoclays at 180 °C and maleic anhydride as a grafting agent. The materials were processed in 20 minute cycles at a temperature of 240-250 °C[238]. Incorporating clay increased the tensile modulus by 36 % due to the strong interaction between PMMA matrix and the benzyl component in the C10A clay. In addition, the modulus increased on increasing the clay loading due to movement restriction of the polymer chains. However, the tensile strength was reduced,

as was the impact strength due to the brittle nature from agglomeration of the clay particles.

Studies using bulk polymerisation have been more successful, where increasing clay content increased the impact strength of PMMA-MMT composites. Hence, if the clay is highly dispersed it can deflect the microcrack propagation[239]. The MMT composite strengthens, stiffens and toughens the PMMA by having a higher resistance to plastic deformation, and higher deformation resistance by reducing elongation from 9.31 % to 7.30 % at 1 %wt loading. The author attributes this to the highly-orientated chains of the polymer backbone being inserted into the clay gallery. However, this report is rare as a considerable number of authors indicate some enhancement in properties, such as increased modulus with increasing clay content, but an inherent loss of the materials' strength[240]. Kiersnowski sums up this idea and his work succinctly by stating that below 5 %wt loading, the tensile strength remains at an "acceptable level" to benefit the inclusion of clay with the enhancement of modulus, but above this loading the loss in mechanical performance renders the materials beyond use[241].

Different methodologies have been used to incorporate nanosilica, from catalytic chain transfer polymerisation[242] to film casting[243-244]. The toughening process can be summarised in three stages: firstly, the particles act as stress concentrators due to differences in elastic properties, then during the second stage the particles de-bond from the matrix as the stress concentration rises, and lastly, shear yielding occurs where the voids alter the stress state of the polymer matrix, reducing sensitivity to crazing[236]. Kopesky added different polyhedral oligomeric silsesquioxanes to PMMA[244]. He observed that the greatest degree of toughening was evident when the nanoparticle de-bonded from the matrix near the yield point, but the brittle nature of PMMA was still evident. To achieve debonding, the particles had to be fully dispersed throughout the matrix and have weak interfacial bonds, found when the silica particles were approximately 100 nm in size. Ash and Jansen found similar results with alumina [245] and rubber particles[246], where toughening was successfully achieved. Muriel[247] and Zulfikar[243] were less successful at toughening, although their conclusions were similar in that particle size, distribution and interaction with the polymer matrix is key to the materials' properties. Cros looked at decreasing the brittleness of the polymer-nanoparticle materials without reducing the gain in modulus provided by the nanoparticles by utilising a layer

structure with alternating MMA grafted to methacryloyl nanosilica and poly(ethyl acrylate) layers[248]. Alternating the PMMA with poly(ethyl acrylate) reduced the brittle nature of the materials when compared to PMMA by halting the propagation of cracks.

8.2.4 Toughening of Porous PMMA

Porous PMMA has been utilised in the making of ceramic artefacts using pressure casting. The polymer provides an open-cell structure, allowing for high water permeability coupled with high mechanical strength and fatigue performance. However, although an improvement is seen when compared to traditional gypsum moulds, the mechanical properties of the polymer require further improvements to offset the large financial increase incurred when purchasing the polymer moulds. Therefore, more recent work on porous PMMA has focussed on toughening the materials in order to increase their mechanical performance and thereby extend the service life of the mould. Recent papers within the area of porous PMMA have focussed on the addition of nanocomposites to the material during the blending stage of the reaction to strengthen the final product, a selection of which are discussed below.

Several papers report the manufacture of PMMA-clay nanocomposites. However, few result in the beneficial toughening of porous PMMA. Dortmans et al. have released a series of papers [85, 249] which use melt intercalation of clay by kneading in the presence of a block co-polymer (poly(ethylene oxide)-*block*-PMMA) prior to free-radical polymerisation with styrene and MMA[85]. Use of 5 % of the modified clay was shown to (i) reinforce the porous PMMA materials by increasing the Young's modulus, (ii) reduce the brittle behaviour of the material by incurring a long plastic deformation period once a maximum stress is obtained, and (iii) most importantly, increase the overall strength of the material by increasing the maximum compressive stress (see Figure 8.5). In addition, 5 % clay increased the number of cycles a material could withstand in a 3 point bend test.

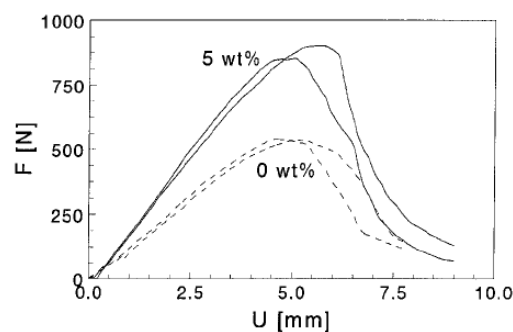


Figure 8.5: Effect of addition of 5 % clay on the maximum compressive stress on porous PMMA[85] where F is the applied force and U the crack propagation in mm in a notched specimen.

In the same paper, a small study was undertaken on clay loading, where an optimum of 3-4 wt% was found. Beyond this loading no real mechanical benefit was observed to offset the increase in cost of the material by increasing the clay content. It should be noted that the wedge opening tests on which the paper bases the significant performance enhancements was only repeated twice for each blend, with no discussion of errors within the measurements. Using knowledge gained from experience with porous PMMA, it could be concluded that errors in the materials are often high, with sometimes significant differences observed between different test areas of the sample. Thus, although trends can be drawn from the results, the overall benefit of clay is yet to be proved. Dortmans released a second article applying the above mechanical data to create an estimate on the lifetime of an actual mould of a standard washbasin cross-section type EUROBASE 60[3] . The calculations indicate that during the moulding process, the pressures over a standard washbasin mould can be considered at 5 MPa, thus a predicted lifetime of a standard porous PMMA mould is 1,000 to 3,000 cycles with large scatter observed in the results. In a reinforced porous PMMA mould, no cracks were apparent after 10,000 production cycles[3]. This result has been verified in an actual production process; however, the exact level of clay loading was not disclosed[249].

Several other authors have released papers on incorporating clay within porous PMMA, including Ergun et al.[84]. Ergun rendered the clay organophilic to increase the interaction with the PMMA matrix and stop the agglomeration of clay particles within the system. Commercially-purchased Na⁺-montmorillonite (Na⁺-MMT) clay was dispersed in water, to which dilute hydrochloric acid and hexadecyltrimethylammonium chloride solution was added (stirred for 1.5 hours at 75 °C). The suspension was filtered and the solid residue washed to remove excess chloride, and the organoclay product dried for 24 hours at 70 °C. To incorporate the clay within the matrix, MMA was mixed with different clay loadings for 2 hours prior to polymerisation using a water-in-oil emulsion to which various sizes of PMMA beads were added. XRD measurements indicated that the structure of the MMT was significantly affected by the modification process, increasing the basal plane from 14.8-19 Å. This increase allows for the intercalation of the hexadecyltrimethylammonium chloride as well as MMA, thereby allowing for a better distribution of clay in the polymer system. Using non-modified clay at a weight loading of 2 %, a reduction in the mechanical properties of the porous material was observed due to agglomeration of the clay particles. However, rendering the clay organophilic produced an enhancement in the mechanical properties by increasing the modulus of the material and the collapse stress at 2 % wt

loading. A 1 % wt loading of organophilic MMT was also trialled, which exhibited a 90 % improvement in the collapse stress and 50 % increasing in Young's modulus when compared to blends of porous PMMA without clay particles. The results are also far above what is observed with non-modified clay at a 2 % loading. In addition, all blends into which organophilic clay was added show plastic deformation, as supposed to a brittle fracture from sudden cracking, so complete mechanical failure was delayed. Overall, the addition of 1 % organophilic clay was shown to enhance the mechanical properties of porous PMMA whilst having no effect on the porosity of the materials. No other weight loadings of organoclay were tested so it is not known if 1 % is the optimum level.

An additional benefit of adding ceramic particles or nanocomposites to PMMA is the reduction in mould shrinkage[250]. As the specimen hardens, the volume of material shrinks, which in the dental industry can lead to large cavities between the cavity wall and the mould. The current shrinkage of a polymer resin upon hardening is estimated to be in the region of 1.5-3 % of the total material volume. The addition of ceramic particles have been shown to reduce this effect, as well as imparting higher hardness and wear resistance, as detailed above. The efficiency of shrinkage reduction depends on the specific surface area of the ceramic-resin interface and on ceramic-resin bonding, with higher bonding resulting in less shrinkage. To increase this, the authors also pre-treated their ceramic fillers with coupling agents to improve adherence.

8.2.5 Literature Review Summary

Overall the literature points to the importance of the interaction of the filler with the polymer matrix, along with a significant emphasis on the weight loading of the filler which has been shown to have a distinct minimum before toughening is observed as well as a maximum which if exceeded results in a considerable decline in compressive properties, due to the agglomeration of filler. The maximum and minimum levels were specific to each combination of filler and polymer reviewed. More specific studies with porous PMMA highlight a difficulty in toughening the materials due to the interconnected porous network which acts as stress nucleation sites. Having such a highly porous material inherently reduces the final stresses that the materials can reach. However, some success has been reported with modified clays if the interaction between the matrix and clay particle is enhanced by modification of the clay surface. The rest of the chapter describes attempts to toughen porous PMMA using rubber-toughening particles and liquid rubber (polybutadiene diacrylate).

8.3 Toughening of Porous PMMA with Rubber Toughening Particles (XC42)

XC42 is a triple layer PMMA toughening particle prepared using sequential emulsion polymerisation. The rubber intermediate layer consists of crosslinked poly{(n-butyl acrylate)-co-styrene}, and the glassy outer layer and core, poly{(methyl methacrylate)-co-(ethyl acrylate)}. The particles are pre-prepared in 3 stages using a seed matrix followed by addition of sequential monomers to produce a layered effect. Full details can be found in patent literature[251-252] and published articles[87]. The particles can be used in the toughening of acrylic materials by inducing extensive yielding in the matrix increasing the ductile nature of the material.

8.3.1 Synthesis of Porous PMMA with XC42

XC42 particles (0.01-6 wt% to monomer) were added to MMA prior to polymerisation and the mixture subjected to high-speed mixing for 2 minutes using a Silverson L4R a with high-shear screen, then left to rest for 5 minutes to ensure the temperature did not rise above 25 °C. This was repeated until a total of 10 minutes mixing was completed.

BPO (1.22 g, 75% active, 0.08 wt %) was dissolved in MMA (146.66 g, 10 wt %) containing XC42 particles (0.01-6 wt% monomer) in a 2 L beaker. Surfactant (Triton X100, 73.22 g, 4.99 wt %) was added to the solution and the mixture was stirred for 3 minutes. Water (439.31 g, 29.96 wt %) was poured into the solution to form an emulsion which was stirred for an additional 3 minutes. DMPT (1.46 g, 0.09 wt %) was added to the emulsion followed by the PMMA beads (Colacryl® DP300, 805.41 g, 54.92 wt %) and the viscous mixture was stirred for 3 minutes before being poured into a heavy duty baking tray (230 mm x 230 mm x 40 mm). The polymer was left to react further for 60 minutes upon which it was placed into an oven at 60 °C overnight. The next day the set material was removed from the mould and washed with water at high pressure to remove excess surfactant. The sample was dried in an oven at 60 °C overnight before being cut for testing.

8.3.2 Results and Discussion

Addition of XC42 particles had a detrimental effect on the properties of the materials, significantly weakening their performance under compression (see Figure 8.6 and Table 8.1). In addition, the energy to failure per unit volume has been calculated by differentiating the area under the stress-strain curve to which gives a representation of the toughness of the materials (see Figure 8.7).

Table 8.1: Results for materials containing varying levels of rubber-toughening XC-42 particles (standard deviations are given in parenthesis)

Sample Name	XC42 wt%	Set Time / Min	Compressive Properties				Porosity/ %	Permeability/ Darcy	Residual Monomer /%	T _g / °C
			Average Max Stress / MPa	Strain at Max Stress / %	Transition Stress/ MPa	Bulk Modulus/ MPa				
XC42-0 (KA055)	0	25.5	18.20 (4.73)	15.70 (2.72)	6.70 (1.46)	384.61 (166.90)	29.63 (3.33)	3.39 (0.55)	2.60	109
XC-42 0.1 (KA197)	0.01	20.0	14.19 (1.26)	12.52 (2.13)	9.87 (1.71)	210.18 (33.00)	32.50 (2.25)	3.85 (0.27)	3.71	105
XC-42 0.1 (KA198)	0.1	23.0	14.93 (1.62)	15.31 (5.02)	19.12 (1.19)	186.77 (33.4)	30.27 (2.70)	2.81 (0.18)	0.75	100
XC42-0.5 (KA163)	0.5	23.5	15.11 (6.80)	15.23 (6.95)	6.30 (2.88)	299.21 (139.42)	28.33 (4.22)	2.04 (0.62)	4.88	102
XC42-1 (KA162)	1	24	16.20 (2.75)	15.62 (4.43)	6.50 (1.38)	294.02 (33.42)	31.39 (3.66)	0.50 (0.17)	6.04	102
XC42-2 (KA160)	2	22.0	13.14 (1.70)	11.18 (2.76)	6.56 (1.21)	247.13 (53.57)	30.29 (4.22)	2.53 (0.44)	4.87	81
XC42-4 (KA159)	4	27.0	13.54 (2.01)	14.93 (2.69)	5.98 (0.78)	205.86 (42.07)	26.69 (1.86)	2.46 (0.61)	4.59	84
XC42-6 (KA161)	6	18.5	8.78 (1.59)	6.87 (1.54)	5.44 (0.81)	204.6 (20.37)	34.34 (3.43)	3.30 (1.14)	4.66	95

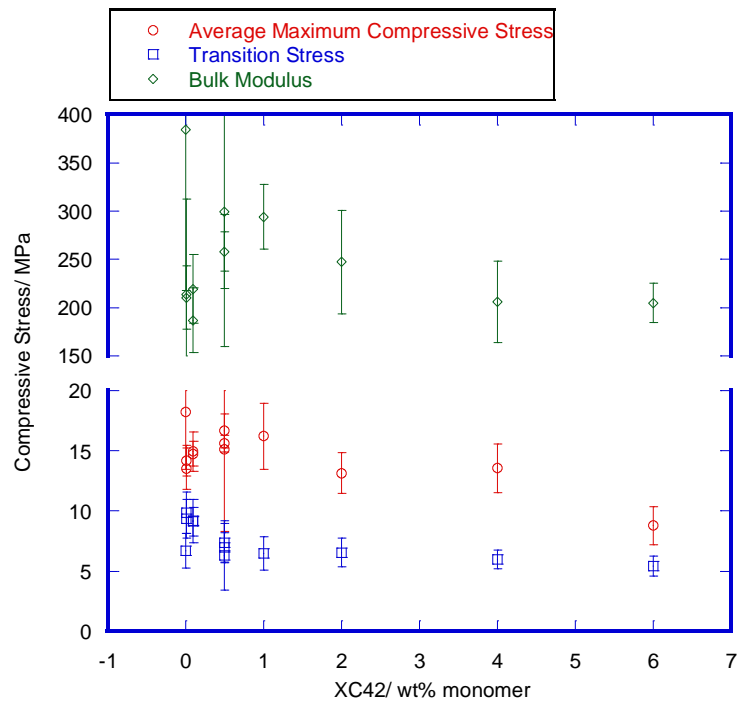


Figure 8.6: Effect of XC42 on compressive properties

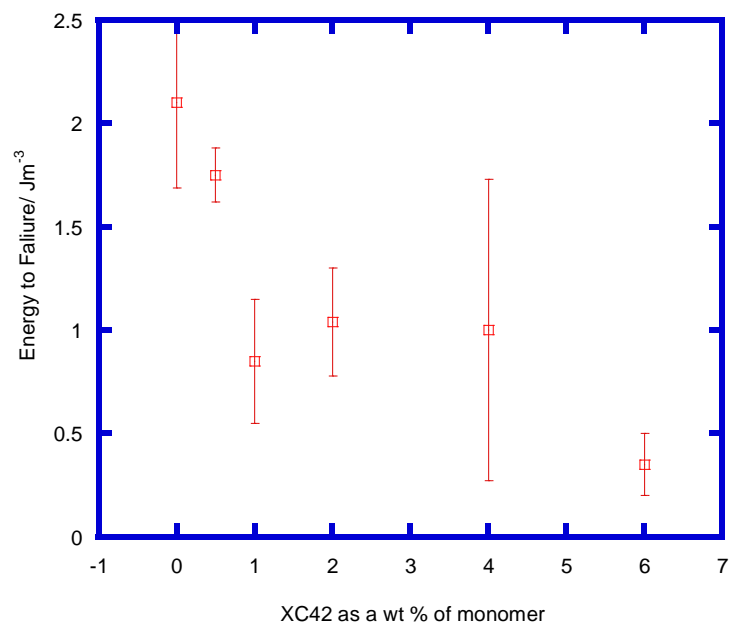


Figure 8.7: Effect of XC42 on fracture toughness

The SEM pictures indicate two factors affecting the formation of ligaments (see Figures 8.8 and 8.9). Firstly, air bubbles are incorporated into the mixture on the dispersion of the XC42 granules resulting in large holes in the ligaments. Secondly, small hollow voids are observed due to loosely-bonded XC42 particles which have been removed in the washing process or during fracture. The XC42 particles concentrate in the ligaments resulting in a deficiency in the PMMA matrix surrounding them. This leads to weakened ligaments with

large voids. Hence, to reduce the agglomeration of particles, the concentration of XC42 was reduced further to levels of 0.01 wt%. However, all the materials produced which incorporated the use rubber-toughening particles were observed to be weaker in compression testing than those without (see Table 8.1).

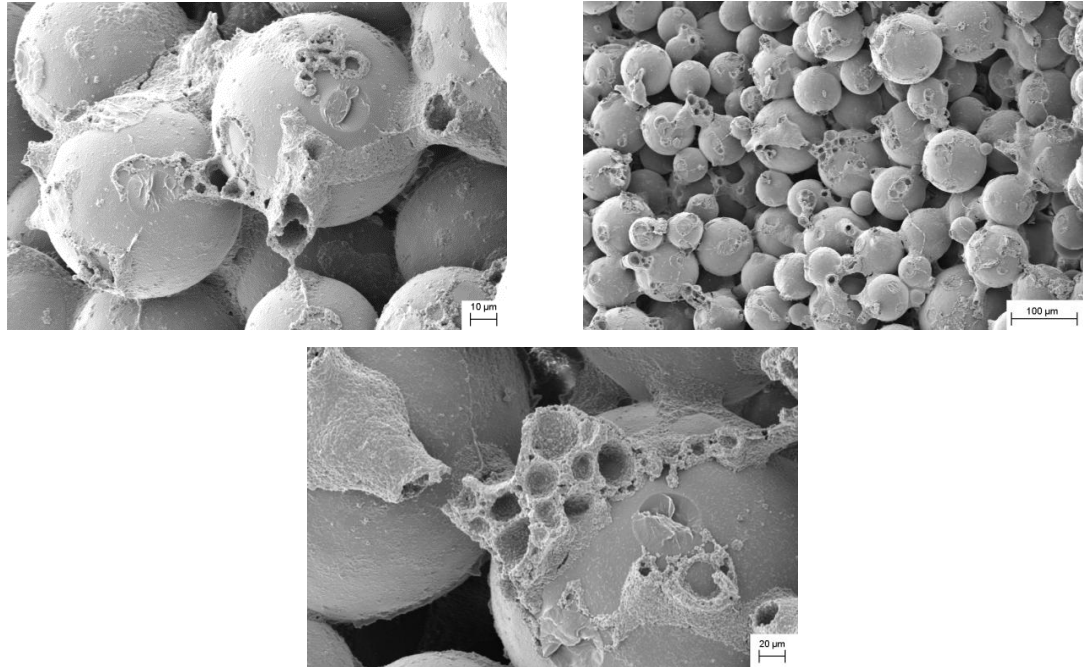


Figure 8.8: SEM of porous PMMA with addition of 1 % XC42 particles

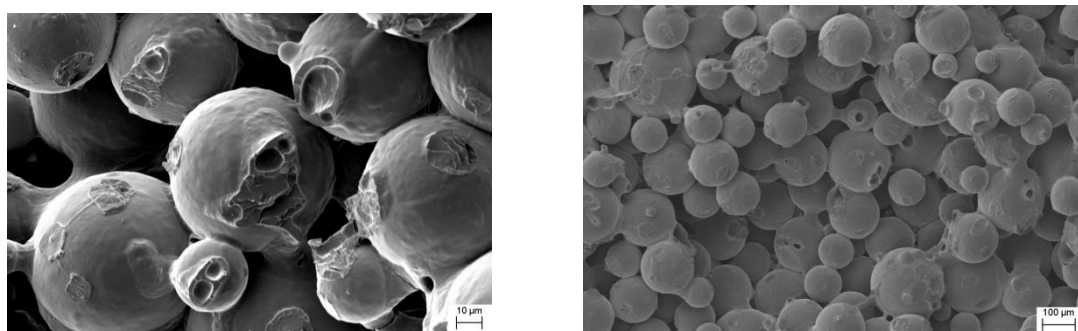


Figure 8.9: SEM of porous PMMA with addition of 0.5 % XC42 particles

Alternative dispersion techniques were tried, including the degassing of the XC42/ MMA mixture prior to use and increasing the emulsion sonication time to 20 minutes. However, although improvements were observed in the SEM images (see Figure 8.10), and the standard deviation between samples reduced, the materials still had worse compressive properties and toughness compared to porous PMMA without toughening particles. Some improvements can be observed in the fracture nature of the materials with 0.5 % XC42 particles, where the sample is observed to show a less brittle fracture with slight elongation after a peak maximum is reached. However, even these improvements were not enough to

toughen the materials, as although the elongation to break is similar, the maximum stress is greatly decreased (see Figure 8.11).

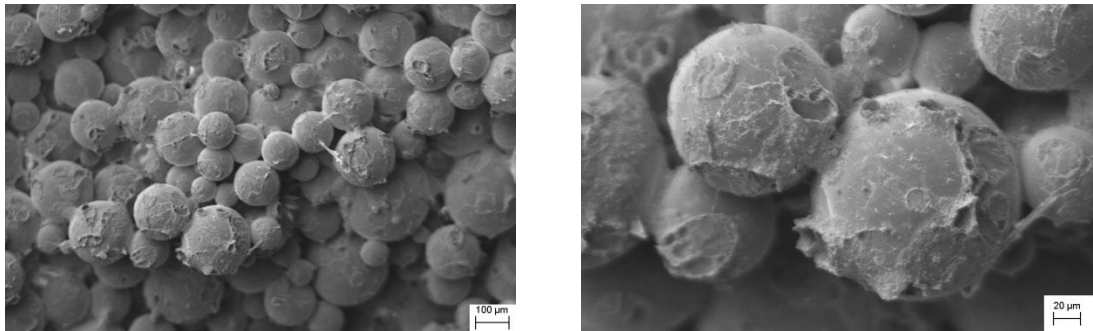


Figure 8.10: SEM image of porous PMMA with 0.1 % XC42 with 20 minutes high shear mixing

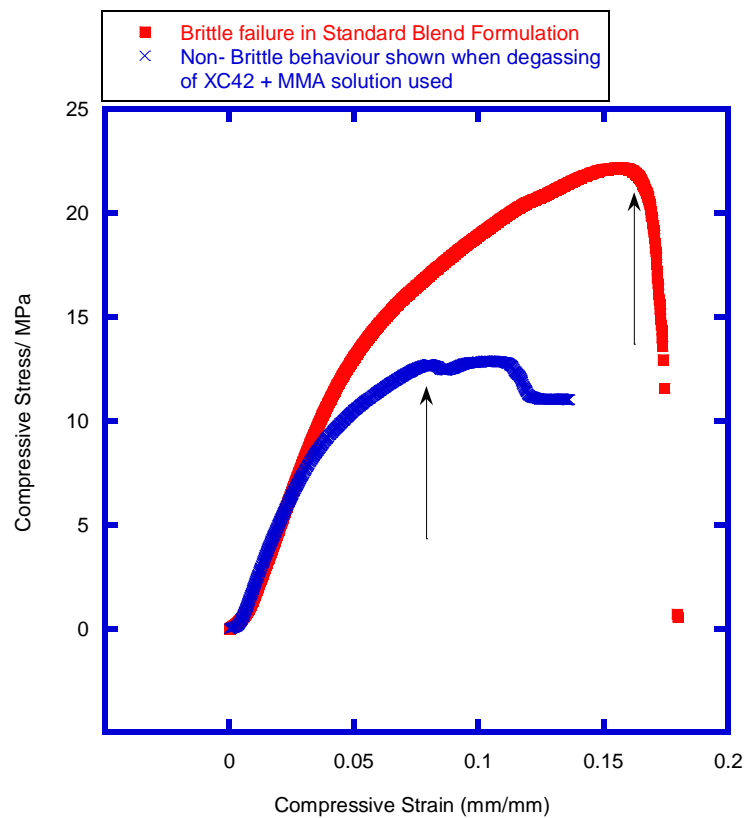


Figure 8.11: Stress-strain curves showing the fracture nature of materials made using the standard blend and by those with XC42 particles at 0.5% with degassing of the mixture prior to use. The arrows indicate the approximate point at which a visible crack appears

Overall, efforts to toughen porous PMMA with XC42 particles indicate considerable difficulties in fully dispersing the particles without introducing air voids which considerably weaken the ligaments. In addition, the XC42 particles were observed to concentrate in the

ligaments due to the method of preparing the porous materials. Previous work by Ergun et al. indicates that additional preparation of the additive particle, as reported for organophilic clays, increases the bond between the filler and matrix. However, standard materials made by Ergun et al. showed considerably different properties, including significant plastic deformation which is converse to the brittle fracture observed throughout this work. The difference may be due to differences in the formulation, including considerably higher MMA concentrations (20 %wt as supposed to 10 %wt), PMMA beads (44.5 % as supposed to 54.92 %) as well as differences in blending and characterisation techniques.

8.4 Toughening with Polybutadiene Diacrylate (PBDDA)

8.4.1 Characterisation of PBDDA

Liquid rubber has also been used to toughen porous PMMA. As the exact structure of PBDDA was unknown, full analysis was undertaken by NMR and GPC to elucidate the structure (see Figures 8.12 and 8.13).

To establish the ratio of trans/cis-1,4- to 1,2- addition, the integral (I_{Hn}) of the protons 'Hn' in the repeat unit (4.82-5.06 ppm) to the integral of the terminal acrylate protons was undertaken (6.29 ppm) as follows where in a polymer there are 4 terminal protons to each 2 H15s:

$$R_y = \frac{I_{(4.82-5.06)}}{I_{(6.29)}} = \frac{2y}{4}$$

where y is the number of repeat units of butadiene in a 1,2 configuration.

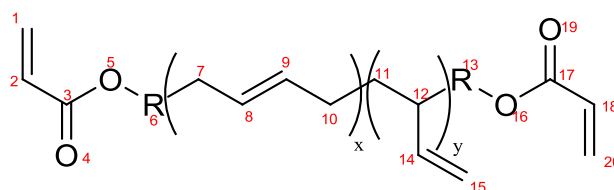
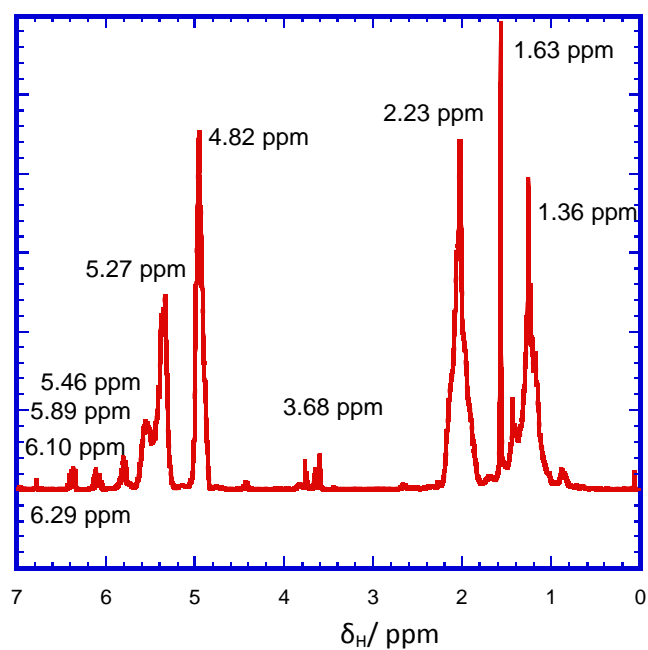
To calculate x, the number of repeat units in a 1,4 configuration of butadiene (both cis and trans), the integral for y has be used as the peak for H8 and H9 overlaps with the peak corresponding to H14(see Figure 8.12). Therefore, knowing that H14 corresponds to 1 proton, the integral (4.82-5.06 ppm) is halved and subtracted from the integral of the unresolved peaks at 5.27-5.66 ppm, resulting in the following equation.

$$R_x = \frac{I_{5.27-5.66} - (I_{4.82-5.06}/2)}{I_{(5.70-5.89)}} = \frac{2x-y}{4}$$

Using the above calculations and rounding to the nearest whole number $x=8$ and $y=37$. As R an unknown quantity, two extreme values can be used to obtain extreme values of

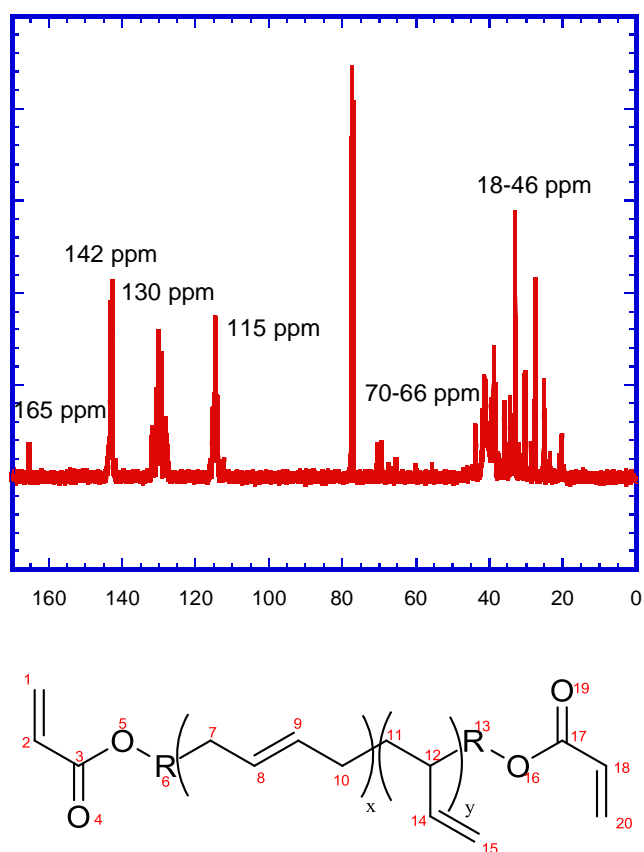
molecular weight. Where R is equal to CH_2 , and M_n of 2600 g mol^{-1} can be calculated. Assuming $R = \text{C}_6\text{H}_{12}$, $M_n=2686 \text{ g mol}^{-1}$.

GPC analysis using a polystyrene standard for calibration indicated an M_n of 3492 g mol^{-1} , a M_w of 4141 g mol^{-1} and a polydispersity of 1.19 of the polybutadiene macromonomer. This is different from the value published by Sartomer in which the molar mass is stated as having an M_n 2200 g mol^{-1} , though the polymer used for calibration is not mentioned in the accompanying product datasheet[253].



δ_H / ppm	Integral	Assignment
1.36-2.23	125.70	R groups in polymer chain H13, H6, Cis/Trans H11, Cis/Trans H7, H10, H12
1.63	4.97	Contaminant
3.68	3.26	OCR H6, H13
4.82-5.06	74.35	H15
5.27-5.46	70.70	Cis/ trans C8 C9 and H14
5.70-5.89	4.49	H1b, H20a with contaminant
6.10	2	H2 ,H18
6.29	2	H1a H20b

Figure 8.12: ^1H NMR spectra of polybutadiene diacrylate and assignment of resonances



δ_c / ppm	Assignment
18-46	Combination of Cis trans and 1,4 and 1,2 addition C7, C10, C11, C12, C13
70-66	C6, C13 OR
115	C15
130	C1, C2, C8, C9, C18, C20
142	C14
165	C3, C17

Figure 8.13: ^{13}C NMR spectra of polybutadiene diacrylate and assignment of resonances

8.4.2 Synthesis of Porous PMMA with PBDDA

Polybutadiene diacrylate (1-10 %wt monomer) was dissolved in MMA prior to incorporation into porous PMMA materials. BPO (1.22 g, 75% active, 0.09 wt %) was dissolved in MMA (9-10 wt %) containing dissolved PBDDA in a 2 L beaker. Surfactant (Triton X100, 14.64 g, 1.04 wt %) was added to the solution and the mixture was stirred for 3 minutes. Water (439.31 g, 31.19 wt %) was poured into the solution to form an emulsion

which was stirred for an additional 3 minutes. DMPT (1.46 g, 0.1 wt %) was added to the emulsion followed by the PMMA beads (Colacryl® DP300, 805.41 g, 57.17 wt %) and the viscous mixture was stirred for 3 minutes before being poured into a heavy duty baking tray (230 mm x 230 mm x 40 mm). The polymer was left to polymerise for 60 minutes after which it was placed into an oven at 60 °C overnight. The next day the set material was removed from the mould and washed with water at high pressure to remove excess surfactant. The sample was dried in an oven at 60 °C overnight.

8.4.3 Results and Discussion

Compression testing reveals that as the concentration of PBDDA increases, the compressive performance of the materials decreases (see Figure 8.14). All other properties remain unchanged from the standard formulation, although set time increases from 25 to 55 minutes when PBDDA concentration exceeds 5 wt% of monomer (see Table 8.2). Measurements of the area under the stress strain curve indicate a decrease in area and hence toughness once a level of 2 % PBDDA is exceeded (see Figure 8.15). Below this, little difference is observable between materials, with a similar pattern to that observed in compression testing.

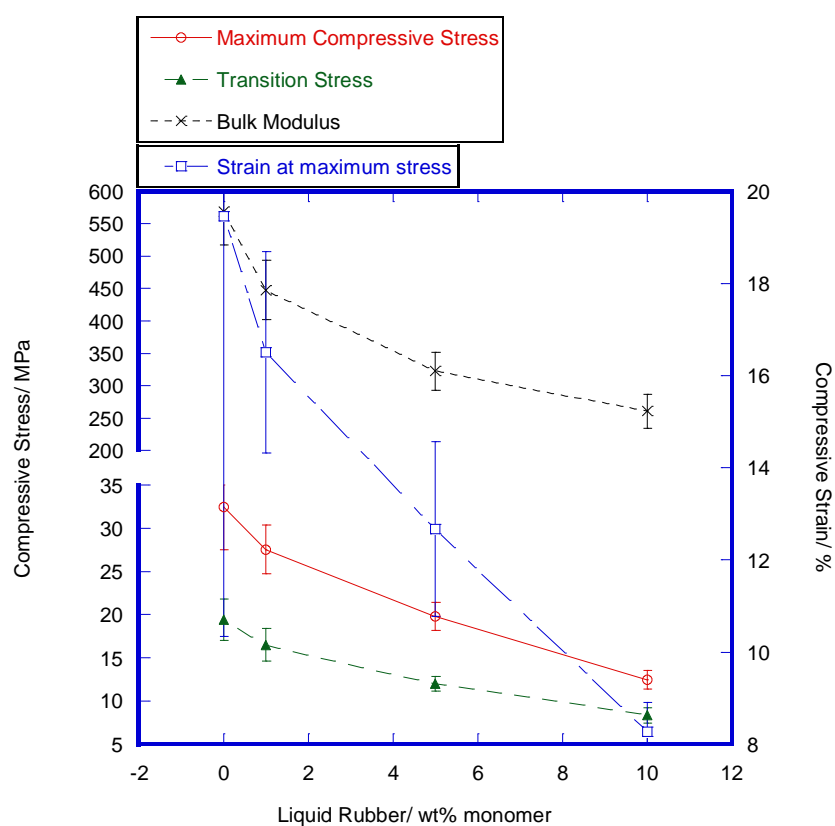


Figure 8.14: Effect on compressive properties of incorporation of PBDDA

Table 8.2: Results in varying the level of polybutadiene diacrylate to porous PMMA

Sample Name	MMA wt %	Set Time / Min	Compressive Properties				Porosity / % (SD)	Permeability/ Darcy (SD)	Residual MMA/%	T _g / °C (SD)
			Average Max Stress / MPa (SD)	Strain at Maximum Stress/ % (SD)	Transition Stress/ MPa (SD)	Bulk Modulus/ MPa (SD)				
PBDDA (0.0) KA070	0	27.5	32.51 (4.94)	19.46 (9.12)	19.45 (2.39)	569.12 (51.90)	33.24 (2.28)	3.87 (0.85)	8.17	114 (1)
PBDDA (0.5) KA203	0.5	24.0	31.98 (5.81)	22.46 (4.47)	19.11 (1.62)	538.49 (29.61)	30.59 (1.65)	2.75 (0.19)	4.66	113 (1)
PBDDA (.0) KA179	1	24.5	27.55 (2.82)	16.51 (2.18)	16.5 (1.90)	447.73 (45.54)	32.51 (2.94)	1.66 (0.55)	6.15	113 (2)
PBDDA (5.0) KA180	5	30.0	19.8 (1.62)	12.67 (1.98)	12.0 (0.88)	322.35 (28.98)	34.31 (4.23)	2.37 (0.46)	5.75	115 (3)
PBDDA (0.0) KA181	10	52.0	12.47 (1.07)	8.27 (0.64)	8.34 (0.92)	260.55 (26.35)	32.78 (3.09)	2.15 (0.40)	6.61	113(2)

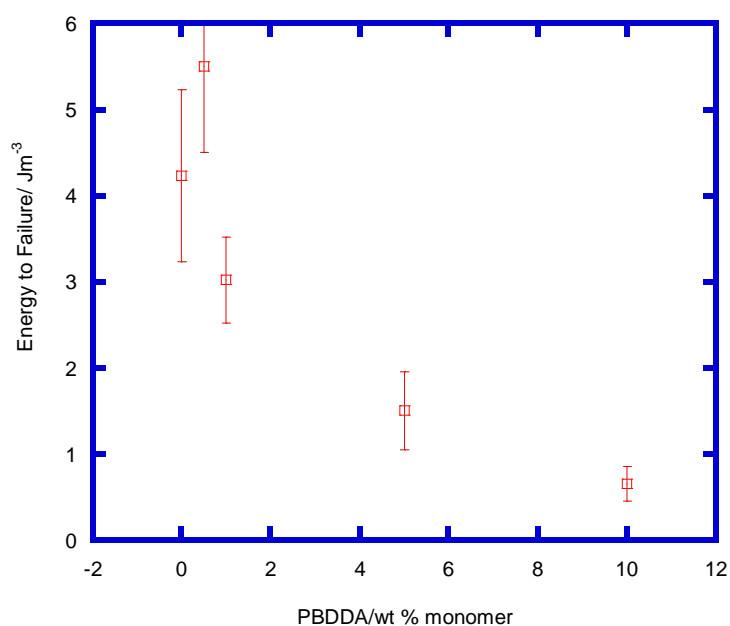


Figure 8.15: Effect of PBDDA incorporation on fracture toughness

SEM images indicate that phase separation may occur as the MMA diffuses at a faster rate into the PMMA beads than the polybutadiene diacrylate, resulting in only partial bead coverage (see Figure 8.16).

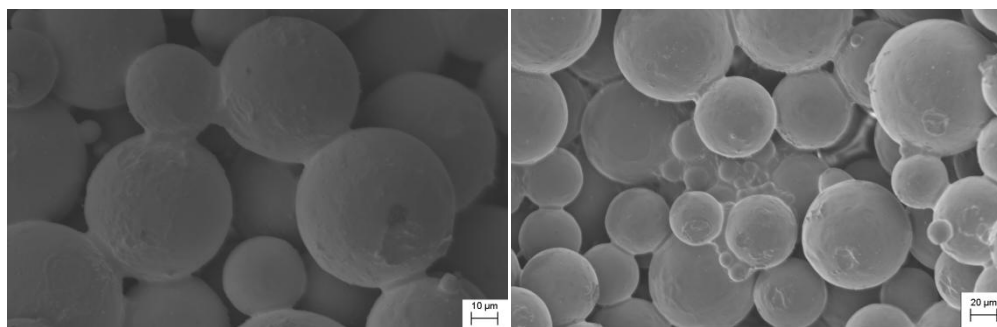


Figure 8.16: SEM images of porous PMMA materials with 10% PBDDA

Difficulties incorporating rubber phases have been observed when using polyisobutylene (PIB) toughened PMMA, where at concentrations in excess of 30 % PIB, toughening of PMMA was greatly reduced, as it was thought that the PIB phases interlink forming a rubberised network that greatly reduces tensile strength[220, 254]. Similarly, when the rubber is poorly bonded to the matrix significant weaknesses occur at the phase-boundaries resulting in a premature collapse of the material. Therefore, many authors end-cap or graft the rubber to the material of the matrix. Kiersnowski et al. treated MMT with (3acrylamidepropyl) trimethylammonium chloride which copolymerises with MMA to ensure a strong bond between the matrix and filler material[241]. Similarly, Kennedy et al. synthesised a three-arm star using PIB end-capped with MMA which was then incorporated into an MMA matrix[220].

8.5 Copolymer of PMMA-PBDDA

To increase the bond between the rubber and polybutadiene diacrylate a graft copolymer of PMMA-PBDDA was synthesised and incorporated into porous PMMA.

8.5.1 Synthesis of PMMA-PBDDA Copolymer

A graft copolymer of PMMA and polybutadiene diacrylate (PMMA-PBDDA) was synthesised using a ratio of 1:1 wt% ratio of polybutadiene diacrylate to MMA in toluene with azobisisobutyronitrile (AIBN) as an initiator. The solution was heated to 80 °C in a water bath and left for 70 minutes. After 70 minutes, the solution was removed and cooled in an ice bath before being concentrated and precipitated in hexane. The hexane was decanted off and the remaining gel re-dissolved in toluene and re-precipitated in hexane before being dried in a vacuum oven at room temperature for 2 days, resulting in an off-white powder.

Analysis of the reactivity ratios for MMA to butyl acrylate can be undertaken to understand the final composition of the material using the Mayo equation

$$\frac{dm_1}{dm_2} = \frac{M_1(r_1M_1+M_2)}{M_2(r_2M_2+M_1)}$$

where m_x is the number of moles of monomer x entering the copolymer, M_x the number of moles of monomer x in the monomeric mixture and r_1 and r_2 are the monomer reactivity ratios which can be obtained from literature[194-195]. See Chapter 7 for full calculation details.

From literature, the r_1 (MMA) and r_2 (butyl acrylate) vary. In this study 3 different combinations were evaluated where (i) $r_1=0.92$ and $r_2=0.2$ [255] (ii) $r_1=1.88$ and $r_2=0.4$ [256] and (iii) $r_1=2.86$ and $r_2=0.32$ [257]. Using the equations above and substituted reactivity ratios from literature, the copolymer synthesised with a 1:1 wt ratio of MMA to polybutadiene diacrylate should have an estimated polymer composition of $\frac{dm_1}{dm_2}=22.40$, $\frac{dm_1}{dm_2}=44.02$ and $\frac{dm_1}{dm_2}=67.15$ respectively where MMA is monomer 1 and polybutadiene diacrylate, monomer 2 where a molar mass of 2348 g mol^{-1} was used for polybutadiene diacrylate (with the assumption that $R=\text{CH}_2$). This was the value obtained from NMR which is considered to be more accurate than that obtained from GC from which M_n is derived by comparison to a standard in this case polystyrene.

Returning this back to the relative weight in the polymer backbone indicates that the level of PMMA:polybutadiene diacrylate would result in a weight percentage of MMA in the backbone of 48.85 wt %, 65.24 wt % or 74.12 wt %.

8.5.2 Characterisation of PMMA-PBDDA Copolymer

The product was analysed using NMR (see Figure 8.17) and GPC (see Figure 8.18).

To obtain the incorporation of PBDDA into the PMMA, the ratio of the integral for the PMMA OCH_3 peak to the saturated proton region of the spectrum was integrated. Considerable incorporation of the liquid rubber to the PMMA backbone was observed as the integral ratio increases from 1:1.16 in PMMA to 1:4.37 with the copolymer. As before, the ratio allows for the mole fraction to be calculated where x_{PMMA} is the mole fraction of the MMA repeat units, x_{rubber} is the mole fraction of polybutadiene diacrylate repeat units and K is the number of protons from the polybutadiene rubber in the range 0.5-2.3 ppm.

$$R_{PMMA} = \frac{I_{OCH_3}}{I_{0.5-2.3}} = \frac{3x_{PMMA}}{5x_{PMMA} + Kx_{rubber}}$$

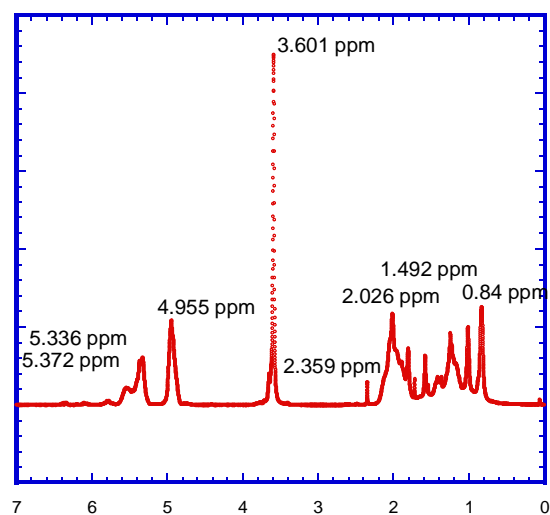
Assuming

$$x_{PMMA} + x_{rubber} = 1$$

then substituting $x_{rubber} = 1 - x_{PMMA}$ and rearranging the equation gives

$$x_{PMMA} = \frac{K}{\left(\frac{3}{R}\right) + K - 5}$$

Due to the exact structure of the R groups in the polybutadiene diacrylate being unknown, two extreme values of K were substituted in the equation ranging from R = CH₂ (K=187) to R=(CH₂)₄ (K=199). When K=187, x_{PMMA} =0.9584 and for K=199, x_{PMMA} =0.937 showing that the accurate identification of R is not important and x_{PMMA} ≈0.94. From this, it can be concluded that there is a weight fraction incorporation of PBDDA of 0.7.



δ_H / ppm	Assignment	Integral
0.841	Saturated region of polybutadiene diacrylate and poly methyl methacrylate	4.37
1.429		
2.026		
2.359	Toluene peak	n/a
3.601	PMMA repeat unit	1
4.995	1,4 addition from polybutadiene diacrylate	1.50
5.336	Unsaturated CH2's from polybutadiene diacrylate	
5.372		
5.377		

Figure 8.17: ¹H-NMR spectrum of PMMA and polybutadiene diacrylate graft and assignment of resonances

GPC data gave an M_n of 132 kg mol⁻¹ and showed high molar mass dispersity. Encouragingly, the monomer peak is minor in the molar mass distribution (MMD), giving confidence in the precipitation technique for purification. The T_g of the material from DSC was 73 °C, also indicating considerable rubber incorporation by mass as the standard T_g stated for PMMA is 105 °C [154].

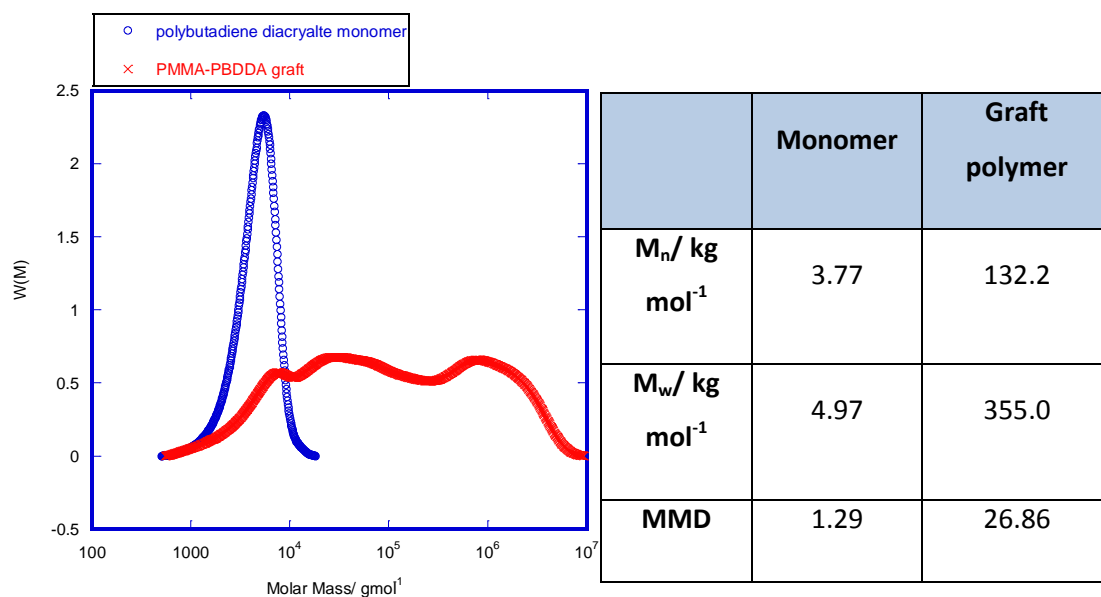


Figure 8.18: GPC chromatograms and molar mass data for polybutadiene diacrylate and its graft copolymer with MMA

8.5.3 Synthesis of Porous PMMA with PMMA-PBDDA Copolymer

PMMA-PBDDA (7.33 g, 0.52 wt%-22.00 g, 1.56 wt%) was dissolved in MMA (124.66 g-139.32 g) prior to polymerisation and the standard process for the preparation of porous PMMA followed.

8.5.4 Results and Discussion of Porous PMMA with PMMA-PBDDA Copolymer

Compressive properties of the porous PMMA materials are observed to decrease with an increase in the PMMA-PBDDA copolymer weight percentage with a drop observed in all the mechanical properties (see Figure 8.19). Interestingly, a drop is also noted in permeability as PMMA-PBDDA increases. However this is not mimicked in porosity (see Figure 8.20 and Table 8.3).

Table 8.3: Results for porous PMMA made with varying levels of polybutadiene diacrylate-MMA graft copolymer

Sample Name	PBDDA -MMA wt %	Set Time / Min	Compressive Properties				Porosity / % (SD)	Permeability/ Darcy (SD)	Residual MMA/%	T _g / °C (SD)
			Average Max Stress / MPa (SD)	Strain at Maximum Stress/ % (SD)	Transition Stress/ MPa (SD)	Bulk Modulus/ MPa (SD)				
KA070	0	27.5	32.51 (4.94)	19.46 (9.12)	19.45 (2.93)	569.12 (51.91)	33.24 (2.28)	3.87 (0.85)	5.89	115
KA207	5	22.5	20.65 (1.68)	13.06 (2.05)	12.72 (1.25)	334.88 (21.30)	32.97 (1.15)	2.76 (0.44)	2.76	113
KA206	10	14	17.19 (1.36)	8.99 (1.42)	11.78 (0.97)	244.12 (25.91)	34.26 (1.66)	2.60 (0.53)	2.6	114
KA208	15	21.5	11.81 (0.93)	6.21 (0.98)	9.29 (0.31)	254.13 (3.24)	35.57 (2.99)	1.48 (0.28)	1.48	113

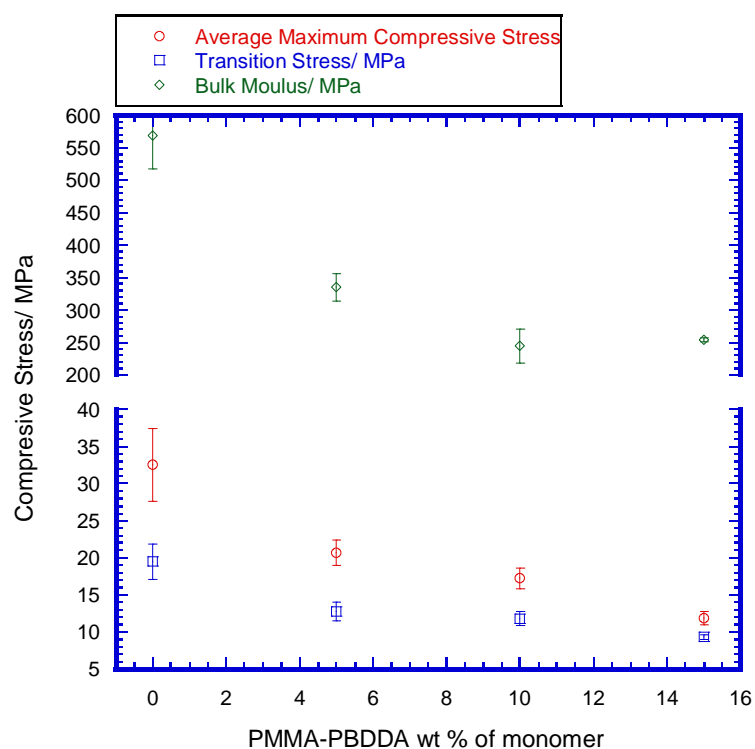


Figure 8.19: Effect of PMMA-PBDDA addition on compressive properties

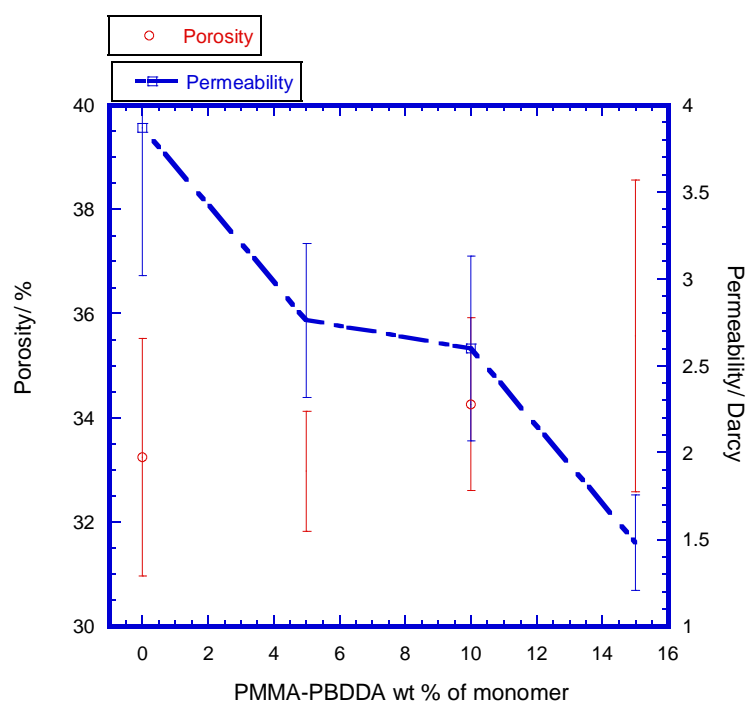


Figure 8.20: Effect of PMMA-PBDDA concentration of porosity and permeability

The area under the stress-strain curve was calculated as a means to assess the toughness of the materials. The results indicated that the grafting to MMA makes little difference in changing the mechanical properties of the materials (see Figure 8.21). This indicates that the grafting may be unsuccessful in bonding the PBDDA to MMA or alternatively, the bonding to the matrix is still insufficient to enable successful toughening.

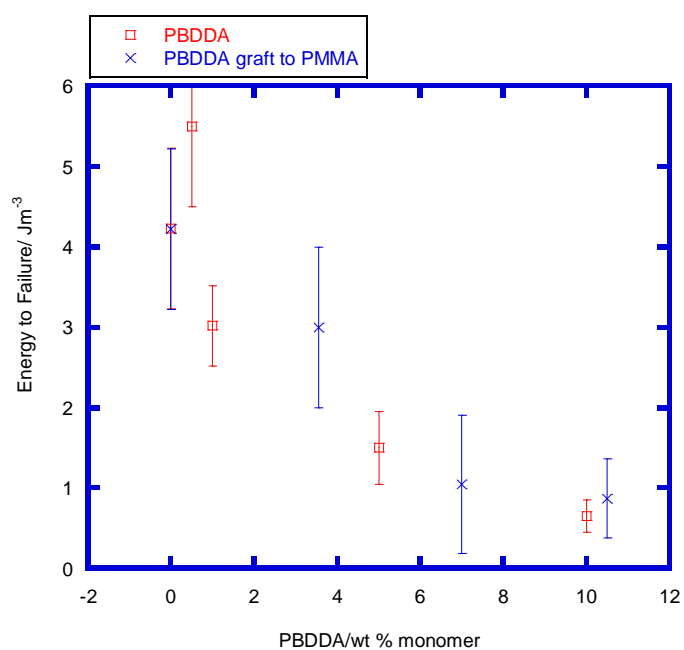


Figure 8.21: Effect of PBDDA on toughness of the materials with a) PBDDA (in red) and b) PMMA-PBDDA graft copolymer (blue)

SEM figures indicate that the PMMA-PBDDA copolymer forms spherical particles in the emulsion which do not coalesce, see Figure 8.22. The ligaments are observed to comprise spherical-shaped particles as supposed to smooth ligaments, as in Figure 8.22 part c) Spherical-shaped particles imply that the monomer droplets which form the ligaments are not coalescing efficiently. This may be due to the formation of smaller monomer droplets which do not coalesce as readily as large droplets as they are more stable. The surfactant is therefore keeping the particles apart, resulting in incomplete formation of the ligaments. Increased agitator speed, geometry and vessel design are all reasons for small monomer droplets. However, throughout the investigation these parameters have been kept constant[258]. Therefore this reduction in size must be down to that of the surfactant level which was lower than in the standard blend, which although beneficial in standard testing with a comonomer may not be sufficient to create an ideal blend for the polymerisation of porous PMMA, where the monomer droplets need to be stable in the initial stages to enable initiation but once the polymer forms, ideally, agitation is desired to enable formation of the ligaments, see Figure 8.23.

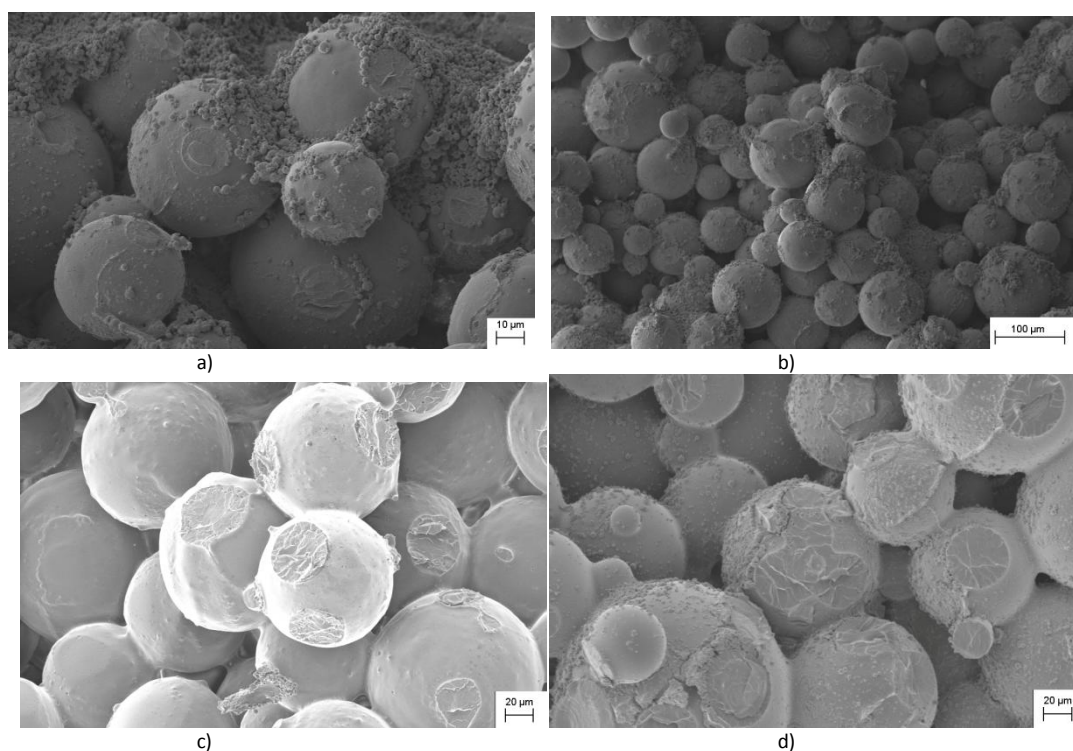


Figure 8.22: SEM images of materials made using 1.04 wt % of Triton X100 with a) 15 % PMMA-PBDDA incorporation at 1.5K magnification, b) 15 % PMMA-PBDDA incorporation at 500x magnification c) 55% PMMA-PBDDA at 1.5K times magnification d) 0% PMMA-PBDDA at 1.5K magnification.

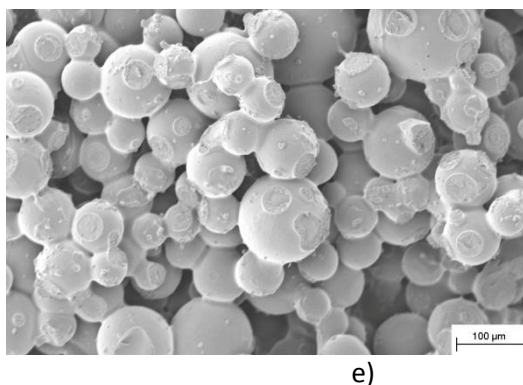


Figure 8.23: SEM image of a standard material which contains 1.04 wt % of Triton X100 indicating smooth ligaments.

8.6 Conclusions

The attempts to toughen porous PMMA were unsuccessful even when incorporating grafting to PMMA. Problems included the non-coalescence of monomer droplets, most likely due to the decrease in size, resulting in the incomplete formation of ligaments. XC42 particles were observed to aggregate in the ligaments which caused areas of high concentration. As observed by previous authors, high concentrations of toughening particles have a detrimental effect on toughening with a reduction seen in the maximum stress. Studies using liquid polybutadiene diacrylate revealed that the rubber domains aggregated causing softening of the matrix. However, the addition of polybutadiene diacrylate showed potential as a toughening route, although much improvement is needed with regards to incorporation of the rubber into the matrix to ensure dispersion and avoid agglomeration with enough surfactant to allow for the coagulation of monomer droplets upon polymerisation. In addition, a lack of coalescence may be due to the higher viscosity of the droplets when the polymer is dissolved in them at time $t=0$.

9. Visualisation of the Ligaments

Throughout this thesis, the importance of the structure of the ligaments has been emphasised. In Chapter 3, a number of visualisation techniques were discussed. This chapter gives more detail about the techniques and their use for visualising porous PMMA ligaments.

9.1 Optical Microscopy

Optical microscopy is a quick and simple technique to use with little sample preparation other than the cutting of a thin sample of material (approximately 2 mm thick). There are two possible modes for the light source which are: (i) transmission (i.e. the light source is below the microscope stage, shining light upwards towards the sample) and (ii) reflectance (where the light source is above the sample and reflected off the materials before being collected in the eye piece[259]). Figure 9.1 gives an example of both modes in the visualisation of porous PMMA.

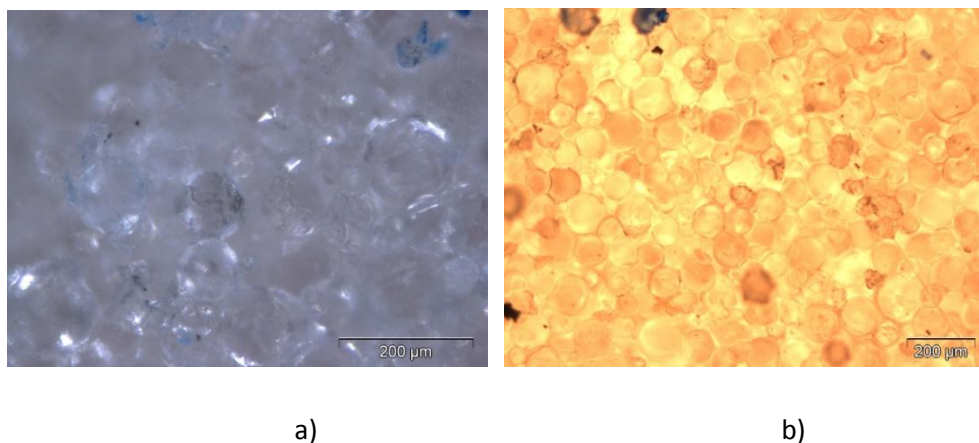


Figure 9.1: Optical microscopy images using a) reflection and b) transmission settings on a standard sample of porous PMMA

The optical microscopy pictures shown in Figure 9.1 indicate that transmission settings allow for better visualisation of porous PMMA materials. However, the technique is plagued by its inability to cope with differences in depth. Due to the nature of the materials, the cut surface is rough with layers of beads bound together by PMMA ligaments. This packing structure of the beads is random, and there are different visualisation depths when viewing the sample, even when thinner samples are utilised. Due to the fragile, brittle nature of the materials, a single layer of bound particles could not be obtained for imaging. The inability to focus on one layer leads to poor sample resolution, rendering the images uninformative with little to no difference being observed

between samples (see Figure 9.2). In addition, the sample preparation causes foreign bodies to be observed in the picture as seen in Figure 9.3 and leads to further disruption of the image. Large holes can also be observed in higher viscosity blends as observed when the surfactant concentration drops below a critical level of 0.11 wt% (see Figure 9.4).

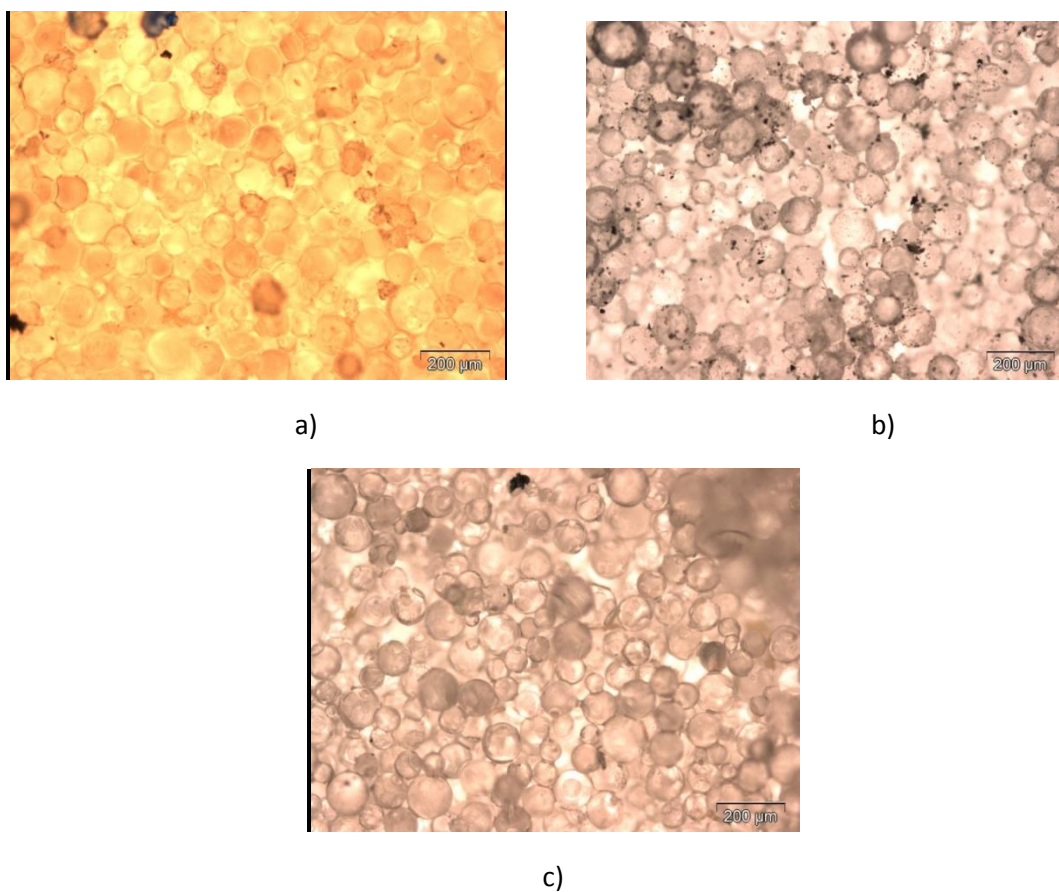


Figure 9.2: Images obtained from transmission optical microscopy for materials made with a) 10.79 % MMA, b) 10.0 % MMA and c) 8.16 % MMA

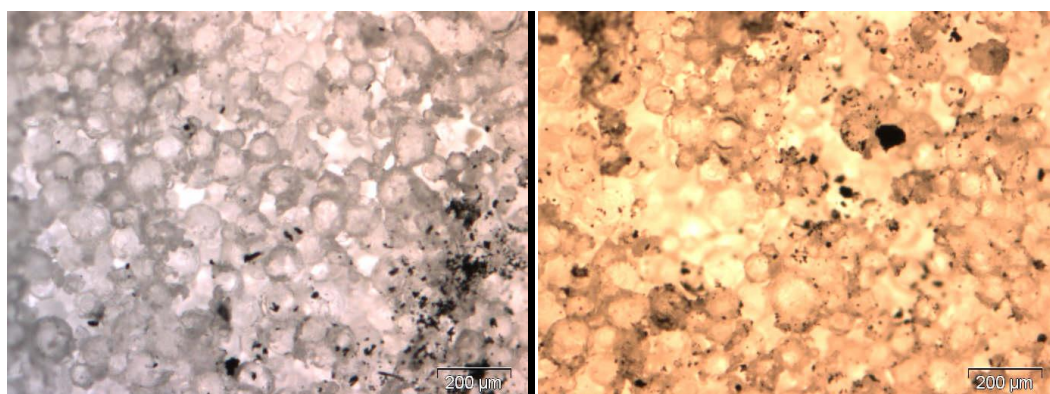


Figure 9.3: Images showing considerable contamination from the saw blade used in the preparation of samples made using the standard blend formulation (4.99 wt% MMA)

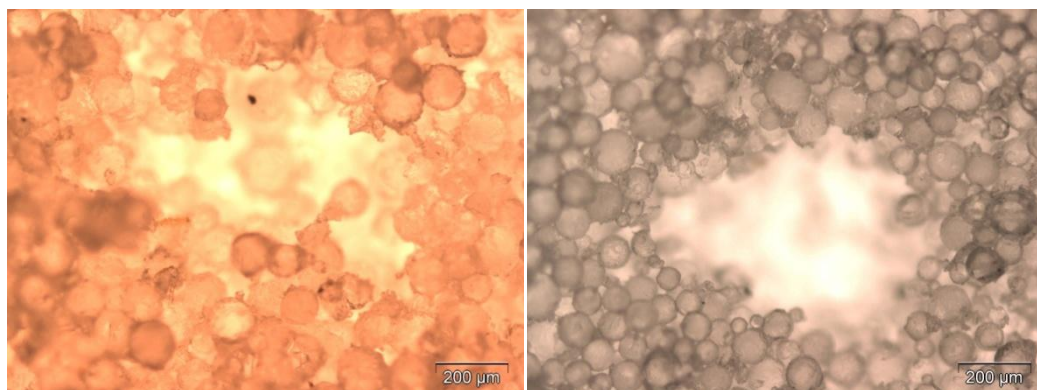


Figure 9.4: Images indicating secondary porosity caused by air being trapped in the mould material during blending in samples made with 8.16 wt% MMA.

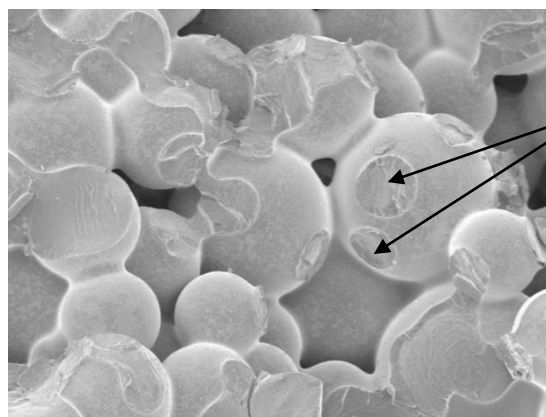
Further refinement of the technique such as reducing sample width and changing the lamp output led to a considerable improvement in the images obtained by optical microscopy (see Figure 9.5). However, the technique still suffers from difficulties with depth resolution which caused blurring and difficulties in visualisation, although the images provide an insight into the random packing of the materials. In Figure 9.5 a ligament is highlighted, which joins adjacent beads forming the structure of porous PMMA.



Figure 9.5: Improvements in optical microscopy highlighting ligaments between beads for materials made using 11.33 wt % of MMA

9.2 Scanning Electron Microscopy (SEM)

SEM is widely used to visualise polymer materials, and SEM images of the porous PMMA samples were instructive and used to reinforce conclusions drawn from this work. SEM requires a clean fracture surface for visualisation but the fracture procedure severs some of the ligaments which are the visualisation target. Therefore, assumptions have been made from the images based upon the fracture pattern (see Figure 9.6), in which the significant amount of pitting indicates high ligament volume prior to fracture.



Assumption that
a ligament was
attached here
prior to fracture

Figure 9.6 Example of an SEM indicating damage caused by fracture technique for samples made using the standard blend procedure.

SEM images are therefore limited by assumptions and artefacts, including discolouration, burning and blurring of the sample images. This is due to a charge build up on the surface of the polymer as they are poor conductors despite a gold coating being used (see Figure 9.7).

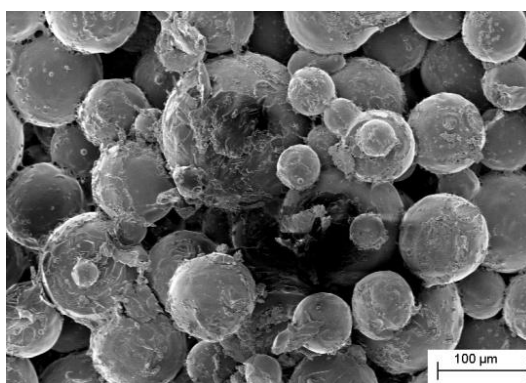
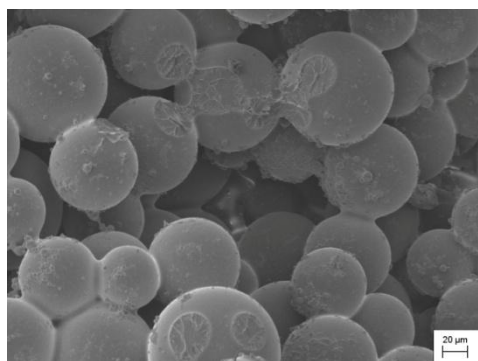
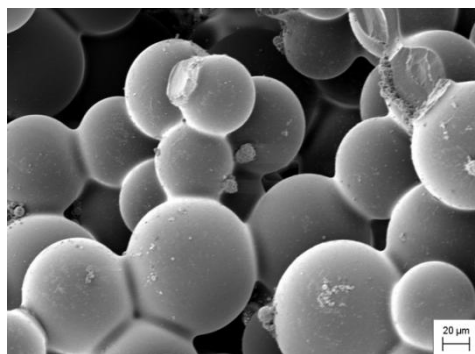


Figure 9.7: SEM micrograph showing dark artefacts in the image caused by burning of the sample for a material made with Lutensol TO15 as a surfactant at 1.10 wt%.

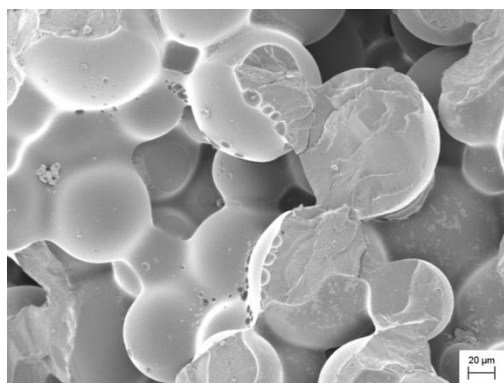
SEM images provide useful information when comparing different formulations (see Figures 9.8 and 9.9) and different preparation techniques (see Figure 9.10) which helped to understand results observed using different mixing intensities. In particular, SEM often gave an insight into weaknesses in the ligaments and produced sound explanatory evidence for differences observed in mechanical properties.



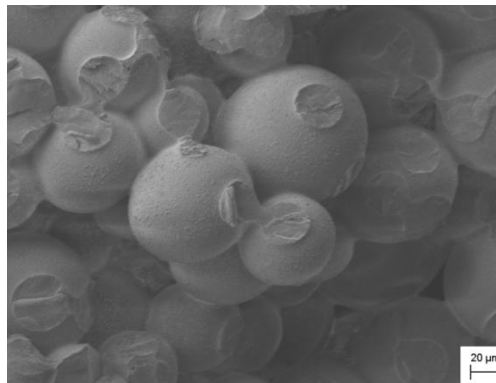
a)



b)

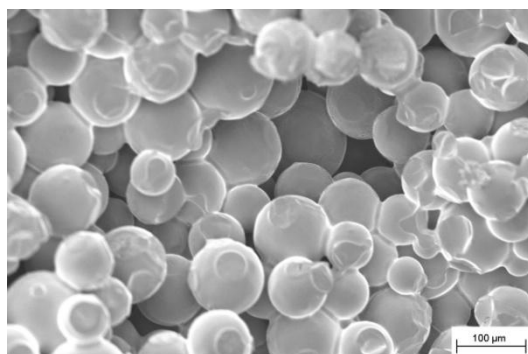


c)

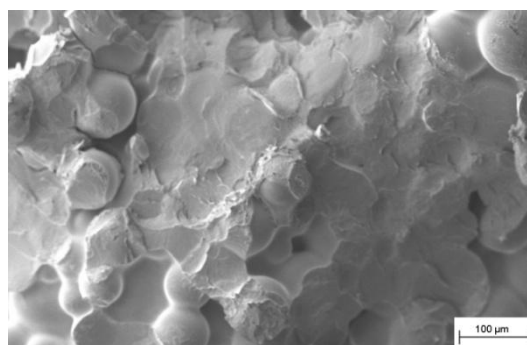


d)

Figure 9.8: SEM images of porous PMMA materials produced with monomer levels at a) 6.60 wt %, b) 10.38 wt%, c) 14.80 wt% and d) 16.05 wt % showing thickening of ligaments as the level increases with Triton X100



a)



b)

Figure 9.9: SEM images indicating the effect of differences in formulation from a) styrene with Triton X100 to b) styrene with TO3

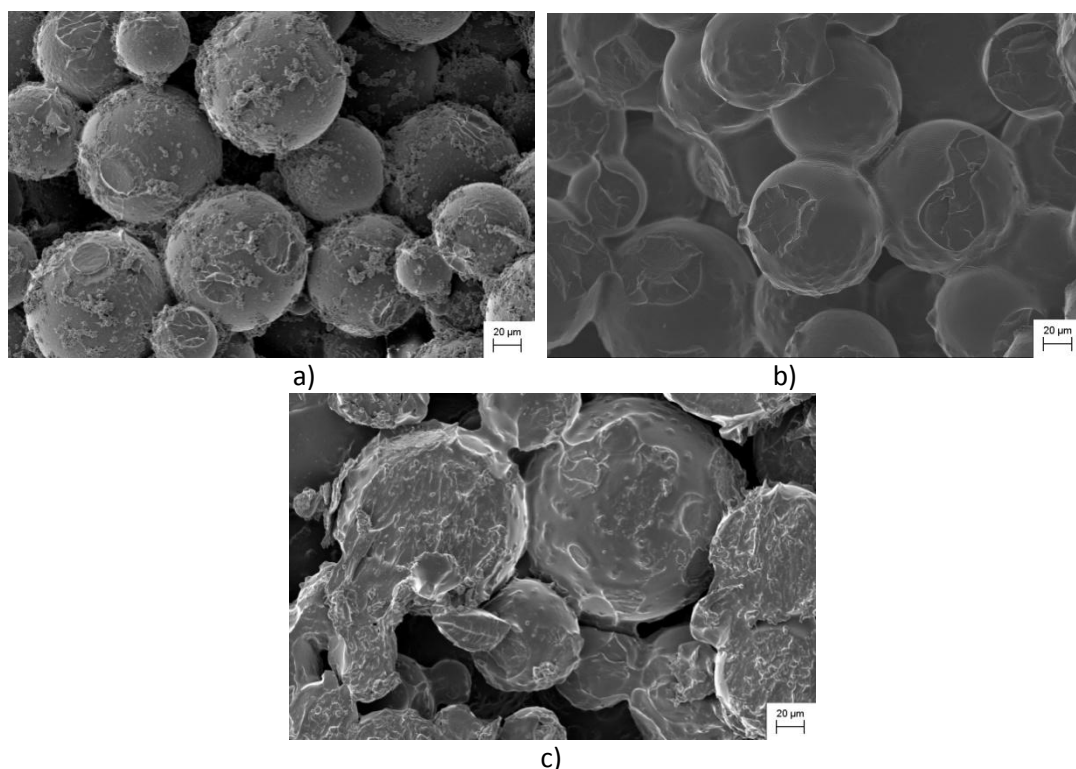


Figure 9.10: SEM images of materials made where the standard emulsion mix has been stirred at different intensities for 10 minutes where a) is from a mechanical overhead stirring b) is from high intensity shearing and c) is from sonication

Figure 9.10 highlights that increasing the stirring intensity changes the nature of the PMMA emulsion such that a more homogenous coverage of the beads is obtained. It is thought that increasing either the length or intensity of stirring can (a) aid the distribution of the monomer by ensuring a better mixed emulsion prior to the addition of beads and (b) reduces the emulsion droplet size and increases the stability of the emulsion, allowing for higher conversions of monomer to polymer prior to the formation of ligaments, thereby resulting in stronger and more homogenous linkages.

Washing of the material was shown to be important to remove excess surfactant and unreacted monomer (see the SEM images in Figure 9.11). If left in the materials, the excess surfactant will eventually plasticise the PMMA ligaments, weakening the materials. The SEM micrographs are of samples that were produced with 1.76 wt % of Triton X100 with and without washing and clearly show that in unwashed samples, levels of surfactant are in excess of what is required to stabilise the emulsion.

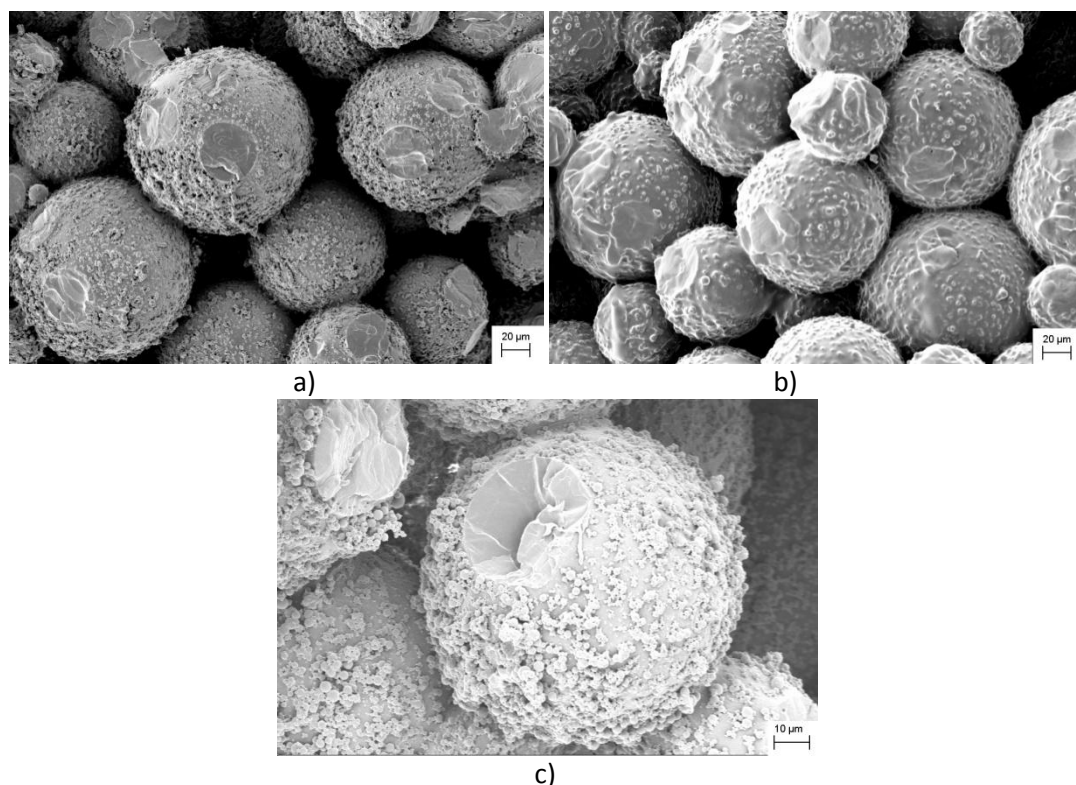


Figure 9.11: SEM images of materials with 1.76 wt % of Triton X100 a) without washing b) post-wash and c) a higher magnification image of an unwashed sample highlighting surfactant around beads.

SEM, therefore, provided useful evidence to support the theories put forward by experimental results, particularly with respect to mechanical testing. However, SEM images are of the fracture surface of a small section of the material, and hence no quantitative data can be obtained for the volume of ligaments.

9.3 Confocal Fluorescence Microscopy

Confocal fluorescence microscopy is used extensively throughout literature to view biological polymers with a fluorescent chromophore[118-119]. Confocal fluorescence microscopy is an optical imaging technique which increases the optical resolution of a micrograph by using point illumination combined with a spatial pinhole to exclude out-of-focus light in specimens thicker than the focal plane. By scanning through different heights, the confocal microscope can reconstruct three-dimensional images from the structures viewed. Fluorescence occurs where a molecule adsorbs a higher-energy photon of light thereby exciting it. The excited molecule loses some of the energy internally, thereby falling to a lower excited energy state. To return to an unexcited ground state, the molecule emits a photon of a lower energy than before, resulting in a longer wavelength which gives rises to a distinct colour. Fluorescein- σ -methacrylate, a fluorescently-tagged monomer (Sigma Aldrich) was copolymerised with MMA at a level of 1 % in an otherwise standard formulation to allow for visualisation at a wavelength of 490 nm. However, as

Figure 9.12, shows, little difference can be discerned between the two areas with little inference being obtainable from the images.

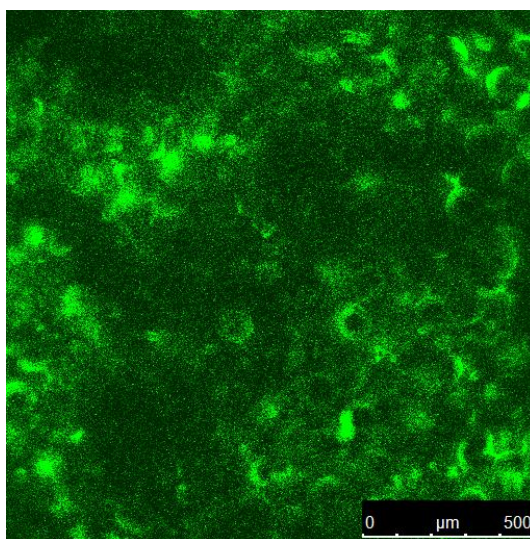


Figure 9.12: Fluorescent image of porous PMMA produced with 1% fluorescein- σ -methacrylate

Contrary to previous research undertaken by Jhaverix et al [260], which reports that MMA copolymerises with fluorescein- σ -methacrylate, the micrographs do not fluoresce enough to observe the ligament structure, although in certain areas, the shape of the beads can be clearly seen at high laser intensity levels. It is apparent that diffusion of the fluorescent monomer into the beads was too large to achieve the contrast desired. In retrospect, it was realised that incorporation of the dye could be improved by partially copolymerising the monomer prior to creating the porous PMMA material, but this was not tried.

A selection of other readily available free non-polymerisable dyes were added to the monomer in a series of well-plate experiments to see if the intensity of the fluorescence could be improved. It was found that all the fluorescent dyes tested were quenched by the monomer and were therefore not suitable. Further investigation into a suitable dye will need to be undertaken before a constructive picture is obtained. This line of experimental work was not continued as it was thought that X ray tomography would provide a more interesting line of enquiry.

9.3 X-Ray Computerised Tomography

X-ray computerised tomography uses computer-processed X-ray transmission data to produce tomographic images. Used widely in the medicinal field and often referred to as a

CAT scan, the technique allows 3-D images to be built up of the specimen through digital geometric processing of 2D slices which are built around a single axis of rotation. X-ray tomography is a non-destructive technique, which requires little to no sample preparation[261]. Hence, the material is not distorted or coated in any way, so the image viewed is a direct representation of the material[262]. First commercialised in 1971 by computer manufacture EMI, computer tomography only became common during the 1990s, primarily in the field of biology hence the use of the technique is still relatively limited[263].

Cylindrical samples measuring 5 mm diameter and length 20mm were cut from various parts of the porous PMMA block, placed in the scanner, see Experimental Section 3.3.5.5 for more details. The stage on which the samples were held was rotated by 360° during the run, and 2001 projections of the material were taken. The orthoslices are then used to reconstruct a 3D image of the sample (see Figure 9.13). Avizo 6.3 software enabled the visualisation and manipulation of the data to obtain qualitative and quantitative information on structural images of the materials.

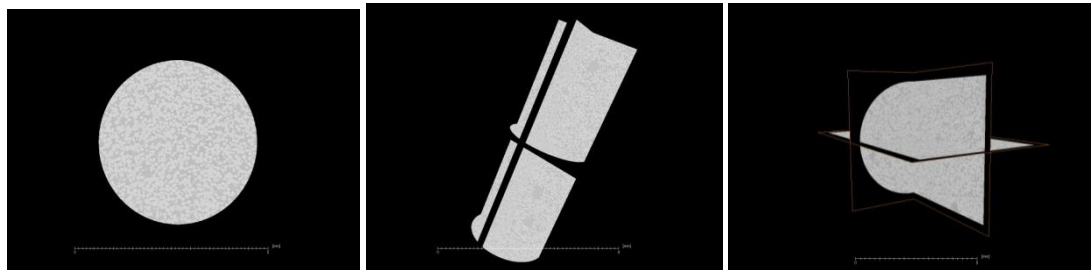


Figure 9.13: X-ray tomography images of orthoslices of porous PMMA materials made using 8.86 wt % showing an orthoslice in the x plane and orthoslices in the x,y plane. Each orthoslice is built up around a single point allow a 3-D image to be recreated.

Due to limited availability of the equipment a select few materials were chosen to evaluate the scope of the technique with respect to porous PMMA and ligament visualisation. The following variants were subjected to 3D X-ray tomography (see Table 9.1 for formulations):

- A sample made with Triton X100 as a surfactant at 3.46 wt % (KA080)
- A sample made with Triton X100 at 1.34 wt % (KA085)
- A sample made with Lutensol TO109 at 4.45 wt % (KA128)
- A sample made with Lutensol TO109 at 0.36 wt % (KA146)
- A sample made with 11.65 wt% MMA using Lutensol TO3 as a surfactant (KA106)
- A sample made with 8.59 wt% MMA using Lutensol TO3 as a surfactant (KA103)
- A sample made with 11.60 wt% MMA using Triton X100 as a surfactant (KA113)

- A sample made with 8.84 wt% MMA using Triton X100 as a surfactant (KA059)
- A material made with 2,500 molecular weight PMMA beads (KA136)
- A material made using styrene as an alternative monomer to MMA (KA071)
- A material made with 1.04 wt % Triton X100, pre and post compression testing (KA070).

Table 9.1: Blend formulations for X-ray tomography samples

Material Description (Sample code)	Monomer /g	Surfactant Name	Surfactant/ g	Water/ g	PMMA/g
Triton X100 at 3.46 wt% (KA080)	146.66	Triton X100	50.00	439.33	805.41
Triton X100 at 1.34 wt % (KA085)	146.66	Triton X100	19.00	439.33	805.41
Lutensol TO109 at 4.45 wt % (KA128)	146.66	Lutensol TO109	65.00	439.33	805.41
Lutensol TO109 at 0.36 wt % (KA146)	146.66	Lutensol TO109	5.00	439.33	805.41
11.65 wt% MMA with Lutensol TO3 (KA106)	219.99	Lutensol TO3	18.79	439.33	805.41
8.59 wt% MMA with Lutensol TO3 (KA103)	89.42	Lutensol TO3	18.79	439.33	805.41
11.60 wt% MMA with Triton X100 (KA113)	242.00	Triton X100	73.22	439.99	1329.67
8.84 wt% MMA with Triton X100 (KA059)	106.77	Triton X100	73.22	439.33	585.75
2,500 molecular weight PMMA beads (KA136)	146.66	Triton X100	73.22	439.33	805.41 (2,500MW)
Styrene as a monomer (KA071)	146.66 (Styrene)	Triton X100	73.22	439.33	805.41
1.04 wt % Triton X100, compression samples (KA070)	146.66	Triton X100	14.64	439.33	805.41

9.3.1 Varying the Surfactant Level

Four different materials were analysed and the images reconstructed using the technique detailed in Chapter 3. The reconstructed images show a highly porous material with an interconnected pore network (see Figure 9.14). Open and closed pores can be segregated allowing for the open (blue) and closed (pink) to be differentiated from each other. Open pores allow a continuous channel of communication with the external body”, allowing flow

of a liquid or a gas through them[37], hence it is through these pores from which the water is extracted from the clay slip thereby drying the ceramic artefact. Closed pores are isolated from the external phase by a solid material therefore they do not help with the drying of the clay slip. Closed porosity reduces the density of the material and have the potential to weaken the mechanical properties of the porous PMMA causing a detrimental effect on the mechanical properties.

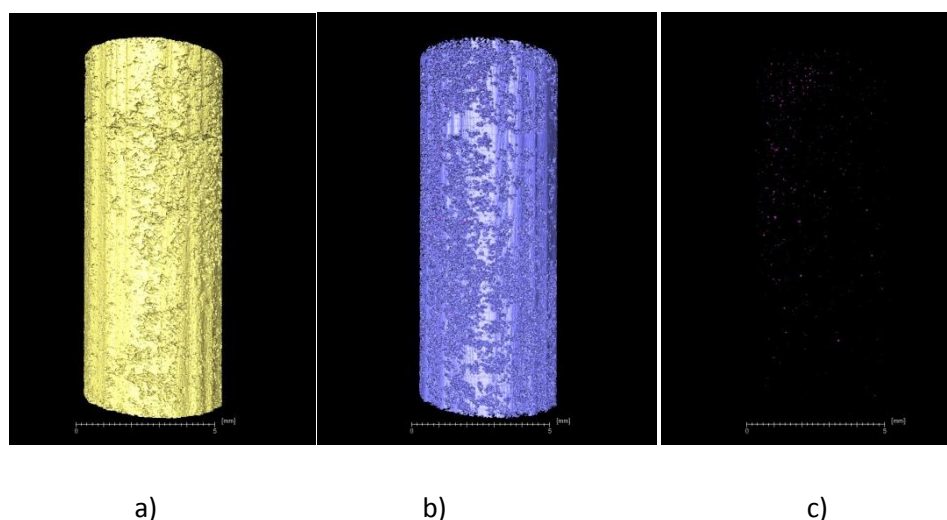
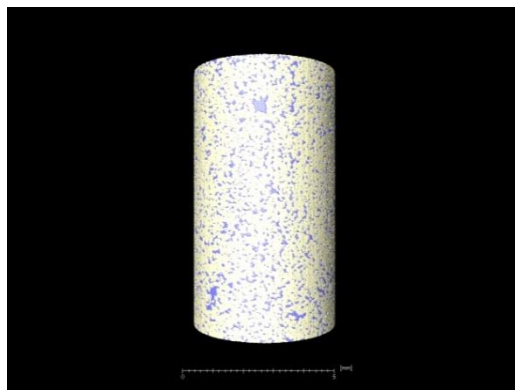


Figure 9.14: X-ray tomography segmentation of a porous PMMA material made with 0.36 wt % of Lutensol TO109 with 146.66 g of MMA a) the PMMA material beads and ligaments b) the open porosity c) the closed porosity

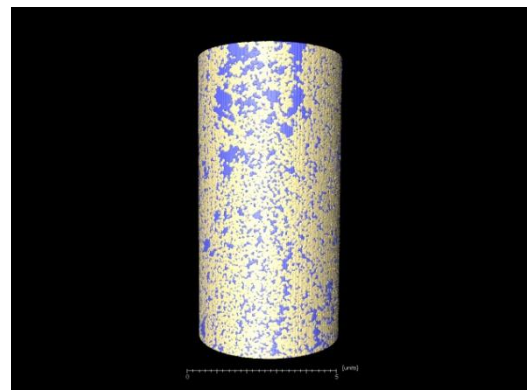
Table 9.2 compares porous PMMA materials made with two different surfactants (Lutensol TO109 and Triton X100) at two different weight percentages. All the materials have a high percentage of open porosity with negligible levels of closed porosity indicating a highly networked pores system for the efficient and effective removal of water from the clay slip enabling rapid drying times to be achieved. The sample made with Lutensol TO109 at 4.45 % shows a comparably higher pore volume, however this is still minute when compared to the overall porosity and is most likely due to small air pockets formed in the processing of the materials. This is further highlighted by the difficulty in observing the pink coloured areas in the Figures 9.15 and 9.16 which show reconstructed images.

Table 9.2: Percentage porosity obtained from segmentation analysis of reconstructed X-ray images with different levels of surfactant

Sample Name	Open Pore Volume/ %	Closed Pore Volume/ %	Total Porosity/ %
3.46 (High) wt % of Triton X100	22.479	0.004	22.482
1.34 (Low) wt % of Triton X100	28.496	0.002	28.498
4.45 (High) wt % of Lutensol TO109	22.314	0.219	22.533
0.36 (Low) wt % of Lutensol TO109	27.284	0.000	27.284

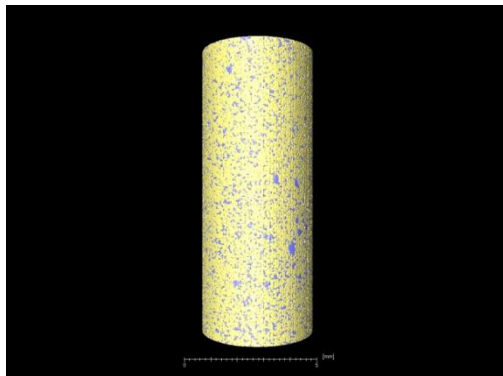


a)

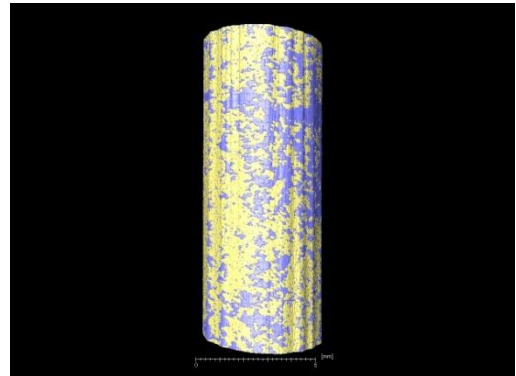


b)

Figure 9.15: Reconstructed images for materials made with a) 3.46 wt % of Triton X100 and b) 1.34 wt % of Triton X100 where blue signifies pores and cream the PMMA (beads and ligaments)



a)



b)

Figure 9.16 Reconstructed images for materials made with a) 4.45 wt % of Lutensol TO109 and b) 0.36 wt % of Lutensol TO109 blue signifies pores and cream, PMMA (beads and ligaments)

Samples with lower level of surfactant were found to have a higher porosity than those with higher levels of surfactant for the four materials when tested by X-ray tomography. This bares no correlation to results obtained from water uptake results which show no variation in porosity with varying the surfactant level. However, both results have to be interpreted with caution. X-ray tomography results are only available on 4 samples of

which on a small section of the overall material made is viewed. Water uptake results are averaged over 5 samples taken from all different areas of the material (see Appendix 1.0). However, the technique is simplistic and air can get trapped in pores with small openings. Alternative pore measuring techniques were explored however all have positive and negative points as discussed in Chapter 2 so were not developed further. It is expected that the increase in porosity observed by X-ray tomography when the surfactant level decreases is due to the increased incorporation of air in mixing process and the more accurate measuring technique which is able to pick up these smaller pores.

9.3.2 Variation of MMA content

Four different materials underwent 3D X-ray tomography, and the images reconstructed using the technique laid out in Chapter 3. These reconstructed images clearly show a difference between materials with low levels of MMA and those with higher levels of MMA (see Figure 9.17), where the PMMA beads and ligaments are coloured cream and the pores blue.

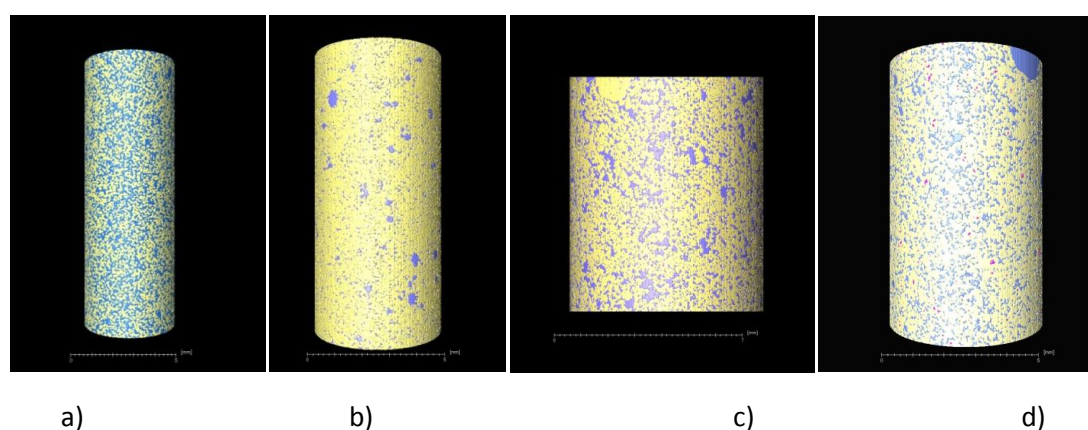


Figure 9.17: Reconstructed 3D images of materials made with a) Triton X100 and MMA at 8.59 wt%, b) Triton X100 and MMA at 11.65 wt%, c) Lutensol TO3 and MMA at 8.59 wt%, and d) Lutensol TO3 and MMA at 11.60 wt%.

As before, the pores are divided into open (blue) and closed pores (pink). The segregation of porosity is most obvious when samples made with low levels of MMA are used (8.84 wt %) and Lutensol TO3 is used as a surfactant (see Figure 9.18 and Table 9.4). However, Table 9.4 highlights that the closed pore volume makes up a small percentage of the overall porosity indicating that the porous PMMA materials are largely formed with a network of open pores

Table 9.3: Percentage porosity obtained from segmentation analysis of reconstructed X-ray images with different levels of surfactant

Sample Name	Open Pore Volume/ %	Closed Pore Volume/ %	Total Porosity/ %
High wt % of MMA with Triton X100 (11.65)	24.41	0.00	24.41
Low wt % of MMA with Triton X100 (8.59)	43.63	0.01	43.63
High wt % of MMA with Lutensol TO3 (11.60)	25.76	0.26	26.11
Low wt % of MMA with Lutensol TO3 (8.84)	30.45	0.36	30.80

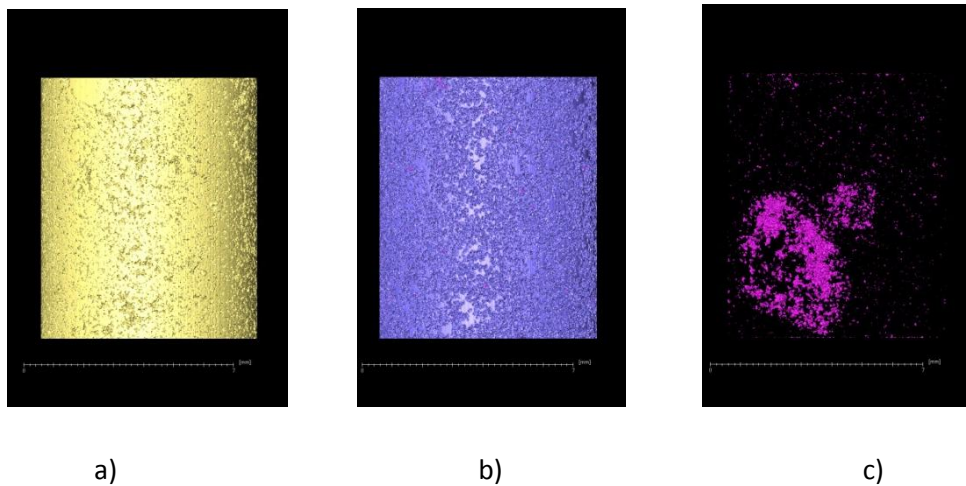


Figure 9.18: X-ray tomography segmentation of a porous PMMA material made with 8.84 % MMA with Lutensol TO3 showing a) the PMMA beads and ligaments b) the open porosity c) the closed porosity

Figure 9.18, indicates the collation of closed porosity in the bottom left hand side of the material with 8.84 % MMA made using Lutensol TO3 as a surfactant as depicted by the pink colouration. In this case, the non-uniform distribution of the closed pores is an anomaly with other samples indicating a homogenous distribution of closed pores where distinguishable. Therefore, it is most likely that in this case the formation of closed pores is due to a processing error in the formation of the sample whereby larger than normal incorporation of air was trapped in the sample in mixing. Similar air bubbles have also observable by SEM in samples where low levels of surfactant are used, see Figure 9.19.

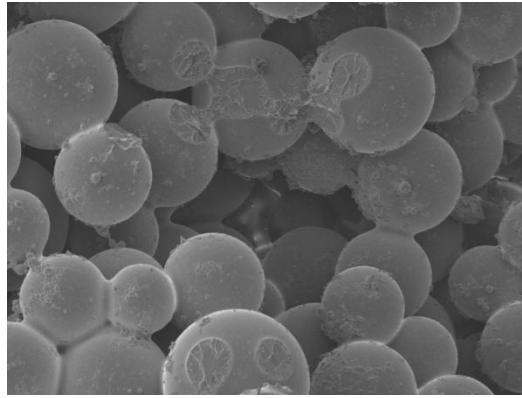


Figure 9.19: SEM image of a large pores most likely caused by the trapping of air in the mixing stage of the materials for a sample with 8.84 wt % MMA with Lutensol TO3

Samples made with higher levels of MMA with Lutensol TO3 and samples made with Triton X100 indicate barely visible levels of closed pores, see Figure 9.20

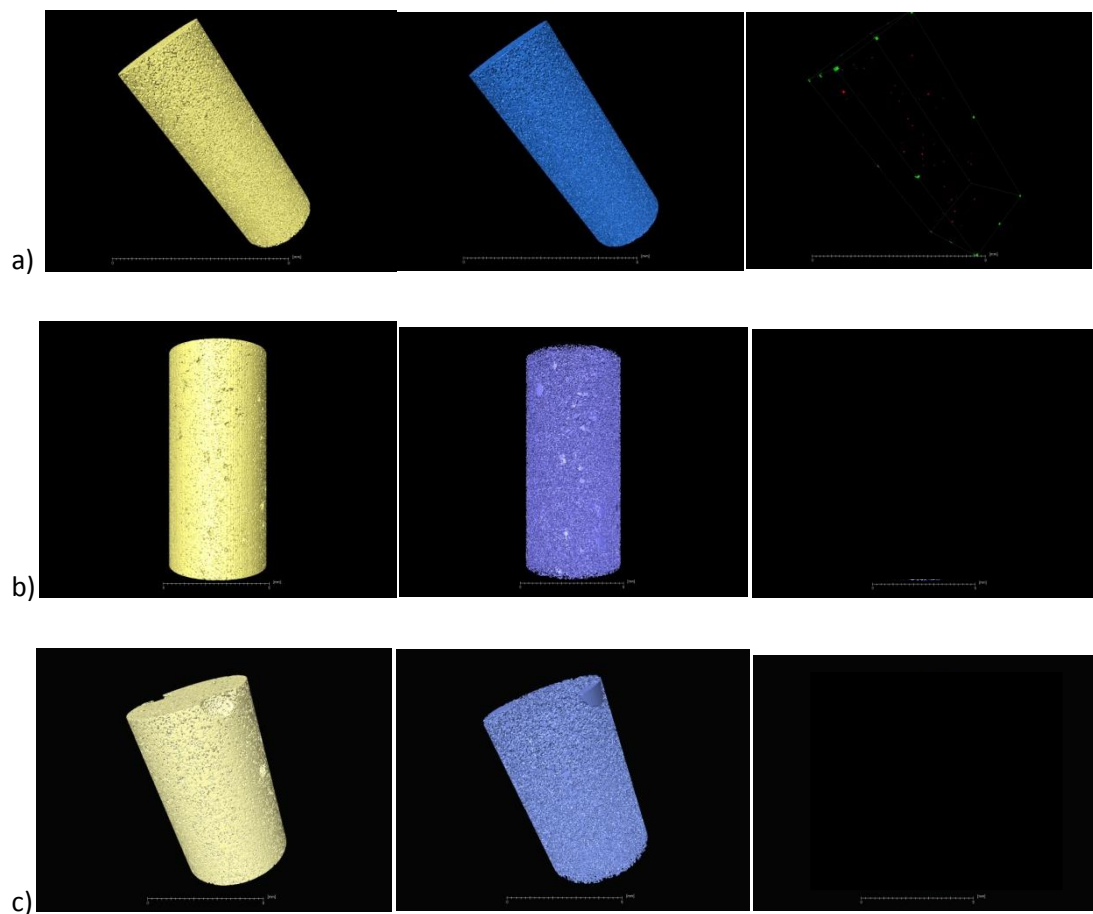


Figure 9.20: X-ray tomography images selecting the polymer, the open pores and the closed pores for materials made with a) 8.59 wt% of MMA with Triton X100 b) 11.65 wt% of MMA with Triton X100 and c) 11.60 wt% of MMA with Lutensol TO3

Segmentation of the block to a smaller area allows for increased processing of the sample using Avizo Fire software. In addition, if it is assumed that the pore width is proportional to the fluid flow rate through the material, a map can be constructed for the pore network where lighter areas signify faster flow (see Figure 9.21).

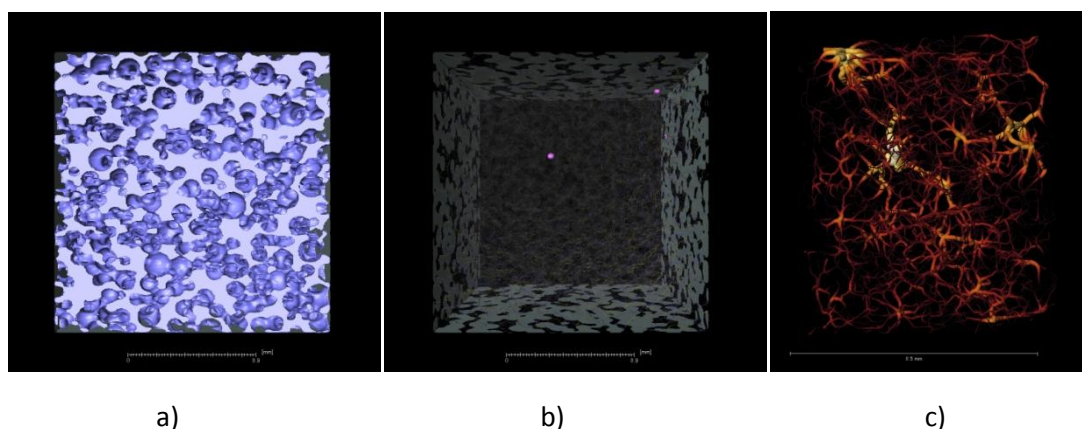


Figure 9.21: X-ray tomography segmentation of a porous PMMA material made with 11.65 % MMA with Triton X100 showing a) the open porosity b) the closed porosity and c) the interconnected porous network when the lighter areas signify higher flow through the area based on pore width.

The interconnectivity and thickness of pore channels can be compared between samples made with different MMA contents, see Figure 9.22. The images reinforce the experimentally measured differences in porosity, with higher levels of MMA restricting the pore channels

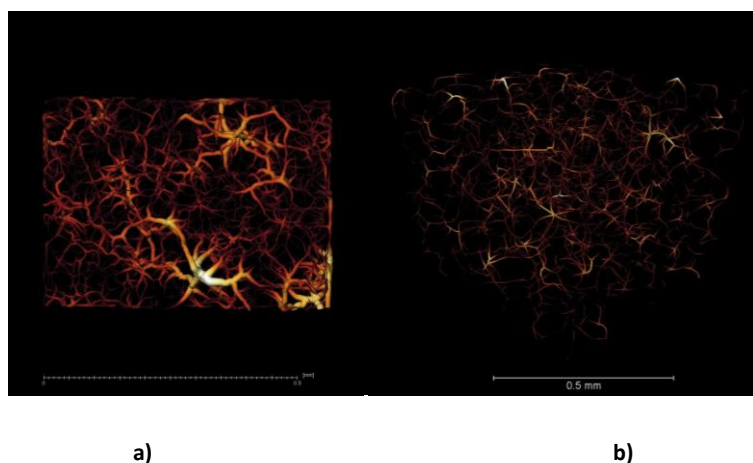


Figure 9.22: X-ray tomography images highlighting pore channels in materials with a) low levels of MMA (8.95 wt%) and b) high levels of MMA (11.95 wt%) with Triton X100

As with previous materials, the X-ray tomography values for porosity can be compared to permeability and porosity values obtained from water uptake and lab experimental data, see Table 9.4.

Table 9.4: Comparison of porosity and permeability data obtained from X-ray tomography and lab experiments for materials with varying MMA levels

Sample Name	Open porosity as obtained by X-ray / %	Open porosity as obtained by water uptake / %	Permeability (Standard Deviation)/ Darcy
High wt % of MMA with Triton X100 (11.65)	24.41	24.47 (2.40)	0.44 (0.01)
Low wt % of MMA with Triton X100 (8.59)	43.63	33.60 (4.32)	6.14 (0.72)
High wt % of MMA with Lutensol TO3 (11.60)	25.76	19.23 (2.83)	0.56 (0.10)
Low wt % of MMA with Lutensol TO3 (8.84)	30.45	29.24 (2.74)	7.39 (0.44)

Comparison between the data highlights that both techniques differentiate between materials made with varying levels of MMA. However, the numerical values obtained are very different. As previously discussed, this may be due to errors in the simplistic water uptake measurements, where air can become trapped in the specimen resulting in a lower porosity value being obtained. X-ray tomography also has higher resolution and may pick up smaller pores in the materials.

Avizo Fire software was used to analyse the segregation micrographs layer-by-layer enabling the porosity to be calculated and graphically represented in each layer (see Figure 9.23). The sample with high levels of MMA shows a gradual decrease of porosity through the block. This indicates that the sample was not entirely homogeneous, which could explain the variability in water uptake measurements. Slicing through the reconstructed blocks reinforces previous observations which indicate that due to the high viscosity in the production of “High MMA (X100)”, there is inclusion of large voids of trapped air (see Figure 9.24). Similar voids have been observed in SEM micrographs (see Figure 9.25).

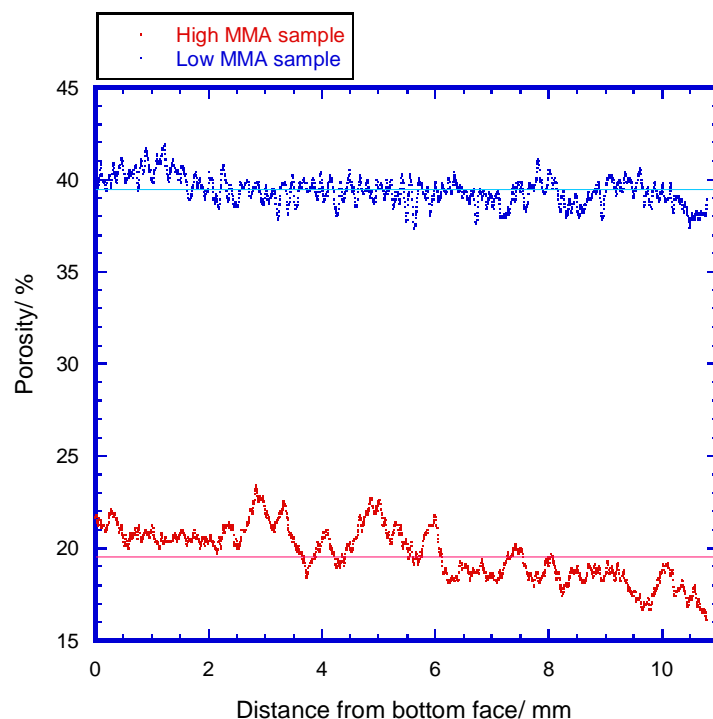


Figure 9.23: Layer by layer porosity from X-ray tomography for sample with high levels of MMA (11.60 wt%) and low levels of MMA (8.84 wt%) made with Triton X100 as surfactant. Straight lines indicate the average value of porosity.

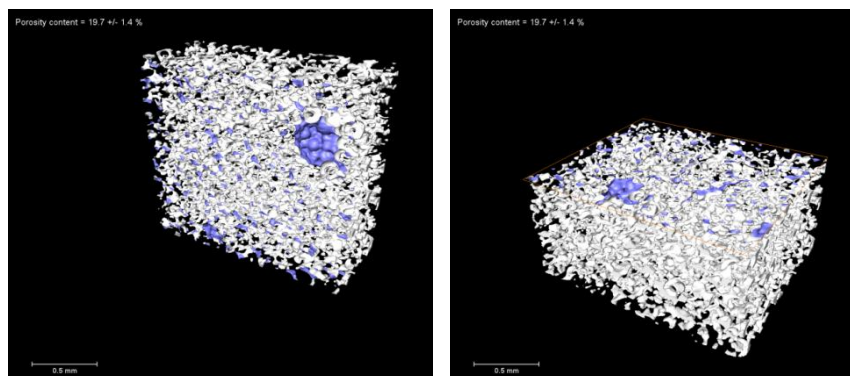


Figure 9.24: X-ray Tomography reconstructed images indicating large voids in the matrix material of materials with high levels of MMA (11.60 wt%) with Triton X100 as a surfactant

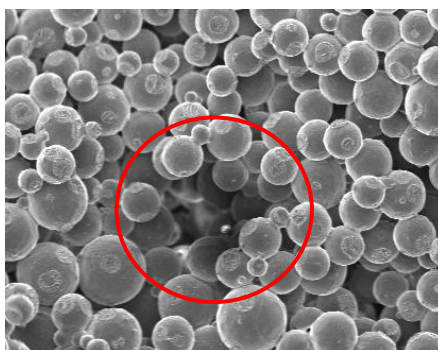


Figure 9.25: SEM images of materials with high levels of MMA (13.35 wt%) indicating large air void

A similar graphical representation of porosity can be created for materials with differing levels of MMA with Lutensol TO3 (see Figure 9.26). The division of the data into layers shows a definitive difference between the two samples with different levels of MMA even through there is considerable variation observed throughout the test piece. Particular variation is observed for the sample with the low level of MMA, however this is a weaker sample than the other materials which has an 8 mm diameter as supposed to 5 mm to increase the stability of the test piece.

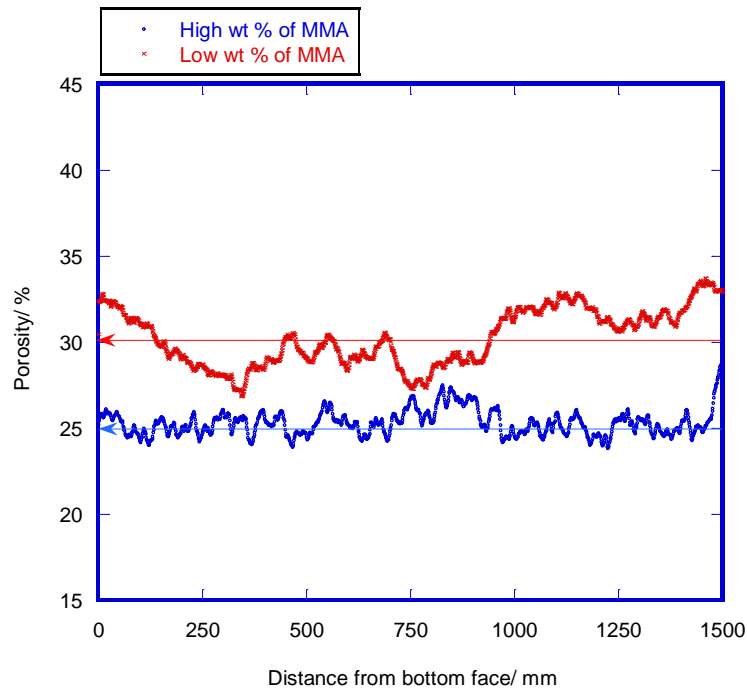


Figure 9.26: Layer by layer porosity from X-ray tomography samples for high (11.65 wt %) and low (8.58 wt %) levels of MMA with Lutensol TO3 as surfactant. Straight lines indicate the average value of porosity.

Fabien Nardoux, an MSc student from Ecole Nationale Supérieure d'Ingénieurs de Limoges (ENSIL) also analysed samples made using varying levels of MMA with Triton X100 as a surfactant. To allow for faster determination of properties and smaller data file sizes, Fabien analysed cubes measuring 1 mm x 1 mm x 1 mm of the X-ray specimen to ease segregation of the data (see Figure 9.27). Once segregated, the data was analysed to obtain porosity, thickness of pore channels and bead size. Segregation required the user to differentiate between elements of the material by using differences in their greyscale value. In Figure 9.27 (a), the pore channels have a lower greyscale than the PMMA which is therefore shown as a lighter grey. Based on this, a threshold value can be set using the software (Avizo 6.3), assigning all voxels (a volumetric element representing a 3D

space[264]) below this threshold value to the background (black) whilst selecting the remainder to allow for labelling of the blue highlighted area.

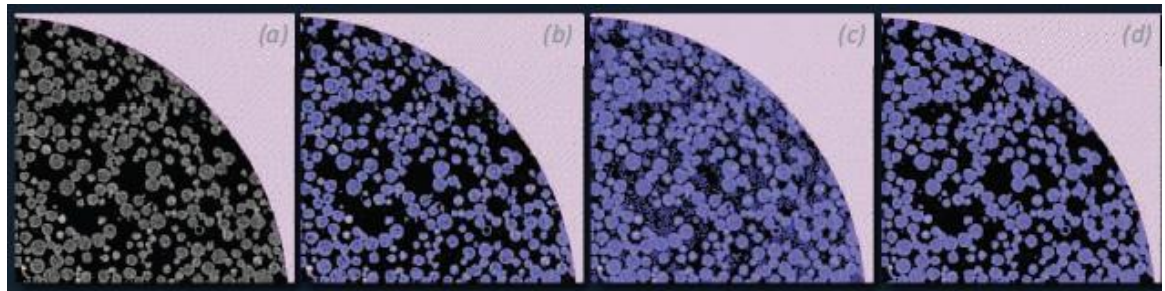


Figure 9.27: Segregation steps: a) section of a porous PMMA specimen b) PMMA segregation with too low a threshold, c) PMMA segregation with too high a threshold value d) PMMA segregation with an ideal threshold [265]

Once the different areas have been labelled, 3D images can be produced which highlight different materials within the cube (see Figure 9.28), enabling focus on both the polymer and the porosity.

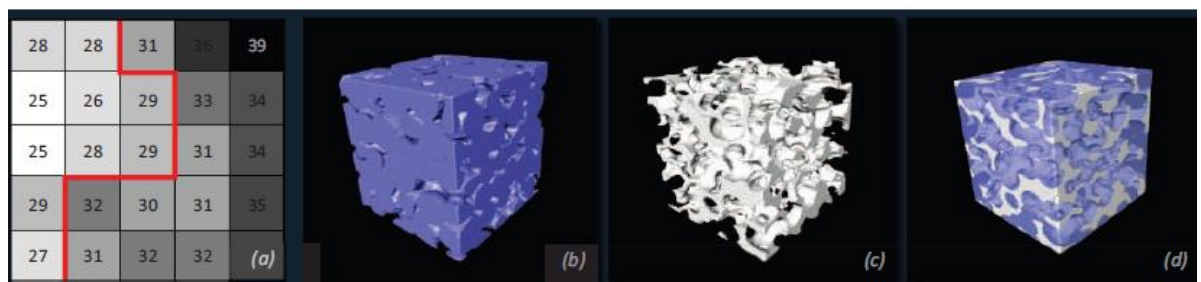


Figure 9.28: a) Representation of the voxel separation with a threshold grey value of 30, b) 3D image of the PMMA in the cube, c) 3D image of the pore network, and d) Assembly of a full 3D image for the material.

Table 9.6 shows comparison of the results obtained from X-ray tomography with those obtained using lab techniques. A graphical representation of the data is shown in Figure 9.29. Porosity by X-ray tomography is shown to be more reproducible with smaller error sources. However, it should be noted that X-ray tomography was only undertaken on one sample specimen whereas water uptake measurements were undertaken on 5 different specimens from different areas of the block of material.

Table 9.5: Comparison of porosity and permeability data determined using X-ray tomography data and laboratory techniques

Wt % MMA	X-ray Tomography		Laboratory Techniques	
	Porosity/ %	Pore Diameter/ mm	Permeability/ %	Porosity / %
8.165	46.00 (0.5)	36	7.09 (0.34)	25.15 (8.53)
8.840	40.00 (0.5)	31	6.14 (0.72)	31.69 (9.66)
9.995	34.00 (0.5)	26	3.39 (0.55)	29.63 (3.33)
10.608	31.00 (0.5)	22	1.26 (0.63)	24.47 (2.40)
10.988	29.00 (0.5)	19	1.46 (0.24)	25.90 (4.41)
11.327	25.50 (0.5)	21	1.41 (0.37)	22.58 (2.15)
11.596	22.00 (0.5)	18	0.44 (0.02)	25.31 (0.72)

A clear trend is observed between materials made with high levels of MMA and those with lower levels of MMA. Increasing the MMA content results in a reduction in the pore diameter as the spaces between the solid PMMA spheres, caused by the random packing arrangement, are being filled by the polymerising monomer. This results in thicker bridges between beads, which reduces the porosity and the pore channel diameter with consequent reduction in permeability. The PMMA bead diameter was also obtained and is in good agreement to that provided by Lucite International, as measured by particle size distribution.

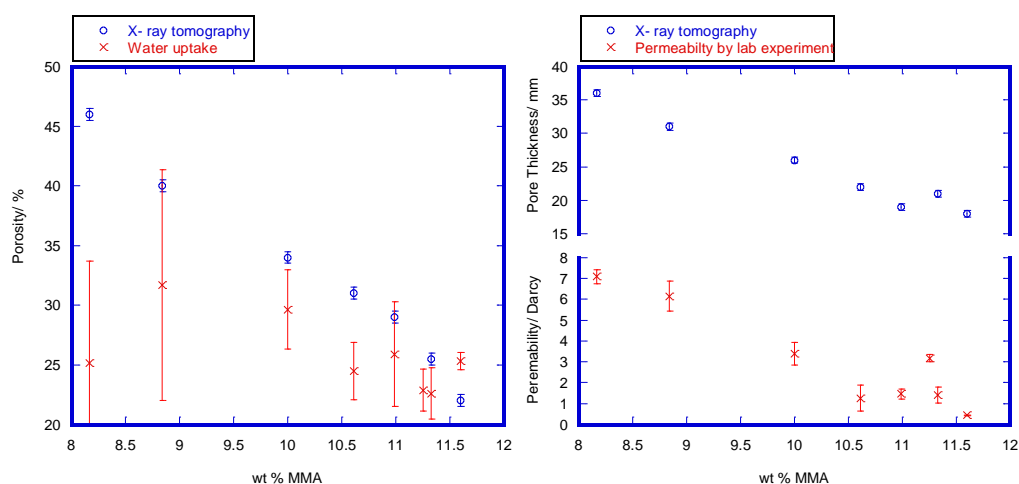


Figure 9.29: Graphical representation for variation of porosity (lhs) and permeability (rhs) with wt % MMA form X-ray tomography and laboratory experiments

9.3.3 Additional Samples Analysed using X-ray Tomography

A selection of additional materials were analysed using X-ray tomography. As with previous samples, the data obtained from X-ray tomography has been compared with that obtained by laboratory-based experimental techniques (see Table 9.6). The data indicate that no correlation can be observed between porosity values obtained by water uptake and those by X-ray tomography. This is most likely due to the considerable differences in measurement between the two techniques, where one is based upon mass differences compared to volume and the other on an image grey scale value. Both show errors, with water porosity being influenced by trapped air in the sample and X-ray tomography by difficulties when segmenting the pores from the background and that of the beads. This can lead to both overestimation and under-estimation of porosity. However, as shown in previous sections (9.3.2 and 9.3.2), when a range of materials are taken where just one factor is changing, a sliding scale of porosity and ligament thickness can be obtained from both techniques.

Table 9.6: Summary of porosity and permeability measurements obtained for additional samples analysed by X-ray tomography

Sample Name	Open porosity as obtained by X-ray / %	Open porosity as obtained by water uptake / %	Permeability (Standard Deviation)/ Darcy
A material made with 2,500 molecular weight PMMA beads	30.16	30.12	4.65 (0.32)
A material made using styrene as an alternative monomer to MMA	37.78	31.97	5.37 (0.46)
A material made with 1.04 wt % Triton X100, pre compression	23.63	33.24	3.87 (0.85)
A material made with 1.04 wt % Triton X100, post compression	26.31	34.20	n/a

9.4 Conclusions

Imaging of porous PMMA has been shown to be possible by the use of optical microscopy, SEM and X-ray tomography. Optical microscopy was found to be limited in its use, with the resolution of the images being limited by the depth of the sample. Poor depth resolution caused blurring of the samples resulting in little inference to the ligament volume and linkages between the beads. Therefore other techniques were sought. SEM has been shown to be a quick and powerful technique which allows for the imaging of materials and comparison of ligaments and polymer coverage. However, the technique requires a fracture surface which results in the breaking of ligaments and distortion of samples. X-ray tomography is a highly time consuming process, because, although obtaining the data is

fairly quick, analysis is complex and often requires specialist input. However, the technique is non-destructive and gives valuable 3-D images which are informative and visually striking.

On selected samples, X-ray tomography provides a valuable insight into the pore network and its interconnectivity. Unfortunately, due to the similar densities of PMMA beads and the ligaments, the technique is unable to quantify the volumes of ligaments in a sample without significant and unrealistic assumptions which, if undertaken, would give unreliable data. The overriding conclusion is that the technique can provide an insight into the materials which SEM or other visualisation techniques are not able to, such as the interconnectivity of pores and the structure throughout different layers of the material. In order to get the high resolution required to visualise the ligaments, small specimens (20 mm by 5 mm diameter cylinder) were utilised with the assumption of mould homogeneity. Materials made throughout this work have been found to be relatively homogenous with SEM and X-ray tomography images revealing that the pores distribution is fairly even through the materials. Only in one sample in which difficulties were found in processing where levels of surfactant were very low was the distribution of pores and hence properties uneven throughout the block of material. In general it is therefore safe to assume that the materials are homogenous throughout and hence properties and pore values obtained on the small section of material can be assumed to be representative of the material as a whole. Despite its limitations, X-ray tomography added depth to the project work and highlighted the intricacies of porous PMMA. A DVD of additional images and videos is attached to the back cover of the thesis.

10. Conclusions and Suggestions for Further Work

Porous PMMA materials have been synthesised for use in the pressure casting of ceramics. The materials have been shown to be significantly stronger than their gypsum competitors and are able to withstand higher stresses under compression. In addition, performance in compression testing was shown to be comparable with cyclic fatigue testing in which the porous PMMA materials lasted in excess of 10,000 cycles under stresses of 14 MPa, well above that of their standard operating stress of 0.5-4 MPa[39]. Porosity was shown to be homogeneous in well formulated samples with tailoring of this property possible through variation in MMA wt %. The work contained in this thesis highlights the differences in the properties of porous PMMA as the components in the formulation are varied, allowing for better design of mould and higher performance. In addition, the work has enabled the mechanism for the polymerisation process and the formation of pores to be quantitatively defined. The major results and important conclusions from this project are summarised below.

10.1 Mechanistic Understanding

Porous PMMA is formed by the binding of PMMA particles together via ligaments which are formed by the polymerising monomer.

Initially, an emulsion is formed which contains surfactant, water, MMA and BPO. Within the emulsion there are three distinct phases (see Figure 10.1), deduced by studies in which the partitioning of the emulsion was observed:

- An aqueous phase; largely consisting of water with small amounts of dissolved monomer and surfactant.
- A micellar phase; containing monomer-swollen surfactant micelles which have little role in the final product.
- A droplet phase; consisting largely of monomer containing surprisingly large amounts of surfactant and some dissolved water.

The monomer droplets are rapidly dispersed between the beads upon mixing and polymerisation occurs within these droplets. Water is utilised primarily as a carrier medium for the monomer droplets. It prevents the monomer from being in direct contact with the beads for sufficiently long time period to allow for the complete dispersion of the monomer prior to polymerisation.

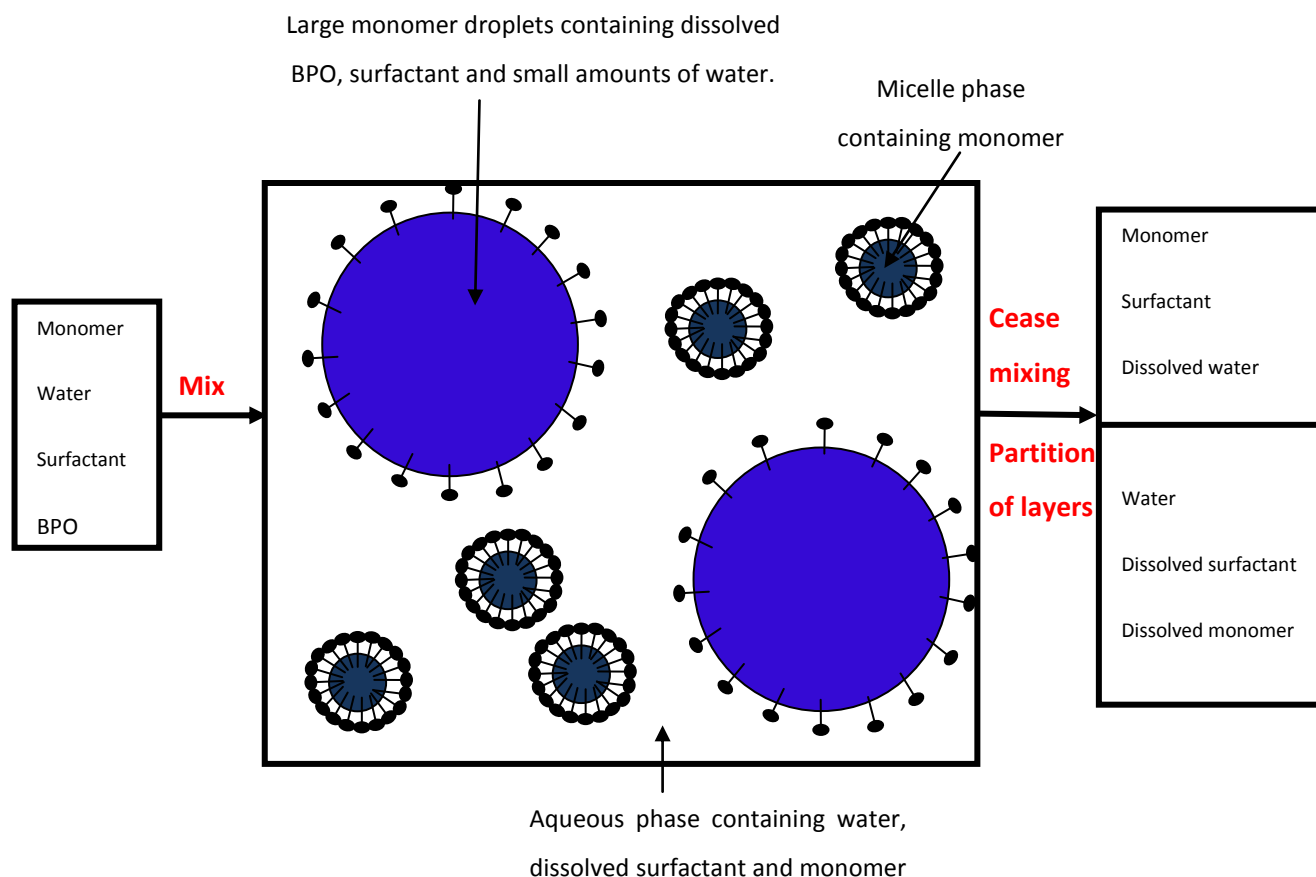


Figure 10.1: Schematic diagram showing partitioning of the emulsion components

Once 3 minutes mixing has passed, DMPT is added to the emulsion. DMPT is the second part of the redox initiator system, which allows polymerisation to occur at room temperature through the donation of an electron from the nitrogen lone pair of the amine to cleave the peroxide bond of BPO. DMPT is not water soluble and, therefore, when it is mixed into the emulsion, it diffuses rapidly into the monomer droplets where it reacts with BPO to initiate polymerisation.

PMMA beads are then added to the emulsion. The dispersed monomer droplets coalesce around the beads at points when they are in close proximity to one another (see Figure 10.2). The viscosity of the monomer ligaments increases rapidly through polymerisation. The polymerisation occurs within the droplets and coalesced droplets in a form of bulk polymerisation and so at levels above 20 % conversion, autoacceleration occurs which increases the temperature of the localised system and therefore increases the rate of polymerisation. The viscosity of the monomer ligaments is also increased by the dissolution of PMMA from the beads into the monomer and by diffusion of MMA into the

PMMA beads. Therefore there is an increase in the polymer concentration within the adjacent ligaments even when no polymerisation is occurring. This inter-diffusion and polymerisation allows for the formation of strong ligaments between the beads. Both processes need to be occurring for strong ligaments to be formed, as highlighted by studies in which crosslinked beads were used, where the resulting porous PMMA material was weak under compression due to the lack of inter-diffusion. The mixture sets when the viscosity of the ligaments is very high and diffusion no longer possible. Polymerisation is completed when the materials are heated at 60 °C for 24 hours, during which the excess BPO thermally decomposes to polymerise any remaining MMA.

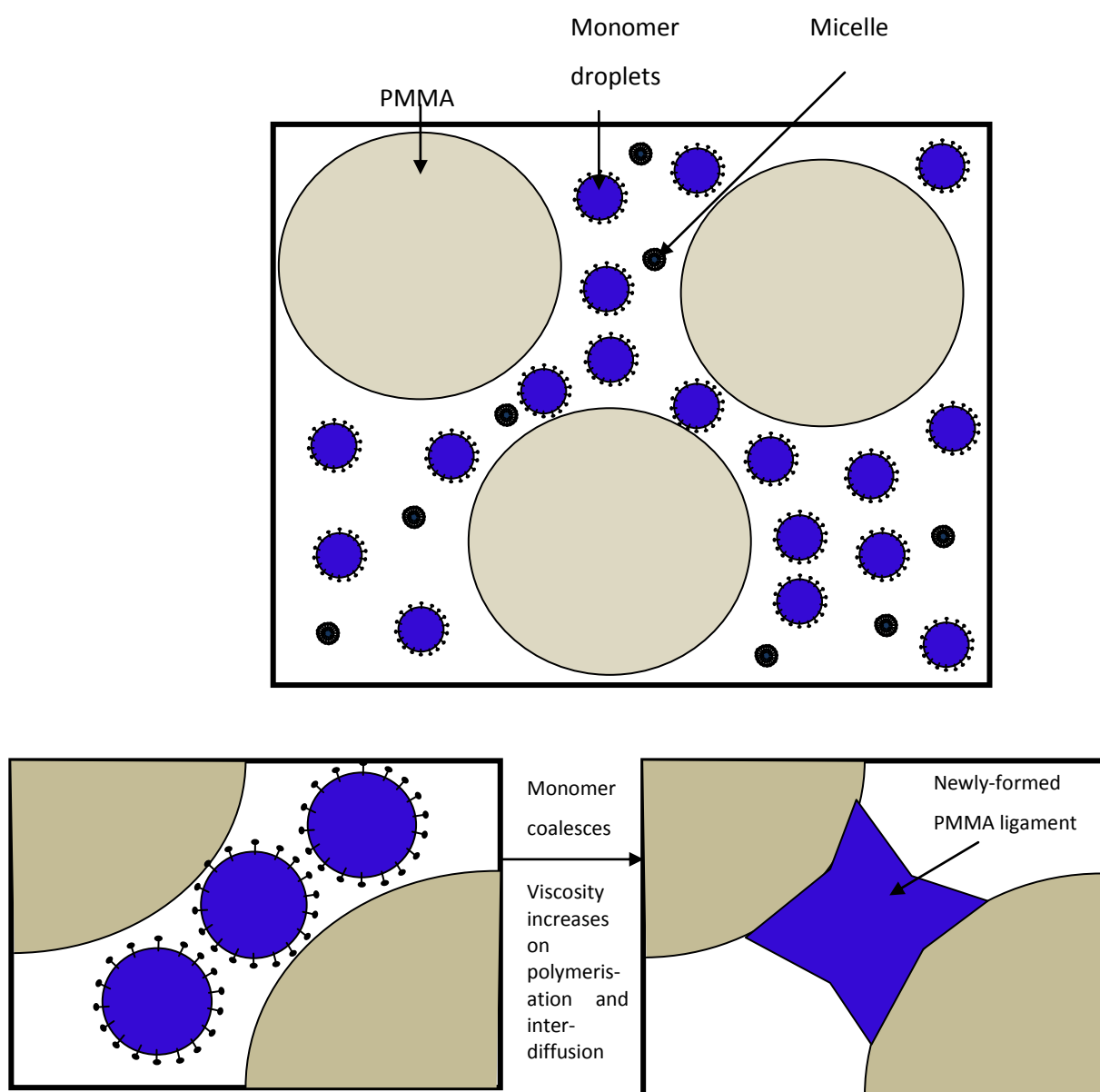


Figure 10.2 Cartoon depicting addition of PMMA beads and formation of ligaments through coalescence of monomer droplets

Surfactant is present in both the monomer droplet phase and the water. When the droplets contact the bead surfaces, the monomer assists diffusion of surfactant into the beads where it plasticises the PMMA decreasing the T_g , but this effect will be small because only a small amount of surfactant is likely to enter the beads. Most importantly, however, the surfactant is present in the MMA droplets/ligaments where its level is sufficient to plasticise the ligaments and therefore weaken the mechanical properties of the materials. The project results highlight that the current commercial levels of surfactant (≈ 5 wt %) are in vast excess of the amount required to form a stable emulsion, and thus surfactant plasticisation of the ligaments readily occurs resulting in weaker materials which fail prematurely in cyclic fatigue and compression testing. The effect of the surfactant on plasticisation is dependent on the level of surfactant in the ligament and the solubility of the surfactant in the monomer.

Porosity is obtained primarily by the close packing of random beads which gives an approximate pore volume of 37 %, which is reduced as the level of MMA is increased. Secondary porosity, significantly larger than the primary pore size, is observed when air becomes trapped in the blend mixture due to a rapid rise in viscosity of the mixture prior to transfer into the mould. Secondary porosity is particularly damaging to the compressive properties of porous PMMA as the large pores readily act as sites for crack nucleation.

Porous PMMA materials are used in the pressure casting of sanitaryware. Current formulations are not competitive in the market when compared to gypsum due to the high material cost and start-up capital required to obtain the equipment. To justify the higher material cost, it is vital that porous PMMA is comparably stronger and can withstand more cycles, hence the higher mould cost can be spread over more ceramic articles, i.e more articles per mould unit. Throughout this work, the strength of ligaments has been found to define the compressive properties of the material, with stronger ligaments resulting in more loading/unloading cycles.

Fundamental studies allowed deeper understanding of the emulsion stage of the polymerisation. The results highlight that a considerable amount of the surfactant is found in the MMA and thus will end up in the PMMA ligaments resulting in plasticisation. Detailed calculations were made from simple inputs including: CMC of the surfactant in water, the concentration of MMA in water, the concentration of water in MMA, and the CMC of the surfactant in an MMA saturated solution. They enabled the amounts of the components in each phase to be derived. Thus, for any formulation, the actual level of

MMA forming the ligaments can be found, and similarly the levels of surfactant can be tailored. This enables a prediction of the final properties of the porous PMMA materials to be obtained prior to making the materials, allowing for the screening of formulations, surfactants and inevitable reduction of waste. In particular, the studies highlighted the gross overuse of Triton X100 in the original formulation provided by Lucite International, which in turn caused a weakening of the ligaments by plasticisation.

10.2 MMA:Water Concentration

Contrary to previous studies, porosity was found to be derived from the close random packing of the PMMA beads. The polymerisation process introduces ligaments which form around the beads and it is these ligaments which control the mechanical properties of the material. The thicker the ligaments, i.e. the more MMA is included in the formulation, the stronger the material and hence the longer the materials last under cyclic testing with little to no deformation of the material and little change in the stress or strain. However, thicker ligaments also result in a loss in permeability and porosity of the material, making the drying process of the mould less efficient and increasing the overall casting time of ceramic bodies. Therefore, a compromise must be achieved between materials high in compressive properties with high MMA levels and good permeability, with larger pore channels made by reducing the MMA content.

10.3 Surfactant

Non-ionic surfactants have been shown to readily plasticise porous PMMA due to a high solubility in both PMMA and MMA. The surfactants therefore readily reduce the T_g of the polymer which weakens its performance in compression testing and cyclic fatigue testing. Partitioning data further indicates a significant proportion of surfactant is present in the MMA layer which readily correlates with the ease of plasticisation of both the ligaments and the porous PMMA. Current levels of surfactant (5 %wt) have been shown to be in vast excess of the required amount needed to obtain a low viscosity and homogenous mixture. Therefore, by reducing the surfactant concentration to 1 %wt, the performance of porous PMMA greatly improves.

The molecular structure of the surfactant was also studied with experiments undertaken on both changing the tail group and the HLB. Changing the tail group from an aromatic to an aliphatic carbon group led to an improvement in the properties of porous PMMA, by better

distribution of the DMPT catalyst through the formation of smaller micelles which creates improved solubilisation. In addition, as phenolic surfactants are under investigation by REACH (an EU regulation on chemicals and their safe use covering registration, evaluation, authorisation and restriction of chemical substances) switching to linear chain ethoxylates would enable the avoidance of potential environmental and legislative issues associated with phenolic surfactants in the future.

Anionic surfactants are insoluble in MMA and hence are an alternative to avoid plasticisation. After initial difficulties in which the DMPT was hindered by the charged sulphonate ion which deactivated the polymerisation initiation reaction, very low levels of anionic surfactant were used to make porous PMMA. The materials were shown to be comparable to materials made with low levels of Triton X100 whilst being able to uphold reasonable mixing viscosities. However, as there were higher levels of residual monomer, present some plasticisation of the ligaments still occurred.

10.4 Alternative Monomers

The substitution of MMA, in part or entirely, by other monomers gave mixed results depending on the miscibility of the monomer in the emulsion containing water, monomer, initiators and a surfactant. Butyl methacrylate formed an unstable water-in-oil emulsion even when alternative surfactants were used, resulting in exceptionally weak materials. Although in part this was expected, as the T_g of butyl methacrylate is lower than that of MMA, the lack of bonding between beads was unexpected with SEM images highlighting incomplete coverage of beads by the polymerised butyl methacrylate. Substitution with styrene was more successful, with particular achievements when Lutensol TO3 was utilised as a surfactant. However, due to the slower rate of polymerisation the production time for making the mould is considerably longer and a significant increase in set time was observed. However, this could be beneficial as the viscosity of the mixture is lower over a considerably longer period of time. Therefore, pouring the mixture into a mould is easier and allows for smaller more detailed articles to be cast.

10.5 Toughening

Toughening attempts undertaken were unsuccessful even with grafting of rubber/PMMA copolymer to additional PMMA. Problems included the non-coalescence of monomer droplets, most likely due to the decrease in size, resulting in the incomplete formation of

ligaments. Rubber-toughening particles (XC42) were observed to aggregate in the ligaments causing areas of high concentration which has a detrimental effect on the compressive properties. Liquid polybutadiene diacrylate similarly weakened the materials, but grafting this monomer to MMA to produce a copolymer gave limited success. Within this work this was not pursued. However, there is significant potential in the area to suggest the continuation of toughening in further work.

10.6 Suggestions for Further Work

Porous PMMA has been found to be a suitable substitute for gypsum in the industrial production of moulds for ceramic sanitary ware. With increased compression resistance and improved cyclic fatigue performance, the initial capital outlay for expensive moulding equipment and increased raw material costs can be spread over a larger number of units resulting in a price-competitive option. This project highlighted significant effects of the surfactant, particularly with reference to the current levels of use, which are exceptionally high and unnecessary causing considerable plasticisation of the ligaments and reduced mechanical properties. In addition, the project has provided new knowledge on key areas of the blend formulation, including the importance of temperature control, dissolution of BPO in the monomer before emulsification with DMPT being added to the emulsion before it is mixing with the beads, the importance of surfactant solubility in monomer, and the importance of diffusion of the PMMA from the beads into the polymerising ligaments and the overall monomer to bead ratio. However, there is still room for improvements to the formations, particularly in the area of toughening which should further reduce the cost per unit by increasing the mould life. Literature indicates that toughening is a subtle art but once achieved has the potential to further the competition of porous PMMA moulds with gypsum. In addition, the scoping of alternative monomers has been limited within this project, and tailoring of the moulds could be further achieved by selecting monomers with desirable properties and copolymerising them with MMA. Most importantly, it should be noted that it is the ligaments which control the properties of the materials; hence it is these which should be targeted to improve the performance of porous PMMA. Furthermore, this thesis has focussed on the use of porous PMMA in the pressure casting of ceramics. However, this material, and work contained herein, could have potential uses elsewhere, including the preparation of bone cements and dental implants.

11. References

1. Schleicher HM. Forms For Slip-casting Ceramics and Method of Making the Same. Google Patents, vol. US 2303303. 1942.
2. Ergun Y, Dirier C, and Tanoglu M. Materials Science and Engineering a-Structural Materials Properties Microstructure and Processing 2004;385(1-2):279-285.
3. Dortmans A, Fischer H, and Nelissen R. Cfi-Ceramic Forum International 2002;79(1-2):E45-E48.
4. Will G. Molding of Ceramic Materials. United States, 1988.
5. De Wijn J. Journal of Biomedical Materials Research 1976;10(4):625-635.
6. Association TNADC. Die casting FAQs. vol. 2012. Wheeling, Illionis: The North American Die Casting Association, 2012.
7. Britannica E. Die Casting. vol. 2012. London: Encyclopedia Britannica, 2012.
8. Callister W. Materials Science and Engineering, 6th Edition ed. New York: John Wiley and Sons Inc, 2003.
9. Ishizaki K, Komarneni S, and Nanko M. Porous Materials: Process Technology and Applications. London: Chapman & Hall, 1998.
10. Lyckfeldt O. Slip Casting- Product Sheet. vol. 2009. Mölndal, Sweden: Swerea-IVF, 2007. pp. Product Sheet on Slip Casting.
11. Lyckfeldt O. Types of Slip Casting. MoIndal, Sweden: IVF-Swerea, 2007.
12. AG fur Keramische. Production of a Plastic Material Sutible for Use as a Material for Casting Moulds. US 13788866. US, 1971.
13. Leach B. Slurry Solution for Sanitaryware. Ceramic Industry: Ceramic Industry, 2000.
14. Deakin RN, British Caramic Research Limited. Slip Casting. WO 97/35698. Great Britain, 1997.
15. Bauer W, Ritzhaupt-Kleissl HJ, and Hausselt J. Ceramics International 1999;25(3):201-205.
16. Young R and Lovell P. Introduction to Polymers, 3rd ed. Boca Ranton, FL: CRC Press, Taylor and Francis Group, 2011.
17. Braun D. International Journal of Polymer Science 2009;2009:10.
18. Jenkins A, Kratchvil P, Stepto R, and Suter U. Pure & Appl. Chem 1996;68(12):2287-2311.
19. Clayden J, Greeves N, Warren S, and Wothers P. Organic Chemistry. Oxford: Oxford University Press, 2001.
20. Zanocco A, Canetem A, and Melendez M. Boletín de la Sociedad Chilena de Química 2000;45:123-129.
21. Horner L. Journal of Polymer Science 1955;18(89):438-439.
22. Pryor WA and Hendrickson Jr WH. Tetrahedron Letters 1983;24(14):1459-1462.
23. Sato T and Otsu T. Die Makromolekulare Chemie 1977;178(7):1941-1950.
24. Brauer G. Chemical Abstracts 1981;94(94):395-409.
25. Horner L and Anders B. Chemische Berichte 1962;95(10):2470-2484.
26. Moad G and Solomon D. The Chemistry of Radical Polymerization. Oxford: Elsevier Science, 2005.
27. Cowie J. Polymers: Chemistry and Physics of Modern Materials, 2nd ed. Bath: Nelson Thornes Ltd, 2001.
28. Alger M. Polymer Science Dictionary. Polymer Science Dictionary. Padstow, Cornwall: Chapman and Hall, 1997. pp. 628.

29. Young RJ and Lovell PA. Introduction to Polymers- 3rd Edition. Boca Ranton, FL: CRC Press, Taylor and Francis Group, 2011. pp. Figure 4.8: Schematic Diagram Showing the 3 Phases that Exist at the Start of Emulsion Polymerisation.
30. Smith W and Ewart R. Journal of Chemical Physics 1948;16:8.
31. Harkins WD. Journal of the American Chemistry Society 1947;69(6):16.
32. Challa G. Polymer chemistry: An Introduction. New York ; London: Ellis Horwood, 1993.
33. Pascual B, Vázquez B, Gurrachaga M, Goñi I, Ginebra MP, Gil FJ, Planell JA, Levenfeld B, and Román JS. Biomaterials 1996;17(5):509-516.
34. Sing K, Everett D, Haul R, Moscou L, Pierotti R, Rouquerol J, and Siemieniewska T. Pure & Appl. Chem 1984;57(4):603-619.
35. Haber J. Pure & Appl. Chem 1991;63(9):1227-1246.
36. Mays T. A New Classification of Pore Sizes. In: P.L. Llewellyn FR-RJR and Seaton N, editors. Studies in Surface Science and Catalysis, vol. Volume 160. Amsterdam: Elsevier, 2007. pp. 57-62.
37. Rouquerol J, Avnir D, and Fairbridge C. Pure & Appl. Chem 1994;66(8):1.
38. Giesche H. Particle and Particle System Characterisation 2006;23:1-11.
39. Ergun Y. Development and Charaterisation of PMMA Based Porous Materials Used for High Pressure Casting of Sanitaryware Ceramics. Science Faculty, vol. Masters Degress. Urla, Turkey: Izmir institute of Technology, 2004.
40. Rasband WS. ImageJ. Maryland, USA: US National Institute of Health, 1997.
41. Yaghi OM, O'Keeffe M, Ockwig NW, Chae HK, Eddaoudi M, and Kim J. Nature 2003;2003(423):705-714.
42. Zhao X, Xiao B, Fletcher A, Thomas K, Bradshaw D, and Rosseinsky M. Science 2004;306:1012-1015.
43. Lee J, Farha O, Roberts J, Scheidt K, Nguyen S, and JT H. Chemical Society Reviews 2009;38:1450-1459.
44. Bojdys MJ, Briggs ME, Jones JTA, Adams DJ, Chong SY, Schmidtman M, and Cooper AI. Journal of the American Chemical Society 2011;133(41):16566-16571.
45. Wright P. Macroporous Framework Solids. Cambridge, UK: Royal Society of Chemistry, 2008. Parts of the Framework Structure of Natually Occuing Zeolites.
46. Baerloche C and McCuske L. Database of Zeolite Structures. vol. 2013: Structure commission fo the International Zeolite Accociation (IZA-SC), 2001.
47. Dienst E, Bakker W, JFJ E, Verboom W, and Reinhouldt D. Pure & Appl. Chem 1993;65(3):387-392.
48. Côté AP, Benin AI, Ockwig NW, O'Keeffe M, Matzger AJ, and Yaghi OM. Science 2005;310(5751):1166-1170.
49. Uribe-Romo FJ, Hunt JR, Furukawa H, Klöck C, O'Keeffe M, and Yaghi OM. Journal of the American Chemical Society 2009;131(13):4570-4571.
50. Uribe-Romo FJ, Hunt JR, Furukawa H, Klöck C, O'Keeffe M, and Yaghi OM. JACS Communications, 2009, 131 (13): 4570-4571.
51. Zaki HS and Kamel IL. Journal of Dental Research 1976;55(2):272-280.
52. Todd RH, Allen DK, and Alting L. Manufacturing Process Reference Guide, 4th Edition ed. New York, USA: Industrial Press Inc., 1994.
53. Reed JS. Introduction to the Principles of Ceramic Processing, 2nd ed. New York: Wiley Interscience, 1995.
54. Uchida A, Nade S, McCartney ER, and Ching W. Journal of Bone and Joint Surgery-British Volume 1984;66(2):269.
55. Pickrell GR, Butcher KR, and Lin LC. Porous Articles and Method of the Manufacture Thereof. United States Patent Office. United States, 2004.

56. Pickrell GR. Porous Ceramic Articles and Method for the Manufacture Thereof. vol. WO 98/43927, 1998.
57. Yao XM, Tan SH, and Jiang DG. Journal of Materials Science-Materials in Medicine 2005;16(2):161-165.
58. Zhou H and Lee J. Acta Biomaterialia 2011;7(7):2769-2781.
59. Jiang P, Hwang KS, Mittleman DM, Bertone JF, and Colvin VL. Journal of the American Chemical Society 1999;121(50):11630-11637.
60. Aroca AS, Pradas MM, and Ribelles JLG. Colloid and Polymer Science 2007;285(7):753-760.
61. Olah L, Filipczak K, Jaegermann Z, Czigany T, Borbas L, Sosnowski S, Ulanski P, and Rosiak JM. Polymers for Advanced Technologies 2006;17(11-12):889-897.
62. Filipczak K, Janik I, Kozicki M, Ulanski P, Rosiak JM, Pajewski LA, Olkowski R, Wozniak P, Chroscicka A, and Lewandowska-Szumiel M. E-Polymers 2005.
63. Guarino V, Causa F, Netti PA, Ciapetti G, Pagani S, Martini D, Baldini N, and Ambrosio L. Journal of Biomedical Materials Research Part B: Applied Biomaterials 2008;86B(2):548-557.
64. Zhou CC, Wang P, and Li W. Composites Part B-Engineering 2011;42(2):318-325.
65. Reverchon E, Rappo ES, and Cardea S. Polymer Engineering & Science 2006;46(2):188-197.
66. Wood CD and Cooper AI. Macromolecules 2000;34(1):5-8.
67. Goel S and Beckman E. Polymer Engineering & Science 1994;34(14):1137-1147.
68. Franz G, Gunther, Will, Helmuth, Will. Porous, hydrophilic acrylic resin structure and method for preparing same. United States: Roehm & Haas GMBH, 1962.
69. Mulligan S. Surgical Wound Dressing. In: Office USP, editor., vol. US 2007/0185463 A1. United States, 2007. pp. 18.
70. Charnley J. Journal of Bone and Joint Surgery-British Volume 1960;42(1):28.
71. Rowley D, Pratt D, Powell E, Norris S, and Duckworth T. Archives of Orthopaedic and Trauma Surgery 1985;103(6):402-407.
72. Morejón L, Mendizábal E, Delgado J, Davidenko N, López-Dellamary F, Manríquez R, Ginebra M, Gil F, and Planell J. Latin American applied research 2005;35(3):175-182.
73. Huiskes R. Acta Orthopedia Scandinavia 1980;185.
74. Boger A, Bisig A, Böhner M, Heini P, and Schneider E. Journal of Biomaterials Science, Polymer Edition 2008;19(9):1125-1142.
75. Wintermantel E, Mayer J, Blum J, Eckert KL, Lüscher P, and Mathey M. Biomaterials 1996;17(2):83-91.
76. Boger A. Influence of Different Mixing Regimes on the Porosity Patterns for PMMA Samples With an Aqueous Fraction of 35 %. J. Biomater. Sci. Polymer Edn, 2007.
77. Guenther W. Process for the production of porous plastics and products comprising polymerizing a monomer in a water-in-oil emulsion. United States: Guenther, Will, 1966.
78. Limited PC. Product Brochure: World Leaders in Pressure Casing Technology. In: Ceramics P, editor. Internet Pamphlet. Kings Lyn, Norfolk, UK: PCL Ceramics Limited, 2012.
79. Will G. Porous Polymeric Compositions, Processes and Products. Free Patents Online. United States, 1973.
80. Will G. Method Of Producing Porous Polymerizates from Water-in-oil Emulsions. vol. US 3734867. United States, 1973.
81. Will G. Mold for Molding Ceramic Materials. United States Patent Office, vol. US 5033950. United States: Sacmi-cooperativa, 1991.

82. Ergün Y, Dirier C, Y Imaz M, Tokman C, and Tano lu M. Key Engineering Materials 2004;264:2235-2238.
83. Dortmans A, Bos B, and Fischer H. Cfi-Ceramic Forum International 2010;87(6-7):E29-E30.
84. Tanoglu M and Ergun Y. Composites Part a-Applied Science and Manufacturing 2007;38(2):318-322.
85. Dortmans A, Fischer H, Batenburg L, and Dominicus-van der Acker M. Advanced Engineering Materials 2001;3(9):717-720.
86. Beruto DT, Botter R, and Fini M. Biomaterials 2002;23(12):2509-2517.
87. Lovell P, Sherratt M, and Young R. Mechanical Properties and Deformation Micromechanics of Rubber-Toughened Acrylic Polymers. In: Riew C and Kinlock A, editors. Toughened Plastics II, Advances in Chemistry, vol. 252. Virginia: American Chemical Society, 1996. pp. 211-232.
88. Mori S and Barth H. Size Exclusion Chromatography. Heidelberg: Springer- Verlag Berlin Heidelberg, 1999.
89. Yau W, Kirkland J, and Bly D. Modern Size Exclusion Liquid Chromatography: Practice of Gel Permeation and Gel Filtration Chromatography, 1 ed. New Jersey: Wiley- Interscience, 1979.
90. Williams D and Flemming I. Spectroscopic Methods in Organic Chemistry, 5th ed. Maidenhead: McGraw-Hill Publishing Company, 1995.
91. Campbell D, Pethrick R, and White J. Polymer Characterisation Physical Techniques, 2nd Edition ed. Florida: CRC Press, 2000.
92. Weisstien EW. Radius of Curvature. MathWorld- A Wolfram Web Resource.
93. Miller R and Liggieri L. Bubble and Drop Interfaces. Volume 2 Progress in Colloids and Interface Science Leiden: Koninklijke Brill NV, 2011. pp. 560.
94. Nguyen A and Stechemesser H. Dynamics of the Impact Interaction Between a Fine Solid Sphere and a Plane Gas-Liquid Interface. Studies in Interface Science, vol. 6. Amsterdam: Elsevier, 1998. pp. 525-562.
95. McNaught A and Wilkison A. IUPAC - Compendium of Chemical Terminology 2nd Edition. Oxford: Blackwell Scientific Publications, 1997.
96. Kunjappu J. Ink Chemistry. RSC Chemistry World. Cambridge: RSC, 2003.
97. Huibers PDT, Lobanov VS, Katritzky AR, Shah DO, and Karelson M. Langmuir 1996;12(6):1462-1470.
98. Crook EH, Trebbi, G.F, Forgyce, D.B. Journal of Physical Chemistry 1964;68:3592.
99. Company DC. Technical Data Sheet: Triton X-100 Surfactant. In: DOW, editor., vol. 119-01882-1207, 2002. pp. 2.
100. Rosen M and Dahanayake M. Industrial Utilization of Surfactants - Principles and Practice: AOCS Press.
101. Abed-Ali S, Harte H, and Chisholm M. Formulation for the Making of Porous PMMA. Newton Aycliffe: Lucite International, 2009. pp. 2.
102. Rashed R. Isis 1990;81(3):464-491.
103. Wolf K and G K. European Journal of Physics 1995;16:14-20.
104. Hanson J. Chemistry Lab Techniques: Refractometry. vol. 2012. Tacoma, WA: Univerisut of Puget Sounds, 2006.
105. Nielsen L. Mechanical Properties of Polymers. New York: Reinhold Publishing Corperation, 1962.
106. Ward I and Hadley D. An Introduction to the Mechanical Properties of Solid Polymers. Chichester: John Wiley and Sons Ltd, 1993.
107. Crawford R. Plastics Engineering, 3rd ed. Oxford: Butterworth-Heinemann, 1998.
108. Crawford RJ. Plastics Engineering. Oxford: Butterworth and Heinemann, 1998. pp. Figure 2.62 Stress Concentration.

109. Haines P. Principles of Thermal Analysis and Calorimetry. Cambridge, UK: Royal Society of Chemistry, 2002.
110. Institution B-BS. Plastics. Differential scanning calorimetry (DSC). General Principles. BSI, 2009. pp. 40.
111. Vafai K. Handbook of Porous Media, 2nd ed. New York: Taylor and Francis Group, 2005.
112. Roy D, Scheetz B, Pommersheim J, and Licastro P. Development of Transient Permeability Theory and Apparatus for Measurements of Cementitious Materials. Strategic Highway Research Program. Washington, DC: National Academy of Sciences, 1993. pp. 30.
113. Zinszner B and Pellerin F. A Geoscientists Guide to Petrophysics. Paris: Editions Ophrys, 2007.
114. Weast RC. Handbook of Chemistry and Physics. Cleveland, Ohio: CRC Press, 1977.
115. Campbell D, Pethrick RA, and White JR. Polymer Characterisation Physical Techniques- 2nd Edn. Florida: CRC Press, 2000. Figure 10.4 pp299 Interaction of a High Velocity Electron with an Atom.
116. Campbell D, Pethrick RA, and White JR. Polymer Characterisation Physical Techniques-2nd Edition. In: signal Eostotse, editor. Florida: CRC Press, 2000.
117. Instrument Database: Carl Zeiss AG- EVO® 60 series. Carl Zeiss AG. pp. <http://www.speciation.net/Database/Instruments/Carl-Zeiss-AG/EVO-60-Series-;i664>.
118. Winnik MA. Polymer Engineering & Science 1984;24(2):87-97.
119. Borisov S, Mayr T, Karasyov A, Klimant I, Chojnacki P, Moser C, Nagl S, Schaeferling M, Stich M, Kocincova A, and Wolfbeis O. New Plastic Microparticles and Nanoparticles for Fluorescent Sensing and Encoding Fluorescence of Supramolecules, Polymers, and Nanosystems. vol. 4. Berlin: Springer Berlin Heidelberg, 2008. pp. 431-463.
120. Disanayaka B, Winnik MA, and Croucher MD. Journal of Colloid and Interface Science 1990;136(2):352-362.
121. Hale J. The Fundamentals of Radiological Science. Springfield, IL: Charles. C. Thomas, 1974.
122. Ter-Pogossian MM. The Physical Aspects of Diagnostic Radiology. New York: Haper and Row, 1967.
123. Epp ER and Weiss H. Physics in Medicine and Biology 1966;11(2):225-238.
124. McCullough EC. Medical Physics 1975;2(6):307-320.
125. Kak AC and Slaney M. Principles of Computerised Tomography Imaging. New York: IEEE Press, 1988.
126. Hoey D and Taylor D. Fatigue & Fracture of Engineering Materials & Structures 2009;32(3):261-269.
127. Hopfenberg HG, Stannett VT, and Jacques CHM. Journal of Applied Polymer Science 1975;19:2485-2491.
128. Piver WT. Environmental Health Perspectives 1976;17:227-236.
129. Chen W, Lee S, and Ho B. Journal of Polymer Research 1998;5(3):187-191.
130. Faldi A, Tirrell M, Lodge TP, and von Meerwall E. Macromolecules 1994;27(15):4184-4192.
131. Duda J, Vrentas J, Ju S, and Liu H. American Institute of Chemical Engineers Journal 1982;28(2):279-285.
132. Fick A. Annalen der Physik 1855;170(1):59-86.
133. Standard B. Recommendations for the Presentation of Plastics Design Data. Other Properties. Data on diffusion. BSI Online: BSI, 1974.

134. Vrentas JS and Duda JL. *Journal of Polymer Science: Polymer Physics Edition* 1977;15(3):417-439.
135. Klemperer D, Sperling L, and Utracki L. *Interpenetrating Polymer Networks. Advances in Chemistry, Vol 239.* Washington, DC: American Chemical Society, 1994. pp. Medium: X; Size: 626 p.
136. Sperling L. *Introduction to Physical Polymer Science*, 4th ed. Hoboken, New Jersey: John Wiley and Sons, 2005.
137. Matinlinna J and Mittal K. *Adhesion Aspects in Dentistry.* London: Taylor & Francis Group, 2009.
138. Reis R and Cohn D. *Polymer Based Systems on Tissue Engineering, Replacement and Regeneration: Proceedings of the NATO Advanced Study Institute Held in Alvor, Algarve, Portugal, 15-25 October, 2001.* NATO Advanced Study Institute on Polymer Based Systems on Tissue Engineering, Replacement and Regeneration. Algarve, Portugal: Springer-Verlag GmbH, 2002.
139. Morejon L, Mendizabal E, Delgado J, Davidenko N, Lopez-Dellamary F, Manríquez R, Ginebra M, Gil F, and Planell J. *Latin American Applied Research* 2005;35(2005):175-182.
140. Fontenot K and Schork F. *Ind. Eng. Chem. Res* 1993;32:373-385.
141. Hunt A. *Complete A-Z Chemistry Handbook*, 3 ed. Tonbridge: Hodder and Stoughton Educational, 2003.
142. Pilemand.P. *Surfactants. Their abilities and Important Physio-Chemical Properties.* Copenhagen: Centre for Miljø og Luftveje, 2002.
143. Engberts JBFN. *Recueil des Travaux Chimiques des Pays-Bas* 1994;113(2):113-113.
144. Huibers P and Shah D. *Langmuir* 1997;13:5762-5765.
145. Johnson KA and Shah DO. *Journal of Colloid and Interface Science* 1985;107(1):269-271.
146. Ash.I AM. *Handbook of Industrial Surfactants: Gower*, 1997.
147. BASF. Lutensol TO types. In: *Information BT*, editor., vol. TI/EO 1029: BASF, 1997.
148. Kunjappu J. *Chemistry in Britain* 2003;39(3):22-25.
149. Unwin P. CH3A9 *Colloid and Interfacial Chemistry Course Lecture Notes.* Warwick, UK: University of Warwick, Department of Chemistry, 2008.
150. Atkins PW. *Physical Chemistry*, 6th ed. ed. Oxford: Oxford University Press, 1998.
151. Goheen S and Matsor R. *Journal of the American Oil Chemists' Society* 1989;66(7):994-997.
152. Cox M. *Journal of the American Oil Chemists' Society* 1989;66(3):367-374.
153. Wypych G. *Knovel Solvents - A Properties Database.* ChemTec Publishing. pp. Row 916.
154. Brandrup J. *Polymer Handbook*, 4th Edition ed. Chichester: Wiley Interscience, 1999.
155. Hoy, K.L. *Journal of Paint Technology* 1970;42:229.
156. Krevelen DWv. *Fuel* 1965;44:229.
157. van Krevelen DWH, P.J. *Journal of Applied Polymer Science* 1967(11):2189.
158. Small PA. *Journal of Applied Chemistry* 1953;3(2):71-80.
159. van Krevelen D and Nijenhuis K. *Properties of Polymers. Their Correlation with Chemical Structure; Their Numerical Estimation and Prediction from Additive Group Contributions*, 4 ed. Oxford: Elsevier, 2009.
160. Chemistry RSo. Methyl Methacrylate. ChemSpider, vol. CSID 6406: RSC, 2013.
161. Chemistry RSo. Water. ChemSpider, vol. CSID: 937: RSC, 2013.
162. NOISH. Methyl Methacrylate. vol. 2013. Atlanta, GA, USA: Centres for Disease Control and Prevention. pp. NIOSH Pocket Guide to Chemical Hazards.

163. Lide D. CRC Handbook of Chemistry and Physics, 79th Edition ed. Oxford, UK: CRC-Press, 1998.
164. Biaselle C and Millar D. Biophysical Chemistry 1975;3(4):355-361.
165. Fernandez AMJ, L The Effect of Surfactant Selection of Emulsion Polyme Properties. PCI Magazine, vol. 2002. Online: Paints and Coatings Industry, 2007. pp. 7.
166. Campbell PM. Alternative to Nonlyphenol Ethoxylates: Review of Toxicity, Biodegradation, and Technical-Economic Aspects. Vancouver, Canada: ToxEcology-Envorinmental Connsulting Ltd., 2002. pp. 79.
167. Agency USEP. DfE Alternatives Assessment for Nonylphenol Ethoxylates. EPA, 2012. pp. 27.
168. Griffin WC. Journal of Cosmetic Science 1949;1(5):311.
169. Griffin WC. Journal of the Society of Cosmetic Chemists 1954;5:249.
170. Schonfeldt.N. Surface Active Ethylene Oxide Adducts, 1st ed.: Pergamon Press, 1969.
171. Mitchell DJ, Tiddy GJT, Waring L, Bostock T, and McDonald MP. Journal of the Chemical Society, Faraday Transactions 1: Physical Chemistry in Condensed Phases 1983;79(4):975-1000.
172. Wu WQ, Tian HF, and Xiang AM. Journal of Polymers and the Environment 2012;20(1):63-69.
173. Bart C. Plastics Additives: Advanced Industrial Analysis. Amsterdam: IOS Press, 2006.
174. Murphy J. Additives for Plastic Handbook. Oxford: Elsevier, 2001.
175. Xie W, Hwu JM, Jiang GJ, Buthelezi TM, and Pan W-P. Polymer Engineering & Science 2003;43(1):214-222.
176. Richard WR and Smith PAS. The Journal of Chemical Physics 1950;18(2):230-231.
177. Nielsen LE, Buchdahl R, and Levreault R. Journal of Applied Physics 1950;21(6):607-614.
178. AN Ghebremeskel CV, M.Lodaya. Pharm res 2006;23(8):1928-1936.
179. Hopfenberg HG, Stannett, V.T, Jacques, C.H.M. Journal of Applied Polymer Science 1975;19:2485-2491.
180. Lambert J, Shurvell H, Lightner D, and Cooks R. Introduction to Organic Spectroscopy. New York: Macmillan Publishing Company, 1987.
181. Jenckel E and Heusch R. Kolloid Z 1953(130):89.
182. Gordon M and Taylor J. Journal of Applied Chemistry 1952;2(9):493-500.
183. Fox T. Bull. American Physical Society 1956;1:123.
184. de Araujo M, Stadler R, and Cantow H. Polymer 1988;29(12):2235-2243.
185. Brekner MJ, Schneider HA, and Cantow HJ. Polymer 1988;29(1):78-85.
186. Kwei TK. Journal of Polymer Science: Polymer Letters Edition 1984;22(6):307-313.
187. Kelley FN and Bueche F. Journal of Polymer Science 1961;50(154):549-556.
188. Hoey D and Taylor D. Micrographs of Fatigue Crack Paths in Bone Cement and Acrylic Glass. Fatigue and Fracture of Engineering Materials and Structures. Dublin, Ireland: Blackwell Publishing, 2009.
189. Hoey DA and Taylor D. Biomaterials 2009;30(31):6309-6317.
190. Topoleski LDT, Ducheyne. P, and Cuckler JM. Biomaterials 1993;14(15):1165-1172.
191. Buback M, Gilbert RG, Hutchinson RA, Klumperman B, Kuchta F-D, Manders BG, O'Driscoll KF, Russell GT, and Schweer J. Macromolecular Chemistry and Physics 1995;196(10):3267-3280.
192. Alger MSM. Polymer science dictionary / Mark S.M. Alger. London ; New York :: Elsevier Applied Science, 1989.
193. Lee HB and Turner DT. Macromolecules 1977;10(2):226-231.
194. Otsu T, Ito T, and Imoto M. Kogyo Kagaku Zasshu 1966(69).

195. Lewis FM, Walling C, Cummings W, Briggs ER, and Mayo FR. *Journal of the American Chemical Society* 1948;70(4):1519-1523.
196. Rieger J. *Journal of thermal analysis* 1996;46(3-4):965-972.
197. Wiley R and Brauer G. *Journal of Polymer Science* 1948;3(3):455-461.
198. Martin G, Rogers S, and Mandelkern L. *Journal of Polymer Science* 1956;20(96):579-581.
199. Murthy S. *Journal of Polymer Science Part B: Polymer Physics* 1993;31(4):475-480.
200. Stoffel NC, Hsieh. M, Kramer. E.J, Volksen. W. *Transactions on Components, Packaging and Manufacturing Technology Part B: Advance Packaging* 1996;19:417.
201. Srinivas SCFE, Graham.M, Gardner.S, Davis, R.M, McGrath. J.E, Wilkes, G.L. *Macromolecules* 1997(30):1012.
202. van Krevelen DWN, K.T Properties of Polymers. Their correlation with Chemical Structure; Their Numerical Estimation and Prediction from Additive Group Contributions, 4 ed.: Elsevier, 209.
203. Silverstein M and Camer N. *Porous Polymers*. Hoboken, New Jersey: Wiley-Blackwell, 2011.
204. Pearson R. *Introduction to the Toughening of Polymers*. *Toughening of Plastics*, vol. 759. Ann Arbor, MI: American Chemical Society, 2000. pp. 1-12.
205. Utracki LA. *Polymer Alloys and Blends: Thermodynamics and Rheology*. Cincinnati, OH, USA: Hanser Gardner Publications, 1989.
206. Pearson RA. *Toughened Plastics I*. *Science and Engineering* 1993;233:405-425.
207. Bowden PB and Raha S. *Philosophical Magazine* 1970;22(177):463-482.
208. Kramer EJ. *Microscopic and Molecular Fundamentals of Crazing*. In: Kausch HH, editor. *Crazing in Polymers*, vol. 52-53. Berlin: Springer Berlin Heidelberg, 1983. pp. 1-56.
209. Lazzeri A and Bucknall CB. *Journal of Materials Science* 1993;28(24):6799-6808.
210. Bucknall CB, Karpodinis A, and Zhang XC. *Journal of Materials Science* 1994;29(13):3377-3383.
211. Griffith AA. *Philosophical Transactions of the Royal Society of London. Series A* 1921;221:163-198.
212. Knott JF. *Fundamentals of Fracture Mechanics*. London: Butterworth, 1979.
213. Broek D. *Elementary Engineering Fracture Mechanics*, 4th ed. Sijthoff Noordhoff, Netherlands: Springer, 1982.
214. Kausch HH. *Polymer Fracture*, 2 ed. New York, USA: Springer-Verlag, 1979.
215. Döll W. *Polymer Engineering & Science* 1984;24(10):798-808.
216. Marshall GP and Williams JG. *Journal of Materials Science* 1973;8(1):138-140.
217. Lovell P. *Trends in Polymer Science(UK)* 1996;4(8):264-272.
218. Cigna G, Lomellini P, and Merlotti M. *Journal of Applied Polymer Science* 1989;37(6):1527-1540.
219. Pearson RA and Yee AF. *Journal of Materials Science* 1991;26(14):3828-3844.
220. Kennedy JP and Richard GC. *Macromolecules* 1993;26(4):567-571.
221. Kennedy JP, Askew MJ, and Richard GC. *Journal of Biomaterials Science, Polymer Edition* 1992;4(5):445-449.
222. Danielsson M, Parks DM, and Boyce MC. *Journal of the Mechanics and Physics of Solids* 2007;55(3):533-561.
223. Tjong SC. *Materials Science and Engineering: R: Reports* 2006;53(3-4):73-197.
224. Fiedler B, Gojny F, Wichmann M, Nolte M, and Schulte K. *Composites Science and Technology* 2006;66(16):3115-3125.
225. Qian D, Dickey E, Andrews R, and Rantell T. *Applied Physics Letters* 2000;76(20):2868-2970.

226. Khare H and Burris D. *Polymer* 2012;51:719-729.
227. Gersappe D. *Physical Review Letters* 2002;89(5):058301.
228. Jordan J, Jacob K, Tannenbaum R, Sharaf M, and Jasiuk I. *Materials Science and Engineering: A* 2005;393(1–2):1-11.
229. Osman MA, Ploetze M, and Skrabal P. *The Journal of Physical Chemistry B* 2004;108(8):2580-2588.
230. Fornes TD, Yoon PJ, Hunter DL, Keskkula H, and Paul DR. *Polymer* 2002;43(22):5915-5933.
231. Sinha Ray S, Okamoto K, and Okamoto M. *Macromolecules* 2003;36(7):2355-2367.
232. Inc SCP. vol. 2012. Gonzales, Texas.
233. Mineraria LC. Nanoclay for Nanocomposites Dellite HPS. vol. 2012. Livorno, Italy: Laviosa Chimica Mineraria S.P.A, 2012.
234. Vaia RA, Ishii H, and Giannelis EP. *Chemistry of Materials* 1993;5(12):1694-1696.
235. Lee J-H, Jung D, Hong C-E, Rhee KY, and Advani SG. *Composites Science and Technology* 2005;65(13):1996-2002.
236. Tjong SC and Meng YZ. *Journal of Polymer Science Part B: Polymer Physics* 2003;41(13):1476-1484.
237. Park JH and Jana SC. *Polymer* 2003;44(7):2091-2100.
238. Unnikrishnan L, Mohanty S, Nayak SK, and Ali A. *Materials Science and Engineering: A* 2011;528(12):3943-3951.
239. Qu X, Guan T, Liu G, She Q, and Zhang L. *Journal of Applied Polymer Science* 2005;97(1):348-357.
240. Sinha Ray S and Okamoto M. *Progress in Polymer Science* 2003;28(11):1539-1641.
241. Kiersnowski A, Trelinska-Wlzlak M, Dolega J, and Piglowski J. *E-Polymers* 2006.
242. Lu Z, Wang J, Li Q, Chen L, and Chen S. *European Polymer Journal* 2009;45(4):1072-1079.
243. Zulfikar MA, Wahab Mohammad A, and Hilal N. *Desalination* 2006;192(1–3):262-270.
244. Kopesky ET, McKinley GH, and Cohen RE. *Polymer* 2006;47(1):299-309.
245. Ash BJ, Siegel RW, and Schadler LS. *Macromolecules* 2004;37(4):1358-1369.
246. Jansen BJP, Rastogi S, Meijer HEH, and Lemstra PJ. *Macromolecules* 2001;34(12):3998-4006.
247. Muriel M, Dubault A, and Halary JL. *Polymer International* 2007;56(2):214-223.
248. Cros S, Burr A, Dubault A, and Halary JL. *Composite Interfaces* 2007;14(2):85-98.
249. Dortmans A. *Nanocomposite Materials: From Lab Scale Experiments to Prototypes. e-Polymers*, 2002. pp. Figure 5.
250. Boguszewski T, Swieszkowski W, Lewandowska M, and Kurzydowski KJ. *E-Polymers* 2005.
251. Huang Y, Hunston DL, Kinloch AJ, and Riew CK. *Toughened Plastics: Science and Engineering* 1993;233:1-35.
252. Rohm and Haas Company, British Patent 1414187, 1975.
253. Sartomer. SR307: Poly(butadiene) Diacrylate Coagent Utilizes Unique Structure to Improve the Radical Cure of Elastomers. Sartomer Company Inc. Exton, PA USA: Sartomer Company Inc, 2006.
254. Kennedy JP. Polyisobutylene Toughened Poly(methyl Methacrylate). US5242983, US Patent 1993.
255. Bevington JC and Harris DO. *Journal of Polymer Science Part B: Polymer Letters* 1967;5(9):799-802.
256. Grassie N, Torrance BJD, Fortune JD, and Gemmell JD. *Polymer* 1965;6(12):653-658.
257. Brosse J-C, Gauthier J-M, and Lenain J-C. *Die Makromolekulare Chemie* 1983;184(3):505-517.

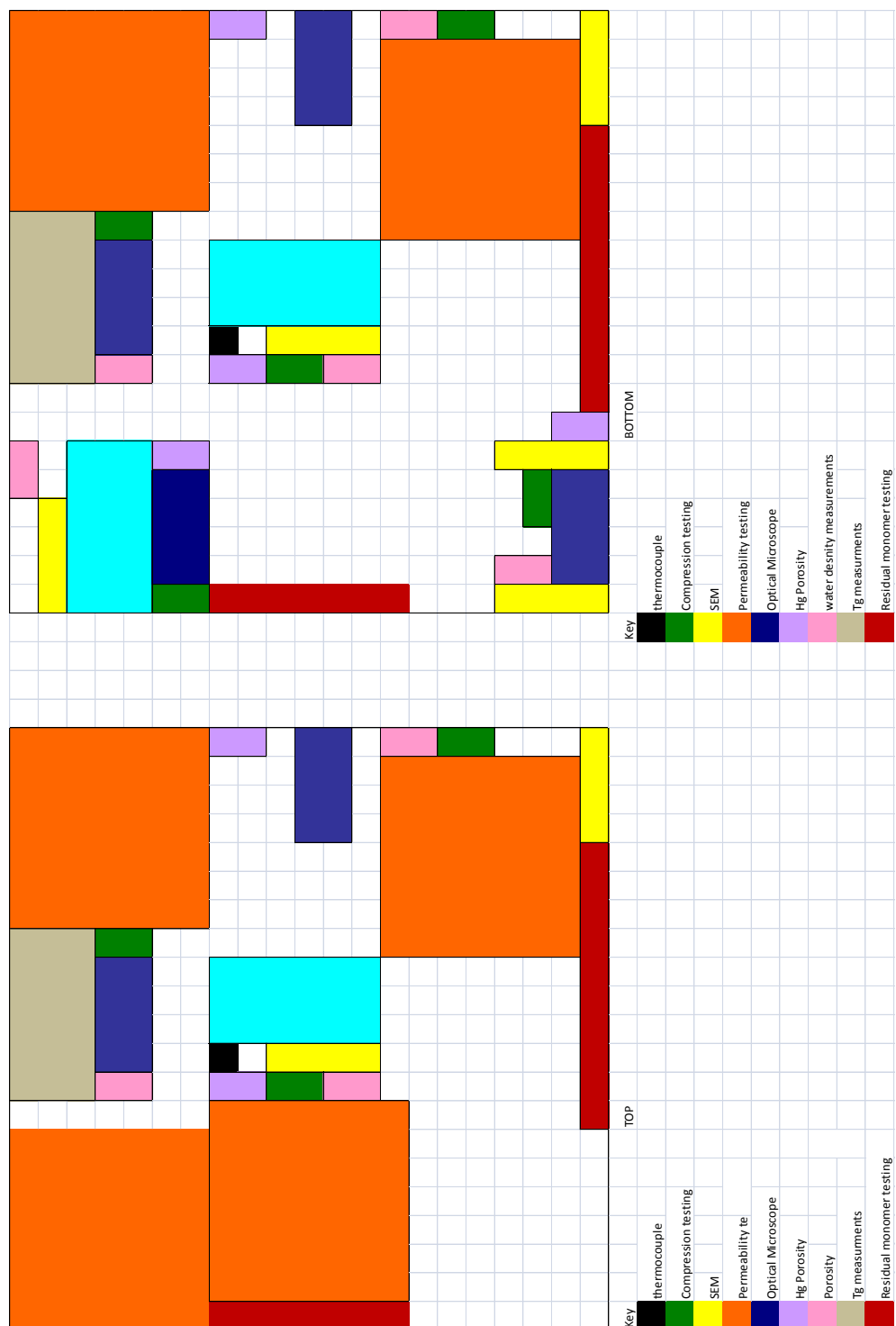
- 258. Padget C. The Basic Principles of Emulsion and Suspension Polymerisation, 1990.
- 259. Lipson A, S.G L, and Lipson H. Optical Physics. Cambridge, UK: Cambridge University Press, 2010.
- 260. Jhaveri SB, Koylu D, Maschke D, and Carter KR. Journal of Polymer Science Part A: Polymer Chemistry 2007;45(9):1575-1584.
- 261. Kak A and Slaney M. Principles of Computerized Tomographic Imaging. New York, USA: The Institute of Electrical and Electronic Engineers Inc (IEEE Press), 1999.
- 262. Herman G. Fundamentals of Computerized Tomography. vol. XII. New York, NY: Academic Press, 2010.
- 263. Extnance E. Tiny Insights. Chemistry World, vol. 10. Cambridge, UK: The Royal Society of Chemistry, 2013.
- 264. McGraw-Hill and Parker SP. McGraw-Hill Dictionary of Scientific and Technical Terms, 6th ed. New York, USA: McGraw-Hill Professional, 2002.
- 265. Nardoux F. Assessment of Porous Poly(Methyl Methacrylate) Materials by X-Ray Computed Tomography. vol. Engineering. Limoges, France: ENSIL, 2012.

Appendix 1: Testing of Porous PMMA, Division of the Material

Porous PMMA materials are moulded in blocks measuring 230 x 230 x 30 mm. These blocks were then divided into suitable size test pieces namely :

- SEM (10 x 10 x 40 mm)
- Permeability (70 x 70 x 10 mm) These are then bored into discs measuring 40 mm x 10 mm
- Porosity (10 x 10 x 20 mm)
- Compression Testing (10 x 10 x 20 mm)
- DSC for T_g measurements (60 x 30 x 10 mm). This block is then filed down to create a fine powder
- Residual monomer (10 X 10 X 40mm). This is then ground down to create a fine powder.
- Optical Microscopy
- Mercury porosity

The cutting plan shows the front and back view of the block formed in the polymerisation process. In the plan, if a piece is shown on both views it is taken from the middle of the block. The large block size enabled test pieces to be taken from all areas of the block , taking into account edge effects and different depths of the block.



Appendix 2: Additional Data Tables and Graphs

Appendix 2.1: Triton X100

Sample Name	Total wt % surfactant	Set Time/ Min	Compressive Properties				Porosity / % (SD)	Permeability/ Darcy (SD)	Residual Monomer /%	T _g / °C (SD)
			Average Max Stress / MPa (SD)	Strain at Maximum Stress/ % (SD)	Transition Stress/ MPa (SD)	Bulk Modulus/ MPa (SD)				
X100 (1.00) KA055	73.22	25.5	18.25 (4.73)	16.00 (3.00)	6.70 (1.46)	385 (167)	29.63 (3.33)	3.46 (0.47)	2.60	101
X100 (0.68) KA080	50.00	24	18.92 (2.52)	17.10 (2.84)	9.50 (2.28)	275 (88)	29.57 (2.23)	3.27 (0.27)	1.60	102
X100 (0.50) KA068	36.61	21	17.33 (2.84)	14.36 (3.40)	9.92 (2.30)	254 (118)	30.60 (1.71)	3.19 (0.31)	5.76	105
X100 (0.41) KA075	30.00	22	20.71 (3.45)	17.95 (5.93)	10.38 (2.18)	348 (116)	29.66 (7.54)	3.32 (0.34)	5.76	103
X100 (0.34) KA078	25.00	18.5	25.09 (7.06)	16.58 (3.13)	13.33 (3.19)	355 (96)	31.12 (1.71)	2.75 (0.38)	2.81	109
X100 (0.31) KA081	23.00	22	29.31 (5.53)	17.29 (4.62)	14.25 (6.24)	494 (132)	28.17 (8.38)	2.42 (0.45)	2.23	113
X100 (0.26) KA085	19.00	18	35.80 (7.39)	23.03 (9.75)	19.82 (0.59)	577 (85)	30.34 (2.34)	3.72 (0.67)	2.28	111
X100 (0.20) KA070	14.64	27.5	32.51 (4.94)	19.46 (9.12)	19.45 (2.39)	569 (52)	33.24 (2.28)	3.87 (0.85)	8.17	115

Appendix 2.2 Hydrophilic Lipophilic Balance (HLB) of the surfactant

Sample Name	solubility paramter	Set Time/ Min	Compressive Properties				Porosity / % (SD)	Permeability/ Darcy (SD)	Residual Monomer/%	T _g / °C (SD)
			Average Max Stress / MPa (SD)	Strain at Maximum Stress / % (SD)	Transition Stress/ MPa (SD)	Bulk Modulus/ MPa (SD)				
Lut TO3 (KA094)	13.81545	25	41.50 (7.26)	24.11 (6.23)	22.97 (3.27)	704.87 (101.8)	21.8 (1.76)	4.33 (0.132)	2.89	104 (3)
Lut TO5 (KA097)	19.23126	24	21.25 (3.00)	12.10 (1.35)	12.55 (0.70)	383.10 (14.07)	31.0 (1.09)	3.30 (0.1666)	2.38	98 (2)
Lut TO6 (KA096)	19.46191	18.5	28.32 (3.45)	16.79 (0.14)	17.03 (0.62)	608.40 (59.70)	32.2 (5.42)	2.52 (0.086)	2.36	106 (1)
Lut TO7 (KA095)	20.08216	18.5	30.68 (3.46)	17.54 (3.68)	17.87 (2.25)	564.01 (79.83)	27.4 (1.18)	2.05 (0.1)	2.01	105 (1)
Lut TO8 (KA088)	20.84444	15	26.97 (6.25)	11.49 (3.67)	17.83 (2.86)	587.33 (128.68)	27.6 (2.24)	2.73 (0.113)	2.65	111 (1)
Lut TO109 (KA086)	20.55219	17	30.84 (3.25)	19.75 (2.45)	16.11 (2.44)	450.00 (55.40)	29.8 (1.11)	3.46 (0.378)	4.93	106 (3)
Lut TO129 (KA090)	19.10133	14	21.93 (2.83)	12.01 (4.31)	15.15 (1.31)	390.09 (1.65)	30.0 (2.65)	3.70 (0.865)	2.56	112 (1)
Lut TO15 (KA089)	20.83727	13.5	6.86 (2.09)	8.26 (4.82)	4.69 (0.23)	151.46 (16.66)	32.5 (2.82)	5.50 (0.36)	2.94	109 (4)
Lut TO20 (KA087)	21.27108	11	11.68 (1.80)	11.16 (2.98)	8.38 (0.19)	208.84 (13.45)	30.3 (2.22)	5.03 (0.281)	2.58	107 (2)

Appendix 2.3 Lutensol T03

Sample Name	Total wt % surfactant	Set Time / Min	Compressive Properties				Porosity / % (SD)	Permeability / Darcy (SD)	Residual Monomer/%	T _g / °C (SD)
			Average Max Stress / MPa (SD)	Strain at Maximum Stress/ % (SD)	Transition Stress/ MPa (SD)	Bulk Modulus/ MPa (SD)				
LutT03 (0.16) KA111	6.00	28.5	31.95 (7.43)	17.52 (2.55)	21.62 (3.66)	580 (94.52)	28.77 (0.95)	3.53 (0.48)	2.56	115 (1)
Lut TO3(0.32) KA107	12.00	32.5	39.91 (6.07)	20.65 (4.00)	27.82 (2.04)	510 (157.67)	23.48 (1.44)	4.62 (0.95)	2.61	118 (1)
Lut TO3(0.50) KA094	18.70	25.0	41.50 (7.26)	24.11 (6.32)	22.97 (3.27)	700 (101.27)	21.81 (1.76)	4.33 (0.13)	2.89	109 (0.35)
Lut TO3(0.67) KA108	25.00	34.0	32.39 (6.90)	18.07 (2.13)	19.58 (4.95)	560 (134.05)	25.95 (1.12)	3.74 (1.2)	4.99	111 (1)
Lut TO3(1.00) KA109	37.58	43.5	24.89 (5.73)	14.29 (3.21)	16.55 (3.91)	470 (150.73)	26.21 (1.41)	2.59 (0.39)	2.10	111 (0.5)
Lut TO3(1.34) KA110	50.00	47.0	19.41 (4.63)	12.82 (0.30)	13.70 (2.65)	430 (150.17)	38.95 (1.75)	3.32 (0.08)	1.82	113 (1)
Lut TO3(1.73) KA117	65.00	39.0	18.43 (2.85)	17.42 (0.97)	8.54 (1.62)	330 (37.30)	29.19 (1.99)	4.13 (0.17)	2.67	104 (1)
Lut TO3(1.95) KA118	73.22	44.0	20.08 (1.74)	20.99 (2.09)	8.52 (0.66)	380 (45.13)	30.42 (2.46)	3.31 (0.38)	3.51	100 (1)

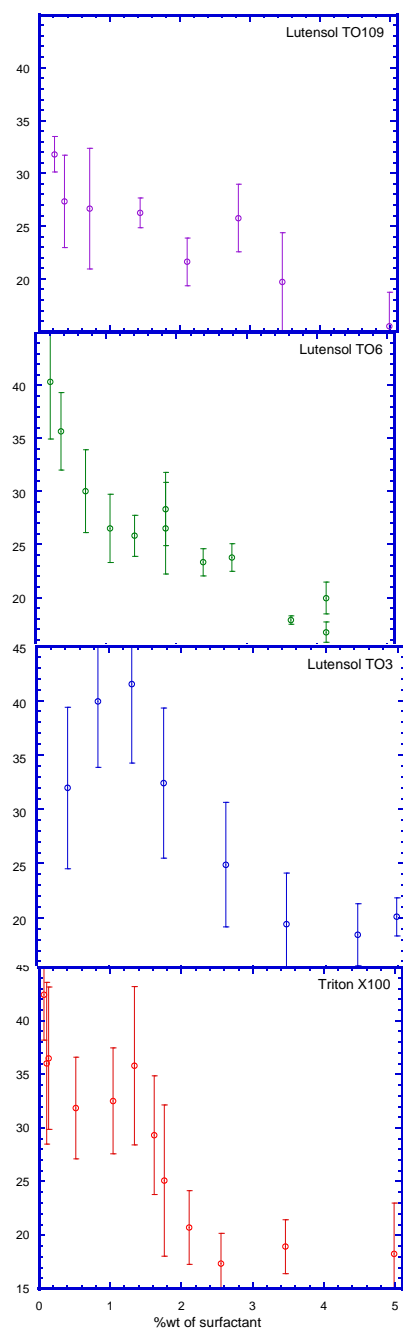
Appendix 2.4 Lutensol T06

Sample Name	Total wt % surfactant	Set Time / Min	Compressive Properties				Porosity / % (SD)	Permeability / Darcy (SD)	Residual Monomer/%	T _g /°C (SD)
			Average Max Stress / MPa (SD)	Strain at Maximum Stress/% (SD)	Transition Stress/MPa (SD)	Bulk Modulus / MPa (SD)				
Lut TO6 3 (KA156)	0.21	21.5	40.34 (5.40)	30.96 (7.07)	19.51 (2.20)	668 (100)	29.39 (1.24)	2.42 (0.88)	6.33	119 (0.4)
Lut TO6 56 (KA150)	0.36	20.5	35.65 (3.67)	23.43 (4.49)	22.78 (2.29)	544 (93)	26.38 (2.53)	1.92 (0.07)	5.66	119 (0.2)
Lut TO6 10 (KA151)	0.71	23	30.01 (3.92)	21.07 (2.80)	16.98 (1.58)	442 (81)	31.2 (2.68)	2.61 (0.12)	5.52	118 (0.2)
Lut TO6 15 (KA149)	1.06	26.5	26.51 (3.22)	18.36 (3.54)	14.61 (0.99)	408 (40)	31.67 (2.80)	3.11 (0.60)	4.18	110 (6.7)
Lut TO6 20 (KA148)	1.41	22.5	25.79 (1.93)	19.66 (1.59)	13.2 (0.91)	368 (46)	29.54 (2.42)	3.27 (0.11)	4.81	116 (1.0)
Lut TO6 26.25 (KA096r)	1.85	21.5	26.51 (4.32)	16.69 (3.65)	13.92 (2.18)	475 (57)	30.82 (2.31)	2.52 (0.09)	1.20	106 (1.3)
Lut TO6 34 (KA154)	2.38	22.5	23.3 (1.30)	17.22 (2.48)	13.91 (1.00)	498 (55)	28.79 (2.04)	3.05 (0.17)	4.13	112 (0.6)
Lut TO6 40 (KA153)	2.79	19.5	23.73 (1.30)	17.21 (1.64)	14.41 (0.24)	443 (62)	37.34 (3.54)	2.57 (0.32)	4.67	110 (1.8)
Lut TO6 52.5 (KA152r)	3.63	33.5	17.85 (0.41)	15.47 (2.27)	10.81 (1.90)	385 (58)	31.51 (3.08)	1.55 (1.08)	3.91	108 (2.1)
Lut TO6 60 (KA155)	4.13	27	16.7 (0.96)	18 (0.80)	9.21 (0.50)	331 (22)	29.8 (1.86)	3.52 (0.60)	3.62	109 (1.0)

Appendix 2.5 Lutensol TO109

Sample Name	Total wt % surfactant	Set Time / Min	Compressive Properties				Porosity / % (SD)	Permeability / Darcy (SD)	Residual Monomer / %	T _g / °C (SD)
			Average Max Stress / MPa (SD)	Strain at Maximum Stress / % (SD)	Transition Stress / MPa (SD)	Bulk Modulus / MPa (SD)				
LutTO109 3 (KA147)	0.21	23	31.79 (1.68)	14.14(2.15)	18.12 (1.31)	611 (29.08)	28.58 (2.64)	4.64 (0.40)	5.99	114 (1)
Lut TO109 5 (KA146)	0.36	24	27.33 (4.38)	15.00 (1.79)	15.32 (1.53)	454 (56.87)	30.57 (1.37)	4.46 (0.13)	5.51	112 (2)
Lut TO109 10 (KA125)	0.71	23.0	26.65 (5.72)	20.00 (6.51)	11.43 (0.68)	394 (10.96)	32.66 (2.38)	3.75 (0.27)	8.22	104 (2)
Lut TO109 20.3 (KA126)	1.44	20.5	26.23 (1.41)	22.09 (1.85)	14.72 (0.93)	368 (63.62)	29.93 (1.75)	3.38 (0.26)	5.70	111 (1)
Lut TO109 30 (KA124)	2.11	17.5	21.60 (2.26)	13.87 (2.77)	13.09 (2.46)	422 (76.36)	28.27 (1.38)	4.47 (0.32)	3.43	99 (3)
Lut TO109 40.6 (KA086)	2.83	24.0	25.75 (3.20)	17.17 (2.95)	13.38 (1.47)	451 (36.06)	29.25 (1.83)	3.46 (0.38)	4.09	91 (2)
Lut TO109 50 (KA127)	3.46	14.5	19.86 (4.69)	13.87(5.43)	10.00 (0.60)	397 (34.77)	31.52 (3.76)	4.51 (0.07)	0.92	98 (1)
Lut TO109 65 (KA128)	4.45	20	12.67 (1.42)	9.21 (2.10)	7.06 (0.86)	302 (25.25)	29.82 (3.26)	4.02 (0.12)	2.29	107 (1)
Lut TO109 73.22 (KA129)	4.99	23	15.48 (3.24)	13.11(3.74)	6.75 (0.48)	325 (25.25)	28.80 (1.52)	3.85 (0.45)	11.54	99 (2)

Appendix 2.6 Stacked Graphical Figure for Compressive Properties of Different Surfactants



Appendix 2.7 MMA Variation with Triton X100

Sample Name	MMA wt %	Set Time / Min	Compressive Properties				Porosity / % (SD)	Permeability / Darcy (SD)	Residual Monomer/ %	T _g / °C (SD)
			Average Max Stress / MPa (SD)	Strain at Maximum Stress/ % (SD)	Transition Stress/ MPa (SD)	Bulk Modulus / MPa (SD)				
KA060	8.75	13.5	3.98 (1.30)	12.30 (3.07)	1.03 (0.23)	256 (125.15)	31.57 (4.95)	7.09 (0.34)	1.00	80 (1).
KA059	9.41	15	3.92 (1.23)	12.11 (3.28)	1.39 (0.29)	84 (28.45)	33.70 (4.32)	6.14 (0.72)	0.91	73 (2)
KA055	10.52	25.5	18.25 (4.73)	15.70 (2.72)	6.71 (1.46)	385 (166.90)	29.63 (3.33)	3.39(0.55)	1.15	112 (2)
KA122	11.10	31	24.43 (1.08)	18.61 (3.35)	9.56 (1.37)	362 (62.26)	22.86 (1.77)	1.26 (0.63)	3.97	91 (2)
KA121	11.45	41.5	33.59 (2.63)	20.40 (2.38)	15.32 (0.94)	672 (33.69)	22.58 (2.15)	1.46 (0.24)	3.22	84 (1)
KA123	11.70	50.5	34.95 (3.80)	21.19 (6.60)	15.98 (1.74)	625 (48.71)	25.31 (0.72)	0.255 (0.06)	6.52	79 (1)
KA062	11.77	42	35.54 (7.86)	19.00 (9.00)	18.68 (3.05)	642 (99.92)	21.76 (1.02)	1.05 (0.84)	0.98	89 (1)
KA113	12.02	42	39.51 (2.28)	23.73 (4.38)	24.99 (1.88)	727 (109.19)	24.47 (2.40)	0.44 (0.01)	6.79	104 (1)

Appendix 2.8 Polybutadiene Dimethacrylate Addition to PMMA

Sample Name	MMA wt %	Set Time / Min	Compressive Properties				Porosity / % (SD)	Permeability / Darcy (SD)	Residual MMA /%	T _g / °C (SD)
			Average Max Stress / MPa (SD)	Strain at Maximum Stress/ % (SD)	Transition Stress/ MPa (SD)	Bulk Modulus/ MPa (SD)				
PBDDA (0.0) KA070	0	27.5	32.51 (4.94)	19.46 (9.12)	19.45 (2.39)	569.12 (51.90)	33.24 (2.28)	3.87 (0.85)	8.17	114 (1)
PBDDA (0.5) KA203	0.5	24.0	31.98 (5.81)	22.46 (4.47)	19.11 (1.62)	538.49 (29.61)	30.59 (1.65)	2.75 (0.19)	4.66	113 (1)
PBDDA (.0) KA179	1	24.5	27.55 (2.82)	16.51 (2.18)	16.5 (1.90)	447.73 (45.54)	32.51 (2.94)	1.66 (0.55)	6.15	113 (2)
PBDDA (5.0) KA180	5	30.0	19.8 (1.62)	12.67 (1.98)	12.0 (0.88)	322.35 (28.98)	34.31 (4.23)	2.37 (0.46)	5.75	115 (3)
PBDDA (0.0) KA181	10	52.0	12.47 (1.07)	8.27 (0.64)	8.34 (0.92)	260.55 (26.35)	32.78 (3.09)	2.15 (0.40)	6.61	113(2)

Appendix 2.9 Monomer Droplet Size

Sample Name	Set Time/ Min	Compressive Properties				Porosity/ % (SD)	Permeability/ Darcy (SD)	Residual MMA/%	T _g / °C (SD)
		Average Max Stress / MPa (SD)	Strain at Maximum Stress/ % (SD)	Transition Stress/ MPa (SD)	Bulk Modulus / MPa (SD)				
Stir time 1 min (KA145)	24.5	21.38 (1.48)	14.38 (2.49)	10.44 (1.15)	295.4 (64.49)	34.60 (1..36)	3.28 (0.29)	1.30	104
Stir time 3 min (KA068)	21	17.5 (2.84)	14.36 (3.40)	9.92 (2.30)	254.39 (118.05)	30.60 (1.71)	3.19 (0.39)	6.5	108
Stir time 5 min (KA140)	29.5	25.50 (2.83)	15.05 (2.24)	13.41 (0.78)	514.90 (73.79)	30.39 (3.43)	2.81 (0.08)	4.7	87
Stir time 10 min (KA091)	25.5	21.29 (2.03)	14.12 (2.74)	12.92 (1.70)	363.03 (97.86)	28.44 (2.41)	2.44 (0.53)	4..3	104
Stir time 15 min (KA138)	25	24.22 (1.59)	16.98 (1.54)	11.69 (0.89)	426.77 (39.63)	29.95 (2.05)	2.40 (0.09)	4.4	100
Stir time 20 min (KA141)	23	19.56 (2.16)	12.61 (2.00)	10.72 (1.37)	381.05 (55.92)	30.79 (2.18)	3.2 (0.25)	6.0	97
Stir time 30 min (KA139)	20	17.31 (1.51)	11.61 (0.38)	9.03 (0.69)	348.20 (42.14)	30.23 (3.23)	2.5 (0.06)	5.7	98